Atmospheric Environment 223 (2020) 117237

Contents lists available at ScienceDirect

Atmospheric Environment

journal homepage: http://www.elsevier.com/locate/atmosenv

Absorbing aerosol influence on temperature maxima: An observation based study over India

P. Dave [a], M. Bhushan [a,b,*], C. Venkataraman [a,b]

[a] Interdisciplinary Programme in Climate Studies, Indian Institute of Technology Bombay, Mumbai, 400076, India
[b] Department of Chemical Engineering, Indian Institute of Technology Bombay, Mumbai, 400076, India

HIGHLIGHTS

- Temperature maxima in northwest India correlate with absorbing aerosol abundance.
- Absorbing aerosols enhance local and non-local temperature maxima.
- The effect, lasting 1–11 days, exacerbates Tmax-2m during heatwave conditions.

ARTICLE INFO

Keywords:
Absorbing aerosols
Surface temperature maxima
Granger causality

ABSTRACT

Increasing trends in summer-time temperature maxima (Tmax) over India, show consequent increases in the intensity and frequency of heatwave events in recent years. Heat waves have been largely attributed to large-scale meteorological blocking, characterized by subsidence, clear skies and low soil moisture, in observational studies, or greenhouse gas enhancements in model studies. While radiative effects of absorbing aerosols are acknowledged, the association of absorbing aerosols with temperature maxima has not been investigated comprehensively. In the current study, statistical tools (such as correlation and Granger causality) were applied to long term (1979–2013) satellite and ground based observations to evaluate influence of absorbing aerosols on Tmax in north-west India (Tmax-NW). Regional absorbing aerosol index (AAI) in the north-west (AAI-NW) and central-India (AAI-CI) showed co-variability with Tmax-NW, implying connections to both local and non-local absorbing aerosols. The effects persisted on seasonal and heatwave event scales, becoming stronger on heatwave days with presence of enhanced AAI loadings. Causal effects of AAI-NW and AAI-CI were identified on Tmax-NW with a lag of 1–11 days, across multiple years, thereby establishing the influence of absorbing aerosols on heatwave events. The absence of confounding effects of surface pressure on these links suggests that, even during heat wave events linked to atmospheric blocking, absorbing aerosols can further enhance temperature maxima and related heatwave intensity.

1. Introduction

From the mid-1970s, large positive anomalies in summer season temperature maxima have been witnessed over the Indian region (Kothawale et al., 2010; Ratnam et al., 2016; Revadekar and Preethi, 2012), prominently over the north-western, north and central Indian regions (Jaswal et al., 2015; Revadekar and Preethi, 2012). Due to this shift in the distribution of temperature maxima in the positive direction, in recent years increased frequency and intensity of heatwave events, which are defined as days with sustained unusually high temperature, have been observed over Indian region (Pai et al., 2013; Rohini et al., 2016; van Oldenborgh et al., 2018). Heatwave events have been observed globally as well (Ding et al., 2010; Perkins et al., 2012) and have severe socio-economic impacts on daily lives of people. Heatwave related mortalities in India have typically exceeded those from any other natural hazard (De et al., 2005). Further, in the very recent past in year 2015, one of the rarest and deadliest heatwave events was witnessed across India which resulted in about 2500 deaths (Burton, 2015).

Different studies have identified multiple causes behind observed increase in global temperature and consequently heatwave phenomena. The observed increase in surface temperature has largely been attributed to emission of green-house gases (GHGs) acting through altered

* Corresponding author. Interdisciplinary Programme in Climate Studies, Indian Institute of Technology Bombay, Mumbai, 400076, India.
E-mail address: mbhushan@iitb.ac.in (M. Bhushan).

https://doi.org/10.1016/j.atmosenv.2019.117237
Received 9 August 2019; Received in revised form 25 November 2019; Accepted 18 December 2019
Available online 23 December 2019
1352-2310/

atmospheric conditions. Over India, Ratnam et al. (2016) identified two types of heatwaves-one occurring over north-west India linked with atmospheric blocking over the north Atlantic and another occurring over eastern coast linked with the Matsuno-Gill response. Rohini et al. (2016) attributed increased variability of heatwave events over north-west India to tropical Indian Ocean and central Pacific sea surface temperature anomalies.

In literature, there is broad agreement about the role of GHGs in increasing the surface temperature maxima (Bindoff et al., 2013; Dileepkumar et al., 2018; Lashof and Ahuja, 1990). However, there is still no consensus regarding the role of aerosols in altering the surface air temperature across the globe. On one hand, studies have reported enhanced surface cooling with increased aerosol loading (Krishnan and Ramanathan, 2002; Mickley et al., 2012; Padma Kumari et al., 2007), while on the other hand positive forcing during heatwaves due to enhanced absorbing aerosols has also been reported (Chazette et al., 2017; Lyamani et al., 2006). Apart from these observation based studies, several modelling studies related with absorbing aerosols, have found that positive radiative forcing potentially offsets the cooling induced by scattering aerosols (Jacobson, 2002). Ban-Weiss et al. (2012) showed that the black carbon (BC) induced heating effect is sensitive to altitude i.e. BC causes heating in the atmospheric layer in which it is present while cooling in the layers below.

Several works in the literature have also investigated the spatial scales at which aerosols affect the surface temperature. Krishnan and Ramanathan (2002) showed an asymmetric cooling during the dry season (winter and pre-monsoon), suggesting its links to enhanced aerosol forcing. They pointed out the possibility of surface warming at regions non-local to the aerosol haze, to balance local cooling. Bond (2007) showed that the heating induced by aerosols is not limited to the source of emission and could extend several hundred kilometres around "*hot-spots*" of absorbing aerosol abundance. Only 10–30% of the total forcing occurred within the "*hot-spots*" while the rest of the forcing was spread across a larger region (Bond, 2007).

Possible links of absorbing aerosol enhancements to high temperatures over India are only beginning to be explored (Mondal et al., 2019; Purnadurga et al., 2018), however, an observational study has not yet been undertaken. A complex mixture of scattering and absorbing aerosols has been reported over the Indian region (Habib et al., 2006) and response of surface temperature to such mixed aerosols has not been investigated in literature. Considering this, the aim of the current work is to investigate the modulation of surface maximum temperature by absorbing aerosols over the Indian region. Towards this end, a long-term dataset (1979–2013), of satellite and ground based observations is analysed using statistical approaches. Correlation and Granger causality (Granger, 1969) are used to understand co-variability and to identify and establish causality between enhanced absorbing aerosols and temperature maxima.

The structure of the paper is as follows: in Section-2 data and methods are described; in Section-3 results and discussions are presented on the scales of aggregated seasonal data, i.e. March to June (MAMJ), across years, year-wise seasonal analysis and heatwave events analysis. Finally, Section-4 concludes the paper with a discussion of implications of findings in this work.

2. Data and methods

2.1. Data

Absorbing aerosol data were obtained from TOMS-OMI satellite for MAMJ for 1979–2013 over India (66.5–100.5E; 6.5–36.5N) at 1° x 1° resolution. The TOMS data, which are available at 1° x 1.25° resolution, are re-gridded to 1° x 1° resolution using climate data operator (Schulzweida, 2019). Here, 1° is approximately equal to 100 km and a region of 1° x 1° is defined as a pixel. This is the longest length data available for absorbing aerosols and has been widely used in various studies (Esposito et al., 2001; Habib et al., 2006; Herman et al., 1997; Jones and Christopher, 2007; Sarkar et al., 2006).

Absorbing aerosols are retrieved in terms of Absorbing Aerosol Index (AAI) which measures the presence of absorbing aerosols in the atmosphere (Torres et al., 1998). The AAI data were downloaded from the following NASA website: https://giovanni.gsfc.nasa.gov/giovanni/. The TOMS-AAI data were used for the time period 1979–2004 and OMI data were used for the time period 2005–2013. Though AAI is a good qualitative measure of absorbing aerosols, quantitatively AAI is sensitive to the height at which absorbing aerosols are present in the atmosphere (Torres et al., 1998), being more sensitive to dust or biomass burning plumes, than to surface concentrations.

Gridded daily temperature product at 1° x 1° resolution for March–June from 1979 to 2013, released by India Meteorological Department (IMD), is used for surface daily maximum temperature (Tmax) and surface daily minimum temperature (Tmin). The temperature data are released by IMD as a final product after re-gridding from irregularly located meteorological stations to a regular grid using Shephard's interpolation method (Srivastava et al., 2009).

For the surface pressure and geopotential height, Modern-Era Retrospective Analysis for Research and Applications, Version 2 (MERRA-2) (Gelaro et al., 2017) data were used for the period of 1980–2013.

2.2. Methods

2.2.1. Anomaly computation

For each year, daily absolute pixel values of all the variables are transformed to anomalies. This is achieved by calculating deviation of absolute value from long-term daily mean for that particular day. Details of anomaly calculation are described in Supporting Information (section-S1).

2.2.2. Trend-computation

For each year seasonally averaged anomaly values of daily Tmax and AAI, are calculated for each pixel. Using these seasonal averaged anomalies, temporal trends of daily AAI and Tmax are obtained. The statistical significance of trends is tested at $\alpha = 0.05$ (95% confidence level).

2.2.3. Correlation analysis

The augmented Duckey-Fuller (ADF) test (Fuller, 1995) was performed to check the stationarity of AAI and Tmax series before calculating the correlation. The alternate hypothesis in ADF test is that the series is stationary. In order to identify Tmax region(s) exhibiting statistically significant correlation with AAI, correlations were computed using following steps:

1. At each pixel a time series of AAI was obtained by concatenating the seasonal daily observations of AAI anomaly for the time period of study. Thus, for a given pixel we obtained a time series of length 4270 days (35 years x 122 days/year). The process was repeated for all the pixels (N). Similarly, time series at all the pixels (N) were obtained for Tmax as well.
2. For a given pixel (let's say N_1) the AAI anomaly correlation with Tmax at all the pixels (N) was calculated. Thus, N correlations were obtained for the given pixel N_1. This process was repeated for all the pixels and hence totally N^2 correlations were obtained.

Along with the correlation, distance between pixel-pairs is obtained using Haversine formula (Brummelen, 2013). The statistical significance of correlation is tested at $\alpha = 0.05$.

2.2.4. Causality analysis

To investigate causal effects of AAI on Tmax, Granger causality (GC) (Granger, 1969) approach is used, which considers past information of

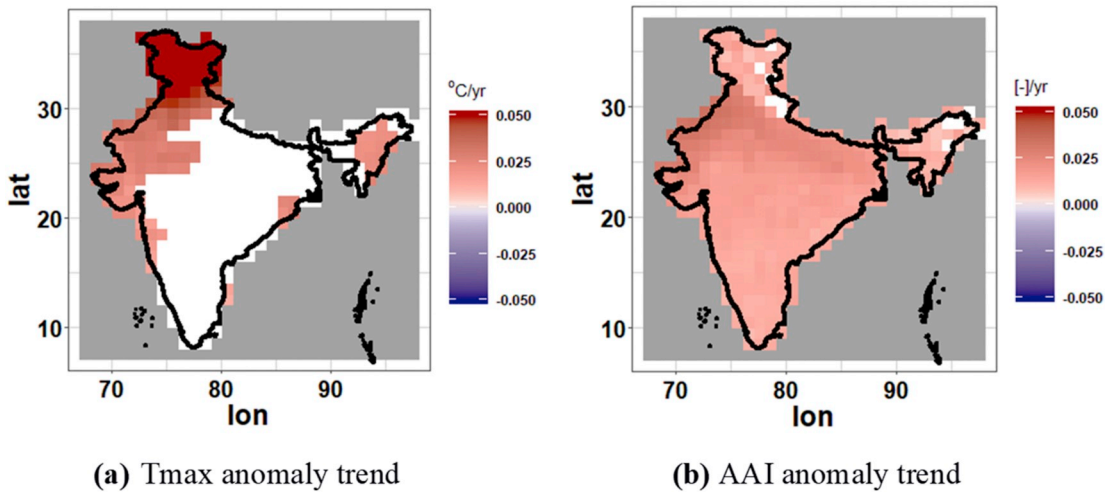

(a) Tmax anomaly trend **(b)** AAI anomaly trend

Fig. 1. Daily maximum temperature (Tmax) and columnar absorbing aerosols (AAI) seasonal average (MAMJ) anomaly trends for years 1979–2013.

variables to establish causality. For the causality analysis the time series have to be stationary. ADF test was performed to check the stationarity of the series (Table-S1). The Temperature (T) at a time *t* can be modelled by regressing Temperature upon past values of AAI and Temperature, as shown in Eq. (1)

$$T(t) = \alpha_0 + \sum_{i=1}^{l} \beta_i AAI(t-i) + \sum_{j=1}^{m} \gamma_j T(t-j) + \varepsilon(t) \quad (1)$$

Here, α_0, β_i and γ_j are the coefficients, $\varepsilon(t)$ is the unexplained part (labelled error) and 'l' and 'm' are the lags.

Another model of Temperature at a time *t* is developed in which the Temperature at *t* is regressed only upon past values of Temperature.

$$T(t) = \tilde{\alpha_0} + \sum_{j=1}^{\tilde{m}} \tilde{\gamma}_j T(t-j) + \tilde{\varepsilon}(t) \quad (2)$$

The model represented in Eq (1) and Eq (2) are unrestricted and restricted model, respectively. In Granger causality the error variance in restricted model ($\sigma^2_{\tilde{\varepsilon}}$) is compared with the decrease in error variance in unrestricted model ($\sigma^2_{\tilde{\varepsilon}} - \sigma^2_{\varepsilon}$) statistically. If the decrease in error variance in Eq. (1) i.e. σ^2_{ε} is significantly smaller than the error variance $\sigma^2_{\tilde{\varepsilon}}$ then we can say that AAI Granger causes Temperature, as inclusion of AAI in modelling of Temperature improves the prediction of Temperature.

Details of Granger causality can be found in Supporting Information (section-S2). Reverse causality of Tmax on AAI is also tested to rule out any feedback in the system. The F-statistics along with P-value for the causality tests between AAI-NW and Tmax-NW, and AAI-CI and Tmax-NW have been reported in Table-S2 and Table-S3 respectively for the lags selected for further analysis. If the P-value was greater than $\alpha = 0.01$, we fail to reject the null hypothesis of no-causality.

3. Results and discussion

3.1. Analysis of aggregated data across years

Data of daily Tmax and AAI absolute values and anomalies are composited for MAMJ months for the years 1979–2013, to perform trends and correlation analysis.

3.1.1. Temperature and absorbing aerosol anomaly trends

Fig. 1 depicts the trends across years of season (MAMJ) mean Tmax and AAI anomaly across India. Anomalies in Tmax showed increasing trends (Fig. 1a) at ~0.02 °C-yr^{-1}. A decadal increasing trend of daily maximum temperature has also been reported by Ross et al. (2018) becoming prominent after 1980. The increase in Tmax is mostly confined to north and north-western India, along with a few areas in north-eastern India. Increase in AAI is spread across the whole country with approximate rate of increase in anomaly value of AAI being ~0.045yr^{-1} (Fig. 1b). The increase in AAI is consistent with the literature (Babu et al., 2013; Habib et al., 2006; Ramachandran et al., 2012). The observed increasing trends of Tmax and AAI provide a motivation to explore the possible link between co-variability and causality of Tmax and AAI.

3.1.2. Correlation between anomalies in AAI and Tmax

Using the ADF test time series of AAI and Tmax were found to be stationary. The spatial plot of P-value obtained for ADF-test has been shown in supplementary information (Figure-S2). As the P-values are <0.01, we reject the null hypothesis of non-stationarity.

A pair-wise correlation between AAI anomaly and Tmax anomaly is calculated and regions with significant and strong correlations are identified (Fig. 2). The deep red colour in Fig. 2 represents positive correlation while blue colour represents negative correlation.

In Fig. 2(a) correlation of Tmax with AAI, where AAI is located within 250 km of Tmax, is shown and in Fig. 2(b) AAI correlation with Tmax, where Tmax is located within 250 km of AAI, is shown. The correlation of AAI with Tmax (Fig. 2b) was found to be positive for the whole country barring some regions in southern India. This implies that with increase in AAI an associated increase in Tmax is observed in most regions across the country.

Similar to Fig. 2(a), Fig. 2(c) depicts the Tmax correlation but with AAI regions located at least 250 km away from Tmax region. Similarly, Fig. 2(d) depicts the AAI correlation but with Tmax regions located at least 250 km away.

One would expect the correlations depicted in Fig. 2(a) and Fig. 2(c) to be exactly same as correlations depicted in Fig. 2(b) and Fig. 2(d) respectively, as the correlations are symmetric in nature. However, the correlation differs in Fig. 2(a) with Fig. 2(b), and Fig. 2(c) with Fig. 2(d) due to the fact that for a given location Tmax can be correlated with AAI from multiple locations and vice-versa. In such scenario, an average correlation is computed and depicted in Fig. 2. The computation of average correlations is illustrated as follows: in Fig. 2(a) daily Tmax depicted with red square exhibits correlation with absorbing aerosols located in central-Indian region depicted with green triangles. In such scenario, an average correlation of Tmax with AAI from multiple locations (three triangles) is computed and depicted in Fig. 2(a). Similarly, in Fig. 2(b) absorbing aerosols at central-Indian region can exhibit correlation with daily Tmax from multiple locations in the north-western

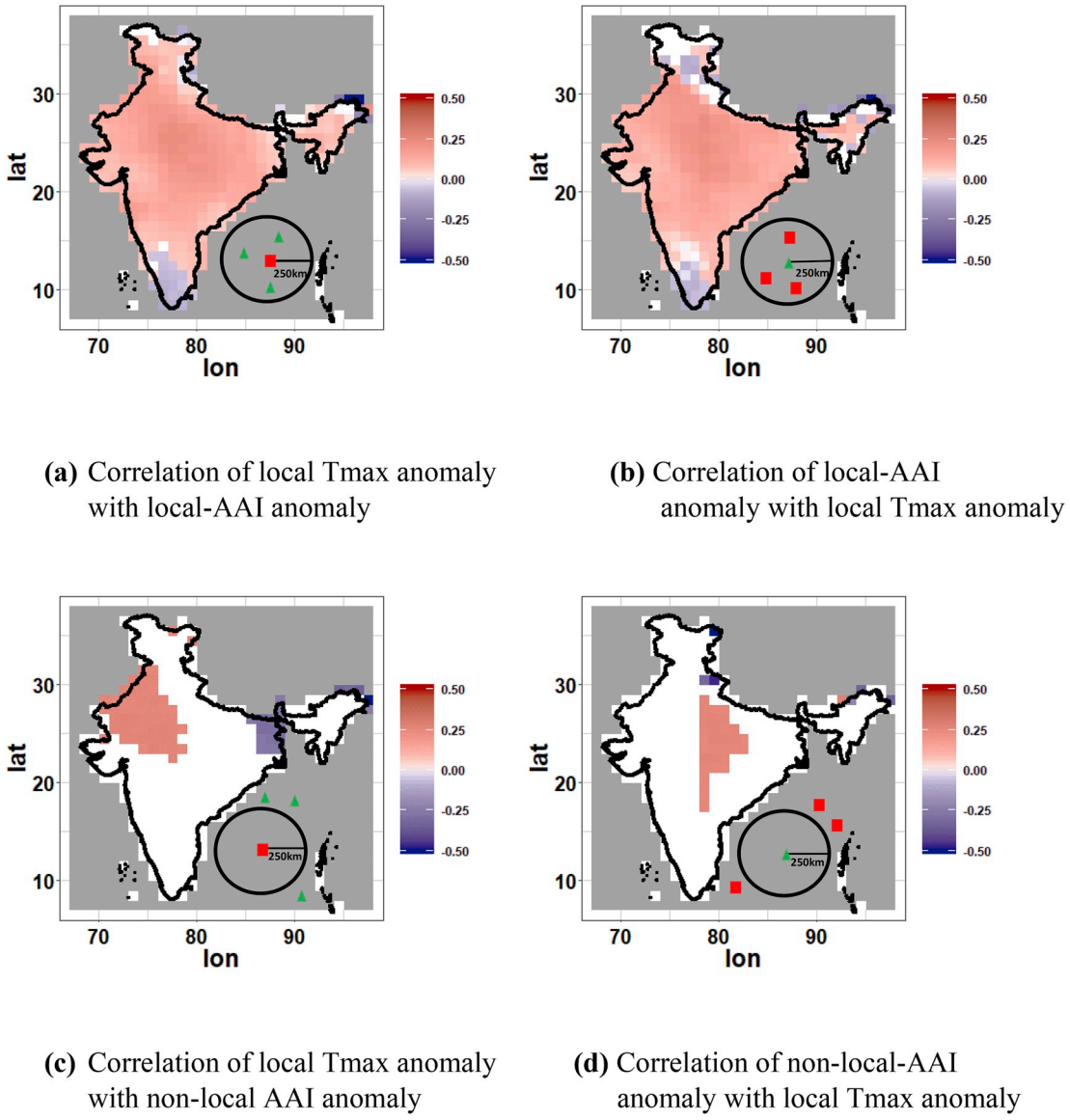

Fig. 2. Correlation analysis between daily maximum temperature anomaly (Tmax) and columnar absorbing aerosols anomaly (AAI) for years 1979–2013: Fig. 2(a) depicts region of Tmax exhibiting statistically significant (significance level $\alpha = 0.05$) correlation with absorbing aerosols located within 250 km. Fig. 2(b) depicts statistically significant AAI correlation with Tmax located within 250 km Fig. 2(c) and Fig. 2(d) are similar to Fig. 2(a) and Fig. 2(b), respectively but with correlation calculated only with distance greater than 250 km and only the strong correlations (correlation $> |0.25|$) are shown. The strength of correlation is shown with the colorbar. Here, green triangle represents AAI pixel and red square represents Tmax pixel location. From Fig. 2(a), we can see that Tmax can exhibit statistically significant correlation with AAI from multiple locations within 250 km. Similarly, AAI at a location can be correlated with temperature at multiple locations (Fig. 2 (b)) within 250 km. In such a scenario, average correlation of Tmax and AAI is depicted in Fig. 2(a) and Fig. 2(b), respectively. Fig. 2(c) and Fig. 2(d) are similar to Fig. 2(a) and Fig. 2(b), with pixels located outside 250 km.

region. In this scenario, an average correlation of AAI with Tmax is computed and depicted in Fig. 2(b). The major outcomes of this analysis are (i) the identification of regions all over India wherein Tmax enhancements exhibit significant correlation with absorbing aerosols from the same region (ii) the identification of the north-west region wherein Tmax exhibits correlations with absorbing aerosol enhancements in the central India region.

It can be seen that the absorbing aerosols at locations far away from location of Tmax can also exhibit significant positive correlation with Tmax, and thus AAI shows a positive covariability with Tmax. While the correlations of AAI with Tmax are found to be spread across India (Fig. 2 (a)) for AAI located within 250 km radius of Tmax region, in case of AAI located far away from Tmax region (beyond 250 km), the correlations of AAI with Tmax are found to be restricted to temperature belonging to north-western region (Fig. 2(c)) and the aerosols located over central-India.

The Tmax anomaly region as identified in the current work mostly comprised of Thar desert which has been witnessing large variability in maximum temperature (Ratnam et al., 2016) along with increased frequency and duration of heatwave events (Rohini et al., 2016). In the 2003 European heatwave, absorbing aerosols were shown to aggravate the heatwave conditions (Lyamani et al., 2006). During European heatwave, desert dust particles combined with forest fire and biomass burning aerosols transported to Spain from Africa identified using back trajectory analysis (Lyamani et al., 2006). The presence of atmospheric blocking with enhanced absorption by these mixed aerosols may have contributed in the intensification of 2003 European heatwave (Pere et al., 2011). Using observational and urban climate model calculations, Cao et al. (2016) identified aerosol haze layer as one of the contributor to urban heat island across China. They attributed summer night-time

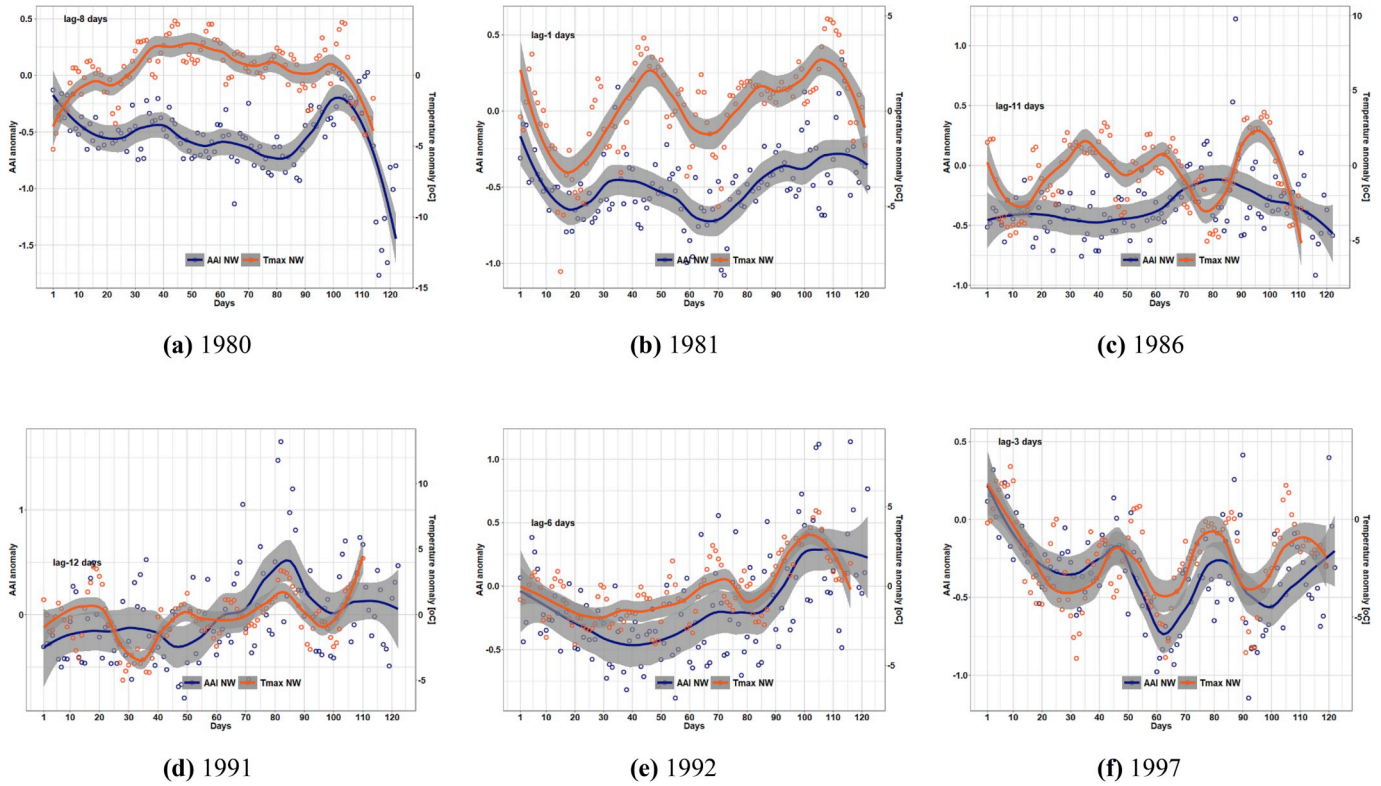

Fig. 3. Spatially averaged temporal plot of AAI-NW (red color) and Tmax-NW (blue color) for years with causality from AAI-NW to Tmax-NW. The Tmax-NW values are shifted as per the lag identified using causality analysis. The smoothed curves are generated using loess method with span of 0.75 (http://www.R-project.org/) and the grey region depicts 95% confidence interval. (For interpretation of the references to color in this figure legend, the reader is referred to the Web version of this article.)

temperature enhancement over urban heat island to increased aerosol haze layer. However, they didn't find any correlation between daytime temperature and aerosol haze layers. In the current work, it is also interesting to note that not only local but non-local aerosols also showed positive co-variability with daily maximum temperature in the north-western region. On a decadal scale, in particular during spring season, the presence of extended brown haze over northern Indian Ocean and South Asia which absorbs the solar radiation has been reported by Ross et al. (2018). It is suggested that aerosol-induced changes in regional circulation, wherein heated air from the northern-eastern and central India rises and sinks over north-western India, increase the temperature over north-western India due to subsidence and compression (Ross et al., 2018).

For the rest of the article, regions depicted in deep red colour in Fig. 2 (c) and Fig. 2(d) will be referred to as "NW" and "CI" respectively, where NW stands for north-west India and CI stands for central-India. The variables corresponding to these regions are named accordingly. E.g. AAI anomaly in CI and Tmax anomaly in NW region are named as AAI-CI and Tmax-NW respectively. These initial results indicate local and non-local positive correlations between AAI and Tmax but the analysis relied on anomaly data aggregated across years. However, heatwave events are sub-seasonal scale phenomena (Perkins, 2015) and thus the effect of absorbing aerosols on daily Tmax is further investigated for each year individually and further analysis is focused on the "NW" and "CI" regions as identified during the initial analysis.

3.2. Yearwise causality analysis between Tmax-NW and AAI-CI and AAI-NW

Although Tmax is found to be correlated with AAI located in NW and CI regions, mere correlation does not imply causation (Pepperberg, 2001). Causality between AAI anomaly and Tmax anomaly is investigated using Granger causality (Granger, 1969) approach applied on area averaged seasonal AAI-NW anomaly, AAI-CI anomaly and Tmax-NW anomaly for each year. The AAI-NW, AAI-CI and Tmax-NW were found to be stationary using ADF test at $\alpha = 0.1$ except for the series AAI-CI for the year 1979 (P-value = 0.138; Table-S1) and we excluded this series for further analysis.

The F-statistics and P-value for AAI-NW to Tmax-NW have been reported in Table-S2 and for AAI-CI to Tmax-NW have been reported in Table-S3. Here, using F-statistics we can conclude that for the lags mentioned in Table-S2 and Table-S3, causality exists for AAI to Tmax while it is absent other way round.

Spatially averaged temporal series for years for which causality exists between AAI-NW and Tmax-NW, and AAI-CI and Tmax-NW are shown in Fig. 3 and Fig. 4, respectively. From Tables S2 and S3 in supplementary information, we can see that the F-statistics is large for the AAI to Tmax causality as compared to Tmax to AAI causality. The causality from AAI-NW to Tmax-NW was identified for 15 years with lags varying from 1 to 14 days (with median lag of 6 days) (Fig. S1(a)). The causality from AAI-CI to Tmax-NW was identified for 23 years with lags varying from 1 to 15 days (with median lag of 5 days) (Fig. S1(b)). Past studies (Rohini et al., 2016) have characterized heatwave events with persistence high blocking resulting into stable atmospheric conditions, which can last for days to weeks. The persistent blocking does not allow the absorbing aerosols to dissipate which usually have a lifetime of days to weeks as well (BC lifetime: 3–14 days (Bond et al., 2013; Cape et al., 2012). Past studies have additionally reported dust lifetime of 4–6 weeks (Mahowald et al., 2014)). The co-existence of stable atmospheric conditions along with absorbing aerosols for days to weeks could be the reason behind the observed effect of absorbing aerosols on Tmax over a period of 1–11 days. Further, in both these cases causality from Tmax

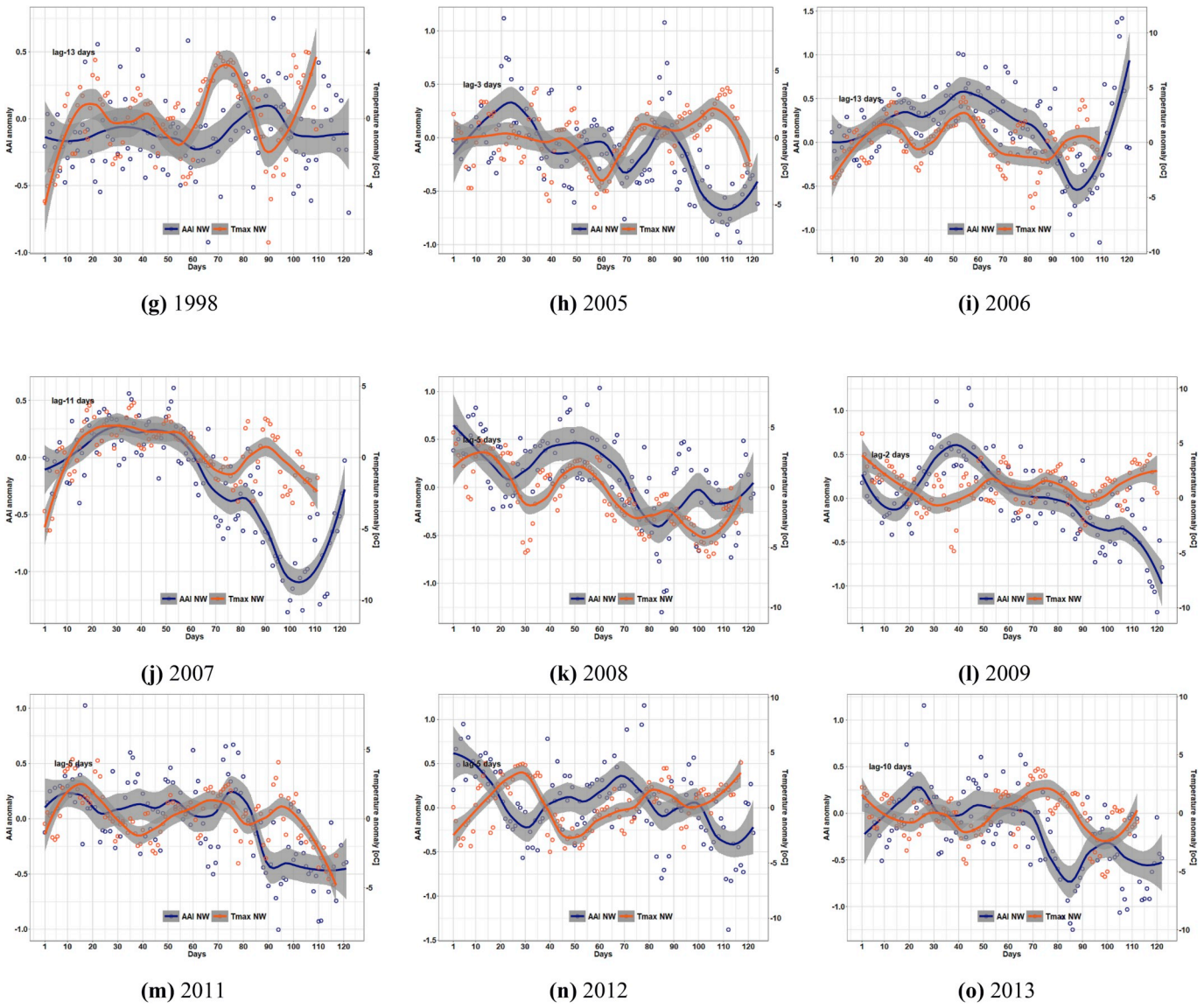

Fig. 3. (*continued*).

anomaly to AAI anomaly was found to be absent for the lags selected for further analysis. The causality analysis strengthens the argument that both changes in locally (NW) and non-locally (CI) absorbing aerosols contribute to the observed changes in daily Tmax, and rules out possibility of spurious correlation between Tmax and AAI.

The co-variability of Tmax-NW with AAI-NW (shifted by lag which was identified by causality analysis) can be seen clearly from Fig. 3 (b,k, m), where the peaks and troughs of Tmax-NW (local daily maximum temperature) can be observed to vary in cohort with AAI-NW (local absorbing aerosols). Similar to the Tmax-NW variability with local absorbing aerosols (AAI-NW), Tmax-NW can be seen to follow the pattern of non-local absorbing aerosols (AAI-CI) prominently in Fig. 4(b, c,g,i,j,q). Fig. 3 and Fig. 4 show that the variations in Tmax bear a significant correlation with AAI variability both locally and non-locally. However there are instances where AAI and Tmax do not follow each other such as Fig. 3(i,o) and Fig. 4(n,o,p). In order to investigate the average effect of AAI on temperature across heatwave years, cumulative frequency of correlation is computed and results are discussed in Supporting Information (Section-S3). The analysis on yearly scale substantiates the findings of positive correlation of Tmax-NW with both local and non-local absorbing aerosols found at climatic scale (Section 3.1.2) and suggests that the co-variability persists on seasonal time scale as well. We next perform further analysis at a finer scale by considering data only for heatwave days.

3.3. Analysis during heatwave events

The temperature during the heatwaves remains exceptionally high, the intensity and frequency of which is increasing (Krishnan and Ramanathan, 2002; Rohini et al., 2016) and AAI absolute and anomaly values have been increasing across heatwave years (Fig. S4). Along with the increased frequency and intensity, we found that the absorbing aerosol anomaly both local as well as non-local was also high during the heatwaves (Figs. S5(a and d)). It is also interesting to note that the local absorbing aerosols anomaly was negative during initial heatwave years (1979–1999; Fig. S5(b)) while in recent heatwave events (2000–2013) highly positive absorbing aerosol anomaly have been found (Fig. S5(c)). For non-local absorbing aerosols the anomaly was positive throughout the time period of study (Figs. S5(e and f)), however an enhancement of absorbing aerosols anomalies has been identified during recent times (Fig. S5(f)).

In order to investigate the absorbing aerosol influence on Tmax-NW during heatwave days, correlation analysis similar to that shown in Fig. 2 is performed. However the analysis is restricted to Tmax from NW

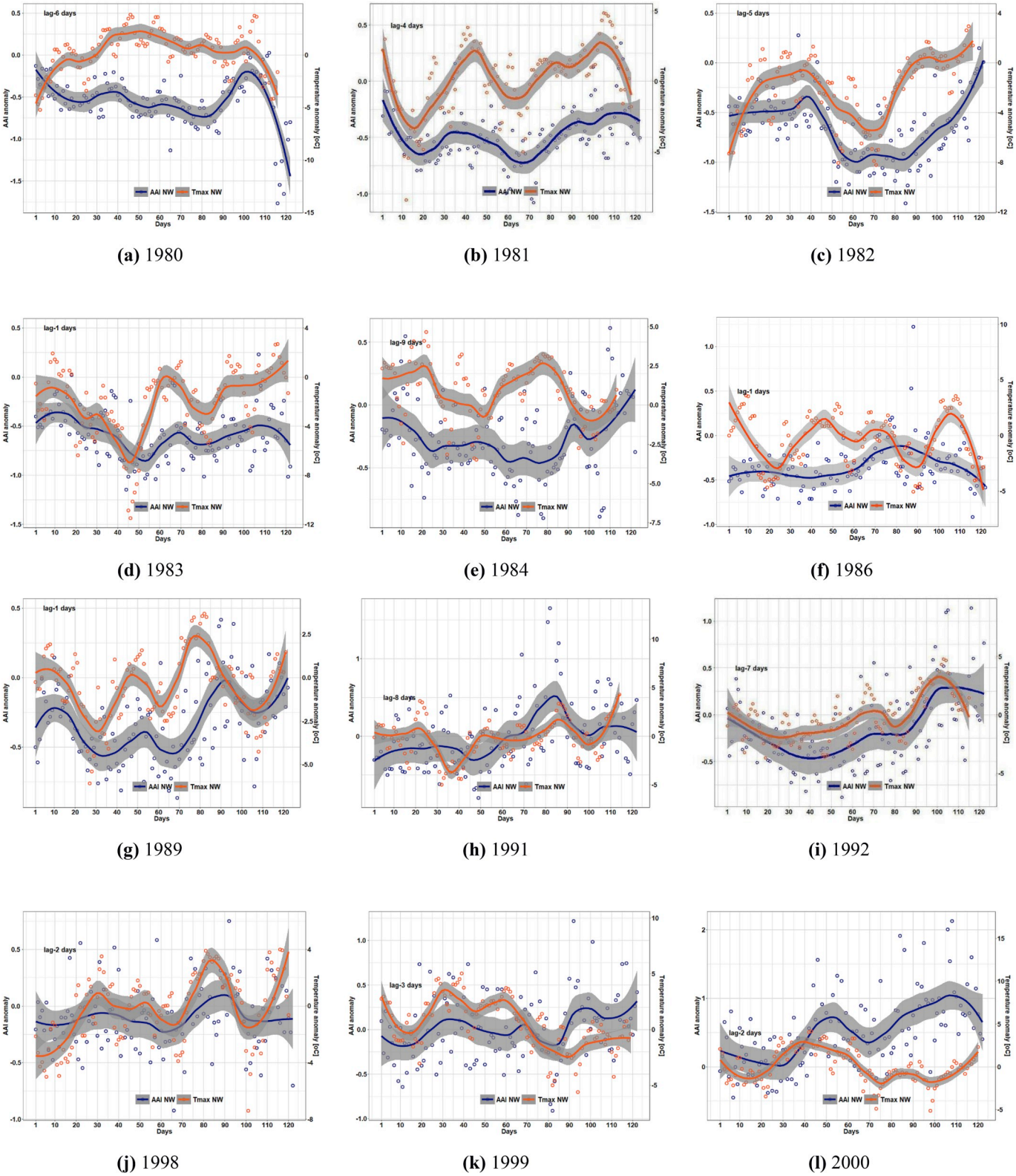

Fig. 4. Spatially averaged temporal plot of AAI-CI (blue color) and Tmax-NW (blue color) for years with causality from AAI-CI to Tmax-NW. The Tmax-NW values are shifted as per the lag identified using causality analysis. The smoothed curves are generated using loess method with span of 0.75 (http://www.R-project.org/) and the grey region depicts 95% confidence interval. (For interpretation of the references to color in this figure legend, the reader is referred to the Web version of this article.)

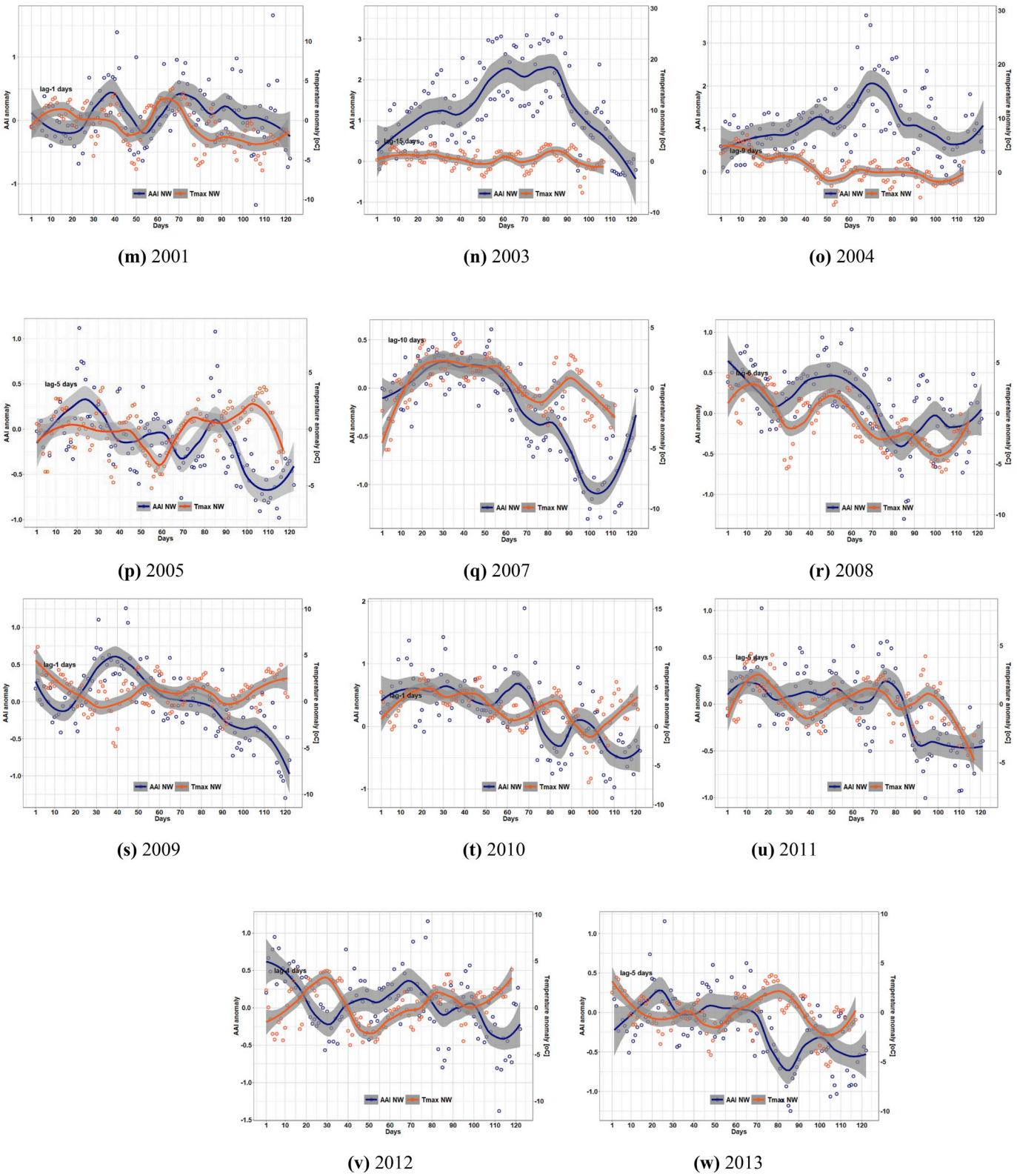

(m) 2001 **(n)** 2003 **(o)** 2004

(p) 2005 **(q)** 2007 **(r)** 2008

(s) 2009 **(t)** 2010 **(u)** 2011

(v) 2012 **(w)** 2013

Fig. 4. (*continued*).

and AAI from NW and CI regions, and only for heatwave days identified by Ratnam et al. (2016) and Rohini et al. (2016). Rohini et al. (2016) used the Excess Heat Factor and 90th percentile of maximum temperatures while Ratnam et al. (2016) used heatwave identification criteria defined by Indian meteorological department to identify the heatwave. A list of identified heatwave events is provided in Table-S4.

From Fig. 5, the correlation of Tmax-NW with AAI-NW, and of Tmax-NW with AAI-CI is seen to be positive and thus it can be said that the absorbing aerosols reinforce the daily maximum temperature during heatwave days both locally as well as non-locally. This implies that the absorbing aerosols contributed to exacerbating heatwave conditions.

Increasing heatwave trends are identified over north-western India,

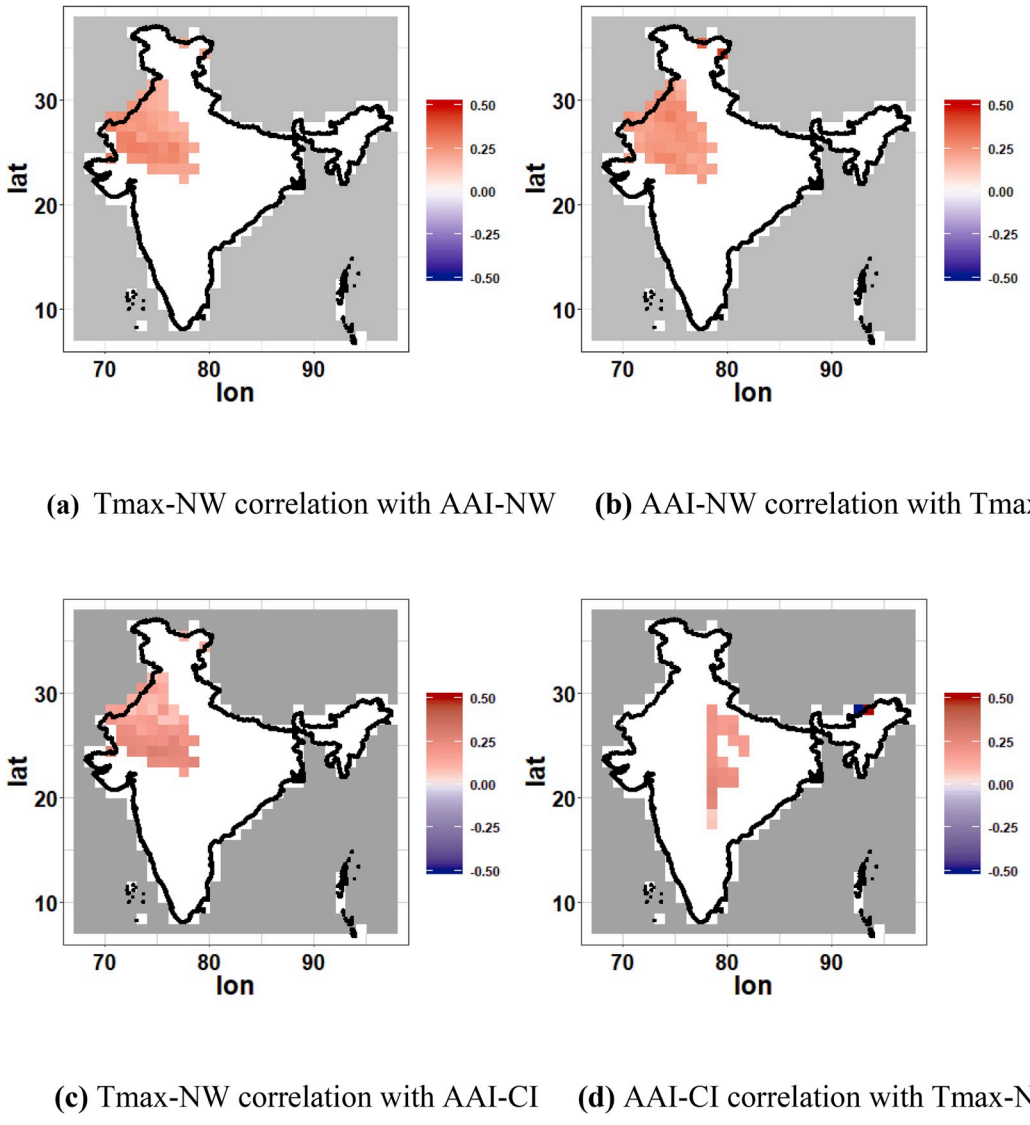

Fig. 5. Same as Fig. 2 but only for heatwave days. Correlation coefficient magnitude is larger than that in Fig. 2, showing a persistent relationship between enhanced daily maximum temperatures with enhanced absorbing aerosols, on the temporal scale of heat-wave periods.

which is a desert region with low soil moisture content during heatwave events (Rohini et al., 2016, see Fig. 4(b) therein). It is quite possible that due to low soil moisture content and direct solar radiation absorption by absorbing aerosols, the latent heat flux decreases giving rise to increase in sensible heat flux which intensifies the temperature increase. Also heatwave events are associated with high pressure zone in general (Perkins, 2015) and in particular heatwave events over India are associated with a sinking motion (Ratnam et al., 2016), which doesn't allow advection of aerosols, which can subsequently contribute to temperature rise as explained earlier. In this manner the local absorbing aerosols can affect the local temperature. However, this mechanism does not explain the non-local effect of aerosols on local temperature. On a climatic scale, a temperature rise can be experienced at a location away from the location of aerosol emission due to transfer of heating (Ross et al., 2018), but so far no such dynamical mechanisms have been explored for seasonal or sub-seasonal time scale. Bond (2007) also showed, through model simulations, a possible effect of absorbing aerosols on temperature enhancements at locations far away from source of aerosol emission. In the current work, using observational data, we found enhancement of temperature maxima by local as well as non-local absorbing aerosols. Local absorbing aerosols can directly affect the local temperature by diabatic heating of the surface atmosphere. Modulation of temperature by non-local absorbing aerosols, through alternate mechanisms such as circulation changes leading to subsidence (Ross et al., 2018), or a balance between spatially asymmetric heating and cooling (Krishnan and Ramanathan, 2002), need further exploration. However, investigation of the mechanisms is beyond the scope of the current work and must rely on future modelling studies.

3.4. *Surface pressure as a confounding factor*

During the heatwave events, anti-cyclonic conditions prevail over India which is linked to increase in temperature due to adiabatic compression (Rohini et al., 2016). In order to account for the confounding effect of pressure on both aerosols and temperature, we segregated the surface pressure anomaly (SP-NW) into 11 bins ranging from −500hPa to 500 hPa. For each bin observation count, mean, standard deviation along with correlations between AI and Tmax and Tmin are summarized in Table-S5. The statistically significant correlations ($\alpha = 0.1$) are highlighted in bold in the table. From Table-S5, we can observe that over the NW region, SP-NW shows either small or no statistically significant correlation with Tmax and Tmin. Additionally, for each bin of SP-NW anomaly AAI-NW exhibits no statistically significant correlation with surface pressure.

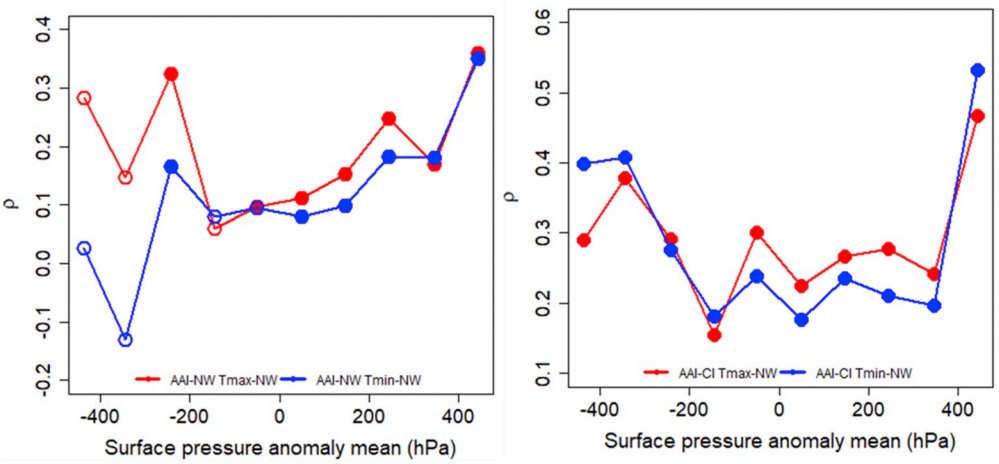

(a) Correlation of AAI-NW with Tmax-NW and Tmin-NW (b) Correlation of AAI-CI with Tmax-NW and Tmin-NW

Fig. 6. Variation of AAI correlation with Tmax and Tmin with surface pressure bins. (a) The red line represents correlations between AAI-NW with Tmax-NW and blue line represents correlations between AAI-NW and Tmin-NW. The filled circle represents statistically significant correlation coefficient ($\alpha = 0.1$). (b) Same as (a) with correlation depicted for AAI–CI–Tmax-NW and AAI–CI–Tmin-NW. (For interpretation of the references to color in this figure legend, the reader is referred to the Web version of this article.)

On the contrary, AAI-NW shows statistically significant correlation with Tmax-NW and Tmin-NW. Similar, observations can be made for AAI-CI in regard to correlation with Tmax-NW and Tmin-NW. The absence of correlation between surface pressure and AAI and presence of positive correlation between AAI with Tmax and Tmin implies that increase in AAI itself augments the increase in temperature. It is also interesting to note that during the heatwave the correlation of Tmax with surface pressure is not statistically significant while it is statistically significant and positive with AAI-NW and AAI-CI. Considering this, during heatwaves which are associated with atmospheric blocking, role of AAI in exacerbating the heatwave conditions cannot be ruled out. Moreover, the varying correlation could be the reason behind observed varying lags in Figure-S1. Further, we also calculated the partial correlation of Tmax and Tmin with both AAI-NW and AAI-CI with given surface pressure for overall and heatwave days (Table-S6). From Table-S6, we can see that AAI exhibits positive correlation with Tmax and Tmin both locally and non-locally.

Further, in Fig. 6(a) we have shown the variation of correlation between AAI-NW and Tmax-NW (red color), and AAI-NW and Tmin-NW (blue color). The statistically significant correlations ($\alpha = 0.1$) are depicted with filled circle. Fig. 6(b) is same as Fig. 6(a) with AAI-NW replaced with AAI-CI. From Fig. 6, we can see that the correlation between AI-Tmax varies with SP-NW. This could lead to varying effect of absorbing aerosols on Tmax as depicted in Fig. 3 and Fig. 4.

Further from Fig. 6, we note that the correlation of AAI with Tmax and Tmin differs where the correlation of AAI with Tmax is high as compared to Tmin. The difference in correlation magnitude indicates absorption of shortwave radiation by absorbing aerosols during the day time thereby imparting more heating during the day temperature (Tmax) as compared to night time temperature (Tmin). To summarize, absorbing aerosols absorb the incoming radiation and heat up the atmosphere; moreover, during the heatwave events due to stationary atmospheric conditions absorbing aerosols do not dissipate quickly and exacerbate the heatwave conditions due to absorption of short-wave radiation. However, this does not explain the non-local effect of aerosols in modulating the local temperature and this requires further study to unravel the mechanisms.

4. Conclusions and implications

The goal of this work was to understand the relationship between absorbing aerosols and summer time maximum temperature and temperature extremes in north-west India. Previous modelling studies infer that trends in extreme temperature in India are masked significantly by cooling due to aerosols blocking sunlight or due to increased evapotranspiration resulting from extensive irrigation (Purnadurga et al., 2018). In the current study, statistical tools were applied to long term (1979–2013) satellite and ground based observations, to evaluate the relationship of absorbing aerosols and temperature maxima in north-west India. Regional absorbing aerosols in the north-west (AAI-NW) and central-India (AAI-CI) showed co-variability with Tmax in north-west India, implying both local and non-local heating effects. The non-local effect of AAI-CI on Tmax-NW showed co-variability with a lag of 1–8 days. The effects persisted on seasonal and heatwave event scales, becoming stronger on heatwave days. Causal effects of AAI-NW on Tmax-NW were identified with a lag of 1–11 days, across multiple years, thereby implying absorbing aerosol influence heatwave events. During the recent heatwave events high absorbing aerosols loading have also been found.

While absorbing aerosols exerting a purely local effect could lead either to surface cooling or heating, based on altitude of aerosol layers, this work suggests that cumulative non-local and local effects, bear a causal relationship to temperature enhancement in the Indian northwest.

Given the recent increase in intensity and frequency of northwest India heatwave events (Rohini et al., 2016) along with increasing trends in anthropogenic emissions over India (Ohara et al., 2007), the current findings have significant implications for action on adaptation and mitigation measures concerning heatwave events. Findings in this work have significant implications to coordinate climate and air-quality action on regional scales.

Author contributions

MB and CV provided the study concepts and interpretation of the results; PD carried out the data analysis, with guidance from MB and CV; PD prepared the figures; MB, CV and PD wrote the manuscript.

Declaration of competing interest

The authors declare that they have no known competing financial interests or personal relationships that could have appeared to influence the work reported in this paper.

Acknowledgments

The Centre of Excellence in Climate Studies project grant at IIT Bombay, from the Department of Science and Technology (DST-CoECS), supported computing systems and assistantship for Prashant Dave. CV acknowledges partial support from the NCAP-COALESCE project (No. 14/10/2014-CC, Vol II) funded by the Ministry of Environment, Forests and Climate Change. We would also like to acknowledge R Core Team, 2018. The AAI data were downloaded from the following NASA website: https://giovanni.gsfc.nasa.gov/giovanni/.

Appendix A. Supplementary data

Supplementary data to this article can be found online at https://doi.org/10.1016/j.atmosenv.2019.117237.

References

Babu, S.S., Manoj, M.R., Moorthy, K.K., Gogoi, M.M., Nair, V.S., Kompalli, S.K., Satheesh, S.K., Niranjan, K., Ramagopal, K., Bhuyan, P.K., Singh, D., 2013. Trends in aerosol optical depth over Indian region: potential causes and impact indicators. J. Geophys. Res. Atmos. 118, 11794–11806. https://doi.org/10.1002/2013JD020507.

Ban-Weiss, G.A., Cao, L., Bala, G., Caldeira, K., 2012. Dependence of climate forcing and response on the altitude of black carbon aerosols. Clim. Dyn. 38, 897–911. https://doi.org/10.1007/s00382-011-1052-y.

Bindoff, N.L., Stott, P.A., AchutaRao, K.M., Allen, M.R., Gillett, N., Gutzler, D., Hansingo, K., Hegerl, G., Hu, Y., Jain, S., Mokhov, I.I., Overland, J., Perlwitz, J., Sebbari, R., Zhang, X., 2013. Detection and attribution of climate change: from global to regional. In: Stocker, T.F., Qin, D., Plattner, G.-K., Tignor, M., Allen, S.K., Doschung, J., Nauels, A., Xia, Y., Bex, V., Midgley, P.M. (Eds.), Climate Change 2013: the Physical Science Basis. Contribution of Working Group I to the Fifth Assessment Report of the Intergovernmental Panel on Climate Change. Cambridge University Press, pp. 867–952.

Bond, T.C., 2007. Can warming particles enter global climate discussions? Environ. Res. Lett. 2 https://doi.org/10.1088/1748-9326/2/4/045030, 045030.

Bond, T.C., Doherty, S.J., Fahey, D.W., Forster, P.M., Berntsen, T., Deangelo, B.J., Flanner, M.G., Ghan, S., Krcher, B., Koch, D., Kinne, S., Kondo, Y., Quinn, P.K., Sarofim, M.C., Schultz, M.G., Schulz, M., Venkataraman, C., Zhang, H., Zhang, S., Bellouin, N., Guttikunda, S.K., Hopke, P.K., Jacobson, M.Z., Kaiser, J.W., Klimont, Z., Lohmann, U., Schwarz, J.P., Shindell, D., Storelvmo, T., Warren, S.G., Zender, C.S., 2013. Bounding the role of black carbon in the climate system: a scientific assessment. J. Geophys. Res. Atmos. 118, 5380–5552. https://doi.org/10.1002/jgrd.50171.

Brummelen, G., 2013. Heavenly Mathematics : the Forgotten Art of Spherical Trigonometry. Princeto University Press, New Jersey.

Burton, C., 2015. India's Deadly Heatwave Nears End as Monsoon Arrives [WWW Document]. Weather Netw. https://www.theweathernetwork.com/uk/news/articles/indias-deadly-heatwave-nears-end-as-monsoon-arrives/52420/. (Accessed 8 September 2018).

Cao, C., Lee, X., Liu, S., Schultz, N., Xiao, W., Zhang, M., Zhao, L., 2016. Urban heat islands in China enhanced by haze pollution. Nat. Commun. 7, 1–7. https://doi.org/10.1038/ncomms12509.

Cape, J.N., Coyle, M., Dumitrean, P., 2012. The atmospheric lifetime of black carbon. Atmos. Environ. 59, 256–263. https://doi.org/10.1016/j.atmosenv.2012.05.030.

Chazette, P., Totems, J., Shang, X., 2017. Atmospheric aerosol variability above the Paris Area during the 2015 heatwave - comparison with the 2003 and 2006 heat waves. Atmos. Environ. 170, 216–233. https://doi.org/10.1561/2200000016.

De, U.S., Dube, R.K., Rao, G.S.P., 2005. Extreme weather events over India in the last 100 years. J. Indian Geophys. Union 9, 173–187.

Dileepkumar, R., Achutarao, K., Arulalan, T., 2018. Human influence on sub-regional surface air temperature change over India. Sci. Rep. 1–9. https://doi.org/10.1038/s41598-018-27185-8.

Ding, T., Qian, W., Yanb, Z., 2010. Changes in hot days and heat waves in China during 1961-2007. Int. J. Climatol. 30, 1452–1462. https://doi.org/10.1002/joc.1989.

Esposito, F., Pavese, G., Serio, C., 2001. A preliminary study on the correlation between TOMS aerosol index and ground-based measured aerosol optical depth. Atmos. Environ. 35, 5093–5098. https://doi.org/10.1016/S1352-2310(01)00323-5.

Fuller, A.W., 1995. Introduction to Statistical Time Series, Sencond. ed. John Willy Sons, New York.

Gelaro, R., McCarty, W., Suárez, M.J., Todling, R., Molod, A., Takacs, L., Randles, C.A., Darmenov, A., Bosilovich, M.G., Reichle, R., Wargan, K., Coy, L., Cullather, R., Draper, C., Akella, S., Buchard, V., Conaty, A., da Silva, A.M., Gu, W., Kim, G.-K., Koster, R., Lucchesi, R., Merkova, D., Nielsen, J.E., Partyka, G., Pawson, S., Putman, W., Rienecker, M., Schubert, S.D., Sienkiewicz, M., Zhao, B., 2017. The Modern-Era retrospective analysis for Research and Applications, version 2 (MERRA-2). J. Clim. 30, 5419–5454. https://doi.org/10.1175/JCLI-D-16-0758.1.

Granger, C.W.J., 1969. Investigating causal relations by econometric models and cross-spectral methods. Econometrica 37, 424–438. https://doi.org/10.2307/1912791.

Habib, G., Venkataraman, C., Chiapello, I., Ramachandran, S., Boucher, O., Shekar Reddy, M., 2006. Seasonal and interannual variability in absorbing aerosols over India derived from TOMS: relationship to regional meteorology and emissions. Atmos. Environ. 40, 1909–1921. https://doi.org/10.1016/j.atmosenv.2005.07.077.

Herman, J.R., Bhartia, P.K., Torres, O., Hsu, C., Seftor, C., Celarier, E., 1997. Global distribution of UV-absorbing aerosols from Nimbus 7/TOMS data. J. Geophys. Res. 102, 16911. https://doi.org/10.1029/96JD03680.

Jacobson, M.Z., 2002. Control of fossil-fuel particulate black carbon and organic matter, possibly the most effective method of slowing global warming. J. Geophys. Res. Atmos. 107 https://doi.org/10.1029/2001JD001376. ACH 16-1-ACH 16-22.

Jaswal, A.K., Rao, P.C.S., Singh, V., 2015. Climatology and trends of summer high temperature days in India during 1969–2013. J. Earth Syst. Sci. 124, 1–15. https://doi.org/10.1007/s12040-014-0535-8.

Jones, T.A., Christopher, S.A., 2007. MODIS derived fine mode fraction characteristics of marine, dust, and anthropogenic aerosols over the ocean, constrained by GOCART, MOPITT, and TOMS. J. Geophys. Res. Atmos. 112, 1–10. https://doi.org/10.1029/2007JD008974.

Kothawale, D.R., Revadekar, J.V., Kumar, K.R., 2010. Recent trends in pre-monsoon daily temperature extremes over India. J. Earth Syst. Sci. 119, 51–65. https://doi.org/10.1007/s12040-010-0008-7.

Krishnan, R., Ramanathan, V., 2002. Evidence of surface cooling from absorbing aerosols. Geophys. Res. Lett. 29, 2–5. https://doi.org/10.1029/2002GL014687.

Lashof, D.A., Ahuja, D.R., 1990. Relative contributions of greenhouse gas emissions to global warming. Nature 344, 529–531. https://doi.org/10.1038/344529a0.

Lyamani, H., Olmo, F.J., Alcántara, A., Alados-Arboledas, L., 2006. Atmospheric aerosols during the 2003 heat wave in southeastern Spain I: spectral optical depth. Atmos. Environ. 40, 6453–6464. https://doi.org/10.1016/j.atmosenv.2006.04.048.

Mahowald, N., Albani, S., Kok, J.F., Engelstaeder, S., Scanza, R., Ward, D.S., Flanner, M.G., 2014. The size distribution of desert dust aerosols and its impact on the Earth system. Aeolian Res 15, 53–71. https://doi.org/10.1016/j.aeolia.2013.09.002.

Mickley, L.J., Leibensperger, E.M., Jacob, D.J., Rind, D., 2012. Regional warming from aerosol removal over the United States: results from a transient 2010-2050 climate simulation. Atmos. Environ. 46, 545–553. https://doi.org/10.1016/j.atmosenv.2011.07.030.

Mondal, A., Sah, N., Sharma, A., Venkataraman, C., Patil, N., 2019. Absorbing aerosols exacerbate high temperature extremes in India: a general circulation modelling study under review.

Ohara, T., Akimoto, H., Kurokawa, J., Horii, N., Yamaji, K., Yan, X., Hayasaka, T., 2007. An Asian emission inventory of anthropogenic emission sources for the period 1980-2020. Atmos. Chem. Phys. 7, 4419–4444. https://doi.org/10.5194/acp-7-4419-2007.

Padma Kumari, B., Londhe, A.L., Daniel, S., Jadhav, D.B., 2007. Observational evidence of solar dimming: offsetting surface warming over India. Geophys. Res. Lett. 34, 1–5. https://doi.org/10.1029/2007GL031133.

Pai, D.S., Nair, S.A., Ramanathan, A.N., 2013. Long term climatology and trends of heat waves over India during the recent 50 years (1961-2010). Mausam 64, 585–604.

Pepperberg, I.M., 2001. The conundrum of correlation and causation. Behav. Brain Sci. 24, 1073–1074. https://doi.org/10.1017/S0140525X01460122.

Pere, J.C., Mallet, M., Pont, V., Bessagnet, B., 2011. Impact of aerosol direct radiative forcing on the radiative budget, surface heat fluxes, and atmospheric dynamics during the heat wave of summer 2003 over western Europe: a modeling study. J. Geophys. Res. Atmos. 116, 1–12. https://doi.org/10.1029/2011JD016240.

Perkins, S.E., 2015. A review on the scientific understanding of heatwaves-Their measurement, driving mechanisms, and changes at the global scale. Atmos. Res. https://doi.org/10.1016/j.atmosres.2015.05.014.

Perkins, S.E., Alexander, L.V., Nairn, J.R., 2012. Increasing frequency, intensity and duration of observed global heatwaves and warm spells. Geophys. Res. Lett. 39, 1–5. https://doi.org/10.1029/2012GL053361.

Purnadurga, G., Lakshmi Kumar, T.V., Koteswara Rao, K., Rajasekhar, M., Narayanan, M. S., 2018. Investigation of temperature changes over India in association with meteorological parameters in a warming climate. Int. J. Climatol. 38, 867–877. https://doi.org/10.1002/joc.5216.

Ramachandran, S., Kedia, S., Srivastava, R., 2012. Aerosol optical depth trends over different regions of India. Atmos. Environ. 49, 338–347. https://doi.org/10.1016/j.atmosenv.2011.11.017.

Ratnam, J.V., Behera, S.K., Ratna, S.B., Rajeevan, M., Yamagata, T., 2016. Anatomy of Indian heatwaves. Nat. Publ. Gr. 6, 1–11. https://doi.org/10.1038/srep24395.

Revadekar, J.V., Preethi, B., 2012. Statistical analysis of the relationship between summer monsoon precipitation extremes and foodgrain yield over India. Int. J. Climatol. 32 https://doi.org/10.1002/joc.2282.

Rohini, P., Rajeevan, M., Srivastava, A.K., 2016. On the variability and increasing trends of heat waves over India. Sci. Rep. 6, 26153. https://doi.org/10.1038/srep26153.

Ross, R.S., Krishnamurti, T.N., Pattnaik, S., Pai, D.S., 2018. Decadal surface temperature trends in India based on a new high-resolution data set. Sci. Rep. 8, 2–11. https://doi.org/10.1038/s41598-018-25347-2.

Sarkar, S., Chokngamwong, R., Cervone, G., Singh, R.P., Kafatos, M., 2006. Variability of aerosol optical depth and aerosol forcing over India. Adv. Space Res. 37, 2153–2159. https://doi.org/10.1016/j.asr.2005.09.043.

Schulzweida, U., 2019. CDO user guide. https://doi.org/10.5281/zenodo.3539275.

Srivastava, A., Rajeevan, M., Kshirsagar, S., 2009. Development of a high resolution daily gridded temperature data set (1969 – 2005) for the Indian region. Atmos. Sci. Lett. 10, 249–254. https://doi.org/10.1002/asl.

Torres, O., Bhartia, P.K., Herman, J.R., Ahmad, Z., Gleason, J., 1998. Derivation of aerosol properties from satellite measurements of backscattered ultraviolet

radiation: theoretical basis. J. Geophys. Res. Atmos. 103, 17099–17110. https://doi.org/10.1029/98JD00900.

van Oldenborgh, G.J., Philip, S., Kew, S., van Weele, M., Uhe, P., Otto, F., Singh, R., Pal, I., AchutaRao, K.M., 2018. Extreme heat in India and anthropogenic climate change. Nat. Hazards Earth Syst. Sci. Discuss. 18, 365–381. https://doi.org/10.5194/nhess-2017-107.

R Core Team, 2018. R: A language and environment for statistical computing. R Foundation for Statistical Computing, Vienna, Austria. https://www.R-project.org/.

Received: 2 June 2019 | Revised: 14 February 2020 | Accepted: 29 July 2020 | Published on: 1 September 2020

DOI: 10.1002/joc.6783

RESEARCH ARTICLE

International Journal of Climatology RMetS

Absorbing aerosols and high-temperature extremes in India: A general circulation modelling study

Arpita Mondal[1,2] | **Neeraj Sah**[1] | **Arushi Sharma**[2] | **Chandra Venkataraman**[2,3] | **Nitin Patil**[2]

[1]Department of Civil Engineering, Indian Institute of Technology Bombay, Mumbai, India

[2]Interdisciplinary Program in Climate Studies, Indian Institute of Technology Bombay, Mumbai, India

[3]Department of Chemical Engineering, Indian Institute of Technology Bombay, Mumbai, India

Correspondence
Chandra Venkataraman, Department of Chemical Engineering and Interdisciplinary Program in Climate Studies, Indian Institute of Technology Bombay, Powai, Mumbai 400076, India.
Email: cv140401@gmail.com; chandra@iitb.ac.in

Funding information
Climate Studies Centre, IITB, Grant/Award Number: DST/CCP/PR/06/2011

Abstract

Heat waves in India during the pre-monsoon months have significant impacts on human health, productivity and mortality. While greenhouse gas-induced global warming is believed to accentuate high temperature extremes, anthropogenic aerosols predominantly constituted by radiation-scattering sulfate are believed to cause an overall cooling in most world regions. However, the Indian region is marked by an abundance of absorbing aerosols, such as black carbon (BC) and dust. The goal of this work was to understand the association between aerosols, particularly those that are absorbing in nature, and high-temperature extremes in north-central India during the pre-monsoon season. We use 30-year simulations from a chemistry-coupled atmosphere-only general circulation model (GCM), ECHAM6-HAM2, forced with evolving aerosol emissions in an interactive aerosol module, along with observed evolving SSTs. A composite of high-temperature extremes in the model simulations, compared to climatology, shows large-scale conditions conducive to heat waves. Importantly, it reveals concurrent positive anomalies of BC and dust aerosol optical depths. Changes in near-surface properties include a reduction in single scattering albedo (implying greater absorption) and enhancement in shortwave heating rate, compared to climatological conditions. Alterations in surface energy balance include reduced latent heat flux, but increased sensible heat flux, consistent with enhanced temperatures. Thus, chemistry-coupled GCM simulations capture an association of absorbing aerosols with high-temperature extremes in north India, arising from radiative heating in the surface layer.

KEYWORDS

absorbing aerosols, chemistry-coupled AGCM, ECHAM6-HAM2, extreme temperature, Indian heat wave, radiative forcing

1 | INTRODUCTION

Extreme temperature and heat wave events in India during the pre-monsoon season (March–June) are critical in terms of their impact on human health, environment, agriculture and economy. Recent trends in extreme temperature are reported to be positive over India (Kothawale *et al*., 2010; Revadekar *et al*., 2012; Panda *et al*., 2014), particularly in the north, north-west and north-central regions (Jaswal *et al*., 2015), in agreement

with observed increasing trends in mean temperature over the country (Arora *et al*., 2005; Kothawale & Rupa Kumar, 2005; Dash *et al*., 2007; Basha *et al*., 2017). Although the definition of a heat wave is not unique, they comprise, most generally, of episodes of consecutive days with above normal high temperatures (Perkins *et al*., 2012). Recent studies have investigated heat wave characteristics in India and observed changes therein (Pai *et al*., 2013; Murari *et al*., 2016; Ratnam *et al*., 2016; Rohini *et al*., 2016; Mazdiyasni *et al*., 2017; Panda *et al*., 2017; Sharma & Mujumdar, 2017; Dileepkumar *et al*., 2018; Sandeep & Prasad, 2018; Van Oldenborgh *et al*., 2018) or future projections thereof (Murari *et al*., 2015; Im *et al*., 2017; Mishra *et al*., 2017). Others (Wehner *et al*., 2016; Pattanaik *et al*., 2017; Gouda *et al*., 2017; Ghatak *et al*., 2017; Van Oldenborgh *et al*., 2018; Dodla *et al*., 2017; Chandran *et al*., 2017; Nair *et al*., 2017) study particular heat wave episodes focusing mainly on the 2015 heat wave event that resulted in more than 2000 deaths in India.

Meteorological conditions and enhancements of atmospheric agents like greenhouse gases and aerosols are linked to atmospheric temperature alterations. Meteorological conditions linked to heatwaves include North-Atlantic blocking related to anti-cyclonic conditions over north-central India (710°–800°E; 210°–300°N), while over coastal eastern India are associated with anomalous cooling in the Pacific (Ratnam *et al*., 2016). Rohini *et al*. (2016) and Pai *et al*. (2013) report significantly increasing frequency, average and maximum duration of heat waves in the north-west India region, similar in extent to the north-central region defined by Ratnam *et al*. (2016).

Greenhouse-gas (GHG)-induced climate change is believed to be exacerbating hot extremes and heat waves across the world (Bindoff *et al*., 2013). Attribution of heat waves in India has been attempted recently in a couple of studies (Wehner *et al*., 2016; Van Oldenborgh *et al*., 2018), both concluding that observed changes in hot extremes in India lie outside the expected range of natural variability. Interestingly, both the studies report better discernibility of trends with an extreme temperature index that includes information on relative humidity along with temperature. Furthermore, van Oldenborgh *et al*. (2018) also infer that trends in extreme temperature in India are masked significantly by cooling due to aerosols blocking sunlight or due to increased evapotranspiration resulting from extensive irrigation.

Aerosol-induced reduction of ground-reaching solar radiation in India is well recognized (Satheesh and Ramanathan, 2000; Padma Kumari *et al*., 2007). However, unlike most world regions where dominance of scattering aerosols such as sulfates can cause an overall cooling, India is marked with abundance of absorbing aerosols such as black carbon (BC) that results from incomplete combustion biomass fuels and agricultural biomass (Venkataraman *et al*., 2005) and can cause atmospheric warming (Ramanathan *et al*., 2002). Modelled aerosol optical depth over most regions in India is significantly larger than that in other world regions, with carbonaceous aerosol constituents contributing 18–32% of the magnitude (David *et al*., 2018). Positive radiative forcing from absorbing aerosols can also offset aerosol scattering effects (Jacobson, 2001; Menon *et al*., 2002), warm surface air (Hansen *et al*., 2005) and contribute to global warming (Jacobson, 2002; Bond & Sun, 2005; Ramanathan *et al*., 2007). Using idealized climate simulations, Ban-Weiss *et al*. (2012) show that the climate response of BC is sensitive to the altitude at which it is present, with low-altitude BC resulting in surface warming through diabatic heating. Absorbing aerosols enhancements (manifested in absorbing aerosol index or AAI) correlate with and exert a causality on temperature maxima in north-west India (Dave *et al*., 2019). The confounding effects of meteorology were ruled out through a significant partial correlation between AAI and T_{max} conditioned upon surface pressure and geopotential height. The study concluded that absorbing aerosols absorb incoming radiation and heat up the atmosphere, especially during heatwave events when stationary atmospheric conditions lead to their build-up and enhanced levels. Atmospheric heating and surface cooling caused by absorbing aerosols could lead to stabilization of the near-surface atmosphere, resulting in a positive feedback that reduces cloudiness, further exposing aerosol to sunlight (Ramanathan *et al*., 2005; Koren *et al*., 2008).

The pre-monsoon season over India is characterized by significant atmospheric abundance of absorbing aerosols, whose influence on redistribution of solar energy and atmospheric heating on regional scales is not yet understood. Given the strong forcing patterns of absorbing aerosols, resulting in surface reduction but atmospheric enhancement in radiative flux, it is not obvious whether the surface will cool or warm in response to the aerosol forcing. On regional scales, Krishnan and Ramanathan (2002) showed an asymmetric cooling during the dry season (Jan–May), suggesting a relation to enhanced absorbing aerosol forcing, and possible surface warming at regions non-local to the aerosol haze. On local scales, in northwest India, increase in aerosol absorption was linked to simultaneous negative surface forcing, but increases in surface radiative heating and surface air temperature (Pandithurai *et al*., 2008a). Gautam *et al*. (2009) report anomalous tropospheric warming in the Himalayan region coincident with increased dust loading and anthropogenic aerosol

pollution in the pre-monsoon season. Lau *et al*. (2010) validate such warming in the Himalayan and Tibetan plateau region through model simulations, reporting large surface cooling over central and eastern India in the model runs that include aerosols. They also hint at the importance of atmospheric feedback processes, and not direct aerosol radiative forcing alone, for explaining the observed warming. Gautam *et al*. (2010) report that pre-monsoon aerosols over north India are primarily of absorbing nature leading to significant warming over northern India, especially over the western Himalayas. Purnadurga *et al*. (2018) show that observed pre-monsoon maximum temperatures in northern India are significantly correlated with BC surface mass concentrations obtained from the MERRA reanalysis data.

In modelling studies, sulfates have been shown to induce a negative surface temperature response on both global (Kloster *et al*., 2010; Koch & Del Genio, 2010) and regional scales (Pere *et al*., 2011; Mickley *et al*., 2012; Zanis *et al*., 2012). Aerosol-induced surface dimming reduced both terrestrial sensible and latent heat fluxes, leading to a radiative cooling of surface air (Pere *et al*., 2011), while aerosol-induced northerly flow, advected relatively cooler air from northern latitudes (Zanis, 2009 in regional model simulations over Europe. General circulation model (GCM) simulations show that an unmasking of GHG-induced warming manifest as larger increases in global mean surface equilibrium temperature under increasing GHG concentrations and reduced aerosol emissions, compared to that under increasing GHG concentrations alone (e.g., Kloster *et al*., 2010). However, the specific role of absorbing aerosols in mediating hot extremes and heat waves is not quite well-understood. This understanding is imperative for India in particular and the South Asian region in general, which are recognized as hotspots of aerosols, of both natural and anthropogenic origins (Ramanathan, 2001). Recent increasing trends in pre-monsoon aerosol optical depth (AOD) in this part of the world (Porch *et al*., 2007; Ramachandran *et al*., 2012; Babu *et al*., 2013) with marked rise in BC emissions (Lu *et al*., 2011; Pandey *et al*., 2014; Sadavarte & Venkataraman, 2014), further underline the importance of assessing the influence of absorbing aerosols on the climate system. Coupled numerical model simulation studies that play an instrumental role in such assessments are rather limited for the Indian region, especially in the context of pre-monsoon hot extremes and heat waves. Furthermore, although analysis of GCM-based temperature projections for the Indian region is common (e.g., Basha *et al*., 2017; Mishra *et al*., 2017; Im *et al*., 2017), no study, to our knowledge, have thus far evaluated representation of synoptic-scale processes in GCM simulations, which influence heat wave conditions in India.

In this study, we use 30-year simulations from the chemistry-coupled atmosphere-only GCM, the ECHAM6-HAM2, forced with evolving aerosols in an interactive aerosol module, along with observed evolving sea-surface temperatures (SSTs), to understand the association between aerosols, particularly those of absorbing nature, and high-temperature extremes in north-central India during the pre-monsoon season, for the period 1981–2010. The model simulations are first validated against observed temperature records. A composite of the most-severe hot extremes from the model simulations is investigated further for understanding the influencing atmospheric conditions, aerosol optical properties and changes in near-surface properties due to the presence of absorbing aerosols, vis-à-vis normal (climatological) conditions.

2 | DATA AND MODEL SETUP

2.1 | Observed data

Observed gridded (10 latitude × 10 longitude) daily maximum temperature data is obtained from the India Meteorological Department (IMD) (Srivastava *et al*., 2009). This dataset is available for the period 1951–2003 and is prepared from observations at 395 quality controlled stations. This dataset has been used previously for studying changes in extreme temperature in India (Rohini *et al*., 2016; Mishra *et al*., 2017; Panda *et al*., 2017). We choose a time period of 1981–2010, consistent with the period of our model simulations, since temperature extremes have been more pronounced in recent years, post rapid industrialization (Kothawale *et al*., 2016), with most of the hottest years recorded post-2000 (Pai *et al*., 2013; IMD, 2015). The influence of anthropogenic forcings such as that from GHGs and aerosols are also expected to be more significant in India during these recent years. To compare with the monthly model simulation outputs of maximum 2 m temperature, we compute monthly maximum temperature data from this observed dataset for the pre-monsoon (MAMJ) months for 1981–2010. This season is the hottest time of the year (Figure 1a), and is also reported to witness major heat waves (Ratnam *et al*., 2016). MAMJ maximum temperatures show an overall increasing trend in India, with significant positive trends in the north-central region (21°–30°N; 71°–80°E, as defined by Ratnam *et al*., 2016), as seen in Figure 1b. The northern Indian region in general is reported in literature to witness frequent occurrence of heat waves (De *et al*., 2005; Srivastava *et al*., 2009) that are projected to intensity in the future (Murari *et al*., 2015). We choose this region for our study since

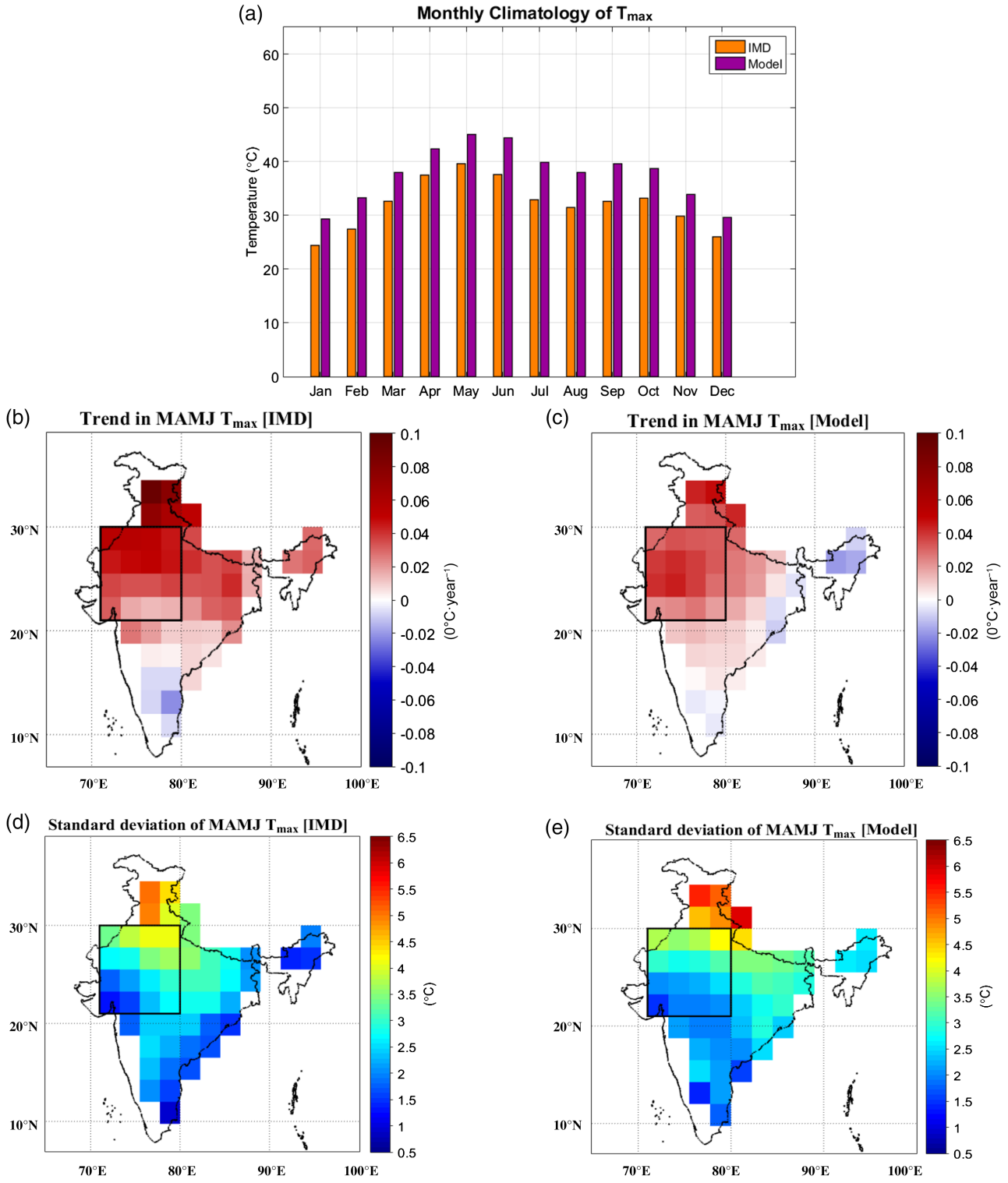

FIGURE 1 Comparison of model-simulated maximum temperature with IMD observations in terms of (a) monthly climatology of maximum temperature (°C) over the north-central region (21°–30°N; 71°–80°E); (b), (c) 30-year (1981–2010) trends (°C·year^{-1}) in maximum temperature in the pre-monsoon season; and (d), (e) standard deviation (°C) of maximum temperature in the pre-monsoon season

the trends in maximum temperatures over this region are much more pronounced as compared to other regions in India (Figure 1b), a finding consistent with other studies (Pai *et al.*, 2013; Ratnam *et al.*, 2016; Rohini *et al.*, 2016). Based on mortality records associated with heat waves during the period 1978–1999, the state of Rajasthan,

included in our study region, ranks the highest impacted state (Chaudhury *et al.*, 2000). This highlights the importance of this region in terms of impacts of high-temperature extreme events. Our study region (21°–30°N; 71°–80°E) is also found to exhibit large standard deviations (2σ or more) of maximum temperature during the pre-monsoon months (Figure 1d). Temperature anomalies during heat waves in this region are also reported to show such large positive deviations (Ratnam *et al.*, 2016).

We consider the composite of standardized anomalies of maximum temperature during five hottest months from the period 1981–2010, as shown in Figure 2a, for understanding prevalent conditions during heat wave type of events. We convert the MAMJ T_{max} series at each grid point to the corresponding anomalies, with respect to the 1981–2010 climatological mean. It may be noted that we consider monthly means for conversion to these anomalies, ensuring that each month (March, April, May or June) has a different mean, and the anomalies represent truly anomalous conditions, thereby avoiding any bias. Next, we consider the five hottest months by considering the largest anomalies in the entire time period. In addition, we impose the condition that these five hottest months belong to different calendar years so that they do not belong to the same hot spell. For observations, these months are April 2010, March 2004, June 1995, April 1999 and March 1985.

Such a composite is statistically significant for all grid points in this region, as found by a two-tailed Students *t*-test at 95% confidence level, which determines if the composite is distinguishable from the 1981–2010 climatological mean. We imposed an additional constraint of these extreme temperature anomalies occurring in different calendar years, to ensure that they do not belong to the same hot spell. This makes our results conservative. However, since we consider a composite of these extreme temperature anomalies for understanding representative conditions, our results are not expected to vary even if we consider extreme temperature months within the same pre-monsoon season in a given calendar year. The warm anomaly in Figure 2a extends all throughout north and north-central India indicating that the composite is representative of large-scale conditions.

2.2 | Model setup

We use the fully-coupled aerosol-climate model, the ECHAM6-HAM2, run at a horizontal T63 resolution, that is, 1.8° longitude × 1.8° latitude and at a vertical resolutions of 31 levels ranging upto 10 hPa. ECHAM6 is the sixth generation GCM created by the Max Planck Institute for Meteorology (Roeckner *et al.*, 2003; Roeckner *et al.*, 2006). The Hamburg Aerosol Module (HAM) (Stier *et al.*, 2005) is coupled to the GCM, to assess the impact of aerosol on the climate by focusing on the coupling between diabatic processes and large-scale circulations, which are primarily driven by radiative forcing (Stier *et al.*, 2007). The radiative transfer model used in ECHAM6 consists of shortwave (SW) radiative scheme on 14 spectral bands and longwave (LW) radiative scheme on 16 spectral bands (Giorgetta *et al.*, 2013). Details of the current version (ECHAM6.1-HAM2.2) are described in Neubauer *et al.* (2014). Five major aerosol compounds in the atmosphere, namely, BC, organic carbon (OC), sulfate (SO_4), sea salt (SS) and mineral dust are considered in the interactive aerosol module.

The JSBACH (version 3.11) land component model (Heidkamp *et al.*, 2018) is embedded in the ECHAM6 GCM. The physical core components of the land processes (energy balance, heat transport and water budget) are adopted from ECHAM5 (Roeckner *et al.*, 2003) with a

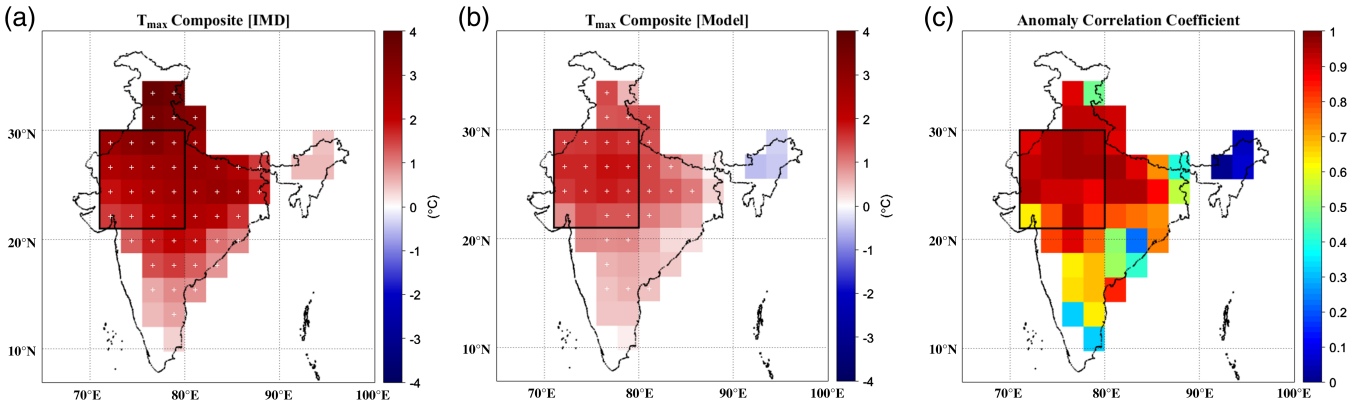

FIGURE 2 A composite of standardized anomalies of maximum temperature during hot extremes in (a) observations and (b) model simulations, and (c) their anomaly correlation coefficient. Stippling in (a) and (b) shows grid points with statistically significant anomalies

fully implicit land-surface-atmosphere coupling scheme. Air temperature at the top of the surface atmospheric layer, is derived using a turbulent heat-flux expression at the surface, with transfer coefficients obtained from Monin-Obukhov similarity theory, by integrating the flux profile relationships over the lowest model layer (Roeckner *et al*., 2003). The ECHAM6 GCM uses a turbulent kinetic energy scheme to account for momentum exchange between atmosphere and land, and uses the RRTM rapid radiative transfer model (Roeckner *et al*., 2003), thus, not permitting an assessment of the sensitivity of aerosol climate impact to changes in these schemes, which have been suggested to be important (e.g., Jin *et al*., 2015).

Observed monthly SST and sea ice concentration (SIC) data from the Atmospheric Model Intercomparison Project (AMIP) are prescribed to the model. Annual mean GHG concentrations are obtained from the International Institute for Applied Systems Analysis (IIASA; http://www.iiasa.ac.at/web-apps/tnt/RcpDb/). The AEROCOM emission inventory data for 1981–2010 (Dentener *et al*., 2006) is used, which includes anthropogenic aerosol and precursor species of BC, organic carbon and sulfur dioxide and biogenic dimethyl sulfide. Forest burning emissions were obtained from the Global Fire Emission Data (GFED). Volcanic sulfate emissions are also included (Andres & Kasgnoc, 1998). The model uses online parameterizations to calculate prognostic dust and sea salt emissions (Roeckner *et al*., 2003). An average of three ensemble members is considered further in the analysis.

Patil *et al*. (2019) also use ECHAM6-HAM2 simulations under four scenarios to segregate the influence of SST and aerosols on the south Asian monsoon. Chemistry-coupled GCM simulations allow meteorological changes to influence levels of atmospheric agents, whose radiative effects feedback to atmospheric circulation in turn. In the present model set-up, the effects of change in oceanic conditions cannot be evaluated, because we use an atmosphere-only GCM, forced with actual observed SSTs. However, such simulations are specifically suitable for investigations made in this work, to isolate aerosol-modulated changes in the components of the climate system such as extreme temperature.

3 | MODEL VALIDATION

Monthly maximum 2 m temperature output from the model simulations is compared with observed monthly maximum temperature from IMD prepared from station-based observations that are made typically at a height of 1.5 or 2 m above the ground. The model is found to capture the climatological behaviour of temperature in north-central India (Figure 1a) reasonably well. The pre-monsoon months (MAMJ) show the highest temperature records. Increasing trends (Figure 1b, c) and large standard deviations (Figure 1d,e) in MAMJ maximum temperatures in the north-central region are also well represented in the model, when compared with observations. An exact match between observations and model simulations is not expected since GCM simulations are run at a relatively coarse scale.

We further consider a composite of standardized anomalies of the five hottest months in the model simulations and find most of them to be statistically significant over north-central India (Figure 2b). The months are April 1988, March 1983, May 2000, June 1998 and April 1999.

These standardized anomalies are found to be similar to those from observations (Figure 2a). Although these extreme temperature anomalies do not correspond to the same months as in the observed records since coarse-resolution GCMs are known to have poor skill in reproducing short time-scale air temperature variations, yet, they are useful in contrasting anomalous periods with the climatology. A composite of these anomalies during the hottest months in the model simulations capture the upper tail behaviour of the distribution of maximum temperatures and are representative of heat wave conditions. The plot of anomaly correlation (Wilks, 2011), alternately called pattern correlation, between the composite of hot extremes in observations and model simulations (Figure 2c) reveal significantly high values in the north-central region with a median correlation coefficient of 0.8, showing that the model is able to capture the pattern of anomalous hot extremes in this part of the country.

We analyse synoptic atmospheric processes, aerosol optical properties and changes in near-surface properties associated with the presence of absorbing aerosols by comparing a composite of these hot extremes with climatological. While this approach does not allow a direct quantification of the effects of individual forcing agents or attribution of responses to a particular forcing agent, it ensures that different forcing elements, like aerosols, GHGs and SST, are consistent with each other. Simulations in atmospheric GCMs with varying levels of atmospheric constituents like GHGs and aerosols typically require to be carefully matched up to corresponding SST forcing boundary conditions (e.g., Guo *et al*., 2016). In these simulations, the difference between a composite of hot extremes and climatological conditions in the transient model simulations are reflective of climate response to a realistic combination of forcing agents. Such a composite analysis is used in earlier studies to analyse prevalent atmospheric conditions during heat wave conditions

in observations (e.g., Ratnam *et al*., 2016; Ghatak *et al*., 2017), or to evaluate the ability of GCMs to represent synoptic and oceanic conditions associated with heat waves (e.g., Purich *et al*., 2014).

4 | RESULTS AND DISCUSSION

4.1 | Atmospheric conditions

Ratnam *et al*. (2016) reported cloud-free skies, strong anomalous anticyclone and sinking motion as conditions conducive to heat waves in north-central India. These conditions are caused by a quasi-stationary wave from Northwestern Africa to India that is generated by the anomalous North-Atlantic Ocean blocking. These large-scale features were previously identified using the ERA-Interim reanalysis data (Ratnam *et al*., 2016), while the present analysis is based on GCM simulations. To investigate prevalent large-scale atmospheric features during hot extremes in our model simulations, we compute composites of atmospheric variables such as geopotential height at 500 hPa (Z500), total cloud cover (TCC), vertical velocity at 500 hPa (ω500), relative humidity at 850 hPa, and lower-tropospheric stability (LTS). LTS is calculated as the difference between potential temperature at 700 hPa and that at 1,000 hPa, following Wood & Bretherton (2006). Figure 3 shows the composite of standardized anomalies of the above atmospheric variables during the hot extremes in the ECHAM6-HAM2 model simulations.

It is observed that in the composite of the hot extremes, the standardized mid-tropospheric geopotential height anomalies (Figure 3a) and downward vertical wind velocity anomalies (Figure 3c) are positive over north-central India indicating anticyclonic flow and sinking motion of air, similar to observed conditions during heat waves, reported by Ratnam *et al*. (2016). Ridges in geopotential height anomalies are commonly used to identify blocking (Trigo *et al*., 2005). Heat waves in other parts of the world such as Europe (Trigo *et al*., 2005; García-Herrera *et al*., 2010), Australia (Pezza *et al*., 2012), China (Wang *et al*., 2016), Brazil (Geirinhas *et al*., 2018), Russia (Lau & Kim, 2012) and Iran (Darand *et al*., 2018) are also found to be associated with anomalous blocking or anticyclonic flow. Persistence of anticyclonic blocking patterns can suppress convection (Ratnam *et al*., 2016), enhance subsidence and increase adiabatic heating of the surface layers (Xoplaki *et al*., 2003; Trigo *et al*., 2005; Darand *et al*., 2018; Sandeep & Prasad, 2018).

Furthermore, the sinking motion and anticyclonic conditions may cause positive outgoing longwave radiation (Ratnam *et al*., 2016) implying long periods of clear sky that can contribute to enhanced solar radiative heating (García-Herrera *et al*., 2005; Ratnam *et al*., 2016). Indeed, the total cloud cover and relative humidity anomalies at 850 hPa during the hot extremes in model simulations (Figure 3b) are negative over the Indian region indicating dry, clear skies in agreement with observations reported by Ratnam *et al*. (2016). Enhanced solar radiation may further deplete soil moisture reducing latent heat transfer into the atmosphere while increasing sensible heat transfer (Rohini *et al*., 2016; Ghatak *et al*., 2017). This may induce a positive feedback between atmospheric heating and further desiccation of land surface, creating coupling between the land surface and the planetary boundary layer (Miralles *et al*., 2014). These effects are captured through the land component model described in Section 2.2. We investigate the surface energy balance in detail in Section 4.3.

In addition, we find positive LTS anomalies during the hot extremes in our model simulations (Figure 3e), implying that the lower troposphere is more stable than normal conditions. Such stable conditions associated with reduced cloud cover and relative humidity further favour heat wave type of events and also prevent mixing and dilution of pollutants such as aerosols. Stable meteorological conditions also alter near-surface latent and sensible heat fluxes (Geirinhas *et al*., 2018) that are investigated further in Section 4.3. Overall, the ECHAM6-HAM2 simulations are thus found to reproduce atmospheric conditions conducive to heat waves in north-central India during the hot extremes and show anomalous synoptic processes with respect to climatological conditions.

4.2 | Role of aerosols

In addition to synoptic processes discussed above, aerosol constituents can influence surface temperature through alteration of the surface radiative balance. Aerosols absorb both shortwave (BC) and longwave (dust) radiation, adding energy to the atmosphere (Lyamani *et al*., 2006b; Das and Jayaraman, 2011). Previous studies of aerosol levels and radiative forcing during heat-wave conditions showed a prevalence of absorbing aerosols and positive atmospheric forcing over the regions experiencing heat waves (Lyamani *et al*., 2006b; Struzewska & Kaminski, 2008; Chazette *et al*., 2017). The presence of absorbing aerosols near the surface could lead to diabatic heating of the surface layer, with associated increase in surface temperature (Ban-Weiss *et al*., 2012). Furthermore, absorbing or scattering aerosols induce reduction in ground-reaching radiation and

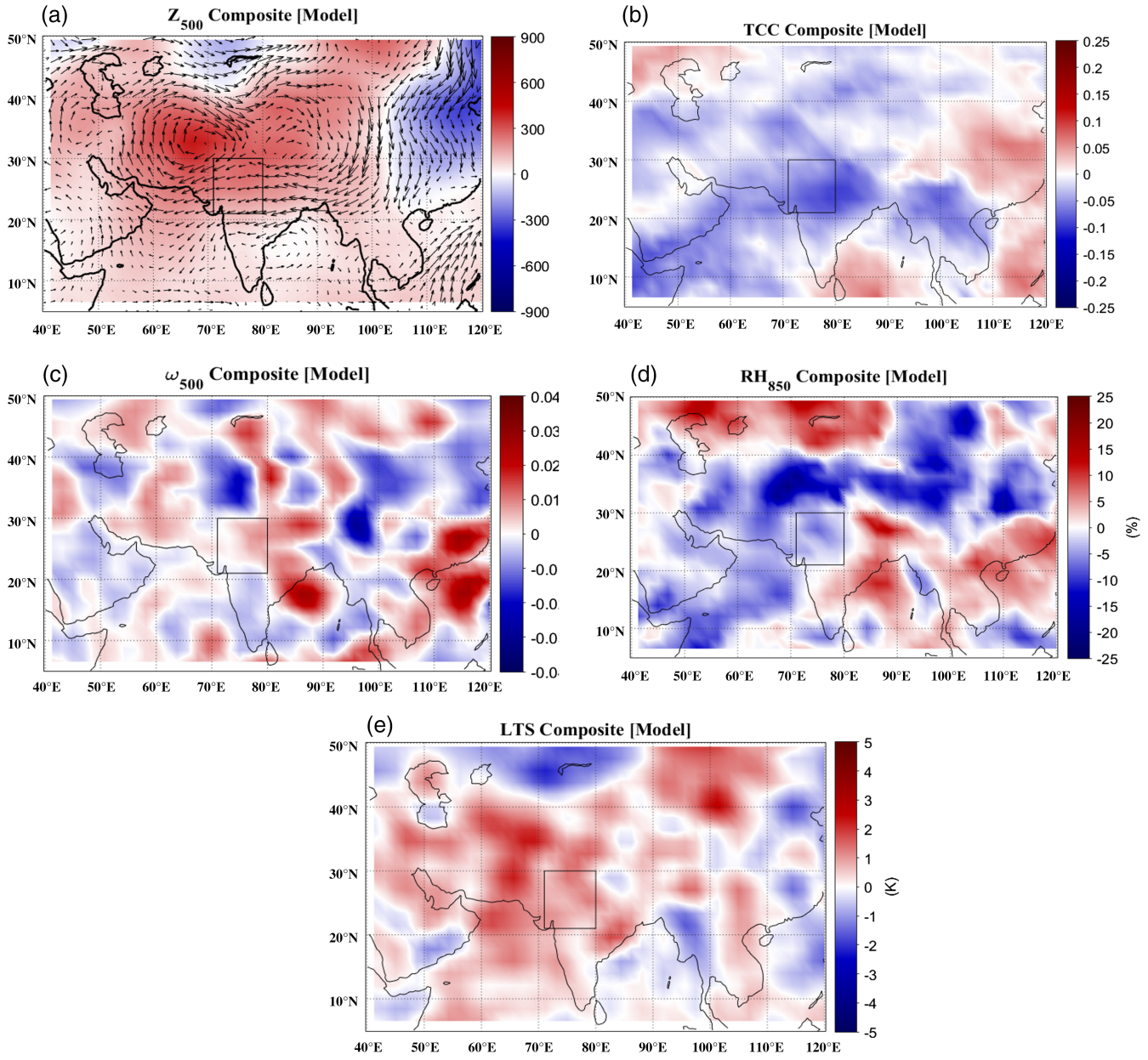

FIGURE 3 Composite anomalies of (a) geopotential height (m) at 500 hPa overlaid on vector winds, (b) Total cloud cover (TCC), (c) vertical velocity (m·sec^{-1}) at 500 hPa (ω_{500}), (d) relative humidity (%) at 850 hPa (RH_{850ss}), and (e) lower tropospheric stability (LTS) (K) during the hot extremes in model simulations

related local cooling (Krishnan & Ramanathan, 2002; Pere *et al.*, 2011). Thus, aerosols could induce either a positive or a negative response of surface temperature, based on predominance of effects. Krishnan and Ramanathan *et al.* (2002) further suggest possible surface warming at regions non-local to the aerosol haze, to balance local cooling.

The variables involved in the mechanism of aerosol modulation of surface temperature are explicitly treated by the ECHAM6-HAM2 model. The surface energy balance is influenced by the net radiation flux absorbed at the surface (Rnet), which is either stored in surface elements as ground heat flux (G) or transported into the atmosphere via sensible (H) or latent (Q) heat fluxes (Heidkamp *et al.*, 2018). Aerosol absorption of short-wave radiation can affect surface air temperature response from either a reduction in surface-reaching radiation, further causing surface heat flux changes, or from increased shortwave heating resulting in direct diabatic heating of surface air (Giorgetta *et al.*, 2013). In the following

sections, we analyse differences between the composite of hot extremes as compared to climatological conditions, in key variables such as aerosol optical depth, radiative forcing, surface fluxes and heating rate to understand the possible role of aerosols.

4.2.1 | Aerosol atmospheric effects

We evaluate the skill of the model in estimating key variables including aerosol levels. The spatial distribution of annual mean AOD climatology averaged over 10 years (2001–2010) broadly captures the AOD distributions over the Indo-Gangetic plains (IGP) and the Indian subcontinent (Patil *et al*., 2019). The average bias of annual AOD over land points of India shows mean normalized bias of −0.31, which indicates some underestimation of AOD within levels seen in previous studies (Ganguly *et al*., 2013; Pan *et al*., 2015). In addition, this underestimation also manifests on a seasonal scale (−0.11), as well as on monthly scales for March (−0.55), April (−0.56) and May (−0.39). However, there is a small positive bias (+0.15) in simulated AOD in June (Figure S1). This small positive monthly bias in June does not affect the sign of the AOD bias during the season in the climatology. The monthly AOD biases in the simulation were influenced by dust AOD, which was 55% of total AOD excluding aerosol water in June, while 32% in March–May, consistent with earlier studies which indicated underestimation of long-range transport of dust in these months (Pan *et al*., 2015; David *et al*., 2018).

The climatological mean AOD during the pre-monsoon months, a composite of the AOD during the hot extremes and the difference between the two are shown in Figure 4. High values of AOD for both the hot extremes as well as climatological conditions reveal aerosol abundance in this region. Figure 4c shows the difference between the composite AOD of the hot extremes (five hottest months, Figure 4a) and the climatological mean AOD (Figure 4b). Therefore, the values in Figure 4c represent AOD anomalies during the hot extremes. Each grid box in the region has a single value in Figure 4c, as shown, and the mean value over the region of interest is positive (+0.0047). Furthermore, it may be noted that the composite of the hot extremes shows much larger AOD values in the surrounding Indo-Gangetic Plains region in central India. On regional scales, it has been suggested in the literature that a redistribution of energy by aerosol absorption could cause surface warming in some locations (Krishnan & Ramanathan, 2002). Therefore, although a few grid points in our region of interest show negative AOD anomalies during the hot extremes, overall, we observe greater abundance of aerosols as compared to climatological conditions.

High AOD values over North India in the pre-monsoon season has been linked to elevated transport of aerosols, as seen from satellites (Gautam *et al*., 2010; Mishra and Shibata, 2012), ground-Lidar observations (Sarangi *et al*., 2016) and models (Pan *et al*., 2015; Feng *et al*., 2016). Absorbing aerosols may heat the lower atmosphere and cause regional redistribution of enhanced heating. To characterize absorbing aerosols, we plot a composite of the standardized anomalies of BC-AOD and dust (DU)-AOD during the hot extremes in Figure 5a,b. In addition, we consider different definitions of the hot extremes by considering composites of 6 months (>95th percentile), 12 months (>90th percentile) and four distinct hottest months (March–June) to investigate the robustness of our findings. For all these cases, the anomalies of BC-AOD and Dust-AOD are consistently positive in the composite of the hot extremes

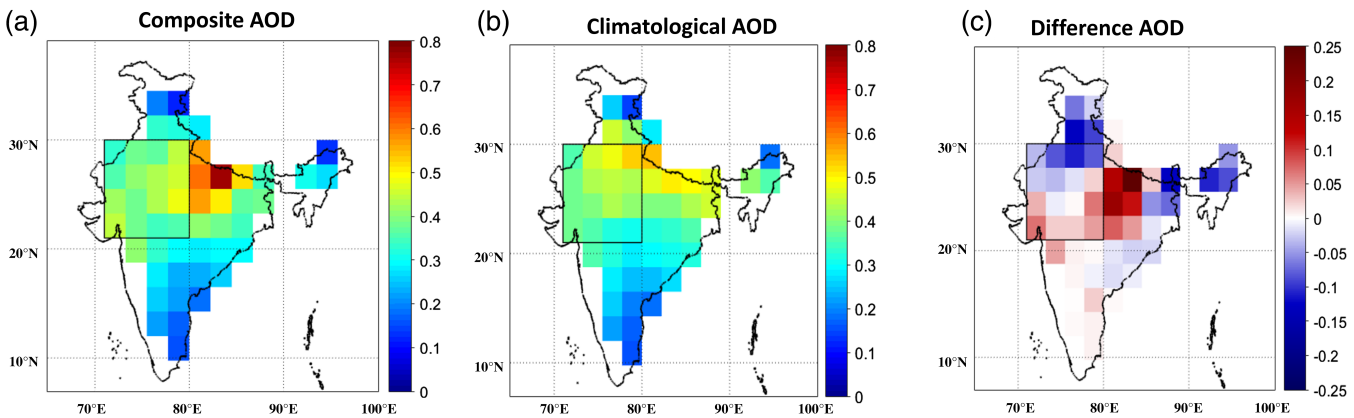

FIGURE 4 Aerosol optical depth (AOD) during the (a) hot extremes, (b) climatological mean and (c) their difference

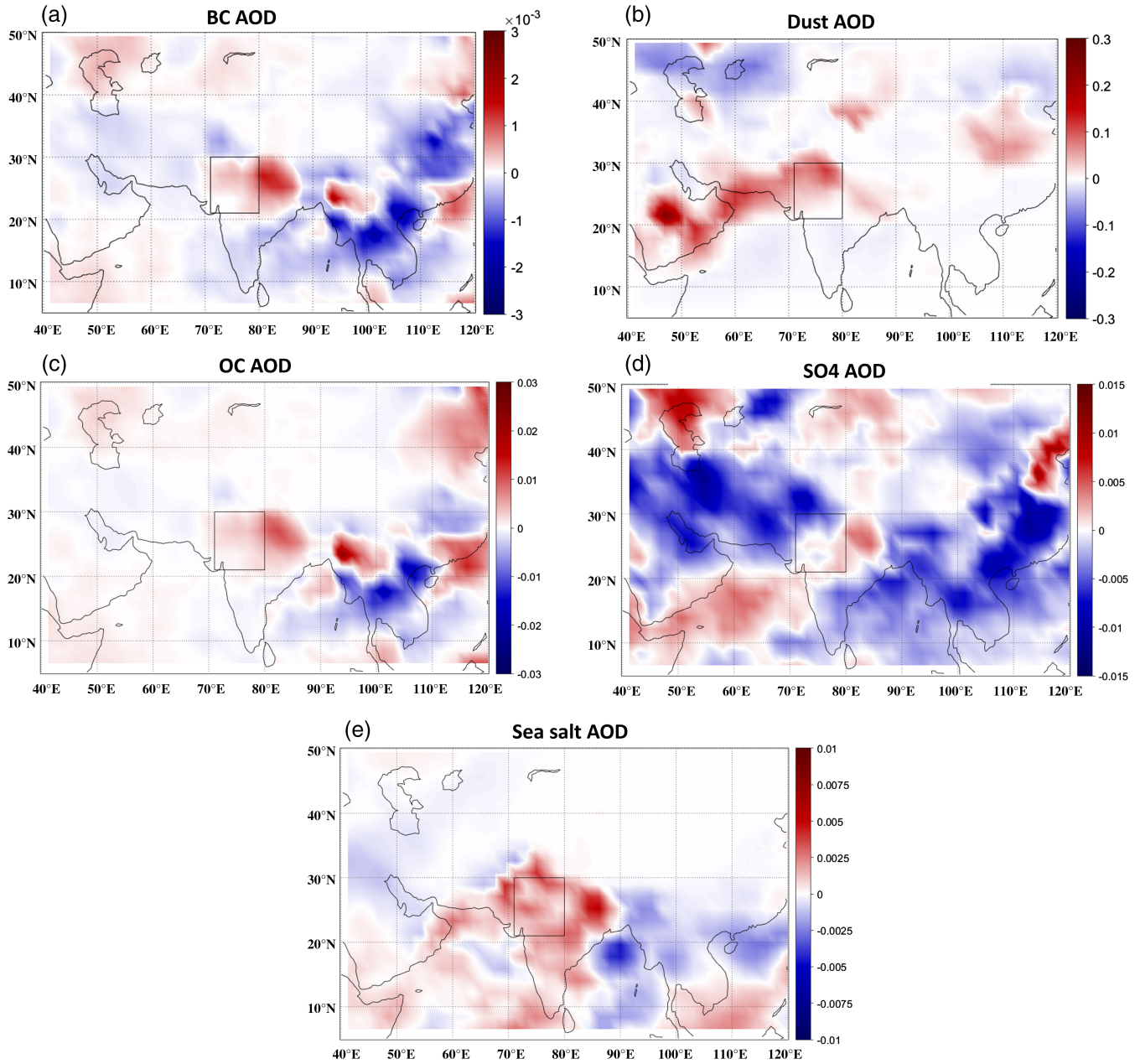

FIGURE 5 Composite anomalies of aerosol optical depth (AOD) for (a) black carbon (BC) (b) dust (DU) (c) organic carbon (OC) (d) sulfate (SO_4) and (e) sea salt (SS) during the hot extremes in model simulations

(Figure S2). Also, the anomalies of scattering aerosol species are also shown (Figure 5c–e). Both BC-AOD and DU-AOD are found to be positive over the north-central region during the hot extremes, as compared to their normal conditions, indicating overall larger concentration of absorbing aerosols in the atmosphere during the hot extremes.

Anthropogenic emissions, including BC, OC and SO_2, do not vary between the hot composite and climatology periods. There is strong seasonality in BC and OC emissions (Figure S4a,b), with the highest emissions in MAM. However, all months are equivalently represented in the hot composite, as well as climatology, indicating increases in anthropogenic aerosol abundance is not an "emission" effect. Increased LTS in the hot-composite (Figure 3e) would correspond to lower ventilation rates and dispersion, indicating a meteorological influence on enhanced anthropogenic aerosol abundance. Dust emission flux in the model is parameterized as a function of threshold wind velocity and upper-layer soil moisture

(Tegen *et al*., 2002). The difference in dust flux, between hot-composite and climatology (Figure S3a) shows enhancement in dust flux over NW India, some parts of Arabia, the eastern horn of Africa and regions to the north of India. The overlaid difference in simulated u–v winds (at 10 m height) between hot-composite and climatology (Figure S3a) shows an increase in surface wind magnitude near the lower end of the NW India box, a factor driving the increased local dust flux in the hot composite. In addition, enhanced surface winds in the hot composite could transport additional dust to NW India from the horn of Africa region. Furthermore, higher-level transport (u–v winds at 500 hPa), which increases between the hot-composite and climatology (Figure S3b), implies possible dust transport from the Arabian Peninsula and the Garagum and Taklamakan deserts to NW India. Thus, meteorological effects during the hot composite period, influence the increased burden of absorbing aerosols, both BC and dust, over NW India.

Enhancement in absorbing aerosol abundances during high-temperature periods is reported from observations in previous studies. High pre-monsoon AOD is reported for northern India along with enhanced BC concentrations and presence of a thick dust layer (Das & Jayaraman, 2011) using multi-instrumental ground-based observations. Transport of dust from the Thar Desert and West Asia is linked to increases in pre-monsoon AOD in this region (Dey *et al*., 2004). In addition, AOD of scattering aerosol species were also found to be enhanced during the hot extremes in the current simulations. Higher AOD is also reported during the European heat waves of 2003 and 2006 associated with both urban-industrial aerosols and long-range transported biomass burning aerosols and desert dust (Lyamani *et al*., 2006a). Enhanced AOD is also reported during the heat waves of 2003, 2006 and 2015 in France, with a diversity in types of aerosols (Chazette *et al*., 2017).

Energy added to the atmosphere, manifested as increases in positive atmospheric radiative forcing, atmospheric radiative forcing efficiency (ratio of the magnitude of atmospheric radiative forcing to AOD) and heating rates, are reported in previous studies during heat wave events. We compute the net change in the total downwelling and upwelling radiative forcing at the top of atmosphere (TOA), at the surface (SUR) and within the atmosphere (ATM) during the hot extremes and their climatological mean, as shown in Figure 6. It is observed that enhanced absorbing aerosols, during hot extremes, are linked with enhanced positive ATM radiative forcing of 3–12 $W{\cdot}m^{-2}$ (Figure 6i), implying greater addition of energy to the atmosphere. Corresponding TOA and SUR radiative forcings in Figure (6 a,d) range -(4–9) and -(10–21) $W{\cdot}m^{-2}$, respectively. The ATM radiative forcing efficiency during hot extremes, calculated here using AOD at 550 nm, ranges 8–29 $W{\cdot}m^{-2}$. These magnitudes of atmospheric forcing and its efficiency are consistent with the lower ranges of those reported in previous studies during heat wave conditions. Using simulations from a regional climate model coupled offline with a chemistry-transport model, Pere *et al*. (2011) report an enhanced positive ATM forcing of + (5–23) $W{\cdot}m^{-2}$ during the heat wave in August 2003 in Western Europe. Such enhancements are also reported in radiative transfer calculations using observations. An increase in positive radiative forcing and enhanced heating rate was associated with rise in columnar aerosols (Das & Jayaraman, 2011) in northern India during the pre-monsoon season. During European heat wave events in 2003 (Lyamani *et al*., 2006b) and 2015 (Chazette *et al*., 2017) magnitudes of ATM radiative forcing about 50 $W{\cdot}m^{-2}$ and forcing efficiency about 59 $W{\cdot}m^{-2}$ (with AOD at 670 nm) were estimated. For the European heat wave of 2015, Chazette *et al*. (2017) conclude that enhanced radiative flux trapped in aerosol layers influenced temperature rise within the planetary boundary layer.

Modelled magnitudes of columnar single scattering albedo (SSA, at 550 nm), a measure of aerosol absorption, ranged 0.92–0.97 in the column (not shown). Typical distributions of measured columnar SSA, during heat-wave events in Europe were centred about 0.85–0.94 at wavelengths between 550 and 670 nm (Lyamani *et al*., 2006b; Chazette *et al*., 2017). Lower SSA values of 0.75–0.80 in the surface layer, in the composite of the hot extremes (Figure 7a), indicate a higher abundance of absorbing aerosols in the surface layer. It may be noted that the ECHAM6-HAM2 uses a modal aerosol scheme, which allows for an accounting of internal mixing of BC and dust with soluble aerosol species in both accumulation and coarse modes (Stier *et al*., 2005), in the SSA and radiative forcing calculations. Modelled SSA are somewhat higher (less aerosol absorption) for climatological conditions (Figure 7b), compared to those during the hot extremes (Figure 7a). The net difference in SSA (Figure 7c) between the hot extremes and climatological conditions is mostly negative in the region, indicating greater presence of absorbing aerosols, during the hot extremes.

Positive atmospheric forcing, or the net gain shortwave radiation of the atmospheric surface layer, associated with the presence of absorbing aerosols, leads to increased positive shortwave heating rate. The average daytime shortwave heating rate, averaged over all solar zenith angles, at the surface layer in the model (32 m) during hot extremes ranged 0.2–0.7·$K{\cdot}day^{-1}$ (Figure 7d). It was higher (0.04–0.16·$K{\cdot}day^{-1}$) in the hot extremes as

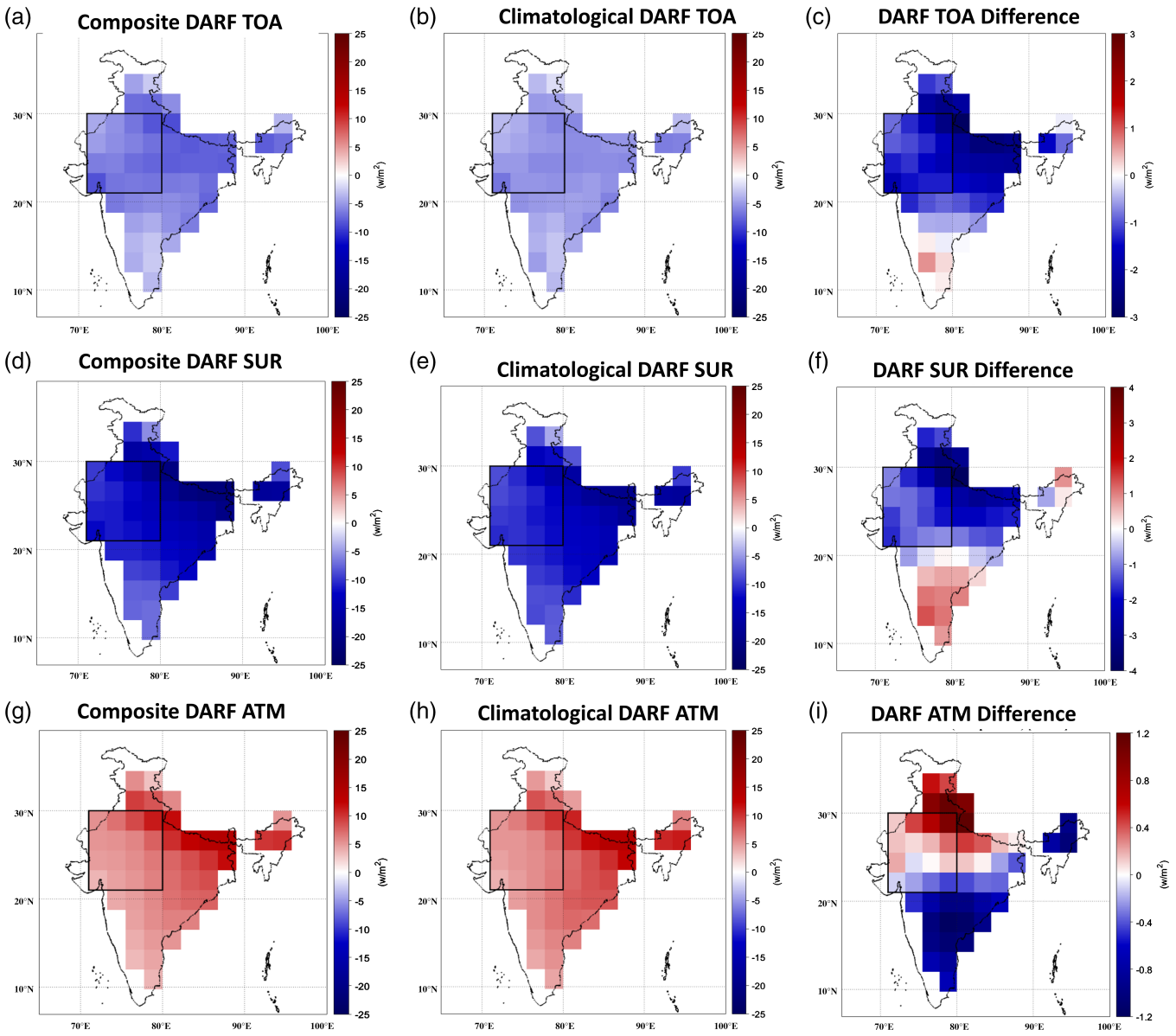

FIGURE 6 Direct aerosol radiative forcing (DARF) ($W \cdot m^{-2}$) at top of atmosphere (TOA) during the (a) hot extremes, (b) climatological mean and (c) their difference. DARF ($W \cdot m^{-2}$) at the surface (SUR) during the (d) hot extremes, (e) climatological mean and (f) their difference. DARF ($W \cdot m^{-2}$) in the atmosphere (ATM) during the (g) hot extremes, (h) climatological mean and (i) their difference

compared to climatological conditions (Figure 7f). It may be noted that the modelled shortwave heating rate forcing is directly related to aerosol abundance and denotes the difference in heating rates between an aerosol and a no-aerosol calculation in the radiative transfer module. Enhanced levels of absorbing aerosols, during hot extremes, lead to a negative shortwave radiative forcing at the surface (Figure 6d–f), much like that from scattering aerosols. However, in contrast to scattering aerosols, absorbing aerosols have the additional effect of radiatively heating the atmosphere. This is reflected in the modelled increases in shortwave heating rate in the surface layer. Aerosol-induced radiative heating has been linked to enhancements in both shortwave heating rate and surface air temperature (Ban-Weiss *et al.*, 2012; Pandithurai *et al.*, 2008a). Increases in surface air temperature were related to decreases in SSA (Pandithurai *et al.*, 2008a) and increases in near-surface BC abundance (Ban-Weiss *et al.*, 2012). Increases in aerosol absorption manifested as largest increases in surface air temperature maxima (Pandithurai *et al.*, 2008a), consistent with links found here between hot extremes and absorbing aerosols.

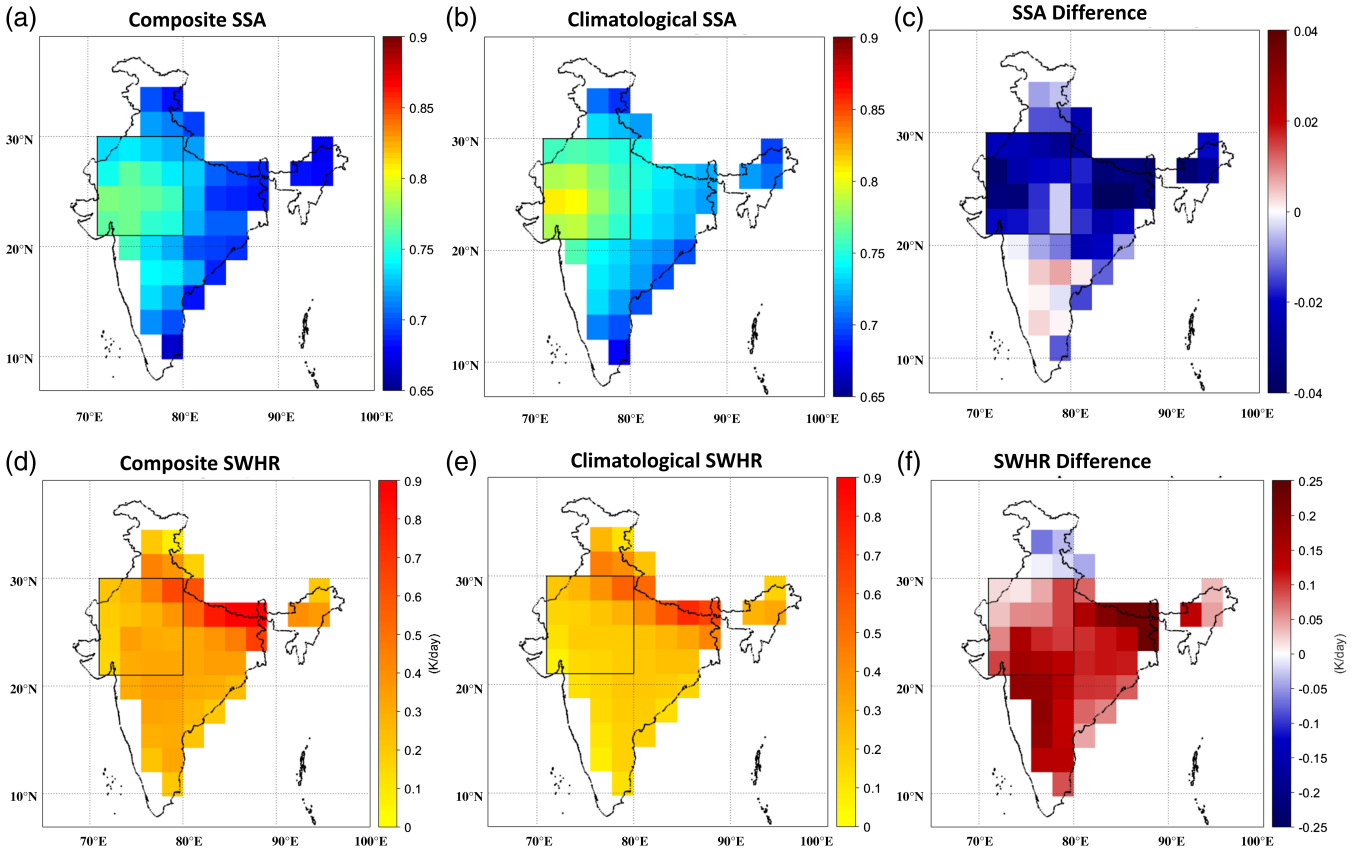

FIGURE 7 Surface single scattering albedo (SSA) during the (a) hot extremes, (b) climatological mean and (c) their difference. Surface shortwave heating rate ($K \cdot day^{-1}$) during the (d) hot extremes, (e) climatological mean and (f) their difference

While modelled daily heating rates are averaged during the relevant months of the hot extremes and climatology, precluding direct comparison with instantaneous heating rates, it is still useful to understand them in the context of those estimated from in situ measurements. Instantaneous heating rates estimated in observational studies at different locations (Ahmedabad, Udaipur, Trivandrum, Delhi) in India, in the pre-monsoon season, under typical urban aerosol loading ranged 0.6–1.3·K·day^{-1} (Das & Jayaraman, 2011; Rajeev *et al.*, 2010; Pandithurai *et al.*, 2008b). Instantaneous heating rates estimated during European heat wave events, in layers containing enhanced fire and dust aerosols (Pace *et al.*, 2005; Chazette *et al.*, 2017), at solar zenith angles of 55–77, ranged 1–2·K·day^{-1}.

Climate effects of dust aerosols over south and East Asia (Gu *et al.*, 2016), include heating of the air column which influences synoptic scale circulation changes, inducing different directions of change in precipitation based on location. Furthermore, over South Asia, there were reductions in sensible heat flux and surface temperature during the monsoon months of JJAS, in an enhanced dust simulation compared to a control. Enhancements in dust typically enhance shortwave heating rate at higher altitudes, but not in the surface layer (Mallet *et al.*, 2009). The current study focuses on the pre-monsoon, rather than the monsoon season, with significantly different synoptic circulation, atmospheric water vapour content and soil moisture, thus, precluding a direct comparison. Importantly, aerosol-induced shortwave heating rate increases occur in the surface layer and at levels up to about 100 m. The additional and perhaps dominant effect of BC aerosols, along with that of dust, influence the increases in surface shortwave heating rates and surface temperature.

4.2.2 | Modulation of surface fluxes

The surface energy balance, in terms of latent and sensible heat fluxes, influences surface temperature by cooling and heating, respectively. Aerosol-induced reductions in ground-reaching radiation can influence these fluxes. During hot extremes, reduced ground-reaching radiation (SUR) forcing of -(10–21) W·m^{-2}) (Figure 6d), and concomitantly decreased latent heat fluxes (Figure 8a,c),

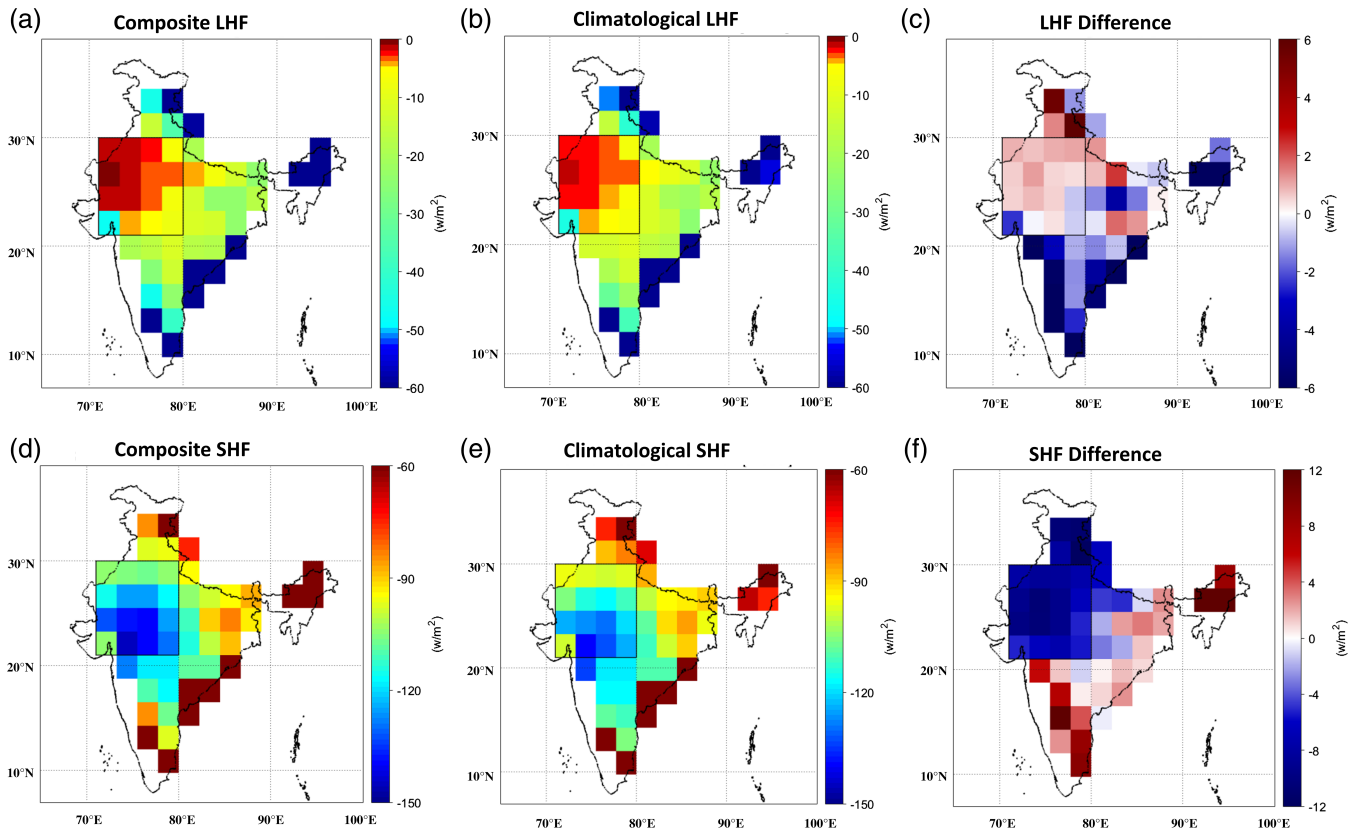

FIGURE 8 Surface latent heat flux ($W \cdot m^{-2}$) during the (a) hot extremes, (b) climatological mean and (c) their difference. Surface sensible heat flux ($W \cdot m^{-2}$) during the (d) hot extremes, (e) climatological mean and (f) their difference. Positive (negative) difference means lower (higher) magnitudes during the hot extremes

indicate lower evaporative cooling of the surface air layer. In contrast, higher sensible heat flux in the hot extremes (Figure 8d, e), consistent with higher land surface temperature (Figure 9a, b), during these periods, implies net heat flow from the ground to the surface air layer. While Pandithurai *et al.* (2008a), estimate lower sensible heat flux with increasing aerosol absorption, effects of other factors could lead to increases in sensible heat flux from temperature increases of the underlying surface, during extreme temperature events, for example, in the Indus valley region (Monteiro & Caballero, 2019).

Furthermore, in our simulations, soil moisture during hot extremes is lower than that during climatological conditions (Figure 9c), which points to drier soil conditions. The occurrence of high sensible heat flux has been related to low soil moisture in previous studies on heat waves in India (Rohini *et al.*, 2016; Ghatak *et al.*, 2017; Van Oldenborgh *et al.*, 2018). Drier soils imply that the incoming energy is used in heating the air and increasing its temperature (Van Oldenborgh *et al.*, 2018). Enhanced radiative warming of the lower troposphere by the surface due to depleted soil moisture and its impact on high-temperature extremes is shown with reanalysis data products (Rohini *et al.*, 2016; Ghatak *et al.*, 2017; Van Oldenborgh *et al.*, 2018), satellite observations (Panda *et al.*, 2017), atmospheric model in global retrospective analysis (Sandeep and Prasad, 2018) and land surface model simulations (Ghatak *et al.*, 2017).

While soil moisture differences between the hot composite and climatology are minor, there is significant enhancement in the sensible heat flux. Enhanced sensible heat flux is also associated with sinking motion of air, reduced precipitation and clear skies (Rohini *et al.*, 2016), as well as direct absorption of solar radiation by absorbing aerosols (Dave *et al.*, 2019). It may be noted here that the differences between sensible and latent heat fluxes, and the soil moisture, between the hot extremes and climatological conditions is lower than earlier reported values (e.g., Ghatak *et al.*, 2017). This underestimation may be attributed to the coarse resolution of the GCM and the consideration of monthly values rather than considering a particular heat wave event. Further, it was shown that the model simulation consistently underestimated aerosol abundance (in terms of AOD vis-a-vis measurements) during the MAMJ season, implying that this underestimation could be linked to the lower levels of aerosol influence on surface flux changes, as manifested here. Nonetheless, the nature of changes in

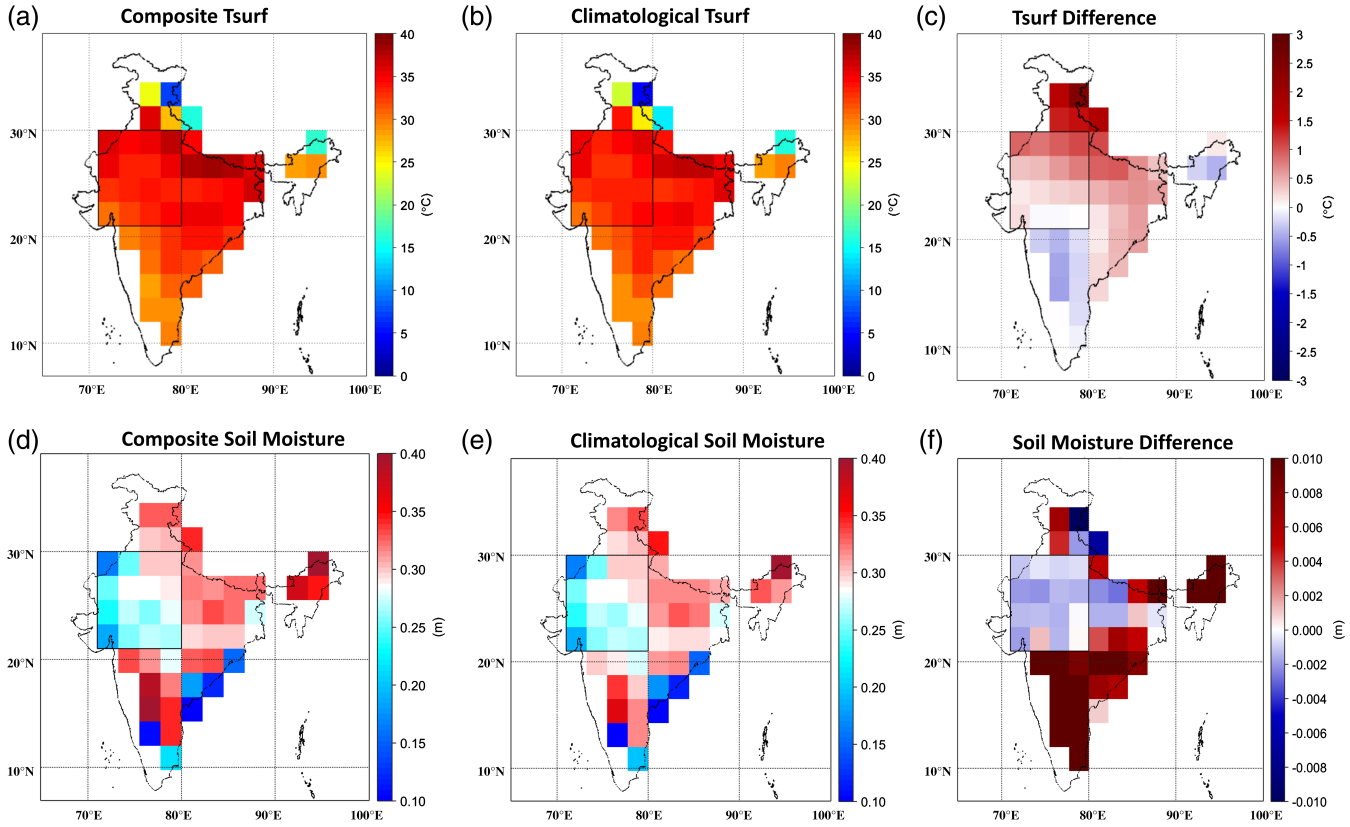

FIGURE 9 Land surface temperature (°C) during the (a) hot extremes, (b) climatological mean and (c) their difference. Root zone soil moisture (m) during the (d) hot extremes, (e) climatological mean and (f) their difference

surface heat fluxes reported here is consistent with conditions expected during temperature extremes.

5 | CONCLUSIONS

The goal of this work was to understand the association between aerosols, particularly those of absorbing nature, and high-temperature extremes in north-central India during the pre-monsoon season. Simulations from 1981 to 2010, from the chemistry-coupled atmosphere-only ECHAM6-HAM2 GCM are used. A composite of high-temperature extremes in our model simulations shows anomalous anticyclonic conditions with positive geopotential height anomalies, enhanced subsidence and LTS, along with reduced cloud cover and increased solar radiative heating, identified in reanalysis observations in previous studies, during heat waves.

We found that absorbing aerosols are associated with pre-monsoon hot extremes in north-central India. The hot extremes in our GCM simulations concur with lowered single scattering albedo and enhanced BC-AOD and Dust-AOD, compared to climatological conditions, revealing abundance of absorbing aerosols. This resulted in positive anomalies in atmospheric radiative forcing and surface shortwave heating rate, during the hot extremes. The surface energy balance showed simultaneous decrease in latent heat flux, but an increase in sensible heat flux. Thus, changes in absorbing aerosol abundance and their radiative effects, along with those in surface heat fluxes are consistent with enhanced temperatures.

Our results illustrate an interplay between synoptic atmospheric dynamics and mesoscale aerosol-induced processes that are associated with high-temperature extremes in north India, which are captured in chemistry-coupled GCM simulations. To our knowledge, this may be one of the first studies to link high-temperature extremes in India to increased abundances of absorbing aerosols (BC and dust), through an enhancement in shortwave heating rate, and alterations in surface heat fluxes, consistent with enhanced surface temperature. This is in contrast to sulfate aerosol-induced cooling reported in most other world regions. Our results emphasize the importance of regional forcings such as those from absorbing aerosols on the climate system, particularly in regions which may experience rising emissions of atmospheric forcing agents such as

GHGs and aerosols. Traditionally, anthropogenic aerosols have been linked to air pollution. This work underlines the need for addressing anthropogenic aerosols in terms of their synergistic impacts on both climate and air pollution on regional scales.

ACKNOWLEDGMENTS

The authors would like to thank RiteshGautam, RibuCherian and Mainak Das for their help. We acknowledge partial financial support from the Industrial Research and Consultancy Center's Seed Grant for Research, IIT Bombay (ArpitaMondal). The NCAP-COALESCE project funded by the Ministry of Environment Forests and Climate Change through grant NO. 14/10/2014-CC (Vol. II) is acknowledged (Arushi Sharma and Chandra Venkataraman). NeerajSah was funded by the DAAD-IIT Bombay program. The Center of Excellence in Climate Studies project grant at IIT Bombay, from the Department of Science and Technology (DST-CoECS, Phase 1), supported the HPC system for ECHAM6-HAM2 simulations and funding for NitinPatil. Observed gridded (10 latitude x 10 longitude) temperature data can be purchased from the India Meteorological Department (details at http://www.imd.gov.in/advertisements/20170320_advt_34.pdf). All other datasets are freely available.

AUTHOR CONTRIBUTIONS

Arpita Mondal and Chandra Venkataraman designed the problem. Neeraj Sah and Arushi Sharma carried out the analysis. Neeraj Sah prepared the figures. Nitin Patil ran the ECHAM6-HAM2 model. Arpita Mondal, Chandra Venkataraman and Arushi Sharma wrote the paper.

ORCID

Arushi Sharma https://orcid.org/0000-0002-2706-5934

REFERENCES

Andres, R.J. and Kasgnoc, A.D. (1998) A time-averaged inventory of subaerial volcanic. *Journal of Geophysical Research: Atmospheres*, 103, 251–261.

Arora, M., Goel, N.K. and Singh, P. (2005) Evaluation de tendances de température en Inde. *Hydrological Sciences Journal*, 50(1), 81–93.

Babu, S.S., Manoj, M.R., Moorthy, K.K., Gogoi, M.M., Nair, V.S., Kompalli, S.K., Satheesh, S.K., Niranjan, K., Ramagopal, K., Bhuyan, P.K. and Singh, D. (2013) Trends in aerosol optical depth over Indian region: potential causes and impact indicators. *Journal of Geophysical Research Atmospheres*, 118(20), 11794–11806.

Ban-Weiss, G.A., Cao, L., Bala, G. and Caldeira, K. (2012) Dependence of climate forcing and response on the altitude of black carbon aerosols. *Climate Dynamics*, 38(5–6), 897–911.

Basha, G., Kishore, P., Ratnam, M.V., Jayaraman, A., Kouchak, A. A., Ouarda, T.B.M.J. and Velicogna, I. (2017) Historical and projected surface temperature over India during the 20th and 21st century. *Scientific Reports*, 7(1), 1–10.

Bindoff, N.L., Stott, P.A., Rao, K.M.A., Allen, M.R., Gillett, N., Gutzler, D. and Hansingo, K. (2013) Detection and attribution of climate change: from global to regional supplementary material. In: *Climate Change 2013: The Physical Science Basis. Contribution of Working Group I to the Fifth Assessment Report of the Intergovernmental Panel on Climate Change*. Cambridge, United Kingdom and New York: Cambridge University Press, pp. 1–25.

Bond, T.C. and Sun, K. (2005) Can reducing black carbon emissions counteract global warming? *Environmental Science and Technology*, 39(16), 5921–5926.

Chaudhury, S.K., Gore, J.M. and Ray, K.S. (2000) Impact of heat waves over India. *Current Science*, 79(2), 153–155.

Chazette, P., Totems, J. and Shang, X. (2017) Atmospheric aerosol variability above the Paris area during the 2015 heat wave—comparison with the 2003 and 2006 heat waves. *Atmospheric Environment*, 170, 216–233. https://doi.org/10.1016/j.atmosenv.2017.09.055.

Darand, M., Garcia-Herrera, R., Asakereh, H., Amiri, R. and Barriopedro, D. (2018) Synoptic conditions leading to extremely warm periods in Western Iran. *International Journal of Climatology*, 38(1), 307–319.

Das, S.K. and Jayaraman, A. (2011) Role of black carbon in aerosol properties and radiative forcing over western India during premonsoon period. *Atmospheric Research*, 102(3), 320–334. https://doi.org/10.1016/j.atmosres.2011.08.003.

Dash, S.K., Jenamani, R.K., Kalsi, S.R. and Panda, S.K. (2007) Some evidence of climate change in twentieth-century India. *Climatic Change*, 85(3–4), 299–321.

Dave, P., Dave, P., Bhushan, M., Venkataraman, C., et al. (2019) Absorbing aerosol influence on temperature maxima: an observation based study over India. *Atmospheric Environment*, 223, 117237. https://doi.org/10.1016/j.atmosenv.2019.117237.

David, L.M., Ravishankara, A.R., Kodros, J.K., Venkataraman, C., Sadavarte, P., Pierce, J.R., Chaliyakunnel, S. and Millet, D.B. (2018) Aerosol optical depth over India. *Journal of Geophysical Research: Atmospheres*, 123(7), 3688–3703.

De, U.S., Dube, R.K. and Rao, G.P. (2005) Extreme weather events over India in the last 100 years. *The Journal of Indian Geophysical Union*, 9(3), 173–187.

Dentener, F., Kinne, S., Bond, T., Boucher, O., Cofala, J., Generoso, S., Ginoux, P., Gong, S., Hoelzemann, J.J., Ito, A., Marelli, L., Penner, J.E., Putaud, J.P., Textor, C., Schulz, M., van der Werf, G.R. and Wilson, J. (2006) Emissions of primary aerosol and precursor gases in the years 2000 and 1750 prescribed data-sets for AeroCom. *Atmospheric Chemistry and Physics*, 6(12), 4321–4344.

Dey, S., et al. (2004) Influence of dust storms on the aerosol optical properties over the indo-Gangetic basin. *Journal of Geophysical Research D: Atmospheres*, 109(20), 1–13.

Dileepkumar, R., Achutarao, K. and Arulalan, T. (2018) Human influence on sub-regional surface air temperature change over India. *Scientific Reports*, 8(1), 1–9.

Dodla, V.B., Satyanarayana, G.C. and Desamsetti, S. (2017) Analysis and prediction of a catastrophic Indian coastal heat wave of 2015. *Natural Hazards*, 87(1), 395–414.

Feng, Y., Kotamarthi, V.R., Coulter, R., Zhao, C. and Cadeddu, M. (2016) Radiative and thermodynamic responses to aerosol

extinction profiles during the pre-monsoon month over. *South Asia. Atmospheric Chemistry and Physics*, 16(1), 247–264. https://doi.org/10.5194/acp-16-247-2016.

Ganguly, D., Rasch, P.J., Wang, H. and Yoon, J.H. (2013) Climate response of the south Asian monsoon system to anthropogenic aerosols. *Journal of Geophysical Research Atmospheres*, 117 (D13). https://doi.org/10.1029/2012JD017508.

García-Herrera, R., Diaz, J., Trigo, R.M. and Hernández, E. (2005) Extreme summer temperatures in Iberia: health impacts and associated synoptic conditions. *Annales Geophysicae*, 23(2), 239–251.

Garcia-Herrera, R., et al. (2010) A review of the european summer heat wave of 2003. *Critical Reviews in Environmental Science and Technology*, 40(4), 267–306.

Gautam, R., et al. (2009) Enhanced pre-monsoon warming over the Himalayan-Gangetic region from 1979 to 2007. *Geophysical Research Letters*, 36(7), 1–5.

Gautam, R., Hsu, N.C. and Lau, K.M. (2010) Premonsoon aerosol characterization and radiative effects over the indo-Gangetic plains: implications for regional climate warming. *Journal of Geophysical Research Atmospheres*, 115(17), 1–15.

Geirinhas, J.L., Trigo, R.M., Libonati, R., Coelho, C.A.S. and Palmeira, A.C. (2018) Climatic and synoptic characterization of heat waves in Brazil. *International Journal of Climatology*, 38 (4), 1760–1776.

Ghatak, D., Zaitchik, B., Hain, C. and Anderson, M. (2017) The role of local heating in the 2015 Indian heat wave. *Scientific Reports*, 7(1), 1–8. https://doi.org/10.1038/s41598-017-07956-5.

Giorgetta, M.A., Roeckner, E., Mauritsen, T., Bader, J., Crueger, T., Esch, M., Rast, S., Kornblueh, L., Schmidt, H., Kinne, S. and Hohenegger, C., 2013. *The Atmospheric General Circulation Model ECHAM6-Model Description*. Hamburg, Germany: Tech. Rep., Max Planck Institute for Meteorology, ISSN 1614-1199.

Gouda, K.C., et al. (2017) Simulation of extreme temperature over Odisha during May 2015. *Weather and Climate Extremes*, 17, 17–28. https://doi.org/10.1016/j.wace.2017.07.001.

Gu, Y., Xue, Y., De Sales, F. and Liou, K.N. (2016) A GCM investigation of dust aerosol impact on the regional climate of North Africa and South/East Asia. *Climate Dynamics*, 46, 2353–2370. https://doi.org/10.1007/s00382-015-2706-y.

Guo, L., Turner, A.G. and Highwood, E.J. (2016) Local and remote impacts of aerosol species on Indian summer monsoon rainfall in a GCM. *Journal of Climate*, 29(19), 6937–6955.

Hansen, J., Nazarenko, L., Ruedy, R., Sato, M., Willis, J., del Genio, A., Koch, D., Lacis, A., Lo, K., Menon, S., Novakov, T., Perlwitz, J., Russell, G., Schmidt, G.A. and Tausnev, N. (2005) Climate change: Earth's energy imbalance: confirmation and implications. *Science*, 308(5727), 1431–1435.

Heidkamp, M., Chlond, A. and Ament, F. (2018) Closing the energy balance using a canopy heat capacity and storage concept—a physically based approach for the land component JSBACHv3. *Geoscientific Model Development*, 11(8), 3465–3479.

Im, E.S., Pal, J.S. and Eltahir, E.A.B. (2017) Deadly heat waves projected in the densely populated agricultural regions of South Asia. *Science Advances*, 3(8), 1–8. https://doi.org/10.1016/10.1126/sciadv.1603322.

IMD. (2015) *Annual Climate Summary*. Pune, India: The meteorological office press, office of the additional director general of meteorology (research), pp. 1–27. http://imdpune.gov.in/Clim_RCC_LRF/Annual_Climate_Summary/annual_summary_2015.pdf.

Jacobson, M.Z. (2002) Control of fossil-fuel particulate black carbon and organic matter, possibly the most effective method of slowing global warming. *Journal of Geophysical Research Atmospheres*, 107(D19). https://doi.org/10.1029/2001JD001376.

Jacobson, M.Z. (2001) Strong radiative heating due to the mixing state of black carbon in atmospheric aerosols. *Nature*, 409 (6821), 695–697.

Jaswal, A.K., Rao, P.C.S. and Singh, V. (2015) Climatology and trends of summer high temperature days in India during 1969–2013. *Journal of Earth System Science*, 124(1), 1–15.

Jin, Q., Wei, J., Yang, Z.L., Pu, B. and Huang, J. (2015) Consistent response of indian summer monsoon to middle east dust in observations and simulations. *Atmospheric Chemistry & Physics*, 15, 9897–9915. https://doi.org/10.5194/acp-15-9897-2015.

Kloster, S., Dentener, F., Feichter, J., Raes, F., Lohmann, U., Roeckner, E. and Fischer-Bruns, I. (2010) A GCM study of future climate response to aerosol pollution reductions. *Climate Dynamics*, 34(7), 1177–1194.

Koch, D. and Del Genio, A.D. (2010) Black carbon semi-direct effects on cloud cover: review and synthesis. *Atmospheric Chemistry and Physics*, 10(16), 7685–7696.

Koren, I., Martins, J. V., Remer, L. A. and Afargan, H. (2008) Smoke invigoration versus inhibition of clouds over the amazon. *Science*, 321(5891), 946–949. http://dx.doi.org/10.1126/science.1159185.

Kothawale, D.R., Deshpande, N.R. and Kolli, R.K. (2016) Long term temperature trends at major, medium, small cities and hill stations in India during the period 1901-2013. *American Journal of Climate Change*, 05(03), 383–398. https://doi.org/10.4236/ajcc.2016.53029.

Kothawale, D.R., Revadekar, J.V. and Kumar, K.R. (2010) Recent trends in pre-monsoon daily temperature extremes over India. *Journal of Earth System Science*, 119(1), 51–65.

Kothawale, D.R. and Rupa Kumar, K. (2005) On the recent changes in surface temperature trends over India. *Geophysical Research Letters*, 32(18), 1–4.

Krishnan, R. and Ramanathan, V. (2002) Evidence of surface cooling from absorbing aerosols. *Geophysical Research Letters*, 29(9), 54–1-54–4. https://doi.org/10.1029/2002GL014687.

Lau, W.K.M., Kim, M.K., Kim, K.M. and Lee, W.S. (2010) Enhanced surface warming and accelerated snow melt in the Himalayas and Tibetan plateau induced by absorbing aerosols. *Environmental Research Letters*, 5(2), 025204 Available at http://stacks.iop.org/1748-9326/5/i=2/a=025204?key=crossref.06c375f9a3600c4cc5c5d72e4dca8aa5.

Lau, W.K.M. and Kim, K.-M. (2012) The 2010 Pakistan flood and Russian heat wave: teleconnection of Hydrometeorological extremes. *Journal of Hydrometeorology*, 13(1), 392–403 Available athttp://stacks.iop.org/1748-9326/5/i=2/a=025204?key=crossref.06c375f9a3600c4cc5c5d72e4dca8aa5.

Lu, Z., Zhang, Q. and Streets, D.G. (2011) Sulfur dioxide and primary carbonaceous aerosol emissions in China and India, 1996-2010. *Atmospheric Chemistry and Physics*, 11(18), 9839–9864.

Lyamani, H., Olmo, F.J., Alcántara, A. and Alados-Arboledas, L. (2006a) Atmospheric aerosols during the 2003 heat wave in

southeastern Spain I: spectral optical depth. *Atmospheric Environment*, 40(33), 6453–6464.

Lyamani, H., Olmo, F.J., Alcántara, A. and Alados-Arboledas, L. (2006b) Atmospheric aerosols during the 2003 heat wave in southeastern Spain II: microphysical columnar properties and radiative forcing. *Atmospheric Environment*, 40(33), 6465–6476.

Mallet, M., Tulet, P., Serça, D., Solmon, F., Dubovik, O., Pelon, J., Pont, V. and Thouron, O. (2009) Impact of dust aerosols on the radiative budget, surface heat fluxes, heating rate profiles and convective activity over West Africa during March 2006. *Atmospheric Chemistry and Physics*, 9(18), 7143–7160.

Mazdiyasni, O., et al. (2017) Increasing probability of mortality during Indian heat waves. *Science Advances*, 3(6), 1–6.

Menon, S., Hansen, J., Nazarenko, L. and Luo, Y. (2002) Climate effects of black carbon aerosols in china and india. *Science*, 297 (5590), 2250–2253. http://dx.doi.org/10.1126/science.1075159.

Mickley, L.J., Leibensperger, E.M., Jacob, D.J. and Rind, D. (2012) Regional warming from aerosol removal over the United States: results from a transient 2010-2050 climate simulation. *Atmospheric Environment*, 46, 545–553. https://doi.org/10.1016/j.atmosenv.2011.07.030.

Miralles, D.G., Teuling, A.J., van Heerwaarden, C.C. and Vilà-Guerau de Arellano, J. (2014) Mega-heatwave temperatures due to combined soil desiccation and atmospheric heat accumulation. *Nature Geoscience*, 7(5), 345–349.

Mishra, A.K. and Shibata, T. (2012) Climatological aspects of seasonal variation of aerosol vertical distribution over central indo-Gangetic belt (IGB) inferred by the space-borne lidar CALIOP. *Atmospheric Environment*, 46, 365–375. Available at. https://doi.org/10.1016/j.atmosenv.2011.09.052.

Mishra, V., Mukherjee, S., Kumar, R. and Stone, D.A. (2017) Heat wave exposure in India in current, 1.5 °C, and 2.0 °C worlds. *Environmental Research Letters*, 12(12), 124012. http://dx.doi.org/10.1088/1748-9326/aa9388.

Monteiro, J.M. and Caballero, R. (2019) Characterization of extreme wet-bulb temperature events in southern Pakistan. *Geophysical Research Letters*, 46, 10659–10668.

Murari, K.K., Ghosh, S., Patwardhan, A., Daly, E. and Salvi, K. (2015) Intensification of future severe heat waves in India and their effect on heat stress and mortality. *Regional Environmental Change*, 15(4), 569–579.

Murari, K.K., Sahana, A.S., Daly, E. and Ghosh, S. (2016) The influence of the El Niño southern oscillation on heat waves in India. *Meteorological Applications*, 23(4), 705–713.

Nair, S., Rao, C.P. and Pai, D.S. (2017) Synoptic Situation Associated with the Heat Wave Condition during 17 May to 1 June 2015 Over India. *Current Science*, 112(02), 364–369. http://dx.doi.org/10.18520/cs/v112/i02/364-369.

Neubauer, D., Lohmann, U., Hoose, C. and Frontoso, M.G. (2014) Impact of the representation of marine stratocumulus clouds on the anthropogenic aerosol effect. *Atmospheric Chemistry and Physics*, 14(21), 11997–12022.

Pace, G., Meloni, D. and di Sarra, A. (2005) Forest fire aerosol over the Mediterranean basin during summer 2003. *Journal of Geophysical Research Atmospheres*, 110(21), 1–11.

Padma Kumari, B., et al. (2007) Observational evidence of solar dimming: offsetting surface warming over India. *Geophysical Research Letters*, 34(21), 1–5.

Pai, D.S., Nair, S.A. and Ramanathan, A.N. (2013) Long term climatology and trends of heat waves over India during the recent 50 years (1961-2010). *Mausam*, 64(4), 585–604 Available at: http://metnet.imd.gov.in/mausamdocs/16441_F.pdf.

Pan, X., Chin, M., Gautam, R., Bian, H., Kim, D., Colarco, P.R., Diehl, T.L., Takemura, T., Pozzoli, L., Tsigaridis, K., Bauer, S. and Bellouin, N. (2015) A multi-model evaluation of aerosols over South Asia: common problems and possible causes. *Atmospheric Chemistry and Physics*, 15, 5903–5928. Available at. https://doi.org/10.5194/acp-15-5903-2015.

Panda, D.K., Mishra, A., Kumar, A., Mandal, K.G., Thakur, A.K. and Srivastava, R.C. (2014) Spatiotemporal patterns in the mean and extreme temperature indices of India, 1971-2005. *International Journal of Climatology*, 34(13), 3585–3603.

Panda, D.K., AghaKouchak, A. and Ambast, S.K. (2017) Increasing heat waves and warm spells in India, observed from a multi-aspect framework. *Journal of Geophysical Research*, 122(7), 3837–3858.

Pandey, A., Sadavarte, P., Rao, A.B. and Venkataraman, C. (2014) Trends in multi-pollutant emissions from a technology-linked inventory for India: II. Residential, agricultural and informal industry sectors. *Atmospheric Environment*, 99, 341–352. Available at. https://doi.org/10.1016/j.atmosenv.2014.09.080.

Pandithurai, G., Seethala, C., Murthy, B.S. and Devara, P.C.S. (2008a) Investigation of atmospheric boundary layer characteristics for different aerosol absorptions: case studies using CAPS model. *Atmospheric Environment*, 42, 4755–4768.

Pandithurai, G., Dipu, S., Dani, K.K., Tiwari, S., Bisht, D.S., Devara, P.C.S. and Pinker, R.T. (2008b) Aerosol radiative forcing during dust events over New Delhi, India. *Journal of Geophysical Research: Atmospheres*, 113(13), 1–13.

Patil, N., Venkataraman, C., Muduchuru, K., Ghosh, S. and Mondal, A. (2019) Disentangling Sea-surface temperature and anthropogenic aerosol influences on recent trends in south Asian monsoon rainfall. *Climate Dynamics*, 52(3–4), 2287–2302.

Pattanaik, D.R., Mohapatra, M., Srivastava, A.K. and Kumar, A. (2017) Heat wave over India during summer 2015: an assessment of real time extended range forecast. *Meteorology and Atmospheric Physics*, 129(4), 375–393.

Pere, J.C., Mallet, M., Pont, V. and Bessagnet, B. (2011) Impact of aerosol direct radiative forcing on the radiative budget, surface heat fluxes, and atmospheric dynamics during the heat wave of summer 2003 over western Europe: a modeling study. *Journal of Geophysical Research Atmospheres*, 116(23), 1–12.

Perkins, S.E., Alexander, L.V. and Nairn, J.R. (2012) Increasing frequency, intensity and duration of observed global heatwaves and warm spells. *Geophysical Research Letters*, 39(20), 1–5.

Pezza, A.B., van Rensch, P. and Cai, W. (2012) Severe heat waves in southern Australia: synoptic climatology and large scale connections. *Climate Dynamics*, 38(1–2), 209–224.

Porch, W., Chylek, P., Dubey, M. and Massie, S. (2007) Trends in aerosol optical depth for cities in India. *Atmospheric Environment*, 41(35), 7524–7532.

Purich, A., Cowan, T., Cai, W., van Rensch, P., Uotila, P., Pezza, A., Boschat, G. and Perkins, S. (2014) Atmospheric and oceanic conditions associated with southern Australian heat waves: a CMIP5 analysis. *Journal of Climate*, 27(20), 7807–7829.

Purnadurga, G., Lakshmi Kumar, T.V., Koteswara Rao, K., Rajasekhar, M. and Narayanan, M.S. (2018) Investigation of

temperature changes over India in association with meteorological parameters in a warming climate. *International Journal of Climatology*, 38(2), 867–877.

Rajeev, K., Parameswaran, K., Thampi, B.V., Mishra, M.K., Nair, A. K.M. and Meenu, S. (2010) Altitude distribution of aerosols over southeast Arabian Sea coast during pre-monsoon season: elevated layers, long-range transport and atmospheric radiative heating. *Atmospheric Environment*, 44(21–22), 2597–2604.

Ramachandran, S., Kedia, S. and Srivastava, R. (2012) Aerosol optical depth trends over different regions of India. *Atmospheric Environment*, 49, 338–347. https://doi.org/10.1016/j.atmosenv.2011.11.017.

Ramanathan, V. (2001) Aerosols, climate, and the hydrological cycle. *Science*, 294(5549), 2119–2124.

Ramanathan, V., Chung, C., Kim, D., Bettge, T., Buja, L., Kiehl, J. T., Washington, W. M., Fu, Q., Sikka, D. R. and Wild, M. (2005) Atmospheric brown clouds: Impacts on South Asian climate and hydrological cycle. *Proceedings of the National Academy of Sciences*, 102(15), 5326–5333. http://dx.doi.org/10.1073/pnas.0500656102.

Ramanathan, V., et al. (2002) The Indian ocean experiment and the Asian brown cloud. *Current Science*, 83(8), 947–955.

Ramanathan, V., Ramana, M.V., Roberts, G., Kim, D., Corrigan, C., Chung, C. and Winker, D. (2007) Warming trends in Asia amplified by brown cloud solar absorption. *Nature*, 448(7153), 575–578.

Ratnam, J.V., Behera, S.K., Ratna, S.B., Rajeevan, M. and Yamagata, T. (2016) Anatomy of Indian heatwaves. *Scientific Reports*, 6, 24395 http://www.nature.com/srep/2016/160415/srep24395/full/srep24395.html.

Revadekar, J.V., Kothawale, D.R., Patwardhan, S.K., Pant, G.B. and Rupa Kumar, K. (2012) About the observed and future changes in temperature extremes over India. *Natural Hazards*, 60(3), 1133–1155.

Roeckner, E., et al. (2003) The atmospheric general circulation model ECHAM5. *Max Planck Institute for Meteorology*, 349 (349), 1–140.

Roeckner, E., Brokopf, R., Esch, M., Giorgetta, M.A., Hagemann, S., Kornblueh, L., Manzini, E., Schlese, U. and Schulzweida, U. (2006) Sensitivity of simulated climate to horizontal and vertical resolution in the ECHAM5 atmosphere model. *Journal of Climate*, 19(16), 3771–3791.

Rohini, P., Rajeevan, M. and Srivastava, A.K. (2016) On the variability and increasing trends of heat waves over India. *Scientific Reports*, 6, 1–9. https://doi.org/10.1038/srep26153.

Sadavarte, P. and Venkataraman, C. (2014) Trends in multi-pollutant emissions from a technology-linked inventory for India: I. industry and transport sectors. *Atmospheric Environment*, 99(2014), 353–364. Available at:. https://doi.org/10.1016/j.atmosenv.2014.09.081.

Sandeep, A. and Prasad, V.S. (2018) Intra-annual variability of heat wave episodes over the east coast of India. *International Journal of Climatology*, 38(January), e617–e628.

SarathChandran, M.A., et al. (2017) Indian summer heat wave of 2015: a biometeorological analysis using half hourly automatic weather station data with special reference to Andhra Pradesh. *International Journal of Biometeorology*, 61(6), 1063–1072.

Sarangi, C., Tripathi, S.N., Mishra, A.K., Goel, A. and Welton, E.J. (2016) Elevated aerosol layers and heir radiative impact over Kanpur during monsoon onset period. *Journal of Geophysical Research Atmospheres*, 121, 7936–7957. https://doi.org/10.1002/2015JD024711.

Satheesh, S.K. and Ramanathan, V. (2000) Large differences in tropical aerosol forcing at the top of the atmosphere and Earth's surface. *Nature*, 405(6782), 60–63.

Sharma, S. and Mujumdar, P. (2017) Increasing frequency and spatial extent of concurrent meteorological droughts and heatwaves in India. *Scientific Reports*, 7(1), 1–9. https://doi.org/10.1038/s41598-017-15896-3.

Srivastava, A.K., Rajeevan, M. and Kshirsagar, S.R. (2009) Development of a high resolution daily gridded temperature data set (1969–2005) for the Indian region. *Atmospheric Science Letters*, 10(4), 249–254.

Stier, P., et al. (2007) Atmospheric chemistry and physics aerosol absorption and radiative forcing. *Atmos. Chem. Phys*, 7, 5237–5261 www.atmos-chem-phys.net/7/5237/2007/.

Stier, P., Feichter, J., Kinne, S., Kloster, S., Vignati, E., Wilson, J., Ganzeveld, L., Tegen, I., Werner, M., Balkanski, Y., Schulz, M., Boucher, O., Minikin, A. and Petzold, A. (2005) The aerosol-climate model {ECHAM5-HAM}. *Atmospheric Chemistry and Physics*, 5(4), 1125–1156.

Struzewska, J. and Kaminski, J.W. (2008) Formation and transport of photooxidants over Europe during the July 2006 heat wave—observations and GEM-AQ model simulations. *Atmospheric Chemistry and Physics*, 8(3), 721–736.

Tegen, I., et al. (2002) Impact of vegetation and preferential source areas on global dust aerosol: results from a model study. *Journal of Geophysical Research: Atmospheres*, 107(D21), AAC–14.

Trigo, R.M., et al. (2005) How exceptional was the early august 2003 heatwave in France? *Geophysical Research Letters*, 32(10), 1–4.

Van Oldenborgh, G.J., et al. (2018) Extreme heat in India and anthropogenic climate change. *Natural Hazards and Earth System Sciences*, 18(1), 365–381.

Venkataraman, C., Habib, G., Eiguren-Fernandez, A., Miguel, A.H. and Friedlander, S.K. (2005) Residential biofuels in South Asia: carbonaceous aerosol emissions and climate impacts. *Science*, 307(5714), 1454–1456.

Wang, W., Zhou, W., Li, X., Wang, X. and Wang, D. (2016) Synoptic-scale characteristics and atmospheric controls of summer heat waves in China. *Climate Dynamics*, 46(9–10), 2923–2941.

Wehner, M., Stone, D., Krishnan, H., AchutaRao, K. and Castillo, F. (2016) The deadly combination of heat and humidity in India and Pakistan in summer 2015. *Bulletin of the American Meteorological Society*, 97(12), S81–S86.

Wilks, D.S. (2011) *Statistical Methods in the Atmospheric Sciences*, Vol. 100, San Diego, California, USA: Academic press.

Wood, R. and Bretherton, C.S. (2006) On the relationship between stratiform low cloud cover and lower-tropospheric stability. *Journal of Climate*, 19(24), 6425–6432.

Xoplaki, E., González-Rouco, J.F., Luterbacher, J. and Wanner, H. (2003) Mediterranean summer air temperature variability and its connection to the large-scale atmospheric circulation and SSTs. *Climate Dynamics*, 20(7–8), 723–739.

Zanis, P. (2009) A study on the direct effect of anthropogenic aerosols on near surface air temperature over southeastern Europe during summer 2000 based on regional climate modeling. *Annales Geophysicae*, 27(10), 3977–3988.

Zanis, P., Ntogras, C., Zakey, A., Pytharoulis, I. and Karacostas, T. (2012) Regional climate feedback of anthropogenic aerosols over Europe using RegCM3. *Climate Research*, 52(1), 267–278.

SUPPORTING INFORMATION

Additional supporting information may be found online in the Supporting Information section at the end of this article.

How to cite this article: Mondal A, Sah N, Sharma A, Venkataraman C, Patil N. Absorbing aerosols and high-temperature extremes in India: A general circulation modelling study. *Int J Climatol*. 2021;41 (Suppl. 1):E1498–E1517. https://doi.org/10.1002/joc.6783

Climate Dynamics (2019) 52:2287–2302
https://doi.org/10.1007/s00382-018-4251-y

Disentangling sea-surface temperature and anthropogenic aerosol influences on recent trends in South Asian monsoon rainfall

Nitin Patil[1] · Chandra Venkataraman[1,2] · Kaushik Muduchuru[1] · Subimal Ghosh[1,3] · Arpita Mondal[1,3]

Received: 9 November 2017 / Accepted: 7 May 2018 / Published online: 14 May 2018

Abstract
Recent studies point to combined effects of changes in regional land-use, anthropogenic aerosol forcing and sea surface temperature (SST) gradient on declining trends in the South Asian monsoon (SAM). This study attempted disentangling the effects produced by changes in SST gradient from those by aerosol levels in an atmospheric general circulation model. Two pairs of transient ensemble simulations were made, for a 40-year period from 1971 to 2010, with evolving versus climatological SSTs and with anthropogenic aerosol emissions fixed at 1971 versus 2010, in each case with evolution of the other forcing element, as well as GHGs. Evolving SST was linked to a widespread feedback on increased surface temperature, reduced land–sea thermal contrast and a weakened Hadley circulation, with weakening of cross-equatorial transport of moisture transport towards South Asia. Increases in anthropogenic aerosol levels (1971 versus 2010), led to an intensification of drying in the peninsular Indian region, through several regional pathways. Aerosol forcing induced north–south asymmetries in temperature and sea-level pressure response, and a cyclonic circulation in the Bay of Bengal, leading to an easterly flow, which opposes the monsoon flow, suppressing moisture transport over peninsular India. Further, aerosol induced decreases in convection, vertically integrated moisture flux convergence, evaporation flux and cloud fraction, in the peninsular region, were spatially congruent with reduced convective and stratiform rainfall. Overall, evolution of SST acted through a weakening of cross-equatorial moisture flow, while increases in aerosol levels acted through suppression of Arabian Sea moisture transport, as well as, of convection and vertical moisture transport, to influence the suppression of SAM rainfall.

Keywords Aerosol–cloud–rainfall interaction · GCM simulations · ECHAM6-HAM · Anthropogenic aerosols

1 Introduction

The South Asian monsoon or SAM is central to the agricultural economy and to water and food security of the South Asian region (Bookhagen and Burbank 2010; Hasson et al. 2013). Anthropogenic forcing elements that induce changes in SAM rainfall development, include greenhouse gases, aerosols and land-use/land-cover changes (e.g. Krishnan et al. 2015). Analysis of multi-model simulations from the Coupled-Model-Intercomparison-Project (CMIP) show wide inter-model variation in the simulated precipitation changes over South Asia (Kripalani et al. 2007; Annamalai et al. 2007; Turner and Slingo 2009; Fan et al. 2010; Saha et al. 2014; Sooraj et al. 2015), making it difficult to glean a clear signal of regional hydro-climatic changes (Sabade et al. 2011; Hasson et al. 2013; Held and Soden 2006). Coupled model simulations report an interplay between thermodynamic factors such as moisture convergence, and dynamic processes such as the monsoon circulation, with the former often dominating the latter (Sooraj et al. 2015). The expected response to increased greenhouse-gas (GHG) concentrations, tends to suggest increases in mean monsoon rainfall (Turner and Annamalai 2012; Ueda et al. 2006; Cherchi et al. 2011; Kitoh et al. 2013). Such an increasing trend of SAM rainfall has been found in the response of several models of phase

Electronic supplementary material The online version of this article (https://doi.org/10.1007/s00382-018-4251-y) contains supplementary material, which is available to authorized users.

✉ Chandra Venkataraman
chandra@iitb.ac.in

[1] Interdiciplinary Program in Climate Studies, Indian Institute of Technology Bombay, Powai, Mumbai 400 076, India

[2] Department of Chemical Engineering, Indian Institute of Technology Bombay, Powai, Mumbai, India

[3] Department of Civil Engineering, Indian Institute of Technology Bombay, Powai, Mumbai, India

5 of the Coupled Model Intercomparison Project (CMIP5) (Saha et al. 2014; Menon et al. 2013). Both Salzmann et al. (2014) and Guo et al. (2015) suggest that CMIP5 models which include aerosol forcing, show drying rainfall trends over South Asia, from both reduced hemispheric temperature contrast, leading to decreased strength of the meridional circulation, as well as, decreased water vapour availability, while Guo et al. (2015) further attribute this specifically to aerosol indirect forcing. Observational studies of the SAM show significant decline of annual mean precipitation over the west coast of India and regions of north and east Central-India during 1951–2005 (Dash et al. 2009; Ghosh et al. 2009), related to a reduction in the frequency of moderate rainfall and drizzle events.

Improving our understanding of the influence of anthropogenic forcers on observed decreases in SAM rainfall is an ongoing endeavour. A major regional signal is the seasonal and decadal evolution of SST magnitude in the equatorial Indian Ocean and its north–south meridional gradient. While annual mean SSTs over the Indian Ocean are highest around the equator, SSTs over the northern Arabian Sea and Bay of Bengal warm significantly in the boreal summer, influencing the development of the South Asian monsoon system. Anthropogenic drivers such as GHGs and aerosols have been linked to changes in the meridional north–south SST gradient. A significant part of the response to greenhouse gases manifests as warming surface temperature trends, particularly in tropical SSTs (Guo et al. 2015, 2016). Further, increases in anthropogenic aerosols weakens the SST gradient, through decreased downwelling radiation at 10°N–25°N, with a maximum reduction in the summer monsoon season (Ramanathan et al. 2005; Ganguly et al. 2012). An independent warming of the equatorial Indian Ocean SST (IOSST) through the last few decades, projected to continue through the twenty-first century (Krishnan et al. 2015), is linked to a dynamical response of the Indian Ocean to reducing surface monsoonal winds, leading to reduction in upwelling of deep-ocean cold waters (Swapna et al. 2014; Mishra et al. 2012). This IOSST warming is further linked to weakening of the summer monsoon cross-equatorial flow, thereby showing a two-way coupling between changes in IOSST and the monsoon circulation (Swapna et al. 2014). While the observed SST trend is dominated by warming in the deep tropics, simulations with prescribed SST trends wherein the component from aerosol emissions is removed, found further warming in the extratropical Northern Hemisphere (NH) that offsets monsoon weakening (Guo et al. 2016).

The South-Asian region has also experienced significant changes in land-use patterns (Paul et al. 2016), leading to conversion of forest land to agricultural land and wetland clearance (Pathak et al. 2017). The roles of land-use land-cover change was highlighted in leading to an overall increase in regional planetary albedo (Krishnan et al. 2015) which reduced precipitation through an albedo-precipitation feedback, required to maintain thermal equilibrium. Land-use and vegetation changes that lead to suppressed evapotranspiration could also reduce the recycling ratio and weaken monsoon rainfall. Further, potential impacts of land surface feedbacks through evapotranspiration on regional precipitation variability over Indian subcontinent (Pathak et al. 2014) act in some periods (i.e., August and September) especially over the northern India, where recycling ratio is significant (~25%).

Anthropogenic aerosol forcing is generally linked to a declining trend in the NH monsoon precipitation in general (Polson et al. 2014) and the SAM in particular (e.g., Ramanathan et al. 2005; Chung and Ramanathan 2006; Bollasina et al. 2011, 2014; Ganguly et al. 2012; Salzmann et al. 2014; Krishnan et al. 2015; Guo et al. 2016). Other than modification of the SST gradient, the aerosol "direct effect" acts through pathways including "surface solar dimming" (Ramanathan et al. 2005; Lau and Kim 2017), an asymmetric cooling of NH or more specifically surface temperatures over Asia (Bollasina et al. 2011, 2014; Guo et al. 2016). This leads to weakening of the overturning Hadley circulation and vertical wind shear (Ganguly et al. 2012; Krishnan et al. 2015; Guo et al. 2016). Increased atmospheric stabilization and reduced convective activity through the aerosol "direct" (Ramanathan et al. 2005) and "indirect" effects (Cherian et al. 2013) are some of the other known pathways through which aerosols can influence rainfall. The inter-hemispheric energy balance change leading to a weakened monsoon is largely linked to scattering aerosols like sulphates (Bollasina et al. 2011; Guo et al. 2016), while convection accommodates positively on daily to monthly timescales due to radiative effects of absorbing aerosols like black carbon leading to short-term increases in rainfall (Lau et al. 2006; Manoj et al. 2011; Ganguly et al. 2012; Vinoj et al. 2014). Combined effects of regional land-use changes, anthropogenic-aerosol forcing and equatorial Indian Ocean warming, along with GHG-forcing, reproduced the recent declining trends in the SAM (Krishnan et al. 2015). The high-resolution simulations with prescribed aerosol optical depth authentically captured responses to aerosol "direct" radiative effects. Importantly, the need to better understand "indirect" effects of aerosols on altering cloud properties and rainfall (Guo et al. 2015, 2016) and the need to decouple different anthropogenic forcing elements has been recently highlighted.

As discussed, a prominent warming of observed recent SST trends in the western Indian ocean (Roxy et al. 2015), is independent of aerosol effects, and has been linked to GHG forcing of tropical SSTs (Guo et al. 2016) or a reduction in upwelling of deep-ocean cold waters (Swapna et al. 2014), because of weakening of the summer monsoon cross-equatorial flow. These studies suggest an

independence of SST and aerosol forcing. In this study the interplay among different forcing elements is examined through disentangling the influence of changes in sea-surface temperature and anthropogenic aerosol emissions on recent changes in SAM rainfall. We use a state-of-the-art global climate model (ECHAM6-HAM), wherein the HAM module dynamically predicts the composition and size distribution of aerosols, which is interactive with the meteorology, internal mixing, and direct as well as indirect radiative effects. Internal variability, or the spread around the ensemble mean, is often enhanced in ocean–atmosphere coupled model studies (e.g. Li and Xie 2014; Infanti and Kirtman 2017), compared to that in AGCM studies, and has been linked to differences in simulation of surface energy fluxes (Infanti and Kirtman 2017). This makes it difficult to discern responses to specific forcing, like those from anthropogenic aerosols. Therefore, in several previous studies addressing aerosol effects on precipitation (Ganguly et al. (2012); Guo et al. (2016); Krishnan et al. (2015)), simulations were made with an AGCM, using prescribed sea surface temperature. Such experiments typically serve to identify mechanisms or pathways of response to different forcing elements, which is the focus of this work. In this study, contrasting a pair of simulations uses identical forcing from SST and GHGs, but differing aerosol emissions levels (1971 versus 2010) produced enhanced drying (Fig. 6a, b) at 90% confidence level over the peninsular region. Moderate resolution simulations were made (T63, or 1.8°×1.8°), to avoid strong limitations of coarse-resolution models in representing regional processes. We choose to run a suite of transient simulations, with three ensemble members, to retain non-linear interactions among different feedbacks to the imposed forcing. A recent period of 1971–2010 was simulated with prescribed evolving and climatological sea surface temperature datasets and varying aerosol emissions. Rapid industrial and population growth in India took place post the 1980s; therefore, anthropogenic aerosols were fixed to 1971 and 2010 levels, and also used in evolving mode. To focus on effects of SST and aerosols, evolving forcing by SST and aerosols is used, while a fixed land-use land-cover scheme (Raddatz et al. 2007) is used, compatible with the relatively coarse model resolution.

The paper is organized as follows: In Sect. 2, we describe the ECHAM6-HAM model overview, simulation setup and observation datasets used to analyze the results. In Sect. 3, we present the validation of the model with observations. In Sect. 4, we present the results of effects of meridional thermal gradient and anthropogenic aerosols, each at fixed and evolving levels, on recent trends in South Asian monsoon rainfall, along with understanding of underlying mechanisms. Our conclusions are presented in Sect. 5.

2 Description of datasets and model

2.1 Datasets (observations)

The daily Level 3 moderate-resolution imaging spectroradiometer (MODIS) (collection V005) global 1° × 1° gridded aerosol optical depth (AOD) at 550 nm from both Terra (approximate local overpass time at about 10.30 local solar time (LST)) and Aqua (overpass at 13.30 LST) satellites was averaged to obtain daily average and ground based observations from Aerosol Robotic Network (AERONET) at Kanpur (26.5°N, 80.2°E) and Pantnagar-Gandhi College (25.9°N, 84.1°E), used to evaluate the model-simulated AOD from 2001 to 2010. The daily mean rainfall data (0.25° × 0.25°) product (Pai et al. 2014) provided by the India Meteorological Department (IMD) is also used to evaluate the model-simulated precipitation fields over the Indian region. We also use the observed gridded (0.5° × 0.5°) monthly precipitation dataset during 1971–2010 from Climate Research Unit (CRU, Harris et al. 2014). Absorbing Aerosol Index (AAI) data were from the Total Ozone Mapping Spectrometer (TOMS, 1° × 1.25°) for 2001–2004 (Herman et al. 1997) and the ozone monitoring instrument (OMI, 1° × 1°) for 2005–2010 (Torres et al. 2007), as per their availability and we interpolated the OMI dataset on the TOMS grid (i.e. 1° × 1.25°). The MOD16 global evapotranspiration dataset (0.5° × 0.5°, Mu et al. 2011) from 2000 to 2010 was used to evaluate the model-simulated evapotranspiration.

2.2 Brief description of ECHAM6-HAM GCM

The model ECHAM6 is the sixth generation general circulation model (GCM) of the Max Planck Institute for Meteorology in Hamburg, Germany. The original model code belongs to the European Centre for Medium Range Weather Forecasts (ECMWF) (Roeckner et al. 2003). The version of ECHAM6-HAM used in this study (ECHAM6.1-HAM2.2) has been described in Neubauer et al. (2014). The model solves the primitive equations for the divergence, vorticity, temperature and surface pressure. The vertical coordinates of the model use the sigma-pressure levels in the lower troposphere and the pressure levels in the middle and the upper atmosphere (Giorgetta et al. 2006; Manzini et al. 2006). The radiative transfer model used in ECHAM6 is an updated version of the rapid and the accurate radiative transfer model (RRTM). It contains the shortwave (SW) and longwave (LW) radiative schemes based on 14 spectral bands in the SW and 16 spectral bands in the LW (Giorgetta et al. 2012).

The ECHAM6 model uses the JSBACH (Raddatz et al. 2007) land vegetation model which computes land-surface

albedo, including a consideration of the snow on soil, bare surfaces, the canopy effect and the forest masking (Brovkin et al. 2013), along with carbon storage from photosynthesis. The ECHAM6 setup used for this work uses the aerosol microphysical core M7, the aerosol module of the HAM model, estimating a multi-modal aerosol size-distribution with seven log-normal modes and a prescribed variance (Vignati et al. 2004). Five internally and externally mixed components: sulfate, black carbon, particulate organic matter, mineral dust and sea salt aerosol are resolved with an internal mixture of soluble and insoluble compounds in the soluble modes, but external mixing in the insoluble mode.

2.3 Simulation setup and approach

In this study, we perform a suite of long-term transient simulations to separately understand the effects of recent changes in the magnitude and north–south gradient of SSTs and aerosol levels on the SAM by performing experiments using both fixed and evolving patterns in both forcing elements. Here, simulations under four set-ups, each with three ensemble members, were made during 1971–2010 (40 years) using a spin-up of 3 years (Table 1). The three ensemble members were generated by slightly perturbing model parameters, by about 0.01%, related to coefficients for horizontal diffusion for divergence, vorticity, and temperature. A pair of simulations, to understand the SST effect, contrast evolving versus climatological sea surface temperature ($E_{SST}E_{aero+GHG}$ and $C_{SST}E_{aero+GHG}$), while other forcing elements, i.e., aerosols and GHGs are used in an evolving mode. A second pair of simulations, to understand the aerosol effect, uses a high and low level of anthropogenic aerosol emissions (at 2010 and 1971 levels) while using evolving forcings of SST (from AMIP observations) and GHGs.

Evolving observed SST and sea ice concentration (SIC) were prescribed using the monthly varying Atmospheric Model Intercomparison Project (AMIP) data sets. Evolving annual mean GHG concentrations from the datasets of International Institute for Applied Systems Analysis (IIASA; http://www.iiasa.ac.at/web-apps/tnt/RcpDb/) are prescribed. Evolving aerosol emissions, based on the AEROCOM emission inventory from 1971 to 2010 (Dentener et al. 2006) are used along with prescribed land-surface properties. Global fire emission data (GFED) were used for forest burning emission sectors. Volcanic emissions of SO_2 are included (Andres and Kasgnoc 1998). Dust and sea salt emissions were calculated online (Tegen et al. 2002) using the ECHAM6 10 m wind speed. Models with interactive aerosol schemes (Wang et al. 2009; Cowan and Cai 2011; Bollasina et al. 2011; Ganguly et al. 2012) allow the changes in model meteorology to feedback onto their predicted aerosol distributions and in return, calculate the radiative effects of aerosols on the atmospheric dynamics. Importantly, the ECHAM6-HAM2 model uses a stratiform cloud parameterization which is explicitly linked to aerosols (Roeckner et al. 2003; Lohmann et al. 2007), thus calculating the aerosol indirect effect on cloud drop size, number concentration and the effect on precipitation formation is parameterized and its consequent effects on SAM rainfall.

3 Comparison with observations

3.1 Aerosol optical depth

We evaluate the skill of the model in estimating key variables including aerosol levels and precipitation. The spatial distribution of annual mean AOD climatology averaged over 10 years (2001–2010), using the base case simulation, with all evolving anthropogenic forcings ($E_{SST}E_{aero+GHG}$) is compared with MODIS-derived Terra and Aqua satellite combined AOD values (Fig. 1a, b). The model broadly captures AOD distributions over the Indo-Gangetic plains (IGP) and Indian subcontinent (Fig. 1a, b). There is significant underestimation in high AOD regions of the IGP (Auxiliary Fig. A1), but satisfactory agreement over the rest of India. The average bias over land points of India shows mean normalized bias (MNB) = −0.31 and root mean square error (RMSE) = 0.14 indicates modest underestimation of AOD within levels seen in previous studies (Ganguly et al. 2012). Increasing trends in AOD during 2001–2010 in the region

Table 1 Summary of simulation setup and emission data sets used in this study

Experiment name	Simulated setup
Evolving sea surface temperature, evolving aerosols and GHGs from 1971 to 2010 ($E_{SST}E_{aero+GHG}$)	Emissions: evolving anthropogenic aerosols BC, OC, and SO_2 (AEROCOM); evolving annual mean GHGs Forcings: fixed land surface properties; evolving SST/SIC (AMIP) Prognostic emissions: DMS, Dust, and Sea Salt Model simulations: 1971–2010, 3 years spin-up, three-member ensemble Climatological SST: monthly varying 1979–2008 average
Climatological sea surface temperature, evolving aerosols and GHGs from 1971 to 2010 ($C_{SST}E_{aero+GHG}$)	
Evolving sea surface temperature, GHGs and high aerosols fixed at 2010 ($E_{SST+GHG}H_{aero}$)	
Evolving sea surface temperature, GHGs and low aerosols fixed at 1971 ($E_{SST+GHG}L_{aero}$)	

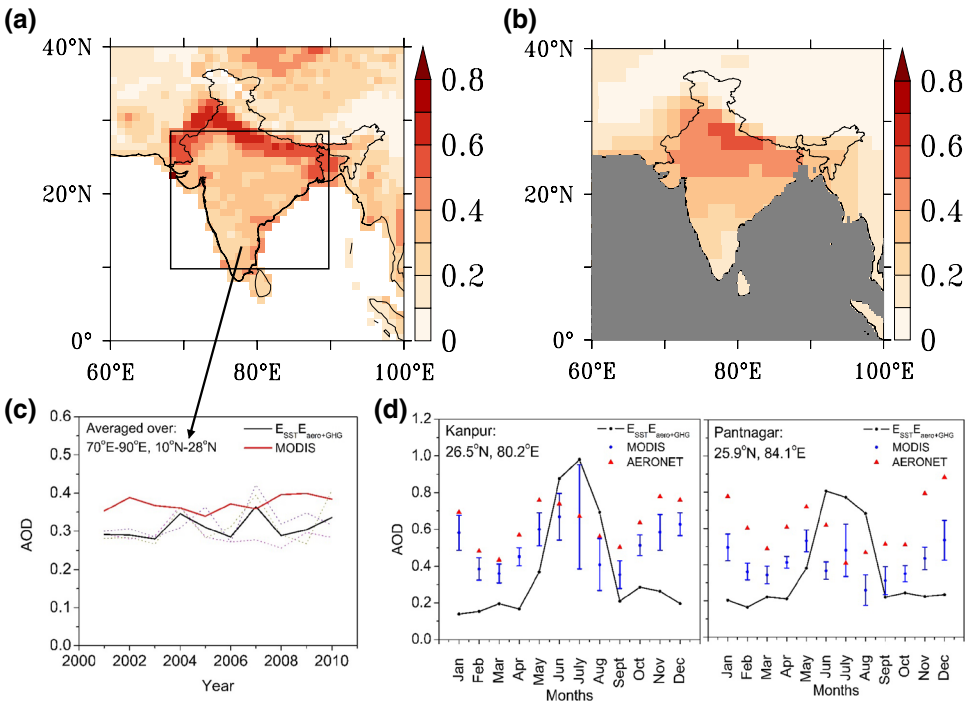

Fig. 1 Annual climatology of AOD at 550 nm over land-points in the Indian region 70°–90°E, 10°–28°N; from **a** MODIS, **b** $E_{SST}E_{aero+GHG}$, **c** Time series for $E_{SST}E_{aero+GHG}$ (Black line) from 2001 to 2010 for the monsoon region (70°E–90°E, 10°N–28°N). The dotted lines represent the three ensemble members for the $E_{SST}E_{aero+GHG}$. **d** Monthly mean AOD climatology from 2001 to 2010 over Kanpur (26.5°N, 80.2°E) and Pantnagar-Gandhi college (25.9°N, 84.1°E) using $E_{SST}E_{aero+GHG}$ and observations from MODIS and AERONET data sets, respectively

(70°–90°E, 10°–28°N, Fig. 1a) reported in recent studies (e.g. Krishnan et al. 2015), show reasonable agreement with those in MODIS observations (Fig. 1c). Direct comparison of in-situ measurements (AERONET) with spatially averaged satellite detection or model output is often fraught with uncertainty. Further, the modelled meteorology in transient model simulations may not faithfully represent the actual meteorological conditions during the measurement period. With these caveats, the modelled seasonal cycle in monthly mean AOD (Fig. 1d), fails to capture wintertime highs during October to February (ONDJF) in both satellite retrievals from MODIS and ground based observations from AERONET at sites in the Indo-Gangetic plains including Kanpur (26.5°N, 80.2°E) and Pantnagar-Gandhi College (25.9°N, 84.1°E), indicating low modelled anthropogenic aerosols. A similar model underestimation in the premonsoon for March–May (MAM) season indicates possible deficiencies in modelled dust. A qualitative comparison of the spatial patterns of aerosol index from TOMS and OMI during MAM (2001–2010 mean) with modelled dust burden (Auxiliary Fig. A2a) for the same time period, indicated model underestimation in dust burden over the Indo-Gangetic plains and the Taklamakan desert, but an overestimation of dust over the Caspian Sea and East Asian regions (Auxiliary Fig. A2b, c). Overall, satellite observations indicate a large influx of desert dust from the western arid and desert regions of West Asia, North Africa, and Thar (Rajasthan, India) during the pre-monsoon season (Dey et al. 2004; Dey and Girolamo 2010), which appear to be underestimated in the model. Further, a possible high bias in model relative-humidity based aerosol growth factor, at larger RH levels, could lead to enhanced water uptake in the monsoon season, thus leading to possible overestimation of modelled AOD during JJAS.

3.2 Precipitation

Modelled rainfall in the base case $E_{SST}E_{aero+GHG}$ simulation, is compared with observations. The seasonal cycles in rainfall, on two scales, over the monsoon region (70°–90°E, 10°–28°N) and over peninsular India (70°–90°E, 10°–20°N) are evaluated against observation from IMD (Pai et al. 2014) and CRU (Harris et al. 2014), during 1971–2010 (Fig. 2). IMD gridded rainfall data are derived from daily rainfall records from 6995 rain-gauge stations over India, while CRU data are from monthly observations at meteorological stations across the world's land areas in which station anomalies are interpolated into (0.5° × 0.5°) grid cells covering the global land surface. The seasonal cycle of rainfall is captured by the model, over both the monsoon region and peninsular India, while its mean magnitude is somewhat underestimated in July, August and September, in the monsoon region (Fig. 2a) but more in the peninsular regions (Fig. 2b).

Overall, the spatial distribution of mean model-simulated precipitation (mm day^{-1}) broadly captures both the IMD-observed patterns over Western Ghats and north east region including the Himalayan foothills (Auxiliary Fig. A3), but underestimates continental precipitation compared to IMD observations. Trends in modelled rainfall (Figure A6) for the $E_{SST}E_{aero+GHG}$ experiment, with all time-varying

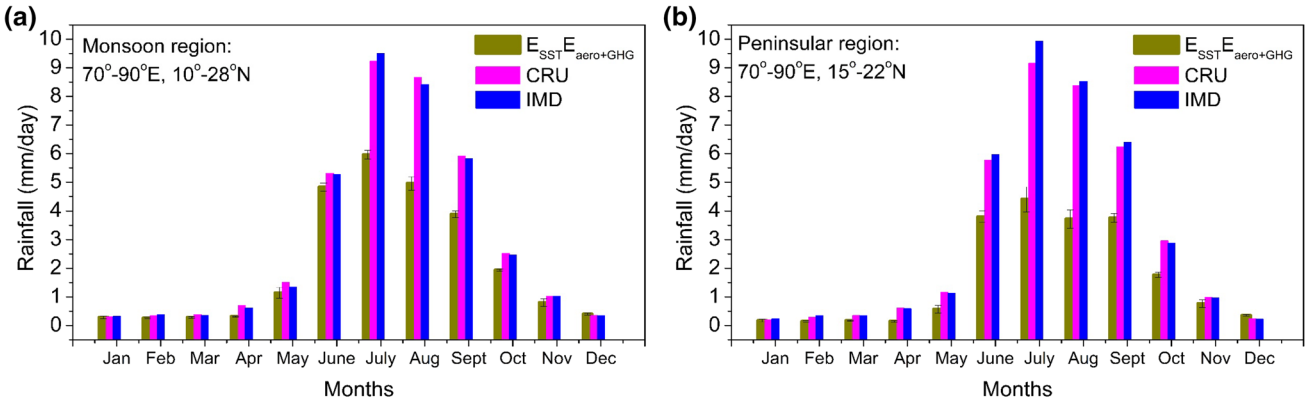

Fig. 2 Seasonal variability of precipitation (mm day^{-1}) over **a** Monsoon region (70°E–90°E, 10°N–28°N), **b** Peninsular region (70°E–90°E, 15°N–22°N) averaged over the Indian land-points from IMD, CRU and $E_{SST}E_{aero+GHG}$

forcings closest to real conditions, show a fair agreement over peninsular India with drying trends over the western Ghats and western Deccan plateau similar to IMD and CRU observations. However, fine spatial features of increasing precipitation trends in the eastern peninsula, are not captured, because of the relatively coarse model resolution. This agreement provides confidence in use of the simulations to study underlying mechanisms, a primary goal of this work. Model skill in estimating the relative contribution of convective and stratiform rainfall, was evaluated compared to the Tropical Rainfall Measurement Mission (TRMM) observations (Pokhrel and Sikka 2013) averaged during June–September (JJAS) over Indian mainland (Auxiliary Table A1). A 45:55% proportion in stratiform:convective rainfall in the measurements as found in TRMM, is captured quite faithfully by the modelled rainfall, with values quite close to absolute rainfall amounts in the TRMM observations (Auxiliary Table A1).

Observational SAM rainfall datasets show differences among them, with CRU showing lower rainfall amounts compared to IMD over central-east India and the Ganga plains (Auxiliary Fig. A3a, b), consistent with previous studies. The spatial distribution (Auxiliary Fig. A3c) of seasonal mean model-simulated precipitation (mm day^{-1}) broadly captures both the IMD (Auxiliary Fig. A3a) and CRU (Auxiliary Fig. A3b) observed patterns over Western Ghats and North-East regions. Largest differences between model simulation and measurements, in terms of spatial distributions of MNB and RMSE (Auxiliary Fig. A4), are found in the Indo-Gangetic plain and northwest India. The averaged values over the monsoon region (MNB = − 0.34, RMSE = 5.3, IA = 0.71; units for MNB and RMSE are mm day^{-1}) are higher than over the peninsular region (MNB = − 0.10, RMSE = 5.3, IA = 0.54) region. The model simulates the broad features of precipitation in the SAM region and has an agreement with the observed precipitation, in the $E_{SST}E_{aero+GHG}$ simulation, which uses all evolving forcings. Enhanced mean precipitation in central India and parts of the east coast, which occur in observations is not captured by the model. However, the orographic rainfall high over the Western Ghats and the eastern Himalayas are captured well. Further, modelled precipitation in peak monsoon months of July and August shows good agreement with IMD over the peninsular Indian region (MNB = − 0.10, R value = 0.57) allowing interpretation of the response of the features to aerosol forcing over peninsular India. Thus, there is model underestimation of rainfall over the IGP and the northwest, better agreement with observations in the peninsular region, but overestimation over the Western Ghats and Himalayas. The results are broadly consistent with a dry bias reported over northern parts of India in most of CMIP5 models due to internal variability (Salzmann et al. 2014).

The ECHAM5 coupled model, evaluated as part of models used in the CMIP5 suite (Sperber et al. 2013) showed some deficiencies in the onset, peak, withdrawal and duration of the Asian monsoon. However, it showed reasonable skill is reproducing the Indian monsoon interannual variability and boreal summer intraseasonal variability. A deficient representation of the tilted band of convection was noted, from replacement or changes to condensation or radiation schemes, post ECHAM4. A study comparing ECHAM4 with ECHAM5-HAM (Lohmann et al. 2007), indicated that coupling the size-resolved aerosol microphysics scheme to a double-moment stratiform cloud microphysics scheme, improved prediction of stratiform cloud properties including cloud water, ice and hydrometeor concentrations. Introducing aerosol effects into GCMs can be done through an online, coupled aerosol microphysical module which ingests aerosol emissions (like with ECHAM-HAM), or by prescribing time-varying 3-dimensional concentrations of natural aerosols (e.g., sea-salt, dust) and anthropogenic aerosols (e.g., sulfates, black carbon, particulate organic matter),

their optical properties or their radiative forcing (Taylor et al. 2012). Some studies indicate that differences in GCM simulations between prescribed aerosol fields versus interactively computed aerosols have little impact in terms of radiation and radiative forcing, for example in the LMDZ atmospheric model (Déandreis et al. 2012). However, the ECHAM6 model, used in this study, is yet to be evaluated in the framework of the CMIP. Further, during August and September, it is suggested that recycled precipitation, or moisture released to the atmosphere through evapotranspiration, has a significant influence on rainfall magnitude, especially in parts of north-central India (Pathak et al. 2014). Most general circulation models are vulnerable to an underestimation of rainfall over the monsoon region of south Asia, for reasons discussed above, also observed in CMIP5 studies (Sperber et al. 2013). $E_{SST}E_{aero+GHG}$ model simulation underestimates rainfall over the central India and parts of the east coast, partly explained as the deficiency of the model in simulating evapotranspiration (Fig. A5), compared to MODIS measurements, with strong underestimation in June, July and August, but better agreement in the other months. While further analysis of the details of the land-surface scheme and underlying mechanisms that affect evapotranspiration lies beyond the scope of this work, this could be a contributing factor to modelled rainfall underestimation.

Internal variability, as the standard deviation of the precipitation trends for the all forcing run $E_{SST}E_{aero+GHG}$, following literature (Salzmann et al. 2014), is found to be significantly lower (0.20 mm day^{-1} (40 year)$^{-1}$) than the drying signal ($-$1.93 mm day^{-1}(40 year)$^{-1}$), averaged over the monsoon region, indicating that precipitation response to the different forcings considered is emerging as significant.

Non-linear feedbacks of aerosol forcing, may occur because of reduced evapotranspiration, leading to enhanced temperatures and wind speeds, which could further affect levels of dust aerosols (Guo et al. 2016). No significant difference was found in climatological mean dust AOD, between simulations made with all forcing and those at different aerosol levels: evolving aerosols [$E_{SST}E_{aero+GHG}$ (0.039 ± 0.024), high aerosols $E_{SST+GHG}H_{aero}$ (0.037 ± 0.023) and low aerosols $E_{SST+GHG}L_{aero}$ (0.039 ± 0.022) (two-sided t-test $p < 0.05$)]. This suggests limited evapotranspiration effects on dust aerosols in the different experiments. Non-linear feedbacks, between aerosol and GHG forcing (Ming and Ramaswamy 2009), showed a precipitation decrease greater than the sum of separate GHG and aerosol effects, in the northern hemisphere. To examine non-linearity between the aerosol and SST forcing in these simulations, the average monsoon trend in the all forcing experiment is compared to the sum of those from evolving aerosols (fixed SST) and evolving SST (fixed aerosols at 1971), over the Indian land areas (70–90°E, 10–28°N). Contrary to opposing responses to GHGs and aerosols, the response to both SST and aerosol evolution is a drying. The trend in the all forcing experiment was suppressed ($E_{SST}E_{aero+GHG} = -1.9 \pm 0.63$ mm day^{-1} (40 year)$^{-1}$) when compared to the sum of the individual forcing experiments ($E_{aero+GHG}C_{SST} = -0.042 \pm 0.37$ mm day^{-1} (40 year)$^{-1}$, $E_{SST+GHG}L_{aero} = -2.36 \pm 0.65$ mm day^{-1} (40 year)$^{-1}$, Sum $= -2.4 \pm 0.75$ mm day^{-1} (40 year)$^{-1}$), however, is not significant with p-value = 0.48.

In further discussion of rainfall changes and underlying mechanisms, an analysis was first carried out month by month, which showed marked differences between contrasting simulations in July and August, but relatively insignificant differences in the other months. Since the model set-up uses transient simulations for a somewhat short period of 40 years, it is expected that response signals may not be adequately strong. Noting that the peak monsoon period is also in the months of July and August (Dash et al. 2009, 2013), it was decided to base further analysis on contrasts in rainfall during July and August.

4 Results and discussion

4.1 Rainfall response to SST changes

In the base-case $E_{SST}E_{aero+GHG}$ simulation, the SST evolves according to the AMIP observational dataset, which, over the period of 40 years from 1971 to 2010, shows basin wide warming (8°S–2°N, 60°E–90°E) in the Indian Ocean (Fig. 3a), whose trend is in excess of the global-warming signal (Krishnan et al. 2015). The AMIP observed SST used in the base-case simulation shows a decadal evolution of the meridional gradient in the July–August months (Fig. 3b), showing the greatest warming of ~ 1 °C between 5°S–7°N between 1971 and 1980 and 2001–2010. The meridional SST gradient (between 10°N–25°N and 0°–15°S) reduces by about ~ 1 °C, between these decades, from cooling of SSTs in the northern belt, attributed to aerosol forcing (Ramanathan et al. 2005) along with warming of SSTs in the southern belt, attributed to equatorial Indian ocean warming (Roxy et al. 2015; Krishnan et al. 2015).

The SST forcing used in the climatological SST simulation ($C_{SST}E_{aero+GHG}$, averaged from 1979 to 2008 years), reflects both southern Indian Ocean warming and northern aerosol surface cooling signals and is closer to a present day SST state, but invariant from year to year. The precipitation response in the $C_{SST}E_{aero+GHG}$ showed a decreasing trend in northern India and further north (Fig. 4a), along with increasing trends over central India and the peninsular region. A decrease over the Western Ghats was not seen. In contrast, in the $E_{SST}E_{aero+GHG}$ (Fig. 4b) simulation, a decreasing trend in SAM rainfall was manifested over most of India, with a pronounced decrease over the Western Ghats, which is exerted over a greater spatial extent,

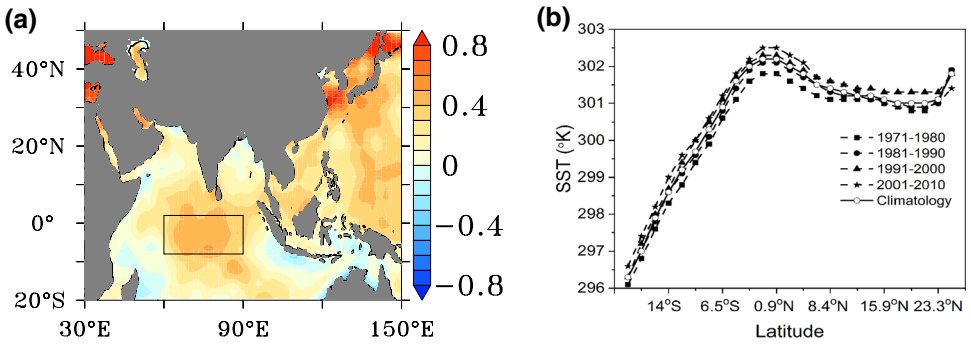

Fig. 3 **a** SST trend [°C (40 years^{-1})] during peak summer monsoon months of July–August for the years 1971–2010 in $E_{SST}E_{aero+GHG}$ simulation shows basin wide warming (8°S–2°N, 60°E–90°E) in the Indian Ocean and **b** Seasonal mean SST (°K) averaged over the longitudinal zone (60°E–100°E) covering the Indian Ocean during July–August decadal and climatology from AMIP observations

possibly because of the relatively coarse resolution of the model, which does not resolve well the sharp gradients in topography of the Western Ghats.

The climatological SST forcing used here is similar to the SST-observation forcing (Guo et al. 2016), from AMIP SSTs for a similar period (1976–2005), used in simulations with the HadGEM2 AGCM model. The SST-observation equilibrium simulation (Guo et al. 2016) in the HadGEM2 AGCM model produced a decrease in rainfall over the Indo-Gangetic Plain and Western Ghats, but not over the central India and the peninsular region. However, there is a difference in the forcings applied between the equilibrium simulation Guo et al. (2016), in which all other forcings (GHG and aerosol) are held at pre-industrial levels, and our $C_{SST}E_{aero+GHG}$ simulation, in which there is an evolution of GHGs and aerosols from 1971 to 2010. Atmospheric response to emission evolution of aerosols and GHGs, not coupled in this simulation to SST (Fig. 4c), when compared to evolution of SST (Fig. 4d), appears to have a weaker feedback on land–sea temperature contrast and the overturning circulation.

4.1.1 Mechanisms underlying SST influence on rainfall

Underlying mechanisms influencing differences in rainfall response between the $C_{SST}E_{aero+GHG}$ and $E_{SST}E_{aero+GHG}$ simulations were further examined. The change in SST in the $E_{SST}E_{aero+GHG}$, led to a widespread feedback on surface heating (2-m temperature; Fig. 4 c, d), compared to the $C_{SST}E_{aero+GHG}$ simulations. Trends in 2-m temperature over all of South Asia show increases of 1–3 °C over the 40-year period, with strongest surface heating over the southern Indian Ocean and a degraded land–sea thermal contrast (Fig. 4d). However, in the climatological SST simulation, a mixed feedback leads to surface cooling up to − 1 °C in northern parts of the subcontinent (Fig. 4c), along with distinct land–sea thermal contrast, particularly related to the Arabian Sea and western Indian ocean. Climatological SST (Fig. 4e), induces a more uniform basin-wide increase in mean sea level pressure (MSLP), over both southern and northern Indian Ocean and the Indian landmass. However, evolving SST feedback in the $E_{SST}E_{aero+GHG}$ simulation produces an increase in MSLP over the northern latitudes, but a reduction (Fig. 4f) in MSLP over the equatorial Indian Ocean. This is accompanied by a weakening trend of MSLP gradient (Fig. 4f) along the transect of the monsoonal flow. The surface temperature and the sea-level pressure changes, together weaken the cross equatorial flow towards Indian land mass and reorient the westerlies along the low MSLP over the Equatorial Indian Ocean (Fig. 4f), leading to an overall trend towards a dominant easterly flow which is related to rainfall reduction.

In a large-scale effect, the normal overturning Hadley-type circulation during the SAM has warm and humid air rising over most regions north of the equator with a sinking branch south of the equator (e.g. Meehl and Arblaster 2002). Changes in vertical velocities are caused by gain or loss of energy by the atmospheric system, mostly through diabatic heating or cooling processes. In both simulations, there is a slowdown in the trend of the overturning circulation (Fig. 4g, h), averaged over 60°E–100°E. However, the $E_{SST}E_{aero+GHG}$ simulation (Fig. 4h) shows a clearer slow down with a broad ascending branch over the equatorial region (10°S–10°N), a response to tropical SST warming, along with a subsiding branch over most of the extent of the Indian subcontinent (5°N–30°N). In contrast, in the climatological SST simulation (Fig. 4g) the ascending and descending branches break up, with mixed behaviour over the equatorial and south Asian regions, indicating a weaker trend in slow down of the meridional circulation, in the climatological SST forcing $C_{SST}E_{aero+GHG}$ simulation. These results are broadly consistent with the precipitation response to late-twentieth SST forcing both in transient (Krishnan et al. 2015) and equilibrium (Guo et al. 2016) simulations.

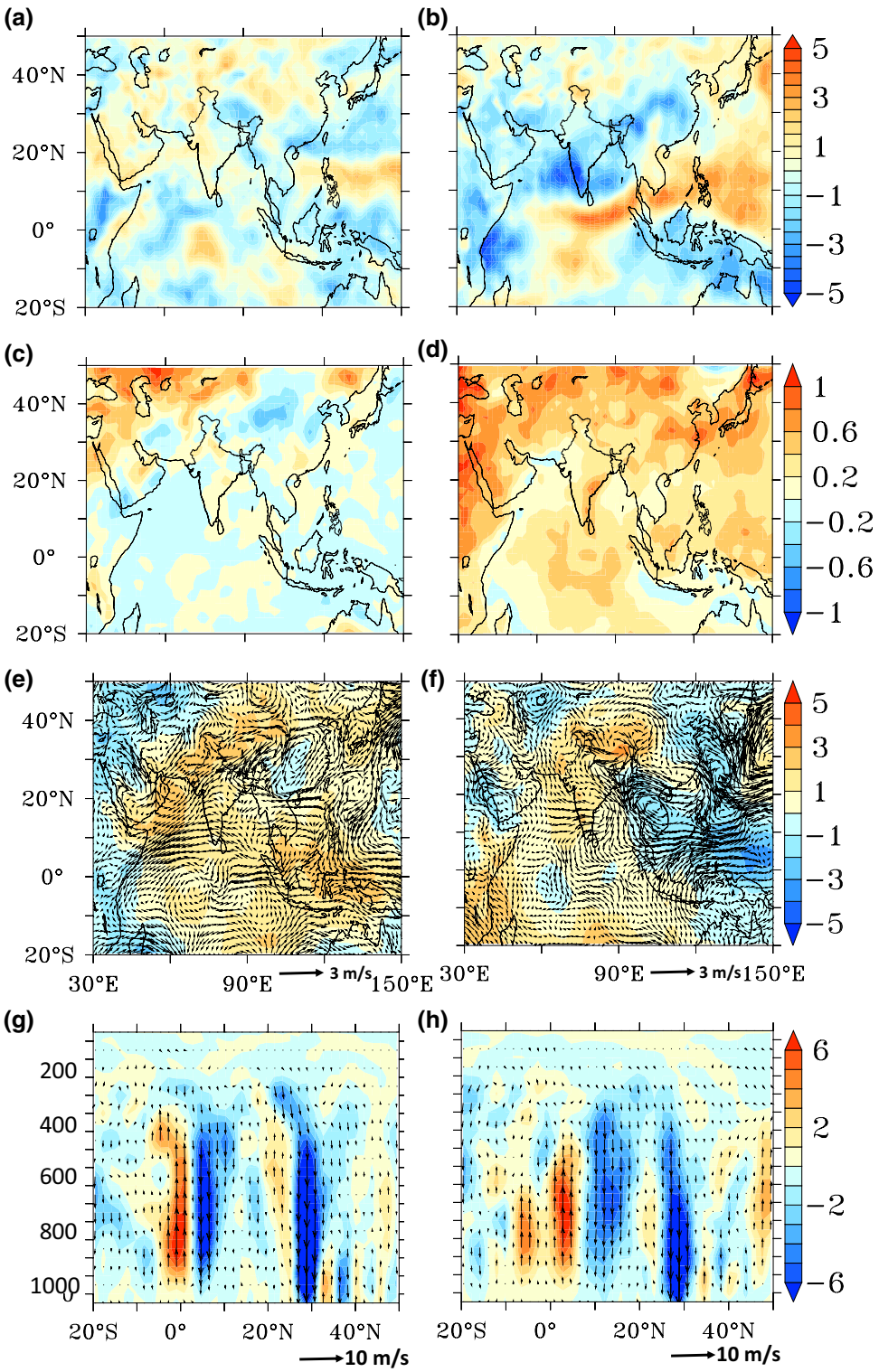

Fig. 4 Trend during peak summer monsoon months of July–August for the years 1971–2010 in $C_{SST}E_{aero+GHG}$ (left column) and $E_{SST}E_{aero+GHG}$ (right column) **a, b** Precipitation [mm day^{-1} (40 years^{-1})], **c, d** 2-m Temperature [^{o}C (40 years^{-1})], **e, f** MSLP [hPa (40 years^{-1})] with winds [m s^{-1} (40 years^{-1})] at 850 hPa and **g, h** meridional circulation [m s^{-1}] averaged over 60°E–100°E, where vertical velocity change [hPa day^{-1} (40 years^{-1})] is also shown as shaded background

4.2 Rainfall responses to aerosol increases

To understand the regional effects of anthropogenic aerosols, a pair of simulations at different anthropogenic aerosol levels of 1971 and 2010 was made, denoted by $E_{SST+GHG}L_{aero}$ and $E_{SST+GHG}H_{aero}$ respectively. These included evolving forcing from SSTs and GHGs during the period in transient mode. We chose to retain a mix of anthropogenic emissions of the near-past and present day, rather than to perturb individual aerosol species, to attempt to capture more realistic recent

changes. Further, this pair of simulations allows isolation of effects of aerosols exerted through atmospheric accommodations including both direct and indirect effects, disentangling them from the effects exerted through SST changes. Results of the simulations are presented as differences between the $E_{SST+GHG}H_{aero}$ and $E_{SST+GHG}L_{aero}$ ensemble means, of variables involved in feedback processes. Model ingested AEROCOM emissions (Dentener et al. 2006) of SO_2, BC and OC, were 4, 1.5, 1.3 times greater, respectively, in 2010 than in 1971 globally, while they over India they were 5.2, 2.1, 1.5 times greater, respectively. The influence of changing aerosol emissions on mean AOD magnitude and its composition, in $E_{SST+GHG}H_{aero}$ and $E_{SST+GHG}L_{aero}$ simulations, is discussed in a following section. As mentioned earlier, the analysis is based on differences during the peak monsoon months of July and August.

Differences, analyzed for July and August, between simulations using 1971 and 2010 aerosol emission levels, show an overall anthropogenic AOD increase of 130% (Fig. 5a), with an increasing fraction of black carbon (BC). Mean AOD from anthropogenic aerosols increased about 40–60% for sulphate (Auxiliary Fig. A7a) and organic carbon or OC (Auxiliary Fig. A7b), treated as purely scattering species in the model, with largest increases over much of northern India. BC AOD increased much more with over 100% increases over most of south Asia (Auxiliary Fig. A7c). The increases in BC AOD, especially over north India, are from residential cooking and heating emissions using biomass fuels, in the densely populated Indo–Gangetic Plains. BC lifetime is influenced by assumed state of hygroscopic or hydrophobic nature (Reddy and Boucher 2004). The ECHAM model assumes BC treated as 80% hydrophobic and 20% hydrophilic with an e-folding time of about 24 h (Hendricks et al. 2004), making it less susceptible to wet deposition than hygroscopic sulphate and OC. These aerosol changes induce both radiative and cloud microphysical effects as discussed below.

Increased aerosol levels between 1971 and 2010, produce simulated changes in model-simulated clear-sky shortwave radiation fluxes during July and August (Fig. 5b) of -1 to -3 Wm^{-2} over Northern and Central India, with increased atmospheric forcing of 2 to 5 Wm^{-2} (Fig. 5d) with clear highs over the Indo-Gangetic plains. Changes in surface downwelling radiation from "direct" aerosol forcing (Fig. 5c) range between -2 and -7 Wm^{-2} while that from "indirect" forcing (Fig. 5e) range between -1 and -4

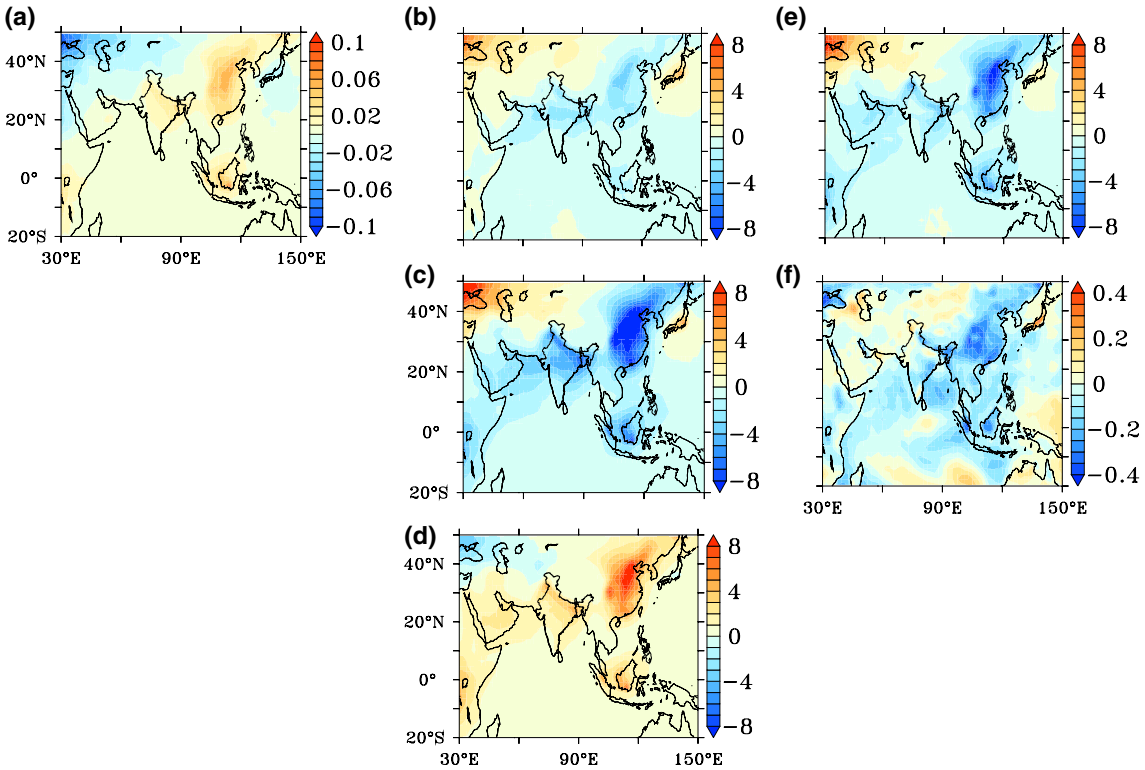

Fig. 5 Difference between $E_{SST+GHG}H_{aero}$ and $E_{SST+GHG}L_{aero}$ in **a** AOD anthropogenic, **b** DARF at TOA (Wm^{-2}), **c** DARF at surface (Wm^{-2}), **d** DARF in atmosphere (Wm^{-2}), **e** IARF at surface (Wm^{-2}), and **f** Evaporation (mm day^{-1}) during peak summer monsoon months of July–August for the years 1971–2010. DARF is the Net Shortwave flux under clear sky conditions with aerosols minus without aerosols. DARF for atmosphere is calculated as the difference of DARF at TOA and the DARF at the surface. IARF is calculated for cloudy sky conditions

Wm^{-2}. Both direct and indirect aerosol forcing thus significantly contribute to reducing ground reaching radiation, while absorbing aerosols like black carbon influence positive atmospheric radiative forcing, which are spatially prominent over north India. These values of aerosol radiative forcing are quantitatively consistent with previous modeling studies of aerosol radiative forcing over the Indian summer monsoon region (Padma Kumari and Goswami 2010; Pandithurai et al. 2012). Perturbation of radiation fluxes by the anthropogenic aerosol reduces ground reaching radiative fluxes causing surface dimming and decrease in evaporation over these regions (Fig. 5f).

4.2.1 Circulation, moisture convergence and dynamical changes

Aerosol influence in these simulations manifests as an intensification of the drying trend in SAM rainfall in the peninsular Indian region (Fig. 6a), using 2010 emission levels of aerosols (termed $E_{SST+GHG}H_{aero}$), compared to 1971 emissions (termed $E_{SST+GHG}L_{aero}$; Fig. 6b). During the peak summer monsoon months of July and August, the trend in precipitation over the subcontinent was negative, with spatially prominent decreases over a band in the Indo–Gangetic plains and north–east India, as well as a region in the peninsula and over the Western Ghats. In the simulation with high aerosols, the entire peninsular region showed a widespread decrease in rainfall (Fig. 6a), significant at the 90% confidence level. Simulations with low aerosol levels (Fig. 6b) also show a decrease in rainfall over the same regions, but lower levels of decrease over a narrower area around the Western Ghats (Fig. 6b), with statistical significance. The change in mean rainfall (Fig. 6c) induced by the different aerosol levels is spatially non-uniform, with increases in the northern region, but decreases in central and peninsular India, however with some increase south of 10°N, and in the Bay of Bengal. Decreases in rainfall over the central and peninsular India, as a difference of mean modelled values between 2010 and 1971 aerosol emission levels, range 10–20% of the 1971 mean values.

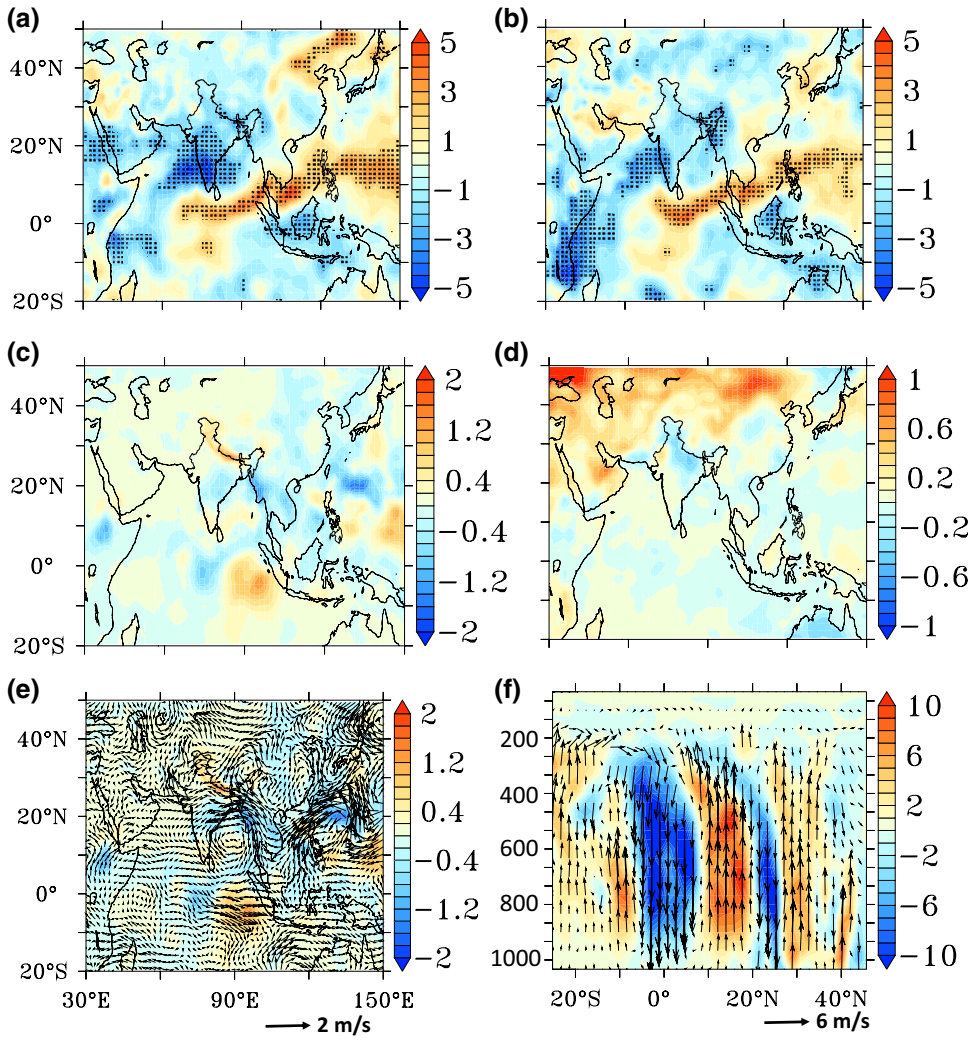

Fig. 6 Trend [mm day^{-1} (40 $years^{-1}$)] in precipitation **a** $E_{SST+GHG}H_{aero}$, **b** $E_{SST+GHG}L_{aero}$ (Stipples indicates significant at 90%), and difference between $E_{SST+GHG}H_{aero}$ and $E_{SST+GHG}L_{aero}$ in **c** Precipitation (mm day^{-1}), **d** 2-m temperature (°C), **e** Precipitation (mm day^{-1}) with winds (m s^{-1}) at 850 hPa and **f** meridional circulation, where v (m s) is the meridional velocity and ω (hPa day^{-1}) is the vertical velocity averaged over 60°E–100°E. Vertical velocity change is also shown as shaded background over Indian subcontinent, during peak summer monsoon months of July–August for the years 1971–2010

Increased aerosol levels act through a surface temperature cooling over the Indo-Gangetic plains (Fig. 6d), similar to responses seen in earlier studies, which is related to aerosol-induced reduction in ground reaching radiation. The enhanced aerosol forcing also influences responses in wind vectors at 850 hPa level over Indian subcontinent (Fig. 6e) with differences between simulations at 2010 and 1971 aerosol levels, showing a cyclonic circulation in the Bay of Bengal (Fig. 6e) and an easterly flow over central north India and peninsular India, opposing the monsoon onflow.

Further, in a dynamical effect, a slow-down of the overturning Hadley circulation was evident in the present simulations, wherein differences between simulations made with high and low aerosol levels ($E_{SST+GHG}H_{aero}$ and $E_{SST+GHG}L_{aero}$ corresponding to 1971 and 2010 emissions, respectively) averaged over 60°E–100°E (Fig. 6f) shows weakened Hadley cell with a rising branch south of 5°S and sinking north of 10°N, with decreases in ascending motion at locations in 20°N–30°N. This is consistent with studies that have suggested a link of anthropogenic aerosols to weakened monsoon circulation during recent decades (Menon et al. 2002; Ramanathan et al. 2005; Lau et al. 2006; Meehl et al. 2008; Bollasina et al. 2011; Ganguly et al. 2012; Sanap et al. 2015). Since SST and GHG forcings were held identical in simulations with differing aerosol emissions, the modelled slow-down of meridional circulation can be attributed to increases in aerosol abundance between 1971 and 2010. Comparing to the effect of SST evolution on Hadley circulation change (Fig. 4h), the effect of aerosol increases (Fig. 6f) was weaker with slow-down of the circulation evident only at its outer edges, around 10°S and 20°N. We conclude that while evolving SST forcing (Fig. 4h) cause a significant weakening of the meridional Hadley circulation, increases in aerosol levels over South Asia (Fig. 6f) somewhat enhance this weakening, when superimposed on evolving regional SST trends.

4.2.2 Atmospheric stabilization, convection and cloud process changes

In this section, we further examine factors influencing changes in modelled convective and stratiform rainfall, individually. Aerosol increases led to a decrease in modelled convective rainfall in the north-central India and the peninsular region (Fig. 7a). Aerosol forcing modified the lapse rate by differential heating of the atmosphere compared to the surface hence increasing the stability of the troposphere, seen here in an increased lower tropospheric stability (LTS), the difference of potential temperature at 700 hPa and surface (Klein and Hartmann 1993). Differences in LTS between $E_{SST+GHG}H_{aero}$ and $E_{SST+GHG}L_{aero}$ simulations, averaged for the peak monsoon months of July and August (Fig. 7b) shows increased stability (positive values) in northern and central India, but small decreases in peninsular India. Reduced vertical velocity at 850 hPa (Fig. 7c) and vertically integrated moisture flux convergence (VIMFC) (calculated for the lower troposphere for the same pressure levels as LTS; Fig. 7d), occurred in peninsular India, along with decreases in parts of central and eastern India (Fig. 7d). Changes in the latent heat fluxes indicate reduced evaporation (Fig. 5f) from aerosol induced decreases in ground reaching radiation, with both variables showing similar

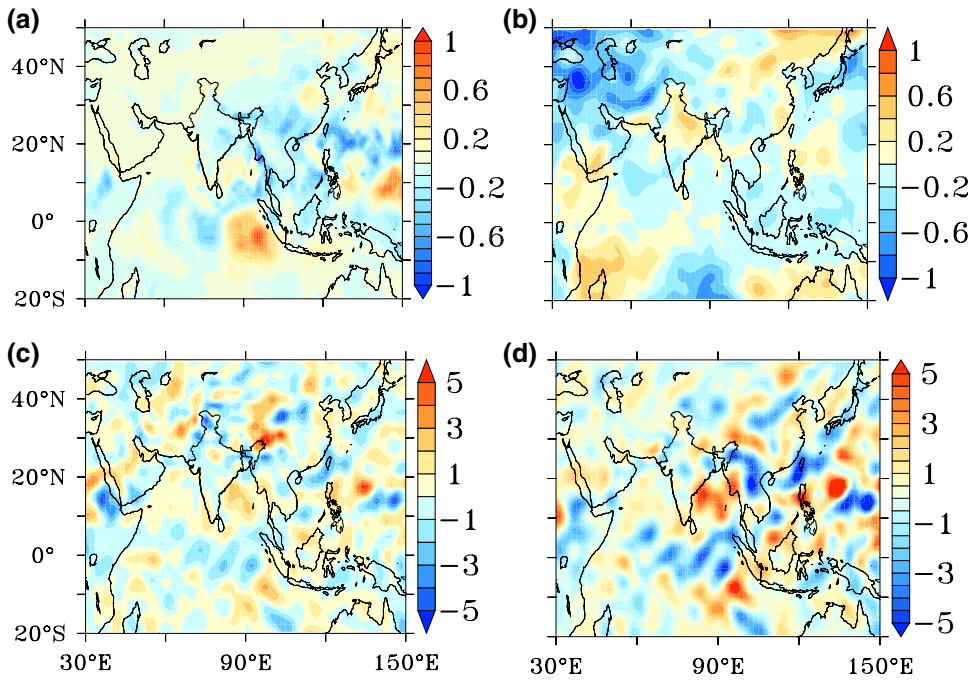

Fig. 7 Difference between $E_{SST+GHG}H_{aero}$ and $E_{SST+GHG}L_{aero}$ for **a** Convective rainfall (mm day^{-1}), **b** Lower Tropospheric Stability (LTS, K), **c** ω850 ($\times 10^{-3}$ m s^{-1}) and **d** Vertically Integrated Moisture Flux (VIMFC, Kg m^{-1} s^{-1}) during peak summer monsoon months of July–August for the years 1971–2010

spatial patterns in the simulations. Overall, these changes were spatially congruent with reduction in convective rainfall (Fig. 7a) in peninsular India, in $E_{SST+GHG}H_{aero}$ compared to $E_{SST+GHG}L_{aero}$ simulations.

Significant decreases in evaporation at the surface occurred as a regional response, consistent with that in CMIP5 models, which includes parameterization of the indirect effects of aerosols (Guo et al. 2015). These effects are consistent with previous studies in which lower tropospheric stabilization has been linked to suppression of convective activity through the aerosol "direct" (Ramanathan et al. 2005) and "indirect" effects (Cherian et al. 2013). Convective rainfall is typically associated with steep lapse rates giving rise to conditional mesoscale instabilities, which promote stronger vertical mixing (Wood and Hartmann 2006). Increased LTS has been linked to stabilization of the shallow layers thereby reducing updraft velocities along with suppressed moisture supply leads to lower convective activity (Ackerman et al. 2000; Hansen et al. 2005; Koren et al. 2008). Aerosol induced mesoscale stabilization has also been linked to suppressed evaporation because of decreased near-surface moisture gradient (Ramanathan et al. 2005).

Stratiform rainfall changes, in response to increases aerosol levels, on the other hand, were more inhomogeneous, with increases over much of north India (particularly the Himalayas), and decreases in central and peninsular India (Fig. 8a). In the model, stratiform rainfall results from autoconversion and droplet accretion processes (Khairoutdinov and Kogan 2000), both of which act as sinks for cloud drop number concentration. While autoconversion is the rate of initiation of drizzle by collision of small drops, accretion is the rate of formation of large drops from collisions of drops of all sizes with drops above a threshold size (greater than 25 μm in radius). In the Khairoutdinov-Kogan scheme, the autoconversion rate increases with increasing cloud water content, but decreases with increasing cloud drop number concentration (CDNC). Accretion rate increases both with increasing cloud and rain water mixing ratios.

The simulation with increased aerosol levels ($E_{SST+GHG}H_{aero}$) showed significant increases in cloud drop number concentration (CDNC) (Fig. 8b), accompanied by larger rates of autoconversion (Fig. 8c) and accretion (Fig. 8d) over all parts of India. The enhanced aerosol leads to increases in both liquid and ice water path (Fig. A8).

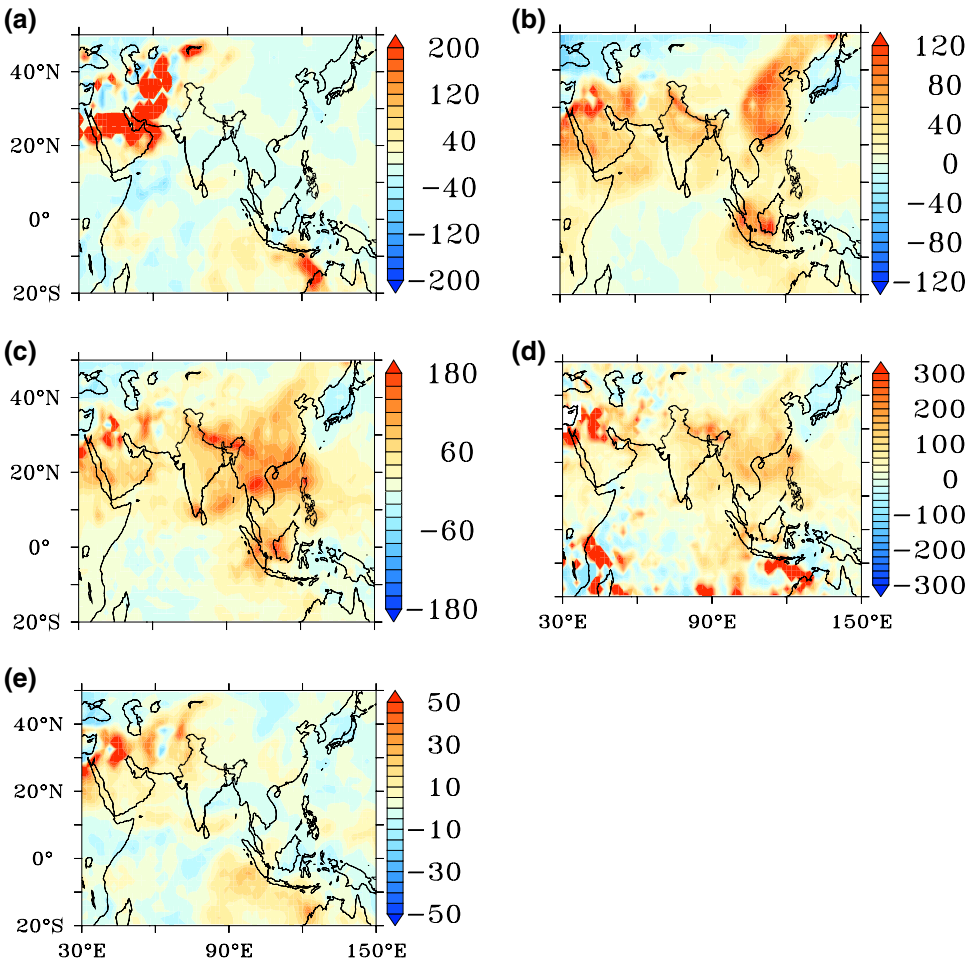

Fig. 8 Difference between $E_{SST+GHG}H_{aero}$ and $E_{SST+GHG}L_{aero}$ expressed in percentage (%) change relative to $E_{SST+GHG}L_{aero}$ for **a** Stratiform rainfall, **b** CDNC, **c** Autoconversion rate (**b, c** are from surface to 500 hPa level), **d** Accretion rate (300–650 hPa level), and **e** Cloud fraction during peak summer monsoon months of July–August for the years 1971–2010

Increases in autoconversion rate, in $E_{SST+GHG}H_{aero}$ simulations with concomitant increases in CDNC, imply that cloud water content, rather than CDNC, appears to control autoconversion rates. The largest increase occurs over north India and the Himalayan region. While the increased efficiency of rainfall processes (autoconversion and accretion rates) is in agreement with increase in stratiform rainfall over northern India, it contradicts the decreased stratiform rainfall over peninsular India. A modest decrease in cloud fraction (Fig. 8e) over peninsular India, spatially coincident with the decrease in stratiform rainfall, could be related to the strong easterly flow and suppressed westerly moisture transport (Fig. 6e), induced by increased aerosol levels in the simulations. Changing aerosol levels thus induce spatially inhomogeneous changes in rainfall formation processes.

5 Concluding remarks

Several studies have investigated effects of distinct forcing elements on changes in the SAM, however, recent studies point to combined effects of changes in regional land-use, anthropogenic aerosol forcing and SST gradient on declining trends in the SAM. Here, we have attempted disentangling the effects produced by changes in SST gradient from those by aerosol levels in a GCM. Recent changes in meridional SST gradient, compared to climatological SST fields, were linked to a widespread feedback on near surface temperature increase that modified the land–sea thermal gradient, as well as, resulted in a slowdown of the meridional Hadley circulation. This, in turn, modulated the strength and flow of the monsoon circulation and weakened cross-equatorial transport of moisture winds towards South Asia.

Recent changes in anthropogenic aerosol levels (1971 versus 2010), when imposed on SST changes, were linked to an intensification of drying in the peninsular Indian region, with prominent decreases over the Western Ghats. Increased aerosol levels act through a host of regional effects. Aerosol radiative forcing at surface, through both direct and indirect effects, leads to reduction in ground reaching radiation and results in surface cooling, prominently observed over north India. This induces north–south asymmetries in temperature and sea-level pressure. Wind vector changes show a cyclonic circulation in the Bay of Bengal, with easterly flow opposing westerly moisture convergence over peninsular India.

Increased direct radiative forcing from increases in black carbon aerosols leads to positive atmospheric forcing, but negative surface forcing. This is linked to overall increase in atmospheric stabilization, decrease in vertical velocity, along with reduced evaporation flux, thus reducing convective rainfall. Changes in stratiform cloud processes tend to enhance rainfall formation processes like autoconversion and accretion, however, a decrease in stratiform rainfall over peninsular India is linked to reduced cloud fraction, from reduced moisture influx to the region.

Limitations in this work include short duration of transient simulations, leading to low amplitude of response signals, non-linearities in the interaction of SST and aerosol forcings and moderately coarse horizontal resolution of the GCM set-up. Further, land-surface feedback on rainfall, resulting from changes in evapotranspiration due to altered land-use/land-cover, was not considered. However, transient simulations in a GCM with an interactive aerosol scheme that includes indirect effect parameterizations, with use of a mix of scattering and absorbing anthropogenic aerosols, at emission levels of 2010 and 1971, allowed investigation of several pathways through which aerosol effects are manifested. Overall, it is found that SST gradient changes act through a weakening of cross-equatorial moisture flow, while aerosol level increases act through weakening of Arabian Sea moisture transport, as well as, of convection and vertical moisture flux, in the peninsula, to influence the suppression of SAM rainfall. The spatial heterogeneity of rain formation processes over South Asia, with changing aerosol levels, needs further investigation.

Acknowledgements This study was supported by the Indian Institute of Technology Bombay, Centre of Excellence in Climate Studies (IITB-CoECS) project of the Department of Science and Technology (DST), New Delhi, India. The ECHAM6-HAM simulations were performed on the IITB-CoECS HPC. We acknowledge Dr. S. Sajani and Dr. K. Rajendran from CSIR-4PI, Bangalore, India for their technical assistance in model porting and simulation set-up at IITB.

References

Ackerman AS, Toon O, Stevens D, Heymsfield A, Ramanathan V, Welton E (2000) Reduction of tropical cloudiness by soot. Science 288(5468):1042–1047

Andres R, Kasgnoc A (1998) A time-averaged inventory of subaerial volcanic sulfur emissions. J Geophys Res Atmos 103(D19):25251–25261

Annamalai H, Hamilton K, Sperber KR (2007) The south Asian summer monsoon and its relationship with ENSO in the IPCC AR4 simulations. J Clim 20(6):1071–1092

Bollasina MA, Ming Y, Ramaswamy V (2011) Anthropogenic aerosols and the weakening of the south Asian summer monsoon. Science 334(6055):502–505

Bollasina MA, Ming Y, Ramaswamy V, Schwarzkopf MD, Naik V (2014) Contribution of local and remote anthropogenic aerosols to the twentieth century weakening of the south Asian monsoon. Geophys Res Lett 41(2):680–687

Bookhagen B, Burbank DW (2010) Toward a complete Himalayan hydrological budget: spatiotemporal distribution of snowmelt and rainfall and their impact on river discharge. J Geophys Res Earth Surf. https://doi.org/10.1029/2009JF001426

Brovkin V, Boysen L, Raddatz T, Gayler V, Loew A, Claussen M (2013) Evaluation of vegetation cover and land-surface albedo in MPI-ESM CMIP5 simulations. J Adv Model Earth Syst 5(1):48–57

Cherchi A, Alessandri A, Masina S, Navarra A (2011) Effects of increased CO_2 levels on monsoons. Clim Dyn 37(1–2):83–101
Cherian R, Venkataraman C, Quaas J, Ramachandran S (2013) GCM simulations of anthropogenic aerosol-induced changes in aerosol extinction, atmospheric heating and precipitation over India. J Geophys Res Atmos 118(7):2938–2955
Chung CE, Ramanathan V (2006) Weakening of north Indian SST gradients and the monsoon rainfall in India and the Sahel. J Clim 19(10):2036–2045
Cowan T, Cai W (2011) The impact of Asian and non-Asian anthropogenic aerosols on 20th century Asian summer monsoon. Geophys Res Lett. https://doi.org/10.1029/2011GL047268
Dash S, Kulkarni MA, Mohanty U, Prasad K (2009) Changes in the characteristics of rain events in India. J Geophys Res Atmos. https://doi.org/10.1029/2008JD010572
Dash S, Mamgain A, Pattnayak K, Giorgi F (2013) Spatial and temporal variations in Indian summer monsoon rainfall and temperature: an analysis based on REGCM3 simulations. Pure Appl Geophys 170(4):655–674
Déandreis C et al (2012) 'Radiative forcing estimates of sulfate aerosol in coupled climate-chemistry models with emphasis on the role of the temporal variability'. Atmos Chem Phys Copernicus GmbH 12(12):5583–5602
Dentener F, Kinne S, Bond T, Boucher O, Cofala J, Generoso S, Ginoux P, Gong S, Hoelzemann J, Ito A et al (2006) Emissions of primary aerosol and precursor gases in the years 2000 and 1750 prescribed data-sets for AEROCOM. Atmos Chem Phys 6(12):4321–4344
Dey S, Di Girolamo L (2010) A climatology of aerosol optical and microphysical properties over the Indian subcontinent from 9 years (2000–2008) of multiangle imaging spectroradiometer (MISR) data. J Geophys Res Atmos. https://doi.org/10.1029/2009JD013395
Dey S, Tripathi SN, Singh RP, Holben B (2004) Influence of dust storms on the aerosol optical properties over the Indo-Gangetic basin. J Geophys Res Atmos. https://doi.org/10.1029/2004JD004924
Fan F, Mann ME, Lee S, Evans JL (2010) Observed and modeled changes in the south Asian summer monsoon over the historical period. J Clim 23(19):5193–5205
Ganguly D, Rasch PJ, Wang H, Yoon JH (2012) Climate response of the south Asian monsoon system to anthropogenic aerosols. J Geophys Res Atmos. https://doi.org/10.1029/2012JD017508
Ghosh S, Luniya V, Gupta A (2009) Trend analysis of Indian summer monsoon rainfall at diff erent spatial scales. Atmos Sci Lett 10(4):285–290
Giorgetta M, Manzini E, Roeckner E, Esch M, Bengtsson L (2006) Climatology and forcing of the quasi-biennial oscillation in the maecham5 model. J Clim 19(16):3882–3901
Giorgetta M, Roeckner E, Mauritsen T, Stevens B, Bader J, Crueger T, Esch M, Rast S, Kornblueh L, Schmidt H et al (2012) The atmospheric general circulation model echam6. Model description. Max Planck Inst for Meteorol, Hamburg
Guo L, Turner AG, Highwood EJ (2015) Impacts of 20th century aerosol emissions on the south Asian monsoon in the cmip5 models. Atmos Chem Phys 15(11):6367–6378
Guo L, Turner AG, Highwood EJ (2016) Local and remote impacts of aerosol species on Indian summer monsoon rainfall in a gcm. J Clim 29(19):6937–6955
Hansen J, Sato M, Ruedy R, Nazarenko L, Lacis A, Schmidt G, Russell G, Aleinov I, Bauer M, Bauer S et al (2005) Efficacy of climate forcings. J Geophys Res Atmos. https://doi.org/10.1029/2005JD005776
Harris I, Jones P, Osborn T, Lister D (2014) Updated high-resolution grids of monthly climatic observations-the cru ts3. 10 dataset. Int J Climatol 34(3):623–642
Hasson S, Lucarini V, Pascale S (2013) Hydrological cycle over south and southeast asian river basins as simulated by PCMDI/CMIP3 experiments. Earth Syst Dyn 4:199–217
Held IM, Soden BJ (2006) Robust responses of the hydrological cycle to global warming. J Clim 19(21):5686–5699
Hendricks J, Kärcher B, Döpelheuer A, Feichter J, Lohmann U (2004) Potential impact of aviation-induced black carbon on cirrus clouds: global model studies with the ECHAM GCM. Project Report. 83, 249 S
Herman J, Bhartia P, Torres O, Hsu C, Seftor C, Celarier E (1997) Global distribution of uv-absorbing aerosols from nimbus 7/TOMS data. J Geophys Res Atmos 102(D14):16911–16922
Infanti JM, Kirtman BP (2017) CGCM and AGCM seasonal climate predictions—a study in CCSM4. J Geophys Res Atmos 122:7416–7432
Khairoutdinov M, Kogan Y (2000) A new cloud physics parameterization in a large-eddy simulation model of marine stratocumulus. Mon Weather Rev 128(1):229–243
Kitoh A, Endo H, Krishna Kumar K, Cavalcanti IF, Goswami P, Zhou T (2013) Monsoons in a changing world: a regional perspective in a global context. J Geophys Res Atmos 118(8):3053–3065. https://doi.org/10.1002/jgrd.50258
Klein SA, Hartmann DL (1993) The seasonal cycle of low stratiform clouds. J Clim 6(8):1587–1606
Koren I, Martins JV, Remer LA, Afargan H (2008) Smoke invigoration versus inhibition of clouds over the Amazon. Science 321(5891):946–949
Kripalani R, Oh J, Kulkarni A, Sabade S, Chaudhari H (2007) South Asian summer monsoon precipitation variability: coupled climate model simulations and projections under IPCC AR4. Theor Appl Climatol 90(3–4):133–159
Krishnan R, Sabin T, Vellore R, Mujumdar M, Sanjay J, Goswami B, Hour-din F, Dufresne JL, Terray P (2015) Deciphering the desiccation trend of the south Asian monsoon hydroclimate in a warming world. Clim Dyn 47(3–4):1007–1027
Lau WKM, Kim KM (2017) Competing influences of greenhouse warming and aerosols on Asian summer monsoon circulation and rainfall. Asia Pacif J Atmos Sci 53(2):181–194
Lau K, Kim M, Kim K (2006) Asian summer monsoon anomalies induced by aerosol direct forcing: the role of the Tibetan plateau. Clim Dyn 26(7–8):855–864
Li G, Xie SP (2014) Tropical biases in CMIP5 multimodel ensemble: the excessive equatorial Pacific cold tongue and double ITCZ problems. J Clim 27(4):1765–1780
Lohmann U, Stier P, Hoose C, Ferrachat S, Kloster S, Roeckner E, Zhang J (2007) Cloud microphysics and aerosol indirect effects in the global climate model ECHAM5-HAM. Atmos Chem Phys 7(13):3425–3446
Manoj M, Devara P, Safai P, Goswami B (2011) Absorbing aerosols facilitate transition of Indian monsoon breaks to active spells. Clim Dyn 37(11–12):2181–2198
Manzini E, Giorgetta M, Esch M, Kornblueh L, Roeckner E (2006) The influence of sea surface temperatures on the northern winter stratosphere: ensemble simulations with the maecham5 model. J Clim 19(16):3863–3881
Meehl GA, Arblaster JM (2002) Indian monsoon GCM sensitivity experiments testing tropospheric biennial oscillation transition conditions. J Clim 15(9):923–944
Meehl GA, Arblaster JM, Collins WD (2008) Effects of black carbon aerosols on the Indian monsoon. J Clim 21(12):2869–2882
Menon S, Hansen J, Nazarenko L, Luo Y (2002) Climate effects of black carbon aerosols in china and India. Science 297(5590):2250–2253
Menon A, Levermann A, Schewe J, Lehmann J, Frieler K (2013) Consistent in-crease in Indian monsoon rainfall and its variability across CMIP-5 models. Earth Syst Dyn 4:287–300

Ming Y, Ramaswamy V (2009) Nonlinear climate and hydrological responses to aerosol effects. J Clim 22(6):1329–1339
Mishra V, Smoliak BV, Lettenmaier DP, Wallace JM (2012) A prominent pattern of year-to-year variability in Indian summer monsoon rainfall. Proc Natl Acad Sci 109(19):7213–7217
Mu Q, Zhao M, Running SW (2011) Improvements to a MODIS global terrestrial evapotranspiration algorithm. Remote Sens Environ 115(8):1781–1800
Neubauer D, Lohmann U, Hoose C, Frontoso M (2014) Impact of the representation of marine stratocumulus clouds on the anthropogenic aerosol effect. Atmos Chem Phys 14(21):11–997
Padma Kumari B, Goswami B (2010) Seminal role of clouds on solar dimming over the Indian monsoon region. Geophys Res Lett. https://doi.org/10.1029/2009GL042133
Pai D, Sridhar L, Badwaik M, Rajeevan M (2014) Analysis of the daily rainfall events over India using a new long period (1901–2010) high resolution (0.25 0.25) gridded rainfall data set. Clim Dyn 45(3–4):755–776
Pandithurai G, Dipu S, Prabha TV, Maheskumar R, Kulkarni J, Goswami B (2012) Aerosol e effect on droplet spectral dispersion in warm continental cumuli. J Geophys Res Atmos. https://doi.org/10.1029/2011JD016532
Pathak A, Ghosh S, Kumar P (2014) Precipitation recycling in the Indian subcontinent during summer monsoon. J Hydrometeorol 15(5):2050–2066
Pathak A, Ghosh S, Martinez JA, Dominguez F, Kumar P (2017) Role of oceanic and land moisture sources and transport in the seasonal and interannual variability of summer monsoon in India. J Clim 30(5):1839–1859
Paul S, Ghosh S, Oglesby R, Pathak A, Chandrasekharan A, Ramsankaran R (2016) Weakening of Indian summer monsoon rainfall due to changes in land use land cover. Sci Rep 6:32177
Pokhrel S, Sikka D (2013) Variability of the TRMM-PR total and convective and stratiform rain fractions over the Indian region during the summer monsoon. Clim Dyn 41(1):21–44
Polson D, Bollasina M, Hegerl G, Wilcox L (2014) Decreased monsoon precipitation in the northern hemisphere due to anthropogenic aerosols. Geophys Res Lett 41(16):6023–6029
Raddatz T, Reick C, Knorr W, Kattge J, Roeckner E, Schnur R, Schnitzler KG, Wetzel P, Jungclaus J (2007) Will the tropical land biosphere dominate the climate-carbon cycle feedback during the twenty-first century? Clim Dyn 29(6):565–574
Ramanathan V, Chung C, Kim D, Bettge T, Buja L, Kiehl J, Washington W, Fu Q, Sikka D, Wild M (2005) Atmospheric brown clouds: Impacts on south Asian climate and hydrological cycle. Proc Natl Acad Sci USA 102(15):5326–5333
Reddy MS, Boucher O (2004) A study of the global cycle of carbonaceous aerosols in the LMDZT general circulation model. J Geophys Res Atmos. https://doi.org/10.1029/2003JD004048
Roeckner E, Bauml G, Bonaventura L, Brokopf R, Esch M, Giorgetta M, Hagemann S, Kirchner I, Kornblueh L, Manzini E et al (2003) The atmospheric general circulation model echam 5. part I: model description. MPI-Report 349, Hamburg
Roxy MK, Ritika K, Terray P, Murtugudde R, Ashok K, Goswami B (2015) Drying of Indian subcontinent by rapid indian ocean warming and a weakening land–sea thermal gradient. Nat Commun 6:ncomms8423
Sabade S, Kulkarni A, Kripalani R (2011) Projected changes in south Asian summer monsoon by multi-model global warming experiments. Theoret Appl Climatol 103(3–4):543–565
Saha A, Ghosh S, Sahana A, Rao E (2014) Failure of CMIP5 climate models in simulating post-1950 decreasing trend of Indian monsoon. Geophys Res Lett 41(20):7323–7330
Salzmann M, Weser H, Cherian R (2014) Robust response of Asian summer monsoon to anthropogenic aerosols in CMIP5 models. J Geophys Res Atmos. https://doi.org/10.1002/2014JD021783
Sanap S, Pandithurai G, Manoj M (2015) On the response of Indian summer monsoon to aerosol forcing in cmip5 model simulations. Clim Dyn 45(9–10):2949–2961
Sooraj K, Terray P, Mujumdar M (2015) Global warming and the weakening of the Asian summer monsoon circulation: assessments from the CMIP5 models. Clim Dyn 45(1–2):233–252
Sperber KR, Annamalai H, Kang IS, Kitoh A, Moise A, Turner A, Wang B, Zhou T (2013) The Asian summer monsoon: an intercomparison of CMIP5 vs. CMIP3 simulations of the late 20th century. Clim Dyn 41(9–10):2711–2744
Swapna P, Krishnan R, Wallace J (2014) Indian ocean and monsoon coupled interactions in a warming environment. Clim Dyn 42(9–10):2439–2454
Taylor KE, Stouffer RJ, Meehl GA (2012) An overview of CMIP5 and the experiment design. Bull Am Meteor Soc 93(4):485–498
Tegen I, Harrison SP, Kohfeld K, Prentice IC, Coe M, Heimann M (2002) Impact of vegetation and preferential source areas on global dust aerosol: results from a model study. J Geophys Res Atmos. https://doi.org/10.1029/2001JD000963
Torres O, Tanskanen A, Veihelmann B, Ahn C, Braak R, Bhartia PK, Veefkind P, Levelt P (2007) Aerosols and surface uv products from ozone monitoring instrument observations: an overview. J Geophys Res Atmos. https://doi.org/10.1029/2007JD008809
Turner AG, Annamalai H (2012) Climate change and the south Asian summer monsoon. Nat Clim Change 2(8):587–595
Turner AG, Slingo JM (2009) Uncertainties in future projections of extreme precipitation in the Indian monsoon region. Atmos Sci Lett 10(3):152–158
Ueda H, Iwai A, Kuwako K, Hori ME (2006) Impact of anthropogenic forcing on the Asian summer monsoon as simulated by eight GCMs. Geophys Res Lett. https://doi.org/10.1029/2005GL025336
Vignati E, Wilson J, Stier P (2004) M7: a size resolved aerosol mixture module for the use in global aerosol models. J Geophys Res 109(D22):202
Vinoj V, Rasch PJ, Wang H, Yoon JH, Ma PL, Landu K, Singh B (2014) Short-term modulation of Indian summer monsoon rainfall by west Asian dust. Nat Geosci 7(4):308–313
Wang C, Kim D, Ekman AM, Barth MC, Rasch PJ (2009) Impact of anthropogenic aerosols on Indian summer monsoon. Geophys Res Lett. https://doi.org/10.1029/2009GL040114
Wood R, Hartmann DL (2006) Spatial variability of liquid water path in marine low cloud: The importance of mesoscale cellular convection. J Clim 19(9):1748–1764

Climate Dynamics (2022) 58:293–304
https://doi.org/10.1007/s00382-021-05908-4

Spatial heterogeneity of aerosol induced rapid adjustments on precipitation response over India: a general circulation model study with ECHAM6-HAM2

Kaushik Muduchuru[1] · **Chandra Venkataraman**[1,2]

Received: 25 March 2021 / Accepted: 25 July 2021 / Published online: 30 July 2021

Abstract
Anthropogenic aerosol induced declining trends in Indian region precipitation are now acknowledged, however, the role of rapid adjustments to aerosol forcing needs further understanding. An atmospheric general circulation model with dynamic aerosol fields, ECHAM6-HAM2, is used to investigate changes in stratiform and convective precipitation through simulations using different levels of aerosol emissions over India. The spatial pattern of precipitation change, with increased aerosol levels, increases over the Northern Indian region, decreasing over peninsular south India. This is driven by the spatial heterogeneity of stratiform precipitation changes, while simultaneous convective precipitation changes are negative throughout the subcontinent, from absorbing aerosol induced stabilization. Stratiform response to the rapid adjustments includes dynamic changes to the divergence of the dry static energy, cloud microphysics and rainfall formation processes. Positive divergence in dry static energy, consistent with moisture convergence, leads to increased water vapour mixing ratios, thus significantly increasing cloud liquid water and cloud fraction in north India. The increases in rainfall formation processes like the autoconversion rate result from those in the liquid water path, which overcome decreases due to increased droplet number concentration. Overall, aerosol induced changes in dynamic dry static energy divergence, rather than on cloud microphysics, play a dominant role in driving the spatial heterogeneity in stratiform and total precipitation change in the Indian region.

Keywords South Asian Monsoon · Aerosol fast responses · Stratiform precipitation · Divergence of dry static energy

1 Introduction

Rainfall observational records over the second half of the twentieth century have shown a 7% decrease with respect to mean boreal summer (June through September) rainfall (Rajendran et al. 2012; Krishnan et al. 2016) over the south Asian monsoon (SAM) region. Observational evidence has indicated an increase in the Indian monsoon region's aridity in the recent decades due to increases in droughts (Kumar et al. 2013). Previous studies using coupled general circulation models have indicated aerosol induced surface "dimming" as the main driver for this weakening of SAM rainfall (Bollasina et al. 2011; Ganguly et al. 2012; Krishnan et al. 2016). This drying trend has been explained through slowing down of the tropical meridional circulation (Bollasina et al. 2011; Guo et al. 2016; Patil et al. 2019) in response to a weaker thermal contrast. Global modelling studies with ocean feedbacks have shown an SST induced slow-down of the meridional circulation crucial to the Indian monsoon leading to weakening seasonal precipitation (Ramanathan et al. 2005; Bollasina et al. 2011; Ganguly et al. 2012; Krishnan et al. 2016). On intra-seasonal timescales, previous studies have shown suppression (Bhattacharya et al. 2017; Dave et al. 2017) as well as an enhancement (Manoj et al. 2011; Vinoj et al. 2014) of Indian monsoon precipitation. Singh et al. (2019) have shown both the wet and dry extremes getting drier over the east-central India region due to local anthropogenic aerosols. This rainfall response to anthropogenic emissions of aerosol changes in

✉ Chandra Venkataraman
chandra@iitb.ac.in

Kaushik Muduchuru
kaushik.reddy.m@gmail.com

[1] Interdiciplinary Program in Climate Studies, Indian Institute of Technology Bombay, Powai, Mumbai, Maharashtra 400 076, India

[2] Department of Chemical Engineering, Indian Institute of Technology Bombay, Powai, Mumbai, India

climate models can further be split into a combination of fast and slow components. The fast responses are a combination of instantaneous changes and rapid adjustments. The instantaneous changes are associated with aerosol direct (scattering and absorption of sunlight) and indirect (ability of aerosols to act as cloud nuclei) effects resulting in a near-instantaneous radiative and thermal reorganization of the atmosphere (Myhre et al. 2017; Samset et al. 2018). The rapid adjustments occur on timescales of a few weeks to months due to the initial change in atmospheric balance through changes in atmospheric temperature, water vapour and clouds. The slow component acts through the ocean's surface temperature changes, hence these feedback processes occur of timescales of years to decades.

Central to the "indirect" aerosol effect is the question of how susceptible is the large-scale rainfall rate to cloud microphysics (Penner et al. 2006; Posselt and Lohmann 2009; Wang et al. 2017). In GCMs with bulk microphysics schemes (Lohmann et al. 2007b; Gettelman et al. 2013), the warm liquid clouds LWP response and rainfall formation is dominated by autoconversion and accretion processes. Using the diagnostic rain schemes shifts the importance of rainfall production from the accretion process to the autoconversion process (Posselt and Lohmann 2009; Gettelman et al. 2015). The autoconversion process is parameterized as droplet concentration to the power $-\alpha$ in several GCMs, including ECHAM6-HAM2. Models and theory show α, which ranges from 0.5 (Kostinski 2008; Seifert and Stevens 2010) to 2 (Khairoutdinov and Kogan 2000), while observational studies suggest $\alpha = 1$ (Comstock et al. 2005; VanZanten et al. 2005). Larger α values suggest a stronger relationship between precipitation and LWP to cloud droplet number concentration (Quaas et al. 2009). Numerous evidences now suggest a weaker sensitivity of autoconversion processes to droplet concentration tipping the balance on the importance of cloud water on autoconversion rate (Boucher et al. 2013).

Several studies have attempted to contrast absorbing aerosols (BC) and scattering aerosol (SO_4) response and indicated significantly different effects on the rapid adjustments of atmospheric circulations, clouds and rainfall. Previous studies (Richardson et al. 2018) demonstrated that negligible effect of black carbon on precipitation changes over land, primarily due to the dry static energy (DSE) flux divergence increases being compensated by increased shortwave absorption. Interestingly for sulfate, because the shortwave absorption is negligible the decreased DSE flux divergence constrains the precipitation to a negative value. However regional studies over the east Asian and south Asian monsoon regions showed a significant contribution of absorbing aerosols fast response to rainfall increases owing to a strengthening of the land-sea thermal contrast. Black carbon was also previously thought to increase tropospheric temperature gradient thereby increasing the monsoonal circulation (Lau et al. 2006; Kim et al. 2016) which is associated with increases in vertical velocity thereby increasing monsoonal rainfall rates.

Previous studies exploring the fast responses on total precipitation (Ganguly et al. 2012; Guo et al. 2016; Wang et al. 2017) show spatially asymmetric response, but do not separate the responses of stratiform and convective precipitation. Most GCMs including ECHAM6-HAM2 capture the aerosol "indirect" effects only on stratiform rainfall rates (Lohmann et al. 2007b; Gettelman et al. 2015; Zhang et al. 2016). Although convective detrainment is considered in LWP response, the aerosol indirect effect is mostly ignored in convective clouds. This work evaluates the interplay among radiative, dynamical and microphysical rapid adjustment's role in affecting both components of precipitation to recent aerosol emission changes during the peak monsoon period using a atmospheric GCM. Specific objectives include:

1. Evaluation of stratiform rainfall response to aerosol-induced fast adjustments.
2. Effects of thermodynamic and rainfall formation processes on spatial heterogeneity of rainfall response.

2 Model and experiments

ECHAM6-HAM2 (6th Generation coupled chemistry GCM from MPI-Meteorology), a global aerosol climate model is used in this study. ECHAM6.2-HAM2.2 (Neubauer et al. 2014) consists of two components, ECHAM6 (Stevens et al. 2013) which is the atmospheric general circulation model coupled to the aerosol module HAM2 (Zhang et al. 2012). The aerosol module is represented as seven overlapping lognormal modes with each mode described by three moments aerosol number, number median radius and standard deviation, where the standard deviation in HAM is fixed and set to 1.59 for the nucleation, Aitken and accumulation models and to 2.00 for the coarse modes. The aerosol water uptake is an important component of the particulate composition affecting size and optical properties. Aerosol water is parameterized following a semi-empirical scheme based on κ-Köhler theory (Petters and Kreidenweis 2007) for which the internally mixed particle's κ value is calculated by taking the volume-weighted sum of the κ parameter of each soluble particle. All the simulations were performed in T63 spectral resolution which corresponds to $1.875° \times 1.875°$ and 31 vertical layers with a top at 10 hPa.

The aerosol indirect effects are included in ECHAM6-HAM2 owing to the implementation of the two-moment cloud microphysics scheme of Lohmann et al. (2007a, b). This scheme considers interaction of stratiform cloud microphysics with aerosol concentrations through aerosol activation in warm clouds (Lin and Leaitch 1997). The

two-moment scheme provides prognostic equations for number and mass concentrations of both cloud water and ice and the mass concentration of water vapor. The gamma distribution for cloud droplets, monomodal distribution for cloud ice and exponential distribution for rain and snow are used to describe the microphysics scheme. The autoconversion rate of cloud droplets to form raindrops is important for the cloud lifetime effect. Here we use the autoconversion rate Qaut (kg kg^{-1} s^{-1}) developed by Khairoutdinov and Kogan (2000):

$$Q_{aut} = 1350 q_l^{2.47} N_l^{-1.79} \quad (1)$$

where q_l is the cloud liquid water mass mixing ratio in kg kg^{-1} and N_l is the cloud droplet number concentration in cm^{-3}. There is an inherent coupling in the cloud liquid water and autoconversion process because the autoconversion rate depends inversely on the cloud droplet number concentration (Eq. 1), an increase in aerosol and, hence, cloud droplet number concentration prolongs the precipitation formation rate, leading to a higher liquid water path and a reduced removal of aerosol concentrations. This suggests a larger contribution of nonlinearity in estimating the relationship of aerosol concentrations and autoconversion rates.

The experiments were performed with transient simulations of three ensemble members for a period of 40 years to simulate climate responses to aerosol changes. The three ensemble members were generated by slightly perturbing model parameters, by about 0.01%, related to coefficients for horizontal diffusion for divergence, vorticity, and temperature. The fast responses are delineated from slow responses in climate models using multiple methods. The different methodologies adopted in previous studies include using prescribed sea surface temperature (Bala et al. 2010; Ganguly et al. 2012; Guo et al. 2016), separating the fast and slow components based on changes occurring in a predefined timescale using transient experiments (Cao et al. 2012; Bony et al. 2013), and linear regression in coupled models (Gregory and Webb 2008; Andrews et al. 2010). The two experiments HA (high aerosol) and LA (low aerosol) are run with aerosol emissions fixed at 1971 and 2010 levels respectively. The ALLF simulation with transient aerosol emissions, SST and GHGs forcings from 1971 to 2010 are used to realistically simulate the effect of all the forcings during the recent climate change. To extract the aerosol induced fast adjustments, climatological differences between the HA and LA experiment is calculated. There are multiple ways to extract rapid adjustments in GCMs, which include using fixed SST like in the present study, linear regression of precipitation changes to surface temperature changes (Andrews et al. 2010) or by separating based on timescales (Cao et al. 2012; Bony et al. 2013). On regional scales, the precipitation response is affected by local circulation changes and surface temperature changes.

Richardson et al. (2016) has underscored agreement between the prescribed SST framework and regression methods in quantifying the precipitation changes to aerosol fast adjustments. Evolving SSTs and GHG forcings with fixed monthly varying aerosol emissions in the HA and LA experiment are designed to reduce the model's internal variability (Figure S1). Figure S1a shows the 40 year trend of peak-monsoon (Jul–Aug) precipitation in the ALLF experiment with most regions showing a drying response to the combined forcing of aerosol, SST and GHGs. The disentangling of aerosol forcing from the SST gradient changes has been previously undertaken from the same set of simulations in Patil et al. (2019). The study focusses on a drying due to SST induced weakening of land-sea contrast and aerosol induced drying over the peninsular Indian region caused by a cyclonic moisture suppression. Figure S1 shows the individual 40-year July–August trends of total precipitation for the various experiments conducted with ECHAM6-HAM2. The internal variability (spread of the individual ensemble member) is markedly larger in the evolving aerosol simulations (see EAESST and EACSST), compared to the fixed aerosol simulations (see F10ESST; HA and F71ESST; LA), justifying the current approach to investigate the aerosol fast adjustments on aerosol–microphysics–precipitation responses.

An atmospheric energy budget (Muller and O'Gorman 2011) is performed which puts a limit on the fast precipitation changes. Globally the latent heat released by the atmosphere is balanced by net atmospheric cooling, but on local scales the energy advection has to be taken into account. A dry static energy (DSE) flux divergence term is introduced to account for the local scale circulation changes. Hence at local scales, the latent heat released due to precipitation has to be balanced by atmospheric heating, sensible heat from the surface, and DSE flux divergence as shown below:

$$L_c \delta P = \delta Q + \delta H = \delta LW + \delta SW - \delta SH + \delta H \quad (2)$$

where δ denotes the perturbation (HA–LA) due to aerosol changes, L_c is the latent heat of condensation, P is the precipitation, Q is atmospheric diabatic cooling, a combination of longwave cooling (LW), shortwave absorption (SW), and sensible heat flux from surface. Changes in DSE flux divergence (H), can be split into the dynamic and thermodynamical effects of the horizontal and vertical advection as shown:

$$\delta H = \delta H_{Dyn_v} + \delta H_{Thermo_v} + \delta H_{Dyn_h} + \delta H_{Thermo_h} \quad (3)$$

$$= \int \delta(\overline{\omega}) \frac{\partial \overline{s}}{\partial p} + \int \overline{\omega} \delta \left(\frac{\partial \overline{s}}{\partial p} \right) + \int \delta(\overline{\boldsymbol{u}}).\nabla \overline{s} + \int \overline{\boldsymbol{u}}.\delta(\nabla \overline{s}) \quad (4)$$

$$\nabla \bar{s} = \frac{1}{r}\frac{\partial \bar{s}}{\partial \theta}\hat{\theta} + \frac{1}{r\sin\theta}\frac{\partial \bar{s}}{\partial \varphi}\hat{\varphi} \tag{5}$$

$$s = gz + C_p T \tag{6}$$

where ω is the vertical velocity, s is the dry static energy, p is the pressure, $\boldsymbol{u}$ is the horizontal wind vector, z is the model geopotential height, T is the air temperature, C_p is the isobaric specific heat of air, and the $\int$ denotes the mass-weighted vertical integration. Overbars signify long term climatological averages. Here it is an average of 40 years of the model simulation time.

3 Results

3.1 Validation of stratiform and convective precipitation components

The ALLF experiment with realistic aerosol, GHGs and SST conditions closely resembles real atmospheric climatology during the 40-year period compared to the accumulated rainfall in JJAS from the Tropical Rainfall measuring mission (TRMM; Huffman et al. 2007). The overlapping period of 10 years (2001–2010) for the summer monsoon period (JJAS) is validated for total, stratiform and convective precipitation. The northern Indian region (22–28 N; 75–90 E) shows considerably less bias of + 0.23 compared to the 8.1 mm d^{-1} climatology, with southern region (12–21 N; 72–80 E) shows a larger bias of + 1.56 mm d^{-1} compared to 2.4 mm d^{-1} climatology. Although the total precipitation the northern regions show good accuracy in predicting total rainfall, the stratiform and convective precipitation components individually show large deviations from observations. Stratiform precipitation is overestimated by + 1.80 mm d^{-1}, while − 1.57 mm d^{-1} underestimation of convective precipitation is shown over the Indian land region. The peninsular region reasonably performs well for stratiform rainfall but significantly overestimates convective precipitation, causing a large bias in the total precipitation. The convective to stratiform precipitation ratio averaged over the Indian land regions in the ECHAM simulations show a 52:48 compared to the TRMM of 55:45. Overall the spatial distribution of modelled total precipitation resembles observations. However, convective and stratiform precipitation show marked deviations in the boreal summer (June to September) average compared to the 10-year observed climatology. Observational studies have shown a stratiform-convective rainfall partitioning of 0.25 on average over the tropics (20 S–20 N) from the precipitation radar data aboard the TRMM satellite (Schumacher and Houze Jr 2003). The monsoon regions were shown to have the most extensive seasonal variations in the stratiform–convective rainfall ratio, with the largest stratiform rainfall contributions during the wet season. The Indian region was shown (Fig. 1) to have large stratiform–convective rainfall ratio of nearly 1.00 compared to the tropical average of 0.25 indicating the abundance of stratiform rainfall over India and the importance in studying the aerosol cloud interactions related to stratiform cloud and rainfall processes. Due to the large spatial variability in precipitation and stratiform–convective partitioning between the north and southern regions, the further analysis focusses on regions averaged over these two regions, north and south. The model overestimates stratiform precipitation in the NI region. Explicit parameterization of warm rainfall processes in GCMs have led to overestimations in stratiform rainfall (Suzuki et al. 2015). Hazra et al. (2017) have shown larger stratiform precipitation owing to the inclusion of ice-phase processes in the cloud microphysics scheme. This acts through more heating and deeper convection which manifests as overestimated rainfall. Mülmenstädt et al. (2020) have shown that ECHAM-HAMMOZ also simulated higher stratiform rainfall owing to a larger enhancement factor and lower effective radius threshold in the warm rain parameterization.

3.2 Alteration in aerosol abundance and links to energetics

Here we attempt to link changes in aerosol abundance, through energetics approach (Muller and O'Gorman 2011) to understand the spatial heterogeneity in precipitation changes. The absorbing AOD (Fig. 2a) increases over the Indian land areas with maximum increases over the Indo-Gangetic plains, starting from east India to north India due to increases in absorbing aerosols. This spatial pattern of absorbing AOD shows the largest increases in absorbing aerosol concentrations (predominantly black carbon and dust) over the NI region, showing a corresponding increase in lower tropospheric stabilization (LTS; Fig. 2b). Increases in scattering aerosols (Figure S2) show region wide increases with maximum increases over the central India not coinciding with absorbing aerosols or the stabilization. LTS signifies the stability of the lower troposphere, approximately the first 3 km above the surface. The shortwave heating rate forcing (defined as heating rate with aerosol minus without aerosol; Fig. 2c) show maximum heating rate forcing changes in the lower troposphere. The heating rate forcing and the absorbing aerosol concentrations increase over the land areas, suggesting a stabilizing effect on the lower troposphere. The increase in lower level heating by absorbing aerosol increases low-level stability, inhibiting vertical motions (see Fig. 2d) indicating convective suppression (Ramanathan et al. 2005; Patil et al. 2019). Figure 2c, show vertical distribution of the changes in heating rate forcing differences between

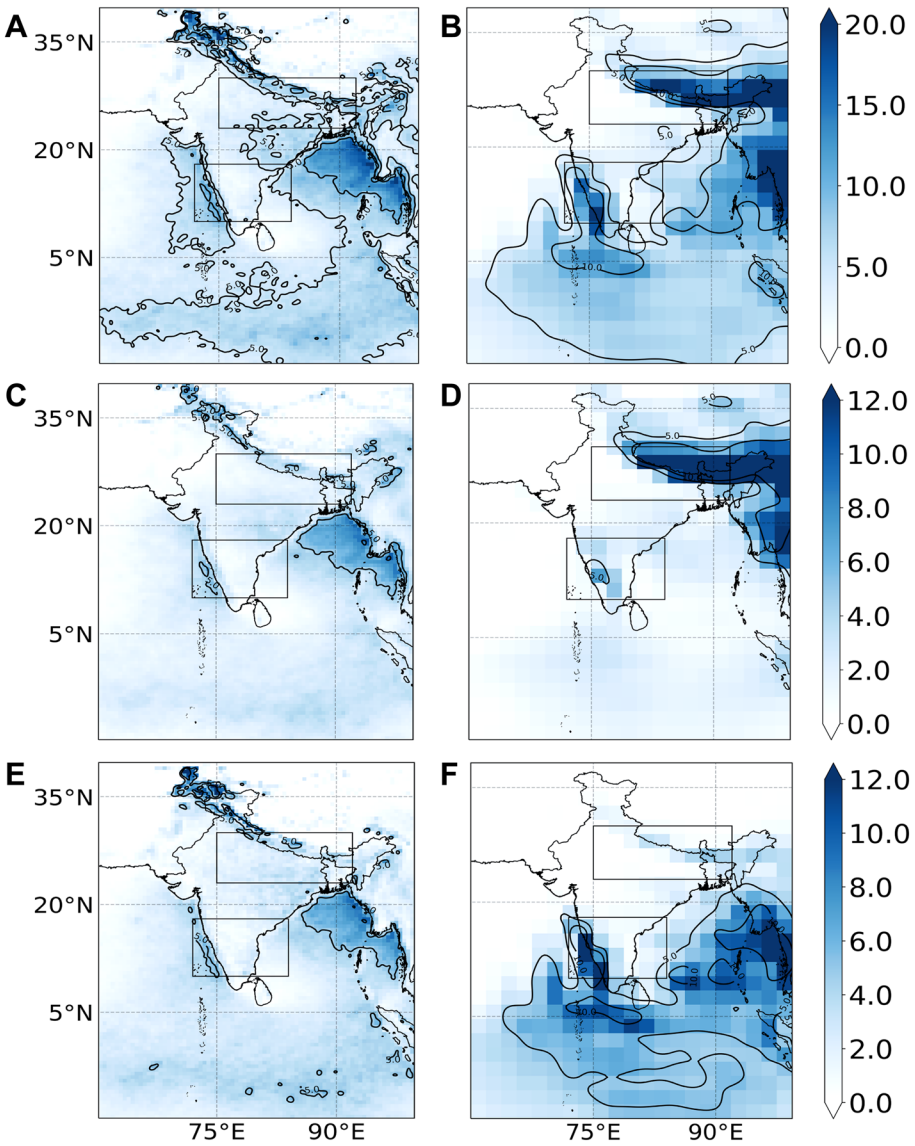

Fig. 1 Boreal summer (June through September) precipitation (mm d^{-1}) averaged from 2000 to 2010 for **a** total precipitation measurement from TRMM, **b** total precipitation simulated from ALLF experiment, **c** stratiform component of total precipitation from TRMM product, **d** model simulated stratiform rainfall, **e** convective component of total precipitation from TRMM product and **f** model simulated convective rainfall. The boxes represent the two study regions NI (north India) and PI (peninsular India)

HA and LA experiments. The differences indicate larger heating rate forcing in the HA experiment compared to the LA experiment over both NI and PI regions. The NI region shows higher aerosol induced heating rate owing to higher AAOD. Andrews et al. (2010) have shown strong correlations between modeled atmospheric absorption and the fast rainfall changes. Samset et al. (2016) and Richardson et al. (2018) have shown global land averaged precipitation responses to aerosol enhancements, with increases in the case of scattering aerosols, but decreases in the case of absorbing aerosols. In contrast, Guo et al. (2016) have shown sulphate aerosols decrease monsoonal precipitation with black carbon causing increases owing to circulation changes over Indian region. This differences between global land-averaged precipitation and regional (India) precipitation fast responses indicate a possible role in local dynamics and aerosol composition changes.

An energy budget analyses for the atmospheric column is performed for both the regions to understand mechanisms governing the fast precipitation adjustments. Figure 3a–c shows the longwave cooling, shortwave absorption and sensible heat flux changes due to the aerosol perturbation. This longwave cooling changes are considerably smaller than the contribution from increases in shortwave absorption. The increases in shortwave absorption are primarily due to absorbing aerosols or absorption due to increases in moisture. The atmospheric shortwave increases over the NI region are ~2.5 W m^{-2} which is orders of magnitude higher than atmospheric longwave cooling (~0.1 W m^{-2}). Aerosol experiments using AGCMs have shown a scaling of fast precipitation responses to atmospheric absorption (Samset et al. 2016; Richardson et al. 2018). Tropospheric temperature increases in response to absorbing aerosol heating increases longwave cooling only partially balancing the

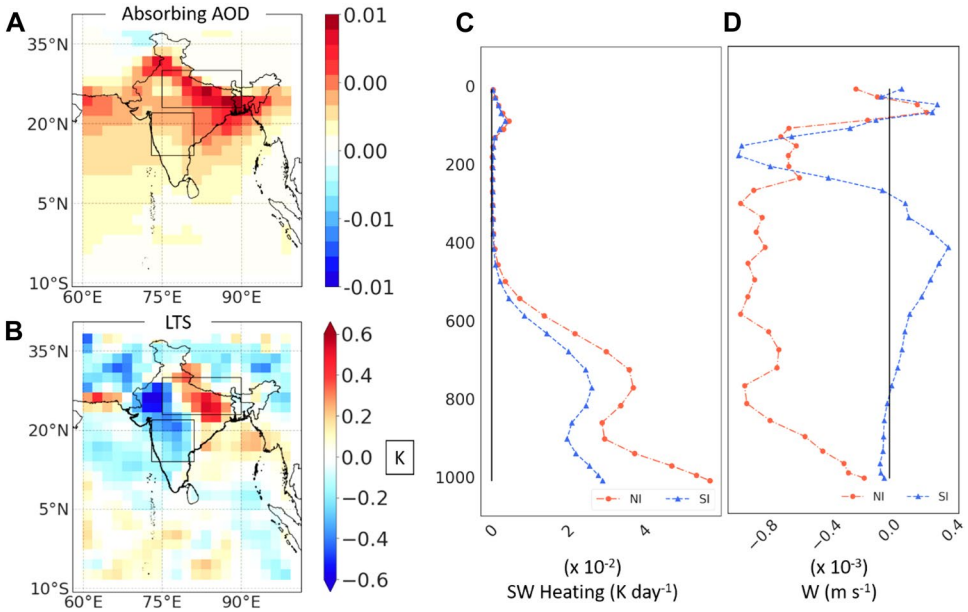

Fig. 2 Peak monsoon 40-year climatology difference between HA and LA experiments for **a** absorbing component of AOD at 550 nm wavelength, and **b** lower tropospheric stability (K) calculated as the temperature difference between 700 hPa and surface. Vertical distribution difference between HA and LA experiments of **c** shortwave heating rate (K d^{-1}), **d** vertical velocity (m s^{-1}) averaged over NI region (red) and PI region (blue) for 40-year peak monsoon

atmospheric absorption. The sensible heat flux decreases from the surface is associated with reduced ground reaching radiation induced by aerosol increases. The dry static energy (DSE) flux divergence mean component was further split (see Eqs. 3–6) into its thermodynamic and dynamic components in the vertical and the horizontal direction (Fig. 3d). The DSE flux divergence compared to radiative fluxes are larger and show a larger significant spatial gradient with positive increases over the NI region and decreases over SI region. The DSE flux divergence's thermodynamic components show uniform increases over the Indian region with maximum increases over the ocean regions.

3.3 Rainfall response to rapid adjustments in dynamical and cloud microphysical processes

The modelled absorbing AOD increases over the Indian land regions with the largest increases over the Indo-Gangetic plains indicate a strong linkage to explaining the fast rainfall responses. The difference between HA and LA experiments for the July–August 40 year climatology (1971–2010) was investigated for variables, affecting responses of total, convective and stratiform rainfall. Figure 4 shows the three-member ensemble average of the peak monsoon fast precipitation changes for total precipitation, stratiform precipitation and convective precipitation, with increase aerosol levels. The total precipitation changes due to aerosol changes from 1971 to 2010 caused a modelled wetting over the north Indian region, but drying over the south Indian region (Fig. 4a). Significant spatial contrast was modelled in the rainfall rate with wetting over the NI region and drying over the SI region. While the spatial pattern is important to note, it is useful to observe the magnitude of − 0.6 to 0.6 mm d^{-1} changes in precipitation which are ~ 5–10% of the mean climatology at the regions considered. The increases over NI region coincide with the overestimation of ECHAM simulated precipitation compared to observations. The PI region's decreases also partly coincide with the model dry bias over the North Central India.

The increases over the NI region are driven mostly due to the increases in δH_{Dyn_v} and δH_{Dyn_h}, spatially co-located with increases in precipitation (Fig. 3d). The increased δH_{Dyn_v} is because of the increased vertical velocity due to aerosol changes indicates absorbing aerosol feedback causing a local instability in the troposphere. The dynamical components of dry static energy divergence show differences over NI and PI (Fig. 3d). Higher energy transport to the NI region is partly also due to strong positive horizontal gradients of dry static energy. These positive gradients arise as a result of the North Indian region sharing boundary with the Himalayan orography. Further an aerosol enhancement leading to an accumulation of moist static energy through atmospheric stabilization (Fig. 2b), implicated in extreme rainfall events mediated by orographic lift (Fan et al. 2015). We can neglect a surface induced feedback because of a net decrease in sensible heat flux associated with decreased surface temperature feedback due to the aerosol perturbation. The increases in δH_{Dyn_h} is due to increased horizontal winds transporting heat towards the NI region. In contrast, the SI region is strongly associated with decreases in δH_{Dyn_v} and accompanying increases in SH flux. The precipitation decrease over the SI region is anti-correlated strongly with increases in the sensible heat flux partially due to dry conditions in the southern region. Here our results indicate a prominent role of local horizontal circulation changes bringing in moisture over the NI region, causing

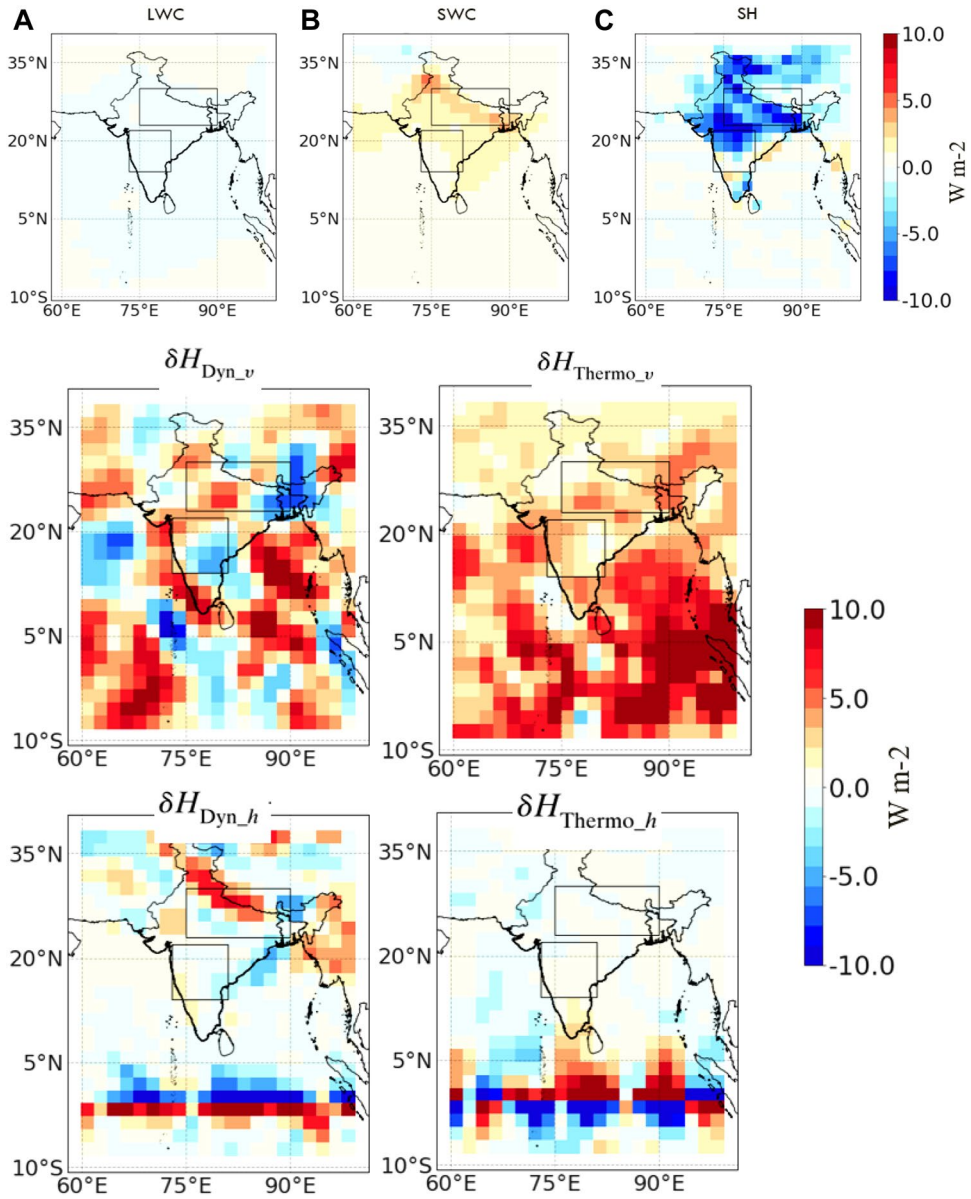

Fig. 3 The peak monsoon (July–August) precipitation (mm d^{-1}) climatology for 40 years (1971–2010) difference between HA and LA experiments is shown for **a** ΔLW, **b** ΔSW, and **c** ΔSH. **d** Contributions to changes in divergence of dry static energy due to rapid adjustments in peak monsoon (Jul–Aug) mean vertical velocity (δH_{Dyn_v}, **d1**), horizontal winds (δH_{Dyn_h}, **d2**), vertical dry static energy gradients (δH_{Thermo_v}, **d3**), and horizontal dry static energy gradients (δH_{Thermo_h}, **d4**)

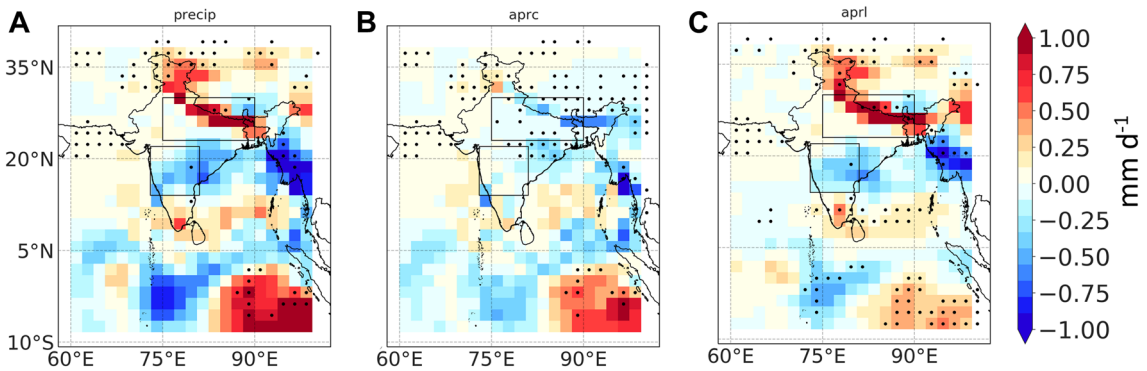

Fig. 4 The peak monsoon (July–August) precipitation (mm d^{-1}) climatology for 40 years (1971–2010) difference between HA and LA experiments is shown for **a** total precipitation, **b** convective precipitation, and **c** stratiform precipitation. The boxes represent the two study regions NI (North India) and PI (peninsular India). The dots represent 90% significance in the differences between HA and LA climatology

increased precipitation and vice versa over the SI region. The longwave cooling partially compensates for increased shortwave absorption over the NI region. Longwave cooling owing to larger tropospheric temperatures (absorbing aerosols have net positive heating rate) is balanced by latent heat release from vapour condensation, therefore, increasing precipitation. The precipitation changes are further broken down into the stratiform and convective parts of the precipitation to further understand them in the context of differences in the treatment of aerosol interactions with stratiform cloud microphysics and lack thereof with cumulus parameterization.

The surface sensible heat decreases over most land regions due to land surface feedback explaining precipitation increases (Fig. 4a). The precipitation changes show a large north–south gradient, which is not evident in the atmospheric energy budget's diabatic cooling components at the local scale. Though the model simulates the large sensible heat flux decreases associated with a positive change in precipitation, the sensible heat flux changes fail to show the regional spatial heterogeneity pattern like the precipitation changes. As expected, the SH flux changes over the oceans are negligible because our experiments have the same prescribed transient SST, which constraints the SH flux changes. Though the SH flux does not show a spatial distribution similar to fast precipitation changes, increased flux over some parts of the SI region indicates a negative contribution to rainfall as simulated. Increased absorption of the atmosphere (Fig. 2a), induced by absorbing aerosols (BC and Dust), leads to a stabilization causing decreased vertical velocity and simultaneously increasing the land-sea thermal contrast increasing the horizontal in-flow of moisture. The NI region shows a more considerable decrease in vertical velocity than the PI region, suggesting suppression of convective instability. This vertical velocity suppression suggests a possible mechanism for convective precipitation decreases over most land regions over the Indian subcontinent.

Figure 5 shows the moisture and microphysics response to changing aerosol concentrations. The autoconversion rate of cloud droplets (Figure S3a) to grow to rain through the collision-coalescence process accounts directly cloud droplet number concentration (CDNC) and cloud water (Figure S3b). CDNC activation is parameterized with vertical velocity and number of interstitial particles in the internally mixed modes (Nucleation, Aitken, Accumulation and Coarse modes) with wet radii larger than 35 nm (Lohmann et al. 2007a, b). Over the NI region, the autoconversion rate (Fig. 6a) shows large increases to rapid adjustments to aerosol changes. There is a larger increase in CDNC and cloud water in response to larger aerosol concentrations over the NI region than PI region. The increases in autoconversion rate with increasing aerosol loading in both regions suggest the sensitivity of autoconversion rate on cloud water (Fig. 6b) and not on CDNC. This increased autoconversion rate due to increased cloud water suggests a macroscale process linked to aerosol forcing. The activation of aerosol is a proportional response to the hydrophilicity of the internally mixed aerosol particles, hence the CDNC increase corresponds to increase in the soluble fraction of aerosol larger than 35 nm, whereas the cloud water increase corresponds to absorbing aerosol induced stabilization leading to increased moisture over the NI region.

Further, the fractional cloud cover is multiplied by the precipitation formation terms (autoconversion, accretion, melting of snow), which gives rise to the spatial heterogeneity of stratiform precipitation. A decrease in cloud cover (Fig. 5c), with markedly smaller increases in autoconversion and accretion over PI region, suggests decreased stratiform precipitation due to decreased cloud cover. In contrast, the NI region shows increased cloud cover along with larger increases in autoconversion rates, thus explaining the increases in stratiform precipitation. The NI region shows a stronger sensitivity of cloud water to water vapor, with the histogram of water vapor mixing ratio showing a right shift to larger values compared to the PI region (Fig. 6a, c). The autoconversion rate which is parameterized to a positive power of cloud water is shown to be strongly sensitive to water vapor over the NI region compared to PI region. The differences in response of autoconversion to water vapor in the PI and NI regions suggest the role of dynamical regimes prevalent in these regions. The dynamical regimes' changes are characterized by changes in vertical velocity (Fig. 3d; Bony and Dufresne 2005) and lower tropospheric stability (Fig. 2b; Medeiros and Stevens 2011). However, use of monthly means to exact the microphysical relationships (Fig. 5) would obscure details where the variability of precipitation and cloud cover is high (Zhang et al. 2016).

4 Discussion and conclusions

In this work, we investigated the aerosol rapid adjustments to precipitation changes using 40-year, three-member ensemble simulations with a coupled aerosol-climate atmospheric general circulation model, ECHAM6-HAM2. The Jul–Aug climatological differences between the higher aerosol experiment and the lower aerosol experiment show considerable total precipitation differences. An examination of the components of precipitation reveals different aerosol induced effects that affect convective and stratiform precipitation. While the simulation results suggest a large-scale decrease of convective precipitation over the Indian region, the stratiform precipitation response is characterized by significant spatial heterogeneity. Our results indicate absorbing aerosol induced lower tropospheric stabilization,

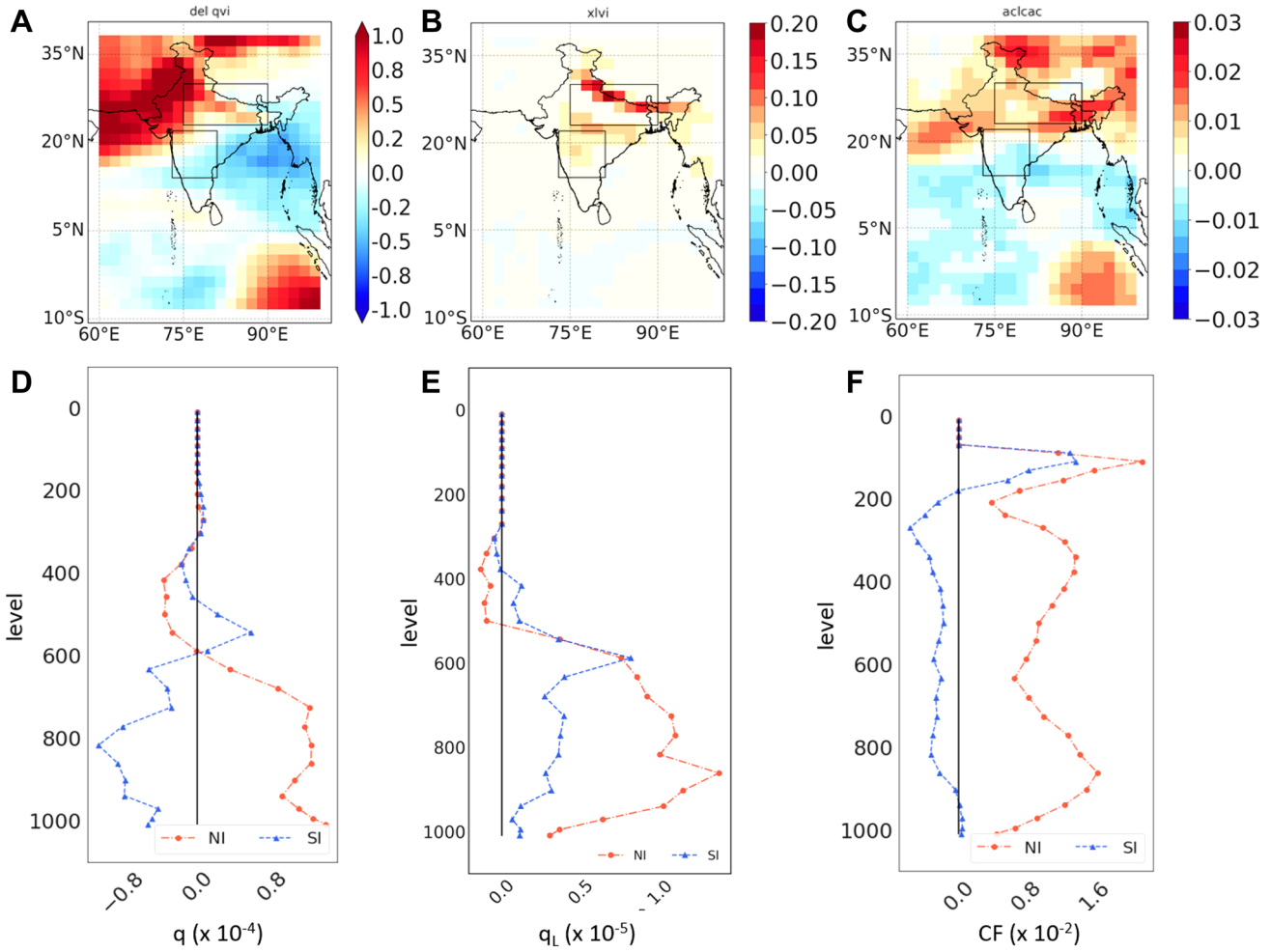

Fig. 5 Peak monsoon 40-year climatology difference between HA and LA experiments for **a** column integrated water vapor (kg m^{-2}), **b** column integrated cloud water (kg m^{-2}) and, **c** column stratiform cloud cover. Vertical distribution difference between HA and LA experiments of **c** water vapor mixing ratio (kg kg^{-1}), **d** cloud water mixing ratio (kg kg^{-1}), and **e** cloud fraction as a function of height, averaged over NI region (red) and PI region (blue) for 40-year peak monsoon months

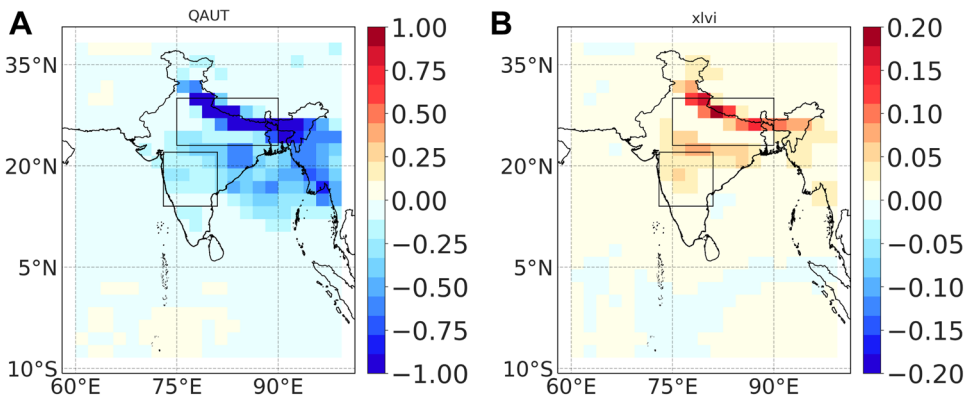

Fig. 6 The peak monsoon (July–August) 40 years (1971–2010) climatological differences between HA and LA experiments for **a** autoconversion (# m^{-3} s^{-1}), **b** liquid water path (kg m^{-2}; column cloud water). The boxes represent the two study regions NI (North India) and PI (peninsular India)

decrease in ascending motions more so over the NI region underscoring this as the pathway for the simulated decrease in convective precipitation whereas increases in liquid water path (indicated as column cloud water) driving both autoconversion and accretion increases underscore the stratiform precipitation response pathway. Positive divergence

in dry static energy, consistent with moisture convergence, leads to increased water vapour mixing ratios, thus significantly increasing cloud liquid water and cloud fraction in north India. The increases in rainfall formation processes like the autoconversion rate result from those in the liquid water path, which overcome decreases due to increased droplet number concentration. The emission levels changed from 1971 in LA experiment to 2010 in HA experiment has large changes in aerosol concentrations, accompanied with increases in absorbing aerosol concentrations in the lower troposphere, hence causing a differential heating with respect to the surface causing an increase in lower tropospheric stability hindering convective activity over the NI region. The PI region shows mixed signals of LTS indicating the decrease in convective precipitation is due to decreases in water vapor. This explains the convective precipitation response to recent aerosol changes over the Indian region in the peak monsoon months of July and August. The theory of increased CCN induced rainfall suppression and increased cloud lifetime (Albrecht 1989) does not agree with the model simulations. The simulations indicate increases in liquid water path, also seen in other GCM studies (Guo et al. 2011; Zhang et al. 2016) and largest microphysical changes over the NI region where the precipitation magnitudes are also large. In the simulations, the NI region, high aerosol abundance associated with positive moisture response and increased cloudiness is responsible for the larger aerosol indirect effects and stratiform precipitation changes.

The CMIP6 model simulated precipitation response to aerosol forcing has underscored aerosol-cloud interactions' importance in explaining the decreasing trend over the Indian region (Salzmann et al. 2014; Guo et al. 2015).Guo et al. (2016) with an atmospheric GCM using sulfate only experiments, simulated a decrease over the Indo-Gangetic plains, with the black carbon only run increasing the rainfall through an EHP mechanism enhancing convection. Previous observational study has shown the absorbing aerosol induced stabilization leads to dynamic changes in moisture convergence, thereby suppressing precipitation with a lag of 1 to 5 days (Dave et al. 2017). Our study showed decreased moisture divergence over the peninsular Indian region linked to dynamic changes related to absorbing aerosols. This work using ECHAM-HAM has shown the increases in precipitation were through increases in liquid water path, thereby increasing autoconversion, unlike the EHP mechanism, which enhances convective activity. The convective rainfall responses to rapid adjustments are lower than the stratiform rainfall, probably due to the detailed inclusion of both the first and second indirect effects in the model. The spatial inhomogeneity in the aerosol concentrations with a strong northward gradient suggests that the local response of cloud microphysical and thermodynamic responses to rapid adjustments could be an important factor in estimating the Indian monsoon response to aerosol changes. The mechanisms explaining the precipitation responses, both stratiform and convective are embedded on the dynamical response of moisture which possibly be explained by the stabilization of lower troposphere by absorbing aerosol concentrations. The increased moisture response over the northern regions explains both the liquid water path increases and the increased cloudiness, however other GCM studies of fast responses have explained the increased monsoon rainfall over the Indian regions through both direct and indirect effects (Ganguly et al. 2012; Salzmann et al. 2014; Guo et al. 2016). This underscores the importance in understanding the precipitation response by decomposing into its respective convective and stratiform components; however, we note that the treatment of prognostic stratiform precipitation, lack of aerosol convective cloud microphysics interactions and coarser spatial grid (180 km) could affect the results significantly. However, in-depth analysis of these effects could further improve the understanding of model differences to various forcings.

Supplementary Information The online version contains supplementary material available at https://doi.org/10.1007/s00382-021-05908-4.

Acknowledgements This work was supported by the MOEFCC under the NCAP-COALESCE project {Grant No.14/10/2014-CC(Vol.II)}. The authors thank the internal review committee of the NCAP-COALESCE project for their comments and suggestions on this paper. The views expressed in this document are solely those of the authors and do not necessarily reflect those of the Ministry. The Ministry does not endorse any products or commercial services mentioned in this publication. We are grateful to functionaries of the Climate Change Division, MOEFCC.

Funding MOEFCC project under the NCAP-COALESCE project {Grant No.14/10/2014-CC(Vol.II)}.

Code and model data availability The ECHAM6-HAM2 model data are not publicly available due to large sizes but are available from the corresponding author on reasonable request. The energetics analysis codes are developed in-house based on the methodology described and are also available on reasonable request.

Declarations

Conflicts of interest The authors declare that they have no known competing financial interests or personal relationships that could have appeared to influence the work reported in this paper.

References

Albrecht BA (1989) Aerosols, cloud microphysics, and fractional cloudiness. Science (80−) 245:1227–1230. https://doi.org/10.1126/science.245.4923.1227

Andrews T, Forster PM, Boucher O et al (2010) Precipitation, radiative forcing and global temperature change. Geophys Res Lett. https://doi.org/10.1029/2010GL043991

Bala G, Caldeira K, Nemani R (2010) Fast versus slow response in climate change: implications for the global hydrological cycle. Clim Dyn 35:423–434

Bhattacharya A, Chakraborty A, Venugopal V (2017) Role of aerosols in modulating cloud properties during active–break cycle of Indian summer monsoon. Clim Dyn 49:2131–2145

Bollasina MA, Ming Y, Ramaswamy V (2011) Anthropogenic aerosols and the weakening of the South Asian Summer Monsoon. Science (80−) 334:502–505. https://doi.org/10.1126/science.1204994

Bony S, Dufresne J-L (2005) Marine boundary layer clouds at the heart of tropical cloud feedback uncertainties in climate models. Geophys Res Lett. https://doi.org/10.1029/2005GL023851

Bony S, Bellon G, Klocke D et al (2013) Robust direct effect of carbon dioxide on tropical circulation and regional precipitation. Nat Geosci 6:447–451

Boucher O, Randall D, Artaxo P et al (2013) Clouds and aerosols. In: Climate change 2013: the physical science basis. Contribution of working group I to the fifth assessment report of the intergovernmental panel on climate change. Cambridge University Press, pp 571–657

Cao L, Bala G, Caldeira K (2012) Climate response to changes in atmospheric carbon dioxide and solar irradiance on the time scale of days to weeks. Environ Res Lett 7:34015

Comstock KK, Bretherton CS, Yuter SE (2005) Mesoscale variability and drizzle in southeast Pacific stratocumulus. J Atmos Sci 62:3792–3807

Dave P, Bhushan M, Venkataraman C (2017) Aerosols cause intraseasonal short-term suppression of Indian monsoon rainfall. Sci Rep 7:17347. https://doi.org/10.1038/s41598-017-17599-1

Fan J, Rosenfeld D, Yang Y, Zhao C, Leung LR, Li Z (2015) Substantial contribution of anthropogenic air pollution to catastrophic floods in Southwest China. Geophys Res Lett 42(14):6066–6075. https://doi.org/10.1002/2015GL064479

Ganguly D, Rasch PJ, Wang H, Yoon JH (2012) Fast and slow responses of the South Asian monsoon system to anthropogenic aerosols. Geophys Res Lett 39:1–5. https://doi.org/10.1029/2012GL053043

Gettelman A, Morrison H, Terai CR, Wood R (2013) Microphysical process rates and global aerosol–cloud interactions. Atmos Chem Phys 13:9855–9867

Gettelman A, Morrison H, Santos S et al (2015) Advanced two-moment bulk microphysics for global models. Part II: global model solutions and aerosol–cloud interactions. J Clim 28:1288–1307

Gregory J, Webb M (2008) Tropospheric adjustment induces a cloud component in CO_2 forcing. J Clim 21:58–71

Guo H, Golaz J-C, Donner LJ (2011) Aerosol effects on stratocumulus water paths in a PDF-based parameterization. Geophys Res Lett. https://doi.org/10.1029/2011GL048611

Guo L, Turner AG, Highwood EJ (2015) Impacts of 20th century aerosol emissions on the South Asian monsoon in the CMIP5 models. Atmos Chem Phys 15:6367–6378

Guo L, Turner AG, Highwood EJ (2016) Local and remote impacts of aerosol species on Indian summer monsoon rainfall in a GCM. J Clim 29:6937–6955

Hazra A, Chaudhari HS, Ranalkar M, Chen J-P (2017) Role of interactions between cloud microphysics dynamics and aerosol in the heavy rainfall event of June 2013 over Uttarakhand India. Q J R Meteorol Soc 143(703):986–998. https://doi.org/10.1002/qj.2983

Huffman GJ, Bolvin DT, Nelkin EJ, Wolff DB, Adler RF, Gu G, Hong Y, Bowman KP, Stocker EF (2007) The TRMM multisatellite precipitation analysis (TMPA): quasi-global, multiyear, combined-sensor precipitation estimates at fine scales. J Hydrometeorol 8(1):38–55. https://doi.org/10.1175/JHM560.1

Khairoutdinov M, Kogan Y (2000) A new cloud physics parameterization in a large-eddy simulation model of marine stratocumulus. Mon Weather Rev 128:229–243

Kim MJ, Yeh S-W, Park RJ (2016) Effects of sulfate aerosol forcing on East Asian summer monsoon for 1985–2010. Geophys Res Lett 43:1364–1372

Kostinski AB (2008) Drizzle rates versus cloud depths for marine stratocumuli. Environ Res Lett 3:45019

Krishnan R, Sabin TP, Vellore R et al (2016) Deciphering the desiccation trend of the South Asian monsoon hydroclimate in a warming world. Clim Dyn 47:1007–1027. https://doi.org/10.1007/s00382-015-2886-5

Kumar KN, Rajeevan M, Pai DS et al (2013) On the observed variability of monsoon droughts over India. Weather Clim Extrem 1:42–50

Lau KM, Kim MK, Kim KM (2006) Asian summer monsoon anomalies induced by aerosol direct forcing: the role of the Tibetan Plateau. Clim Dyn 26:855–864. https://doi.org/10.1007/s00382-006-0114-z

Lin H, Leaitch WR (1997) Development of an in-cloud aerosol activation parameterization for climate modelling. In: Proceedings of the WMO workshop on measurement of cloud properties for forecasts of weather, air quality and climate. pp 328–335

Lohmann U, Stier P, Hoose C et al (2007a) Cloud microphysics and aerosol indirect effects in the global climate model ECHAM5-HAM. Atmos Chem Phys Discuss 7:3719–3761. https://doi.org/10.5194/acpd-7-3719-2007

Lohmann U, Stier P, Hoose C et al (2007b) Cloud microphysics and aerosol indirect effects in the global climate model ECHAM5-HAM. Atmos Chem Phys 7:3425–3446

Manoj MG, Devara PCS, Safai PD, Goswami BN (2011) Absorbing aerosols facilitate transition of Indian monsoon breaks to active spells. Clim Dyn 37:2181–2198

Medeiros B, Stevens B (2011) Revealing differences in GCM representations of low clouds. Clim Dyn 36:385–399

Muller CJ, O'Gorman PA (2011) An energetic perspective on the regional response of precipitation to climate change. Nat Clim Chang 1:266–271

Mülmenstädt J, Nam C, Salzmann M, Kretzschmar J, L'Ecuyer TS, Lohmann U, Ma P-L, Myhre G, Neubauer D, Stier P, Suzuki K, Wang M, Quaas J (2020) Reducing the aerosol forcing uncertainty using observational constraints on warm rain processes. Sci Adv 6(22):eaaz6433. https://doi.org/10.1126/sciadv.aaz6433

Myhre G, Forster PM, Samset BH et al (2017) PDRMIP: a precipitation driver and response model intercomparison project-protocol and preliminary results. Bull Am Meteorol Soc 98:1185–1198. https://doi.org/10.1175/BAMS-D-16-0019.1

Neubauer D, Lohmann U, Hoose C, Frontoso MG (2014) Impact of the representation of marine stratocumulus clouds on the anthropogenic aerosol effect. Atmos Chem Phys 14:11–997

Patil N, Venkataraman C, Muduchuru K et al (2019) Disentangling sea-surface temperature and anthropogenic aerosol influences on recent trends in South Asian monsoon rainfall. Clim Dyn 52:2287–2302. https://doi.org/10.1007/s00382-018-4251-y

Penner JE, Quaas J, Storelvmo T et al (2006) Model intercomparison of indirect aerosol effects. Atmos Chem Phys 6:3391–3405

Petters MD, Kreidenweis SM (2007) A single parameter representation of hygroscopic growth and cloud condensation nucleus activity. Atmos Chem Phys 7:1961–1971

Posselt R, Lohmann U (2009) Sensitivity of the total anthropogenic aerosol effect to the treatment of rain in a global climate model. Geophys Res Lett. https://doi.org/10.1029/2008GL035796

Quaas J, Ming Y, Menon S et al (2009) Aerosol indirect effects—general circulation model intercomparison and evaluation with satellite data. Atmos Chem Phys 9:8697–8717

Rajendran K, Kitoh A, Srinivasan J et al (2012) Monsoon circulation interaction with Western Ghats orography under changing climate. Theor Appl Climatol 110:555–571

Ramanathan V, Chung C, Kim D et al (2005) Atmospheric brown clouds: impacts on South Asian climate and hydrological cycle. Proc Natl Acad Sci USA 102:5326–5333

Richardson TB, Samset BH, Andrews T et al (2016) An assessment of precipitation adjustment and feedback computation methods. J Geophys Res Atmos 175:238

Richardson TB, Forster PM, Andrews T et al (2018) Drivers of precipitation change: an energetic understanding. J Clim 31:9641–9657

Salzmann M, Weser H, Cherian R (2014) Robust response of Asian summer monsoon to anthropogenic aerosols in CMIP5 models. J Geophys Res Atmos 119:11321–11337

Samset BH, Myhre G, Forster PM et al (2016) Fast and slow precipitation responses to individual climate forcers: a PDRMIP multimodel study. Geophys Res Lett 43:2782–2791. https://doi.org/10.1002/2016GL068064

Samset BH, Myhre G, Forster PM et al (2018) Weak hydrological sensitivity to temperature change over land, independent of climate forcing. Npj Clim Atmos Sci. https://doi.org/10.1038/s41612-017-0005-5

Schumacher C, Houze RA Jr (2003) Stratiform rain in the tropics as seen by the TRMM precipitation radar. J Clim 16:1739–1756

Seifert A, Stevens B (2010) Microphysical scaling relations in a kinematic model of isolated shallow cumulus clouds. J Atmos Sci 67:1575–1590

Singh D, Bollasina M, Ting M, Diffenbaugh NS (2019) Disentangling the influence of local and remote anthropogenic aerosols on South Asian monsoon daily rainfall characteristics. Clim Dyn 52:6301–6320

Stevens B, Giorgetta M, Esch M et al (2013) Atmospheric component of the MPI-M earth system model: ECHAM6. J Adv Model Earth Syst 5:146–172

Suzuki K, Stephens G, Bodas-Salcedo A, Wang M, Golaz J-C, Yokohata T, Koshiro T (2015) Evaluation of the warm rain formation process in global models with satellite observations. J Atmos Sci 72(10):3996–4014. https://doi.org/10.1175/JAS-D-14-0265.1

VanZanten MC, Stevens B, Vali G, Lenschow DH (2005) Observations of drizzle in nocturnal marine stratocumulus. J Atmos Sci 62:88–106

Vinoj V, Rasch PJ, Wang H et al (2014) Short-term modulation of Indian summer monsoon rainfall by West Asian dust. Nat Geosci 7:308–313. https://doi.org/10.1038/NGEO2107

Wang Z, Lin L, Yang M et al (2017) Disentangling fast and slow responses of the East Asian summer monsoon to reflecting and absorbing aerosol forcings. Atmos Chem Phys 17:11075–11088

Zhang K, O'Donnell D, Kazil J et al (2012) The global aerosol-climate model ECHAM-HAM, version 2: sensitivity to improvements in process representations. Atmos Chem Phys 12:8911–8949. https://doi.org/10.5194/acp-12-8911-2012

Zhang S, Wang M, Ghan SJ et al (2016) On the characteristics of aerosol indirect effect based on dynamic regimes in global climate models. Atmos Chem Phys 16:2765–2783

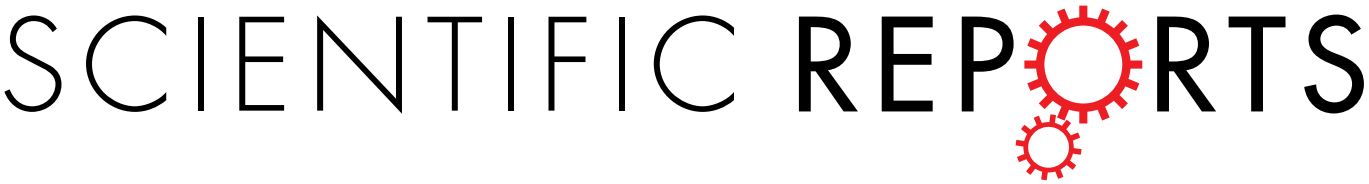

OPEN

Aerosols cause intraseasonal short-term suppression of Indian monsoon rainfall

Received: 23 June 2017
Accepted: 24 November 2017
Published online: 11 December 2017

Prashant Dave[1], Mani Bhushan[1,2] & Chandra Venkataraman[1,2]

Aerosol abundance over South Asia during the summer monsoon season, includes dust and sea-salt, as well as, anthropogenic pollution particles. Using observations during 2000–2009, here we uncover repeated short-term rainfall suppression caused by coincident aerosols, acting through atmospheric stabilization, reduction in convection and increased moisture divergence, leading to the aggravation of monsoon break conditions. In high aerosol-low rainfall regions extending across India, both in deficient and normal monsoon years, enhancements in aerosols levels, estimated as aerosol optical depth and absorbing aerosol index, acted to suppress daily rainfall anomaly, several times in a season, with lags of a few days. A higher frequency of prolonged rainfall breaks, longer than seven days, occurred in these regions. Previous studies point to monsoon rainfall weakening linked to an asymmetric inter-hemispheric energy balance change attributed to aerosols, and short-term rainfall enhancement from radiative effects of aerosols. In contrast, this study uncovers intraseasonal short-term rainfall suppression, from coincident aerosol forcing over the monsoon region, leading to aggravation of monsoon break spells. Prolonged and intense breaks in the monsoon in India are associated with rainfall deficits, which have been linked to reduced food grain production in the latter half of the twentieth century.

The Indian summer monsoon affects water availability and therefore water management related to rain-fed agricultural practices[1,2]. Long-term changes in Indian monsoon precipitation that are linked to aerosol radiative forcing, termed slow-responses, have been caused by thermodynamic adjustments of mean temperature and moisture content[3,4], reductions in land–sea temperature differences and zonal winds, and dynamic circulation adjustments to regional energy imbalances[5–7]. These, in turn, have been associated with precipitation deficits on multi-decadal time scales. Short-term changes in Indian monsoon precipitation that are linked to aerosols, termed fast-responses, occur through the enhancement of meridional surface temperature or pressure gradients[6,8] and mid-tropospheric diabatic heating[9], which cause an increase in the northward transport of moisture, leading to the onset and enhancement of precipitation on time scales of days to a month.

The importance of synoptic, large-scale convection in supporting vertically integrated moisture transport in monsoon systems is well established[4,10,11]. Aerosols were linked to significant decreases in convective instability over India, inferred from modeled lower atmosphere warming[4] and increased tropospheric temperature trends, in agreement with microwave sounder measurements during 1979–2003. In studies not specifically related to the Indian monsoon, aerosols have been linked to the inhibition of cloud and precipitation development, by altering the vertical profile of heating rate, inducing stabilization[12] and suppressing mesoscale convective motion.

Aerosol abundance is persistent over the Indian subcontinent during the summer monsoon season[13–15]. Aerosol-induced effects on cloud microphysical properties have been linked to both precipitation suppression[16] and invigoration[17], at different aerosol levels. These occur through changes in cloud droplet size distributions, redistribution of precipitable water, and latent heat changes associated with condensation and evaporation[12]. Reduction in the median size and width of cloud droplet distributions reduces the efficiency of droplet growth[18]. Fast microphysical effects have been linked to precipitation shut-off in ship tracks for pristine marine clouds[19]. Recently, influences of aerosols in the monsoon region have been reported, suggestive of inhibition or invigoration of clouds and rainfall[20,21].

[1]Interdisciplinary Programme in Climate Studies, Indian Institute of Technology Bombay, Mumbai, 400076, India. [2]Department of Chemical Engineering, Indian Institute of Technology Bombay, Mumbai, 400076, India. Correspondence and requests for materials should be addressed to C.V. (email: chandra@iitb.ac.in)

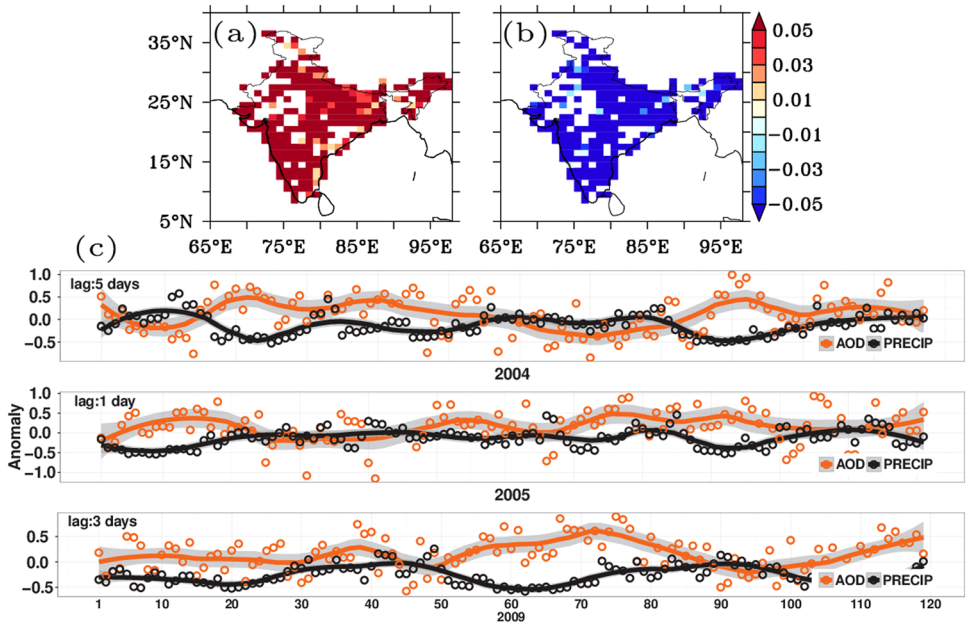

Figure 1. HL cluster pixel distribution and co-variability of AOD-Precipitation: Spatial distribution of pixels with high AOD and low precipitation anomaly along with cluster averaged temporal series for individual years: (**a**) and (**b**) Seasonal averaged spatial distribution of HL overlapping clusters for years 2004, 2005 and 2009 for AOD and precipitation respectively. (**c**) Cluster averaged time series over HL cluster (precipitation shifted by lag corresponding to maximum correlation magnitude). The composite plot of pixels shows that the high AOD-low precipitation covers wide area across the country. In the time series plot between AOD and precipitation anomaly, precipitation anomaly was shifted by the lag corresponding to maximum correlation coefficient magnitude. Multiple instances of enhanced AOD associated with suppressed precipitation can be seen in Fig. 1(c). Figure was created using R statistical tool v3.3.1 (https://www.r-project.org/) and FERRET v7.0 (http://www.ferret.noaa.gov/Ferret/).

To our knowledge, the causal effects of coincident aerosols on the changes in Indian monsoon precipitation have not been investigated through observational analysis. Here we find causal relationships between aerosol enhancement and suppression of lagged daily precipitation and mean cloud drop sizes, through atmospheric stabilization, increased moisture divergence and reduced convection, leading to a higher frequency of prolonged rainfall breaks.

Results

Aerosol and cloud properties from satellite observations[22–24], precipitation from ground based measurements[25], and meteorological variables from European Centre for Medium-Range Weather Forecasts (ECMWF) re-analysis (ERA)-interim reanalysis data[26] from 2000–2009 over the Indian subcontinent (6.5–40°N and 66.5–100°E), at $1 \times 1°$ resolution for the monsoon months of June to September (JJAS), were used for the analysis (for more information see Methods). Precipitation data used were from 1803 irregularly located meteorological stations over India[25], reported to be gridded to $1 \times 1°$, using Shepard's interpolation methodology, yielding approximately 350 pixels over the Indian domain. Normalized daily anomaly was calculated for each variable, as deviation for a specific day and pixel from its mean (calculated across years), normalized by its standard deviation (for more information see Methods). The data were clustered for each year using hierarchical clustering[27], using season average of normalized anomaly of AOD and precipitation, to identify clusters of (a) high AOD-low precipitation (HL), (b) low AOD-low precipitation (LL), (c) high AOD-high precipitation (HH), and (d) low AOD-high precipitation (LH). Cluster average time series of normalized anomalies of AOD and precipitation were used to detect Granger causality[28] which tests statistically significant improvement in the prediction of precipitation, using past information of AOD, as compared to only past information of precipitation (for more information see Methods). In case of causal association, path analysis[29] was used to enable identification of mechanisms through which AOD influenced precipitation (for more information see Methods).

Causal Influence of Aerosols on Short-term Precipitation Suppression. It was found that high aerosol-low precipitation (HL) clusters extended over large parts of India in 2004, 2005 and 2009 (Supplementary Fig. 2). In HL clusters, a leading positive AOD anomaly caused a negative precipitation anomaly, with a lag time of 1–5 days, during the JJAS monsoon season in 2004, 2005, and 2009 (Fig. 1a,b). However, no causal influence was found in the corresponding LL clusters, characterized by low aerosol abundance (Supplementary Figs. 3,4). Precipitation suppression lagged aerosol enhancement and lasted one to five days (2004, 2–5 days; 2005, 1–2 days; 2009, 2–5 days), with the maximum influence, in terms of correlation coefficient magnitude, occurring on different days (2004, day 5; 2005, day 1; 2009, day 3). The corresponding lagged time series between AOD

anomaly and precipitation anomaly (Fig. 1c), corresponding to maximum correlation magnitude, showed several intra-seasonal periods of high AOD anomaly followed by periods of low precipitation. These negative causal relationships did not manifest in 2000, 2001, and 2002; 2006 and 2008 lacked sufficient data (<50 pixels in HL and LL clusters) for conclusive results. A positive causal effect of daily AOD on daily precipitation was found in 2003 and 2007, identified as abundant monsoon years[30].

In addition to total aerosol abundance (measured by AOD), the effects of absorbing aerosols (measured by absorbing aerosol index, AAI) were examined in the HL and LL clusters. Again a positive anomaly in AAI exerted a strong causal influence on lagged negative precipitation anomaly (2004 and 2005, 2–5 days; 2009, 1 day), which lasted one to five days, with strongest causal influence occurring on different days (quantified as correlation coefficient) in different years (2004, day 5; 2005, day 5; 2009, day 1). This behavior also manifested in LL clusters (with negative AOD anomalies) in 2005 and 2009. Since clustering was performed with AOD, the LL clusters contained many (30–40%) positive AAI anomaly values and thus included several days of high absorbing aerosol levels. Overall, enhanced levels of aerosols caused suppression of lagged daily precipitation, 3–5 times during the monsoon season, in high aerosol-low precipitation regions (HL).

Other studies found positive correlations between AOD and cloud properties[20] and daily precipitation over the monsoon region[31], suggesting a cloud invigoration effect, however, did not test for causation. The aerosol-cloud invigoration effect is beyond the scope of the present study, which focuses only on variables linked to aerosol-induced suppression of precipitation.

Cause–Effect Model Development and Validation. The physical mechanisms (causality) underlying the observed aerosol caused suppression of precipitation are studied using cause-effect model and path-analysis.

To unravel the mechanism of AOD- or AAI-induced precipitation suppression, it was postulated that a microphysical pathway linked AOD with precipitation through the mean cloud droplet effective radius (CDER) (AOD–CDER–PRECIP), while a radiative pathway linked aerosols (AOD or AAI) with precipitation through the lapse rate (defined as AOD–lapse rate–PRECIP and AAI–lapse rate–PRECIP). Causality was first tested between AOD and CDER, AOD and lapse rate, and AAI and lapse rate, and path analysis was used to segregate and quantify the effects of the two mediating pathways. These pathways were compared with pathways that directly linked column water vapor (CWV) with both precipitation (PRECIP) and CDER, to evaluate their respective strengths[32].

In high aerosol-low precipitation (HL) regions, enhancement of AOD caused a reduction in lapse rate (2004) and in CDER (2005), extending to five days (panels 1 and 3, Fig. 2a,b). No significant effect of AOD on CDER was found in 2004 or 2009. Here we found aerosol induced increase in static stability and decrease in moisture availability, with short time-lags of 1-5 days, subsequently, causing reduction in cloud droplet size (CDER). This effect of reduction in CDER via divergence of moisture takes place over a period of days as compared to microphysical effects, where increases in aerosols within clouds leads to formation of larger number of smaller drops on time scales of minutes to hours. Enhancement of AAI exerted suppression of lapse rate (stabilization) at shorter lag times of one day (panel 2, Fig. 2a,c), indicating that the radiative effects on lapse rate changes were largely influenced by absorbing aerosols in all three years. In contrast, no causal influences were found in low aerosol-low precipitation (LL) regions, implying absence of these effects.

Cloud Microphysical Pathway. The cause-effect model and lagged correlation coefficients were used as input in the path analysis; the overall correlation coefficients were segregated into path coefficients whose sign and magnitude indicated the direction and strength of the causal influence (Fig. 3a,b). The cloud microphysical pathway (Fig. 3a) showed inverse effects of AOD on CDER (blue color; arrow direction) or mean drop size, but direct effects of CDER on PRECIP (red color; arrow direction), indicating increases in AOD causing lagged decreases in CDER and rainfall. A positive causal influence of water vapor availability (CWV) on both PRECIP and CDER showed the expected relation of increased moisture availability to cloud and rainfall development. The CWV–PRECIP direct positive pathway was significantly stronger than the negative AOD–CDER–PRECIP pathway, based on the magnitudes of the overall path effects (Supplementary Table 1), indicating that rainfall suppression through changes in cloud drop size was not a strong pathway. In the low aerosol-low precipitation (LL) regions no causal influence of aerosol level on CDER was found (missing causal lines between AOD and CDER in Fig. 3b), however, moisture availability exerted positive causal effects on rainfall, both directly (CWV–PRECIP, Fig. 3b) and indirectly through CDER (CWV–CDER–PRECIP). Thus, the aerosol effects acted only in the high-aerosol regions, but moisture effects acted in both high and low aerosol regions.

Cloud microphysical processes, which influence rainfall suppression, result from direct increases in aerosols at cloud level, leading to the redistribution of moisture to a larger number of smaller drops. This reduces coalescence efficiency, slowing down the conversion of cloud drops to raindrops or graupel[18]. Raindrop formation is initiated from vapor condensation and collision/coalescence processes, on time scales of a minute, but it subsequently intensifies from scavenging of small cloud drops by gravitational settling of larger drops (termed autoconversion). This leads to precipitation onset on time scales of about 15–20 minutes[33]. Such fast microphysical effects have been linked to precipitation shut-off in ship tracks in pristine marine clouds[19]. Microphysical and radiative processes are largely independent, occurring at different ranges of AOD values; the time responses of the microphysical processes are much shorter than those of the radiative processes[34]. The presence of 1–5 day lag times between aerosol enhancement and CDER or precipitation suppression indicates that these causal relationships might not be a direct microphysical effect, which typically acts on time scales of minutes to hours.

Radiative Pathway. In regions of high-aerosol and low-precipitation, the radiative pathway (Fig. 3a) showed inverse effects of AOD on lapse rate (blue color; arrow direction) calculated as the slope of potential temperature, with a lower magnitude of lapse rate, indicating higher atmospheric stability. Positive effects of lapse rate on PRECIP (red color; arrow direction), indicated increases in AOD causing lagged decreases in

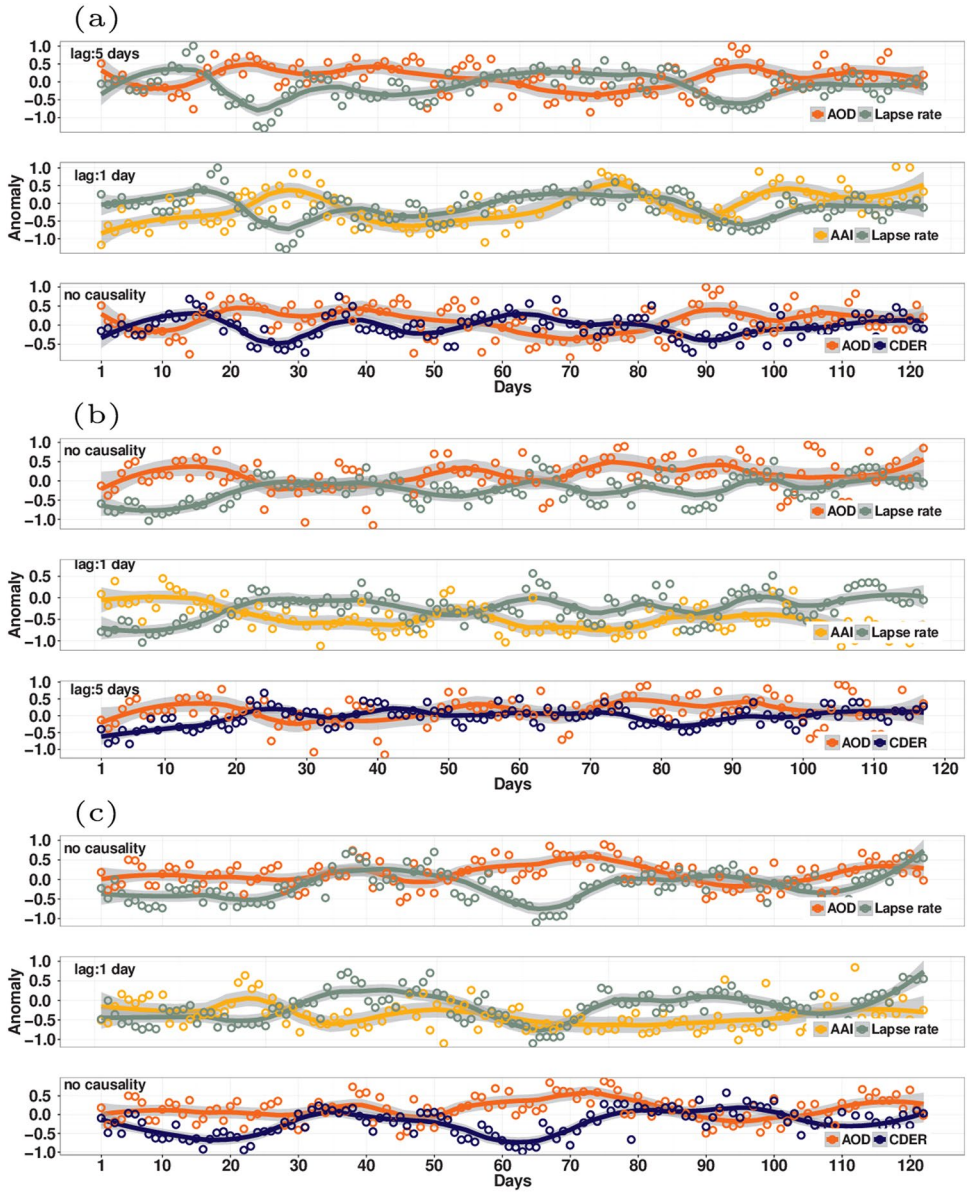

Figure 2. Co-variation of aerosols: AOD-lapse rate (lapse rate shifted by lag corresponding to maximum correlation magnitude), AAI-lapse rate (lapse rate shifted by lag corresponding to maximum correlation magnitude) and AOD-cloud droplet effective radius (cloud droplet effective radius shifted by lag corresponding to maximum correlation magnitude) time series plots, for years (**a**) 2004, (**b**) 2005 and (**c**) 2009, in HL cluster. Similar to Fig. 1(c), here multiple instances of enhanced AOD anomaly associated with suppressed cloud droplet size and suppressed lapse rate can be seen. The AAI anomaly enhancement with suppression of lapse rate can also be seen in the current figure. Figure was created using R statistical tool v3.3.1 (https://www.r-project.org/).

lapse rate and rainfall. The causal influence between AAI and lapse rate was especially strong in 2004, 2005 and 2009, substantiated by larger magnitudes of negative path coefficients (Supplementary Table 1), compared to that of AOD which acted only in 2004. The radiative pathway of absorbing aerosols (AAI–lapse rate–PRECIP), equaled the moisture-rainfall (CWV-PRECIP) effect in strength in some years, indicating the potential for strong aerosol-induced rainfall suppression. A stronger influence of the radiative pathway, than the cloud microphysical pathway, was found (larger negative values of path coefficients; Supplementary Table 1) on rainfall suppression. The radiative pathway showed significant effects even in the low-aerosol regions (LL clusters which were based on AOD) indicating overall more spatially widespread effects of aerosols on rainfall suppression. The radiative and cloud microphysical pathways, along with CWV, together explained approximately half of total precipitation variability (PRECIP $R^2 > 0.50$; Supplementary Table 1). Exclusion of the radiative pathway from the model resulted in a significant drop in PRECIP R^2 for the HL and LL clusters (Supplementary Table 2), highlighting the strong effects of aerosol-induced atmospheric stabilization on precipitation suppression. The distributions of anomaly values of CWV and cloud fraction (CF), which could influence rainfall development, were not

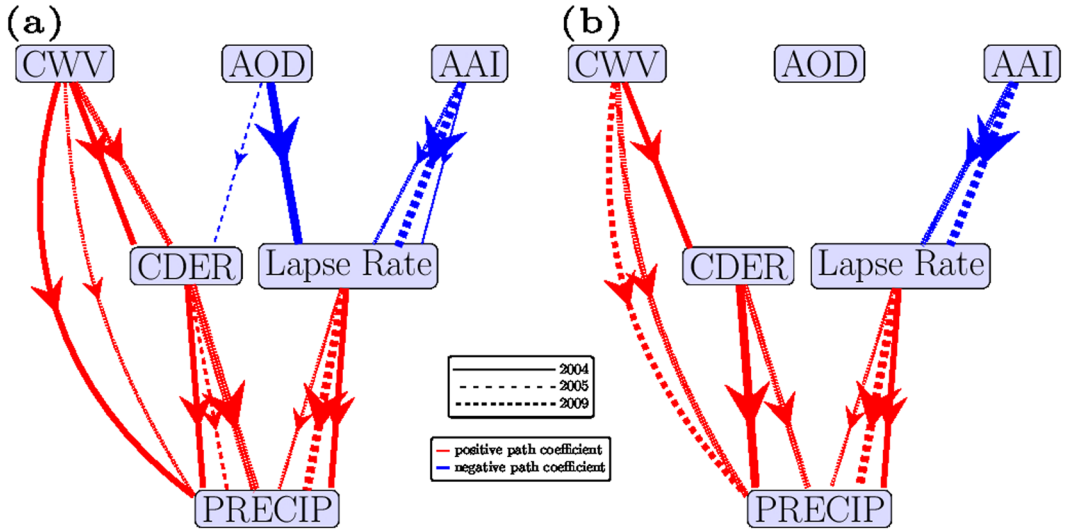

Figure 3. Path diagram: Cause-effect model for 2004, 2005 and 2009: (**a**) HL (**b**) LL (line-width represents absolute magnitude of path coefficient, larger width implying greater absolute path-coefficient). Arrows represent the direction of causal influence, and color indicates the sign of causal influence, with red showing positive, blue showing negative, and different line styles representing different years.

statistically different (Supplementary Fig. 5a,b) between the high- and low-aerosol regions, further supporting aerosol-induced stabilization as the primary cause of the observed rainfall suppression.

Short-term radiative effects can manifest within a day of an increase in aerosol levels and last for two or more days[35–38]. The absorption of solar radiation by aerosols has been linked to local atmospheric heating, with cooling of the surface leading to a reduction in the atmospheric lapse rate or a consequent increase in stability[36,39]; this is consistent with the radiative pathway seen in this study. The effect is further linked to a suppression of moisture and heat fluxes from the surface[34], a reduction of convection[12], and the vertical mixing of moisture. Aerosol levels were linked to a reduction in cloud fraction and drop sizes of shallow continental clouds[34,40]. Higher atmospheric stabilization by aerosols was linked to modeled decreases in monsoon precipitation on multi-decadal time scales[4], while it was suggested as significant on short time scales in another study[5]. An increase in black carbon aerosols increased stability of the boundary layer and reduced convection, which further reduced cumulus precipitation in large eddy simulations (LES)[12] and general circulation model simulations[41]. To our knowledge, the findings here are the first demonstration of causality of aerosol-induced atmospheric stabilization on Indian monsoon precipitation suppression.

In contrast with the aerosol-induced suppression of precipitation found in this study, Sarangi *et al.*[31] found an increase in daily precipitation intensity with increased aerosol loading over the core monsoon zone. Differences in the studies include the use of clustering into HL and LL regions here, in contrast with the use of non-segregated data in the other study. Further, cloud fraction in the present study ranged from 0.5 to 1 in the HL and 0.3 to 1 in the LL regions, in contrast with larger cloud fractions considered in the other study. Aerosol-induced invigoration of rainfall acts at different levels of AOD on different regimes of cloud fraction, in comparison with the suppression mechanism investigated here, and manifests in changes in micro- and macro-physical cloud properties, the analysis of which is beyond the scope of the present study.

Mechanisms of Short-term Precipitation Suppression. Further analysis was performed to link the observed causality between enhanced aerosol levels and short-term precipitation suppression to factors typically used to explain monsoon variability, such as, vertical integral of divergence of moisture flux (VIDMF), vertical wind (ω850) and surface pressure[10,42,43]. Increases in VIDMF and ω850 have been linked to suppression in precipitation, while an increase in surface pressure has been associated with short monsoon break spells[44].

In periods of high aerosol levels (AOD anomaly >0.7 for at least three consecutive days) in the high-aerosol regions, VIDMF and ω850 anomalies (upward wind being negative) were found to be positive (Fig. 4a,c,e), indicating higher moisture flux divergence and a simultaneous reduction in convective activity in the column, in contrast to that in low aerosol periods (Fig. 4b,d,f). These effects were more pronounced during periods of higher aerosol levels (at different AOD anomaly thresholds; Supplementary Fig. 6) from an increase in gross moist stability, defined as the ratio of vertically integrated horizontal divergence of moisture to vertical convection, consistent with earlier studies[45], associated with subsequently reduced precipitation.

The role of common moderating meteorological variables is often debated in relation to aerosol–cloud–precipitation interactions. Surface pressure is typically identified as one of these variables, whose positive anomalies have been linked to break spells in monsoon precipitation[44]. Increases in AOD anomalies had causal effects on increases in anomalies of surface pressure and VIDMF, with lags of 1–5 days (Supplementary Table 3). In HL regions, a greater frequency of positive surface pressure anomalies was found (Supplementary Fig. 7). However,

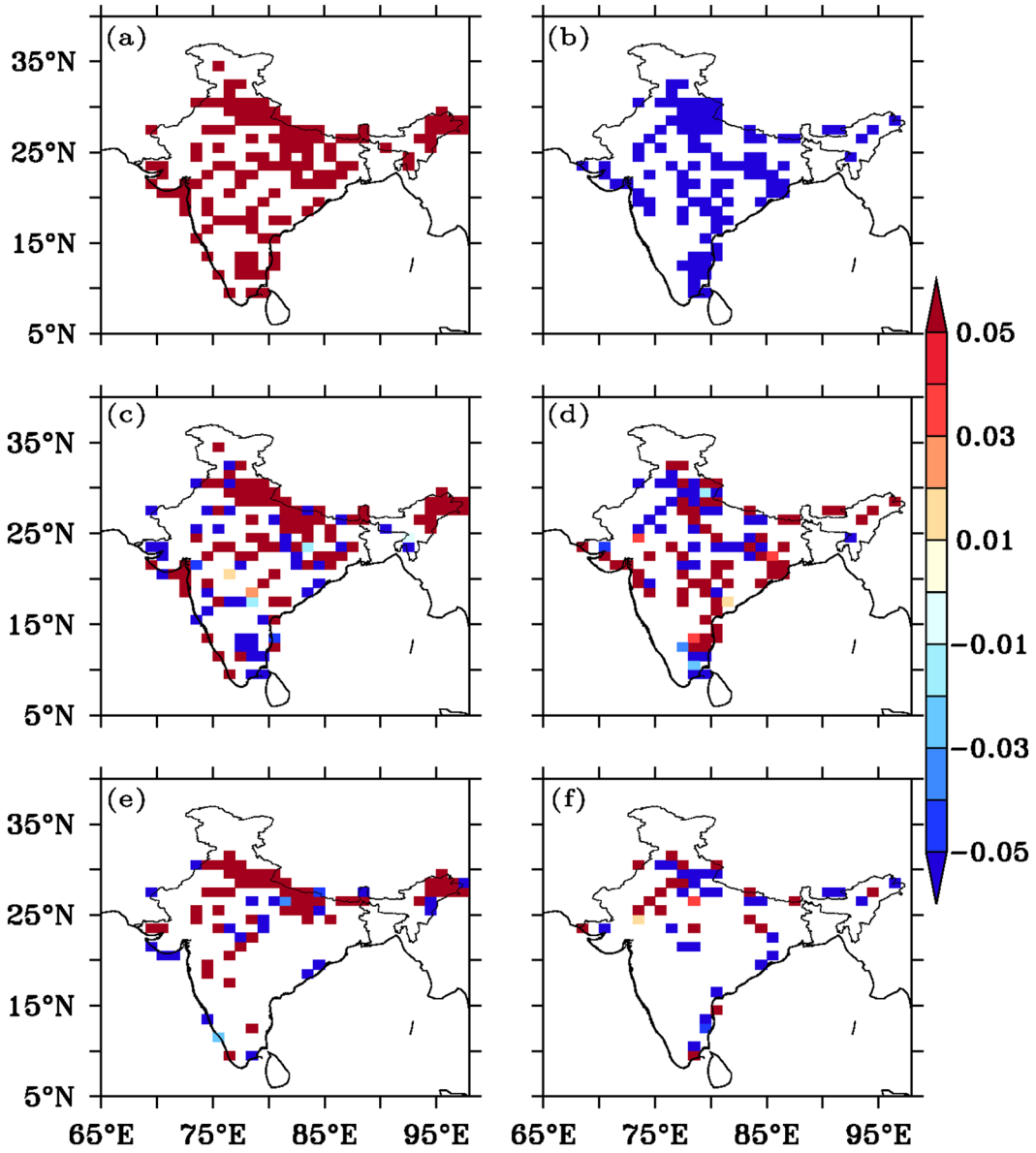

Figure 4. VIDMF and ω850 anomaly variation with AOD anomaly: VIDMF anomaly and ω850 anomaly composite with varying AOD anomaly threshold. (**a**) AOD anomaly >0.7, (**b**) AOD anomaly <−0.7 (**c**) VIDMF anomaly (AOD anomaly >0.7), (**d**) VIDMF anomaly (AOD anomaly <−0.7) (**e**) ω850 anomaly (AOD anomaly >0.7) and (**f**) ω850 anomaly (AOD anomaly <−0.7). It can be seen that high AOD anomaly (>0.7) is associated with more divergence of moisture and downward wind as compared to low AOD anomaly (<−0.7). Figure was created using FERRET v7.0 (http://www.ferret.noaa.gov/Ferret/).

there was no causality between increased anomalies in surface pressure and those in VIDMF (Supplementary Table 3), ruling out the role of surface pressure in the observed effects.

The monsoon region is reported to experience the persistence of both dust aerosols[13,46] and build-up of anthropogenic fine particles[47–49], the combined effects of which can diminish surface reaching radiation and can cool the surface, subsequently increasing the atmospheric stability. Further, transient occurrence of black carbon aerosols has been measured both at surface and at elevations of 1 to 3 km over India and adjoining oceans[50,51].

Convection is reported to accommodate positively, on daily to monthly timescales, to radiative effects of absorbing aerosols like black carbon leading to short-term increases in precipitation[8,9]. Specifically, active phases following monsoon break periods, were linked to a build-up of aerosols which caused aerosols moisture convergence and onset of rainfall[47,52], on time-scales of about 20 days. However, reduction in convection with increases in black carbon aerosols is reported, both in observation studies of biomass burning[40] and modelling studies[12]. Modeling study conducted by Das *et al.*[53] reported increase in moisture divergence with increased absorbing aerosols. Guo *et al.*[54] point out that a significant threshold of black carbon loading is necessary to induce convection, which was found only in simulations using 5xBC of present day emissions. The overall mesoscale mechanism observed here (Fig. 5), is enhancement in aerosol levels causing atmospheric stabilization, with increased

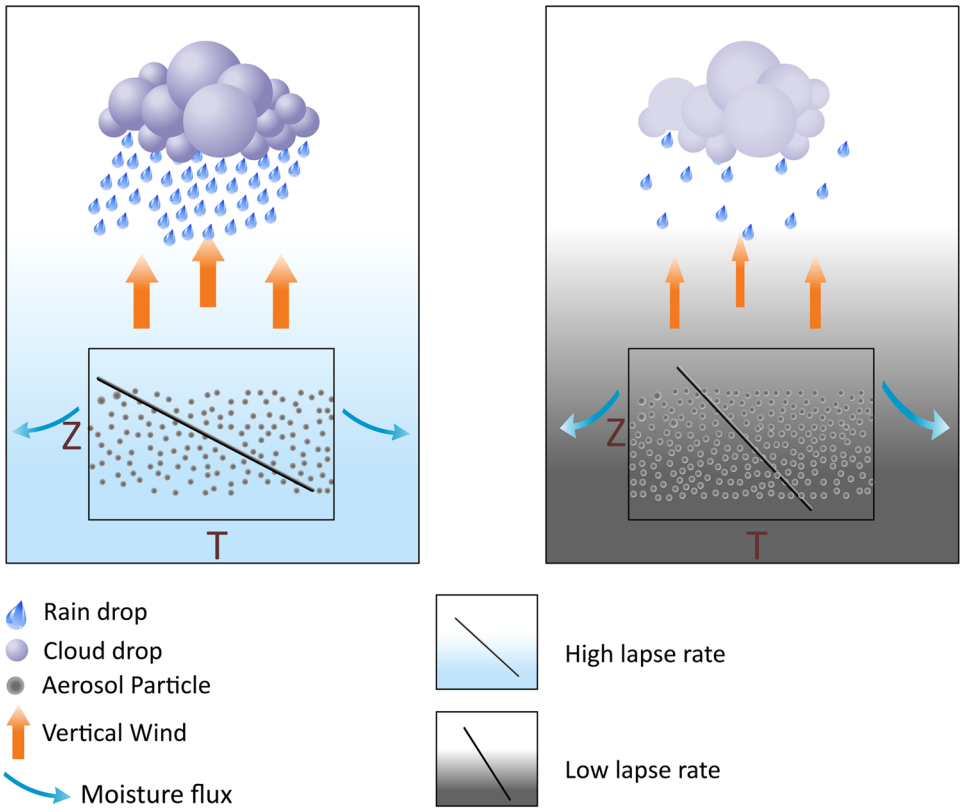

Figure 5. Mechanisms of aerosol induced suppression: Reduced aerosol loading makes the atmosphere unstable causing reduced divergence of moisture and normal convection leading to uplift of moisture and subsequently normal precipitation. While in case of increased aerosol loading the divergence of moisture is enhanced accompanied with stable atmospheric conditions. Conflation of these effects suppresses the precipitation. Figure was created using CorelDRAW × 6 (www.coreldraw.com).

horizontal moisture divergence, reduced convection and vertical velocity and subsequent suppression of precipitation. These two effects of limited moisture availability and restricted convection conflate and contribute to the suppression of precipitation.

Implications for Monsoon Break Spells. Break spells are inherent to the Indian monsoon. However, their intensity and duration plays an important role in determining deficient precipitation or drought conditions[2,55]. While several definitions are used to identify monsoon break spells, a widely accepted one is based on a normalized anomaly threshold of one standard deviation below the mean[2,55,56], which occurs for at least three consecutive days (Fig. S7).

The possible influence of aerosols on mediating break spells was examined through comparing break occurrence in regions of higher (HL) and lower (LL) aerosols (Fig. 6). A larger number of total break days and increased frequency of break spells and prolonged break spells (lasting seven days or longer) was found in HL regions (3–4 times in a season) than in LL regions (1–2 times in a season). The chosen threshold of precipitation anomalies corresponded to the negative one standard deviation and more stringent decreases (Supplementary Fig. 8) and results were averaged over all threshold values. It is accepted that prolonged or extended breaks (lasting seven days or more) often result in droughts[2,55]. Recent studies examining monsoon variability over India during the last 50 years found an increased duration[57] and frequency[58] of break spells. However, explicit attribution to aerosol effects was not investigated in the earlier studies.

The widespread nature of aerosol-induced rainfall suppression observed here, is evidenced by their occurrence not only in 2004 and 2009, widely reported as deficient monsoon years on sub-continental scales[14,35], but also in 2005, acknowledged as a normal monsoon year. It was suggested that when the Indian summer monsoon anomaly is large (>15%), it is often uniform across the country, but when it is within a few percent of the mean, several regions could have deficit or excess precipitation[1]. This suggests that the aerosol-induced causal mechanisms uncovered here could aggravate break spells and precipitation deficits in normal monsoon years with modest monsoon precipitation anomalies. In other years, where the analysis was inconclusive due to lack of data, the use of a finer resolution or larger dataset could yield better insights.

Intra-seasonal oscillations of the Indian monsoon typically occur on cycles of 6–9 days, 10–20 days, and 30–60 days[59]. Monsoon break periods are generally associated with increased surface pressure anomalies, weaker moisture-laden low-level flows from the southern Indian Ocean, decreased cyclonic vorticity over the monsoon region, and positive anomalies in outgoing longwave radiation associated with the scarcity of clouds[44,55,60]. The

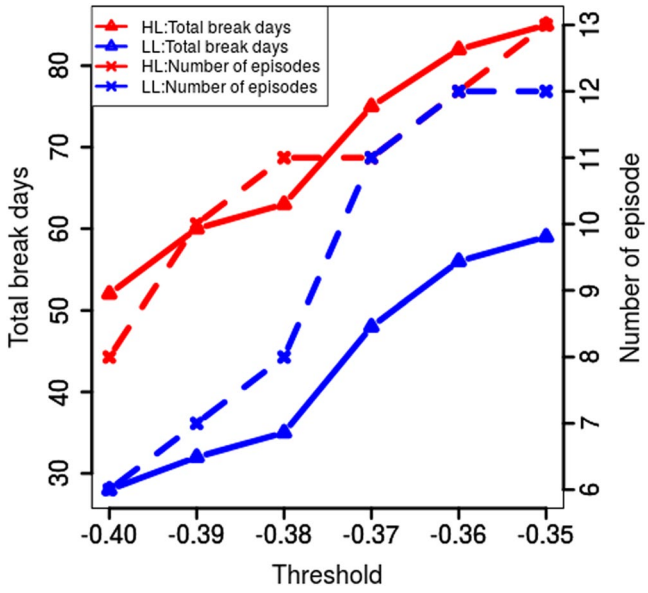

Figure 6. Break characteristics in HL and LL clusters: Total number of break days and frequency of episodes of break spells in HL and LL cluster with varying AOD threshold. Increased number of break days and break episodes were found in regions with increased aerosol levels. Figure was created using R statistical tool v3.3.1 (https://www.r-project.org/).

aerosol-induced suppression of precipitation seen in this study, which results from mesoscale atmospheric stabilization on shorter time scales of 3–5 days (Fig. 1c), is therefore a distinct phenomenon, whose interplay with monsoon break dynamics warrants further investigation.

Summary and Discussion

Anthropogenic pollution particles over South Asia comprise a mixture of light scattering species (including sulfate, nitrate, organic carbon and others) and light absorbing black carbon (or soot), the latter emitted primarily by traditional technologies burning biomass fuels[61]. This study uncovered a causal influence of aerosols on repeated meso-scale suppression of precipitation, which occurred throughout the monsoon season. The suppression mechanism was mediated primarily through a radiative pathway acting to increase atmospheric stability and horizontal divergence of moisture.

Consensus in previous studies points to monsoon rainfall weakening linked to an asymmetric inter-hemispheric energy balance change attributed to aerosols[5,7] and short-term rainfall enhancement linked to radiative effects of non-local absorbing aerosols[8,9,47,52]. In this study, short-term rainfall suppression is linked to radiative effects of coincident aerosols, acting through repeated atmospheric stabilization, reduction in convection and increased moisture divergence, leading to aggravation of monsoon break conditions. Interestingly, in addition to being manifested in deficient monsoon years, causal influences of aerosols on precipitation suppression also occurred in a normal monsoon year, indicating the possibility of a widespread occurrence of this phenomenon.

The causal influence of aerosols on precipitation suppression is relevant to the inter-annual variability of monsoon precipitation and the timing of monsoon break spells. Prolonged and intense breaks in the monsoon were associated with rainfall deficits[55], which have been linked to reduced food grain production during latter half of the twentieth century[1]. Thus, aerosol-induced precipitation suppression and aggravation of break spells, uncovered here, could influence future rainfall deficits and agricultural vulnerability in India.

Methods

Data set. Aerosol and cloud properties from satellite observations[22–24], precipitation from ground based measurements[25], and meteorological variables from European Centre for Medium-Range Weather Forecasts (ECMWF) re-analysis (ERA)-interim reanalysis data[26] from 2000–2009 over the Indian subcontinent (6.5–40° N and 66.5–100° E), at $1 \times 1°$ resolution for the monsoon months of June to September (JJAS), were used for the analysis. Level-3 (L3) atmospheric aerosol data, retrieved from the moderate resolution imaging spectroradiometer (MODIS) on board the Earth Observing System's (EOS) Terra (MOD08_D3v6) and Aqua (MYD08_D3v6) satellites, made available through the National Aeronautics and Space Administration (NASA) Deep blue (Collection-6) algorithm[24], were used for aerosol optical depth (AOD). The data includes AOD retrievals over regions with high reflectance. Positive values of absorbing aerosol index (AAI) from the total ozone mapping spectrometers (TOMS) on board the Earth Probe satellites and the ozone monitoring instrument (OMI) sensor on board the EOS Aura satellite, were derived using the Earth Probe TOMS[22] and OMAERUV[62] algorithms. These measure absorbing aerosols that are within the range of 0.5 and 3.5 km[63] and neglect the residues related to purely scattering aerosols[62]. MODIS L3 cloud droplet effective radius (CDER) data, obtained from both EOS Terra (MOD08_v3) and Aqua (MYD08_v3) satellites, were used. Lapse rate was calculated using the temperature of

nine layers of atmosphere between 1000 and 750 hPa, corresponding to the lower troposphere in the ERA-interim dataset[26]. Precipitation data, as a gridded product, were obtained through the interpolation of data from 1803 irregularly located meteorological stations over India, with approximately 350 pixels over the Indian domain[25].

Data Processing. The description and source of the data is listed in Table S4 for years 2000–2009 at resolution of 1×1^{o}. The spatial coverage for the study region was 6.5–40 °N to 66.5–100 °E. AOD values less than 0.8 were retained for the analysis as higher values may be due to misclassification of clouds as aerosols[40]. Daily pixel-wise absolute value for each variable was transformed into normalized anomaly. To achieve this, at a given pixel, deviation of daily absolute value from its mean daily value (across years) was divided with standard deviation of daily absolute value (across years). This was repeated for all the pixels. Further, season average anomaly was calculated by taking mean of normalized anomaly for each year and every pixel. Normalized daily anomaly (Δx_{tiy}) for each variable was calculated as described below:

The normalized anomaly (Δx_{tiy}) was the deviation of variable for a specific day (t) and pixel (i) from the mean (calculated across years), normalized by its standard deviation. Further, seasonal average anomaly ($\overline{\Delta x_{iy}}$) was calculated for each year and each pixel. Depending upon the value of $\overline{\Delta x_{iy}}$ the complete 122-day temporal series of anomaly (Δx_{tiy}) was assigned to either low value cluster or high value cluster.

$$\overline{x_{ti}} = \frac{\sum_{y=1}^{Y} x_{tiy}}{Y}, \{i = 1, 2, \ldots., N; t = 1, 2, \ldots., \mathrm{T}\} \tag{1}$$

$$\sigma(x_{ti}) = \sqrt{\frac{\sum_{y=1}^{Y} (x_{tiy} - \overline{x_{ti}})^2}{Y - 1}}, \{i = 1, 2, \ldots., N; t = 1, 2, \ldots., \mathrm{T}\} \tag{2}$$

$$\Delta x_{tiy} = \frac{x_{tiy} - \overline{x_{ti}}}{\sigma(x_{ti})}, \{i = 1, 2, \ldots., N; t = 1, 2, \ldots., \mathrm{T}; y = 1, 2, \ldots.,\mathrm{Y}\} \tag{3}$$

$$\overline{\Delta x_{iy}} = \frac{\sum_{t=1}^{T} \Delta x_{tiy}}{T}, \{i = 1, 2, \ldots., N; y = 1, 2, \ldots., \mathrm{Y}\} \tag{4}$$

$$\overline{\Delta x_{iy}} = \begin{cases} >0, & i \text{ is an high value pixel in year } y \\ <0, & i \text{ is a low value pixel in year } y \end{cases}, \{i = 1, 2, \ldots., N; y = 1, 2, \ldots., \mathrm{Y}\} \tag{5}$$

here t denotes a day in June-September (JJAS) ($t = 1, 2, \ldots, T$). Pixels are denoted as i ($i = 1, 2, \ldots, N$) and y denotes years ($y = 1, 2, \ldots, \mathrm{Y}$). T is total number of days in JJAS, N is total number of pixels and Y is total number of years.

The season averaged pixel-level AOD and precipitation anomalies were subjected to hierarchical clustering for each of the years (2000–2009). Pixels were assigned to (a) high AOD-low precipitation (HL), (b) low AOD-low precipitation (LL), (c) high AOD-high precipitation (HH), and (d) low AOD-high precipitation (LH) clusters. The high AOD-low precipitation and low AOD-low precipitation clusters were selected to investigate possible effects of different levels of aerosols on precipitation suppression. Clustering process is described below:

Pixels were first clustered into high and low AOD anomaly pixels depending upon $\overline{\Delta x_{iy}}$ AOD values. These pixels were further clustered into high and low precipitation anomaly pixels using $\overline{\Delta x_{iy}}$ precipitation values. Thus, pixels were clustered into four clusters i.e. (a) high AOD-low precipitation (HL), (b) low AOD-low precipitation (LL), (c) high AOD-high precipitation (HH), and (d) low AOD-high precipitation (LL). Once the pixels were assigned to respective clusters, cluster average of all the pixels was taken to get an average temporal series Δx_{ty} for each year which was used for causality analysis.

$$\Delta x_{ty} = \frac{\sum_{i=1}^{\mathrm{M}(y)} \Delta x_{tiy}}{M(y)}, \tag{6}$$

where M(y) is the number of pixels in a given cluster, t is the day and y is the year.

HL clusters for years 2004, 2005 and 2009 are shown in Supplementary Fig. 2 while LL clusters are shown in Supplementary Figs 3,4. For year 2004, HL cluster had 113 pixels while LL cluster had 98 pixels while year 2009 had 156 and 169 pixels respectively for HL and LL clusters. HL cluster corresponded to highly deficient region for year 2004 and peninsular regions for 2009, as reported in literature[35,64]. Though 2005 was normal year the HL pixels (belonging to north-eastern region of India) received less precipitation compared to other years[65]. The above clustering and analysis was based on normalized anomaly values. The definition of anomaly ensured that regional effects were excluded while establishing causality.

The individual time series were found to be stationary using Kwiatkowski-Phillips-Schmidt-Shin (KPSS) test or were made stationary by first order differencing, if the original time series was non-stationary. In the cause-effect model, Granger causality (GC) was tested pair-wise both ways and once the causality was established, the lagged correlation coefficient (lag obtained from GC analysis as discussed next) was calculated and provided as input to path analysis. Lags with washout (i.e. precipitation causing AOD, feedback (i.e. AOD causing precipitation and precipitation causing AOD), and lags associated with statistically not significant correlations were excluded from the analysis. The statistical significance tests were performed at $\alpha = 0.1$ throughout the study.

Granger causality. The notion of Granger causality (*GC*) was first introduced by Granger[28]. It relies on the principle that the causal event leads its effect and has unique information about the future. A variable Y is said to Granger cause variable X, if inclusion of past information of both Y and X gives statistically significant improvement in the prediction of X as compared to only inclusion of past information of X. *GC* has been applied in climate domain for causal attribution[66–68].

Consider stationary time series of Y_t and X_t to test the null hypothesis of no Granger causality. Towards this end, an auto-regressive model of X_t is compared with auto- and cross-regressive model of X_t involving Y_t as,

$$X_t = \alpha_0 + \alpha_1 X_{t-1} + \ldots\ldots + \alpha_n X_{t-n} + \varepsilon_x \tag{7}$$

$$X_t = \tilde{\alpha}_0 + \tilde{\alpha}_1 X_{t-1} + \ldots\ldots + \tilde{\alpha}_n X_{t-n} + \beta_1 Y_{t-1} + \ldots\ldots + \beta_n Y_{t-n} + \varepsilon_{xy} \tag{8}$$

If the variance of the residual in the second model, labelled $\sigma^2_{\varepsilon_{xy}}$, is significantly less than the variance of the residual in the first model, labelled $\sigma^2_{\varepsilon_x}$, then the inclusion of information of Y is improving the prediction of X_t implying that Y is Granger causing X. *GC* was tested at varying lags, and lags with statistically significant causality were retained for further analysis. First order difference was performed for all the variables to ensure stationarity before performing *GC* test for years 2004, 2005 and 2009. Along with this, causality of a particular day was also tested by comparing the regression model with and without inclusion of a particular day value.

$$X_t = \alpha_0 + \alpha_1 X_{t-1} + \ldots\ldots + \alpha_n X_{t-n} + \tilde{\varepsilon}_x \tag{9}$$

$$X_t = \tilde{\alpha}_0 + \tilde{\alpha}_1 X_{t-1} + \ldots\ldots + \tilde{\alpha}_n X_{t-n} + \beta_n Y_{t-n} + \tilde{\varepsilon}_{xy} \tag{10}$$

If $\sigma^2_{\tilde{\varepsilon}_{xy}}$ is significantly less than $\sigma^2_{\tilde{\varepsilon}_x}$ the inclusion of information of Y_{t-n} is improving the prediction of X_t implying that Y_{t-n} (i.e. a particular nth day in the past) is Granger causing X. The results found were same as with conventional causality methods.

Path Analysis. Proposed by Wright[29], path analysis enables splitting of the net effect of one variable on other variables into direct and indirect effects. The direct effect is the path coefficient of the directed edge between two variables under consideration. The indirect effect is the sum of product of path coefficients for all paths, other than the direct edge, connecting the variables under consideration. To illustrate, consider the example in Supplementary Fig. 9[69] where two exogenous variables Z_1 and Z_2 are affecting a common endogenous variable Y. The variables Z_1 and Z_2 are correlated with Y. The correlation coefficients ρ_{12}, ρ_{1y} and ρ_{2y} are available for a given data set. In Supplementary Fig. 9 the double headed arrow between the exogenous variables Z_1 and Z_2 represents the correlation between exogenous variables. The single headed arrow from exogenous variables Z_1 to Y and Z_2 to Y signifies that Y is dependent on Z_1 and Z_2. The self-loop on variable Y represents the error term and coefficient $p_{y\varepsilon}$ represents the error path coefficient. The regression model of Y, in standardized form, can be written as:

$$Y = p_{1y} Z_1 + p_{2y} Z_2 + p_{y\varepsilon}\varepsilon \tag{11}$$

Path coefficients p_{1y}, p_{2y} and $p_{y\varepsilon}$ are calculated using:

$$\rho_{1y} = p_{1y}(1) + p_{2y}\rho_{12} \tag{12}$$

$$\rho_{2y} = p_{1y}\rho_{12} + p_{2y}(1) \tag{13}$$

$$1 = \sigma_Y = p^2_{1y} + p^2_{2y} + p^2_{y\varepsilon} + 2\rho_{12}p_{1y}p_{2y} \tag{14}$$

Once the path coefficients are calculated the total effect can be segregated into direct and indirect effects. The direct and indirect effects of exogenous variables Z_1 and Z_2 on Y are shown in Supplementary Table 5.

In the current work, path analysis was used to segregate the causal influence of aerosol on precipitation into cloud microphysics and radiative pathways. The strength of each path was quantified as product of path-coefficients of edges appearing in that path. The presence (absence) of a statistically significant path coefficient indicates the presence (absence) of the effect.

References

1. Gadgil, S. & Gadgil, S. The Indian Monsoon GDP and Agriculture. *Economic and Political Weekly* 4887–4895 (2006).
2. Prasanna, V. Impact of monsoon rainfall on the total foodgrain yield over India. *J. Earth Syst. Sci.* **123**, 1129–1145 (2014).
3. Meehl, G. A., Arblaster, J. M. & Collins, W. D. Effects of black carbon aerosols on the Indian monsoon. *J. Clim.* **21**, 2869–2882 (2008).
4. Ramanathan, V. *et al*. Atmospheric brown clouds: Impacts on South Asian climate and hydrological cycle. *Proc. Natl. Acad. Sci. USA* **102**, 5326–5333 (2005).
5. Bollasina, M. A., Ming, Y. & Ramaswamy, V. Anthropogenic aerosols and the weakening of the South Asian summer monsoon. *Science.* **334**, 502–505 (2011).
6. Ganguly, D., Rasch, P. J., Wang, H. & Yoon, J. H. Fast and slow responses of the South Asian monsoon system to anthropogenic aerosols. *Geophys. Res. Lett.* **39**, 1–5 (2012).
7. Krishnan, R. *et al*. Deciphering the desiccation trend of the South Asian monsoon hydroclimate in a warming world. *Clim. Dyn.* **47**, 1007–1027 (2016).
8. Vinoj, V. *et al*. Short-term modulation of Indian summer monsoon rainfall by West Asian dust. *Nat. Geosci.* **7**, 308–313 (2014).

9. Lau, K. M. & Kim, K. M. Observational relationships between aerosol and Asian monsoon rainfall, and circulation. *Geophys. Res. Lett.* **33**, 1–5 (2006).
10. Fasullo, J. Atmospheric hydrology of the anomalous 2002 Indian summer monsoon. *Mon. Weather Rev.* **133**, 2996–3014 (2005).
11. Maharana, P. & Dimri, A. P. Study of intraseasonal variability of Indian summer monsoon using a regional climate model. *Clim. Dyn.* **46**, 1043–1064 (2015).
12. Feingold, G., Jiang, H. & Harrington, J. Y. On smoke suppression of clouds in Amazonia. *Geophys. Res. Lett.* **32**, 1–4 (2005).
13. Dipu, S. *et al*. Impact of elevated aerosol layer on the cloud macrophysical properties prior to monsoon onset. *Atmos. Environ*. https://doi.org/10.1016/j.atmosenv.2012.12.036 (2013).
14. Hazra, A., Goswami, B. N. & Chen, J. P. Role of interactions between aerosol radiative effect, dynamics, and cloud microphysics on transitions of monsoon intraseasonal oscillations. *J. Atmos. Sci.* **70**, 2073–2087 (2013).
15. Ramachandran, S. & Kedia, S. Aerosol, clouds and rainfall: Inter-annual and regional variations over India. *Clim. Dyn.* **40**, 1591–1610 (2013).
16. Seifert, A., Nuijens, L. & Stevens, B. Turbulence effects on warm-rain autoconversion in precipitating shallow convection. *Q. J. R. Meteorol. Soc.* **136**, 1753–1762 (2010).
17. Rosenfeld, D. *et al*. Flood or drought: how do aerosols affect precipitation? *Science* **321**, 1309–13 (2008).
18. Gunn, R. & Phillips, B. B. An experimental investigation of the effect of air pollution on the initiation of rain. *Journal of Meteorology* **14**, 272–279 (1957).
19. Radke, L. F., Coakley, J. A. & King, M. D. Direct and remote sensing observations of the effects of ships on clouds. *Science.* **246**, 1146–1149 (1989).
20. Patil, N., Dave, P. & Venkataraman, C. Contrating influence of aerosols on cloud properties during deficient and abundant monsoon years. *Sci. Rep*. https://doi.org/10.1038/srep44996 (2017).
21. Sarangi, C., Tripathi, S. N., Kanawade, V. P., Koren, I. & Sivanand Pai, D. Investigation of the aerosol-cloud-rainfall association over the Indian summer monsoon region. *Atmos. Chem. Phys.* **17**, 5185–5204 (2017).
22. McPeters, R. *et al*. Earth Probe Total Ozone Mapping Spectrometer (TOMS) Data Product User's Guide. (1998).
23. Torres, O., Bhartia, P. K., Herman, J. R., Ahmad, Z. & Gleason, J. Derivation of aerosol properties from satellite measurements of backscattered ultraviolet radiation: Theoretical basis. *J. Geophys. Res. Atmos.* **103**, 17099–17110 (1998).
24. Remer, L. A. *et al*. The MODIS Aerosol Algorithm, Products, and Validation. *J. Atmos. Sci.* **62**, 947–973 (2005).
25. Rajeevan, M., Bhate, J., Kale, J. D. & Lal, B. Development of a high resolution daily gridded rainfall data set for the Indian region. *Curr. Sci.* **91**, 296–306 (2006).
26. Dee, D. P. *et al*. The ERA-Interim reanalysis: Configuration and performance of the data assimilation system. *Q. J. R. Meteorol. Soc.* **137**, 553–597 (2011).
27. Ward, J. H. Hierarchical grouping to optimize an objective function. *Journal of the American Statistical Association* **58**, 236–244 (1963).
28. Granger, C. W. J. Investigating causal relations by econometric models and cross-spectral methods. *Econometrica* **37**, 424–438 (1969).
29. Wright, S. The method of path coefficients. *Ann. Math. Stat.* **5**, 161–215 (1934).
30. Bhatia, R. C. & Rajeevan, M. *Monsoon 2007 A Repo*rt. (2008).
31. Sarangi, C., Tripathi, S. N., Kanawade, V. P., Koren, I. & Pai, D. S. A long-term observational analysis of aerosol-cloud-rainfall associations over Indian summer monsoon region. *Atmos. Chem. Phys. Discuss. Chem. Phys* 1–42 https://doi.org/10.5194/acp-2016-947 (2016).
32. Lebsock, M. D., L'Ecuyer, T. S. & Stephens, G. L. Detecting the ratio of rain and cloud water in low-latitude shallow marine clouds. *J. Appl. Meteorol. Climatol.* **50**, 419–432 (2011).
33. Xue, Y., Wang, L.-P. & Grabowski, W. W. Growth of cloud droplets by turbulent collision–coalescence. *J. Atmos. Sci.* **65**, 331–356 (2008).
34. Koren, I., Martins, J. V., Remer, L. A. & Afargan, H. Smoke invigoration versus inhibition of clouds over the Amazon. *Science.* **321**, 946–949 (2008).
35. Manoj, M. G., Devara, P. C. S., Joseph, S. & Sahai, A. K. Aerosol indirect effect during the aberrant Indian summer monsoon breaks of 2009. *Atmos. Environ.* **60**, 153–163 (2012).
36. Jacobson, M. Z. Control of fossil-fuel particulate black carbon and organic matter, possibly the most effective method of slowing global warming. *J. Geophys. Res. Atmos.* **107**, ACH 16-1–ACH 16–22 (2002).
37. Ackerman, T. P. A Model of the effect of aerosols on urban climates with particular applications to the Los Angeles Basin. *Journal of the Atmospheric Sciences* **34**, 531–547 (1977).
38. Koren, I. Measurement of the effect of Amazon smoke on inhibition of cloud formation. *Science.* **303**, 1342–1345 (2004).
39. Venkatram, A. & Viskanta, R. Radiative effects of elevated pollutant layers. *J. Appl. Meteorol.* **16**, 1256–1272 (1977).
40. Ten Hoeve, J. E., Remer, L. A. & Jacobson, M. Z. Microphysical and radiative effects of aerosols on warm clouds during the Amazon biomass burning season as observed by MODIS: Impacts of water vapor and land cover. *Atmos. Chem. Phys.* **11**, 3021–3036 (2011).
41. Cherian, R., Venkataraman, C., Quaas, J. & Ramachandran, S. GCM simulations of anthropogenic aerosol-induced changes in aerosol extinction, atmospheric heating and precipitation over India. *J. Geophys. Res. Atmos.* **118**, 2938–2955 (2013).
42. Chou, C., Neelin, J. D., Lohmann, U. & Feichter, J. Local and remote impacts of aerosol climate forcing on tropical precipitation. *J. Clim.* **18**, 4621–4636 (2005).
43. Wei, J., Su, H. & Liang, Z. Impact of moisture flux convergence and soil moisture on precipitation: a case study for the southern United States with implications for the globe. *Clim. Dyn*. 467–481 https://doi.org/10.1007/s00382-015-2593-2 (2016).
44. Krishnan, R., Zhang, C. & Sugi, M. Dynamics of breaks in the Indian summer monsoon. *J. Atmos. Sci.* **57**, 1354–1372 (2000).
45. Neelin, J. D. & Held, I. M. Modeling tropical convergence based on the moist static energy budget. *Monthly Weather Review* **115**, 3–12 (1987).
46. Padmakumari, B. *et al*. In situ measurements of aerosol vertical and spatial distributions over continental India during the major drought year 2009. *Atmos. Environ*. 107–121 https://doi.org/10.1016/j.atmosenv.2013.07.064 (2013).
47. Manoj, M. G., Devara, P. C. S., Safai, P. D. & Goswami, B. N. Absorbing aerosols facilitate transition of Indian monsoon breaks to active spells. *Clim. Dyn.* **37**, 2181–2198 (2011).
48. Bollasina, M., Nigam, S. & Lau, K. M. Absorbing aerosols and summer monsoon evolution over South Asia: An observational portrayal. *J. Clim.* **21**, 3221–3239 (2008).
49. Harikishan, G., Padmakumari, B., Maheskumar, R. S., Pandithurai, G. & Min, Q. L. Macrophysical and microphysical properties of monsoon clouds over a rain shadow region in India from ground-based radiometric measurements. *J. Geophys. Res. Atmos.* **119**, 4736–4749 (2014).
50. Tripathi, S. N., Dey, S., Tare, V. & Satheesh, S. K. Aerosol black carbon radiative forcing at an industrial city in northern India. *Geophys. Res. Lett.* **32**, 1–4 (2005).
51. Ansmann, A. *et al*. Vertical profiling of the Indian aerosol plume with six-wavelength lidar during INDOEX: A first case study. *Geophys. Res. Lett.* **27**, 963–966 (2000).
52. Das, S., Dey, S., Dash, S. K., Giuliani, G. & Solmon, F. Dust aerosol feedback on the Indian summer monsoon: Sensitivity to absorption property. 1–11 (2015).

53. Das, S., Dey, S. & Dash, S. K. Direct radiative effects of anthropogenic aerosols on Indian summer monsoon circulation. *Theor. Appl. Climatol.* **124**, 629–639 (2016).
54. Guo, L., Turner, A. G. & Highwood, E. J. Local and remote impacts of aerosol species on indian summer monsoon rainfall in a GCM. *J. Clim.* **29**, 6937–6955 (2016).
55. Gadgil, S. & Joseph, P. V. On breaks of the Indian monsoon. *Proc. Indian Acad. Sci. Earth Planet. Sci.* **112**, 529–558 (2003).
56. Rajeevan, M., Gadgil, S. & Bhate, J. Active and break spells of the Indian summer monsoon. *NCC Research Report: March 2008.* **2002**, 229–247 (2008).
57. Dash, S. K., Kulkarni, M. A., Mohanty, U. C. & Prasad, K. Changes in the characteristics of rain events in India. *J. Geophys. Res. Atmos.* **114** (2009).
58. Singh, D., Tsiang, M., Rajaratnam, B. & Di, N. S. Observed changes in extreme wet and dry spells during the South Asian summer monsoon season. *Nat. Clim. Chang.* **4**, 1–6 (2014).
59. Mandke, S. K., Sahai, A. K., Shinde, M. A., Joseph, S. & Chattopadhyay, R. Ocean circulation: Thermohaline circulation. *Int. J. Climatol.* **27**, 837–859 (2007).
60. Sikka, D. R. Some aspects of the large scale fluctuations of summer monsoon rainfall over India in relation to fluctuations in the planetary and regional scale circulation parameters. *Proc. Indian Acad. Sci. - Earth Planet. Sci.* **89**, 179–195 (1980).
61. Bond, T. C. *et al*. Bounding the role of black carbon in the climate system: A scientific assessment. *J. Geophys. Res. Atmos.* **118**, 5380–5552 (2013).
62. Torres, O. *et al*. Aerosols and surface UV products form Ozone Monitoring Instrument observations: An overview. *J. Geophys. Res. Atmos.* **112**, 1–14 (2007).
63. Herman, J. R. *et al*. Global distribution of UV-absorbing aerosols from Nimbus 7/TOMS data. *J. Geophys. Res.* **102**, 16911 (1997).
64. Ramachandran, S. & Kedia, S. Aerosol-Precipitation interactions over India: Review and future perspectives. **2013** (2013).
65. IMD. *Annual Climate Summary 2005*. www.imdpune.gov.in/Clim_RCC_LRF/Products.html (2006).
66. Stern, D. I. & Kaufmann, R. K. Robust Granger causality testing of the effect of natural and anthropogenic radiative forcings on Global temperature. (2013).
67. Mosedale, T. J., Stephenson, D. B., Collins, M. & Mills, T. C. Granger causality of coupled climate processes: Ocean feedback on the North Atlantic Oscillation. *J. Clim.* **19**, 1182–1194 (2006).
68. Mokhov, I. I. & Smirnov, D. A. Diagnostics of a cause-effect relation between solar activity and the Earth's global surface temperature. *Izv. Atmos. Ocean. Phys.* **44**, 263–272 (2008).
69. Johnson, R. A. & Wichern, D. W. *Applied Multivariate Statistical Analysis*. (Prentice-Hall, Inc., 1988).

Acknowledgements

This study was supported by the Indian Institute of Technology Bombay, Centre of Excellence in Climate Studies (IITB-CECS) project of the Department of Science and Technology (DST), New Delhi, India. The author(s) wish to acknowledge use of the Ferret program for analysis and graphics in this paper. Ferret is a product of NOAA's Pacific Marine Environmental Laboratory (http://ferret.pmel.noaa.gov/Ferret/). We would also like to acknowledge R Core Team (2013): A language and environment for statistical computing. R Foundation for Statistical Computing, Vienna, Austria (http://www.R-project.org/).

Author Contributions

M.B. and C.V. provided the study concepts and interpretation of the results; P.D. carried out the data analysis, with guidance from M.B. and C.V.; M.B., C.V. and P.D. wrote the manuscript.

Additional Information

Supplementary information accompanies this paper at https://doi.org/10.1038/s41598-017-17599-1.

Competing Interests: The authors declare that they have no competing interests.

Publisher's note: Springer Nature remains neutral with regard to jurisdictional claims in published maps and institutional affiliations.

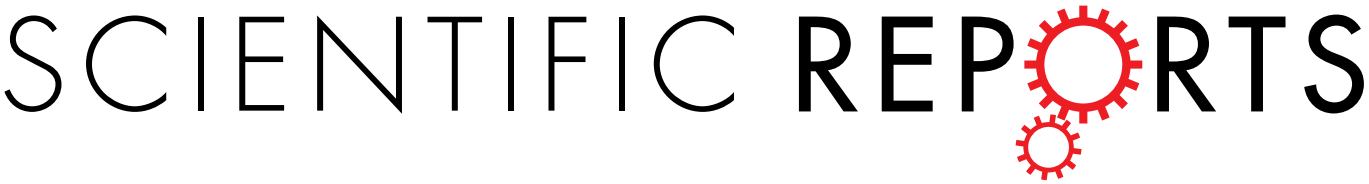

OPEN

Contrasting influences of aerosols on cloud properties during deficient and abundant monsoon years

Received: 30 August 2016
Accepted: 17 February 2017
Published: 24 March 2017

Nitin Patil[1], Prashant Dave[1] & Chandra Venkataraman[1,2]

Direct aerosol radiative forcing facilitates the onset of Indian monsoon rainfall, based on synoptic scale fast responses acting over timescales of days to a month. Here, we examine relationships between aerosols and coincident clouds over the Indian subcontinent, using observational data from 2000 to 2009, from the core monsoon region. Season mean and daily timescales were considered. The correlation analyses of cloud properties with aerosol optical depth revealed that deficient monsoon years were characterized by more frequent and larger decreases in cloud drop size and ice water path, but increases in cloud top pressure, with increases in aerosol abundance. The opposite was observed during abundant monsoon years. The correlations of greater aerosol abundance, with smaller cloud drop size, lower evidence of ice processes and shallower cloud height, during deficient rainfall years, imply cloud inhibition; while those with larger cloud drop size, greater ice processes and a greater cloud vertical extent, during abundant rainfall years, suggest cloud invigoration. The study establishes that continental aerosols over India alter cloud properties in diametrically opposite ways during contrasting monsoon years. The mechanisms underlying these effects need further analysis.

The Indian monsoon is influenced by multiple complex factors, from local physical processes to large-scale forcing. The role of aerosols has received recent attention[1–10]. Many studies have focused on monsoon rainfall changes, which are mediated by slow changes in sea surface temperatures; when changes in the sea surface temperatures degrade the north–south temperature gradient in the northern Indian Ocean, circulation changes occur that are correlated with reduced monsoon rainfall[1,5]. More recently, rapid changes in radiative forcing, because of both anthropogenic and natural aerosols[6–11], have been linked to increases in northward moisture transport and, consequently, increases in rainfall, on daily and monthly timescales. Over continental areas of north India, changes in aerosols were linked to asymmetric changes in precipitation, with increases west, and decreases east, of 80°E[8]. Some studies have identified the influences of spatially separated aerosols (dust and black carbon over Himalaya; dust outbreak over Africa) on observed increases of net diabatic heating rates in the middle to upper troposphere or a strengthened northward pressure gradient over the Arabian Sea, with consequent increases in synoptic scale moisture convergence over India.

Significant aerosol concentrations over the Indian subcontinent occur during the summer monsoon season; the aerosol levels correlate with cloud properties, as illustrated for the monsoon month of July[12] and for the deficient monsoon year of 2009[13]. Different mechanisms by which aerosols mediate cloud and rainfall development have been proposed. Meteorological covariance can obscure observational evidence of the aerosol modification of clouds. However, recent observational studies have attempted to control for meteorological effects through the classification of clouds into regimes. Absorbing aerosols could lead to stabilization of the near-surface atmosphere, leading to positive feedback that reduces cloudiness[14]. Observational evidence from the Amazon biomass burning season supports the theory that black carbon aerosols inhibit warm cloud development[15]. Absorptive dust aerosol outbreaks over the Taklimakan desert[16] and East Asia's arid regions[17], have been linked to large atmospheric warming effects and to significant reduction in the liquid and ice water path in dust-contaminated clouds[18]. In contrast, an increase in the availability of cloud condensation nuclei at the cloud base could enhance cloud "invigoration", and increase rainfall intensity[19,20]. Observations support aerosol-mediated increases in the transition from stratocumulus to convective cloud regimes[21] and rainfall intensity[22]. However, to the best of our

[1]Interdiciplinary program in Climate Studies, Indian Institute of Technology Bombay, Powai, Mumbai, India. [2]Department of Chemical Engineering, Indian Institute of Technology Bombay, Powai, Mumbai, India. Correspondence and requests for materials should be addressed to C.V. (email: chandra@iitb.ac.in)

knowledge, the modulation of monsoon clouds by both spatially and temporally coincident aerosols has received little attention.

This study focussed on three of six homogeneous monsoon rainfall regions identified on the basis of similarity in rainfall characteristics and association of sub-divisional monsoonal rainfall with regional/global circulation parameters[23]. The three selected regions, together account for over 85% of annual summer monsoon rainfall and constitute the "core monsoon zone" over the Indian subcontinent[24,25]. To investigate the aerosol modulation of clouds and rainfall during deficient and abundant monsoon years, we used observational data from June to September (JJAS), from 2000 to 2009. These data were coincident in space and time and include gridded monsoon rainfall[26,27], aerosol optical depth (AOD) and cloud properties, sourced from the Moderate Resolution Imaging Spectroradiometer (MODIS) Terra and Aqua Level 3 satellites.

A seasonal normalized precipitation anomaly was used to identify deficient and abundant rainfall years in each region. The season mean variables in abundant and deficient rainfall years, respectively, were aggregated at a pixel level, to analyse the anomalies in coincident aerosol abundance and cloud properties, during the summer monsoon months of 2000–2009. The specific issue addressed in this work relates to whether the nature of aerosol modulation of cloud properties remain the same under distinct conditions encountered in different monsoon years, i.e. in deficient versus abundant monsoon years, do aerosols affect clouds in similar or dissimilar ways.

Results

Season mean rainfall, aerosol and cloud properties. The deficient and abundant rainfall years differed in the three regions studied (Supplementary Fig. S1). The combined rainfall anomalies, calculated at pixel level, for the "deficient" and "abundant" rainfall years in each region, ranged from -3 to 0 and 0 to $+3$ mm day^{-1}, respectively, for over 95% of the pixels (Fig. 1a,b). Deficient rainfall years were characterized by a greater number of "break periods" than abundant rainfall years (Table S1); a break period was defined as three or more consecutive days with the normalized rainfall anomaly below -1 (ref. 25). During the deficient rainfall years, there were eight, eight and two break periods, respectively, in R1, R2 and R3; during abundant rainfall years there were one, four and zero break periods, respectively. The numbers of days that fell within the break periods were significantly larger during deficient years (35, 42 and 8 days, respectively, in R1, R2 and R3) than in abundant years (3, 21 and 0 days, respectively) (Table S1).

An understanding of the aggregated aerosol and cloud properties during deficient and abundant rainfall years would allow an analysis of how the aerosols mediate the cloud properties. Aerosol and cloud cannot be observed simultaneously at the scale of Level-1 MODIS retrievals, wherein only pixels identified as cloud-free are used for making Level-2 aerosol retrievals. However, for the Level-3 product (at $1° \times 1°$), both cloud-free aerosol retrievals and cloud retrievals are averaged, from the respective Level-2 datasets[28], leading thereby to presence of both aerosol and cloud retrievals in the same Level-3 pixel. In the present dataset, 20–50% (70–190 data pairs) of daily retrievals at Level 3, contained both AOD and CDER data (Supplementary Fig. S2). We follow previous studies using the MODIS Level 3 product[12,13,22] to investigate aerosol-cloud interactions. Aerosol build-up has been observed, even during the JJAS monsoon months; anthropogenic emissions and dust were seen to increase columnar aerosol abundance during rainfall break periods and sometimes even during active surface rainfall periods[29], in the case of elevated dust plumes. During deficient monsoon rainfall years, largely positive anomalies in AOD were found (83% of pixels) while in abundant rainfall years these were largely negative (69% of pixels) (Fig. 1c,d). Contrasting AOD anomalies were also seen in the absolute AOD data and were larger in deficient than in abundant rainfall years for all regions, with high statistical significance ($P < 0.10$) (Supplementary Fig. S3a). Examination of the aerosol index, or the aerosol absorbing index (AAI), showed that absorbing aerosols had a similar behaviour to AOD (Supplementary Fig. S4a–c). This implies that the abundances of absorbing aerosols (dust and possibly black carbon), and those of the total aerosols, were larger in deficient monsoon years.

Key cloud properties, coincident with the aerosols detected, were significantly different between deficient and abundant rainfall years. Mean cloud drop size, measured through the cloud drop effective radius (CDER), had almost exclusively negative anomalies in all regions during the deficient rainfall years (Fig. 1e; 99% pixels) and positive anomalies during the abundant rainfall years (Fig. 1f; 84% pixels). The contrasts in the CDER anomalies were consistent with those of the CDER season mean for each region, being lower in the deficient, compared with the abundant rainfall years (Supplementary Fig. S3b) ($P < 0.10$). It is generally accepted that a critical cloud drop radius is necessary for settling and initiating auto-conversion processes; these processes mainly result from drop sweep-out by falling raindrops, leading to drop growth and the onset of precipitation. Mean cloud drop size (Supplementary Fig. S3b) observed during deficient rainfall years, particularly in R3, could inhibit rainfall development. These findings are consistent with more frequent observations of smaller cloud drop sizes in the month of July during deficient rainfall years[12]. In addition to the microphysical effects, the greater abundances of absorbing aerosols, discussed above, could potentially exert a radiative effect, through stabilization of the near-surface atmosphere[30] and lead to the inhibition of vertical moisture transport. Season mean lower tropospheric stability (Supplementary Fig. S5) showed a positive anomaly in deficient monsoon years, in contrast to a negative or negligibly positive anomaly in abundant monsoon years, over almost all parts of the three selected regions, which merits further investigation.

Analyses of other cloud properties revealed that the deficient monsoon years were characterized by largely negative anomalies of the ice water path (IWP; 91% of pixels), but positive anomalies (98%) in cloud top pressure (CTP) (Fig. 1g and i). Abundant monsoon years were characterized by positive anomalies in IWP (93%), but negative anomalies in CTP (86%) (Fig. 1h and j). Region mean values of IWP (Supplementary Fig. S3c) were lower (higher), but those of CTP were higher (lower) in all regions during deficient (abundant) rainfall years ($P < 0.10$). Similar anomalies were observed in cloud liquid water path (LWP; data not shown). At the mean cloud top height during abundant monsoon years (with a CTP of 410–580 mb) temperatures reached below freezing point (257–318 K), while during deficient rainfall years (CTP of 460–650 mb) the temperatures were largely above freezing

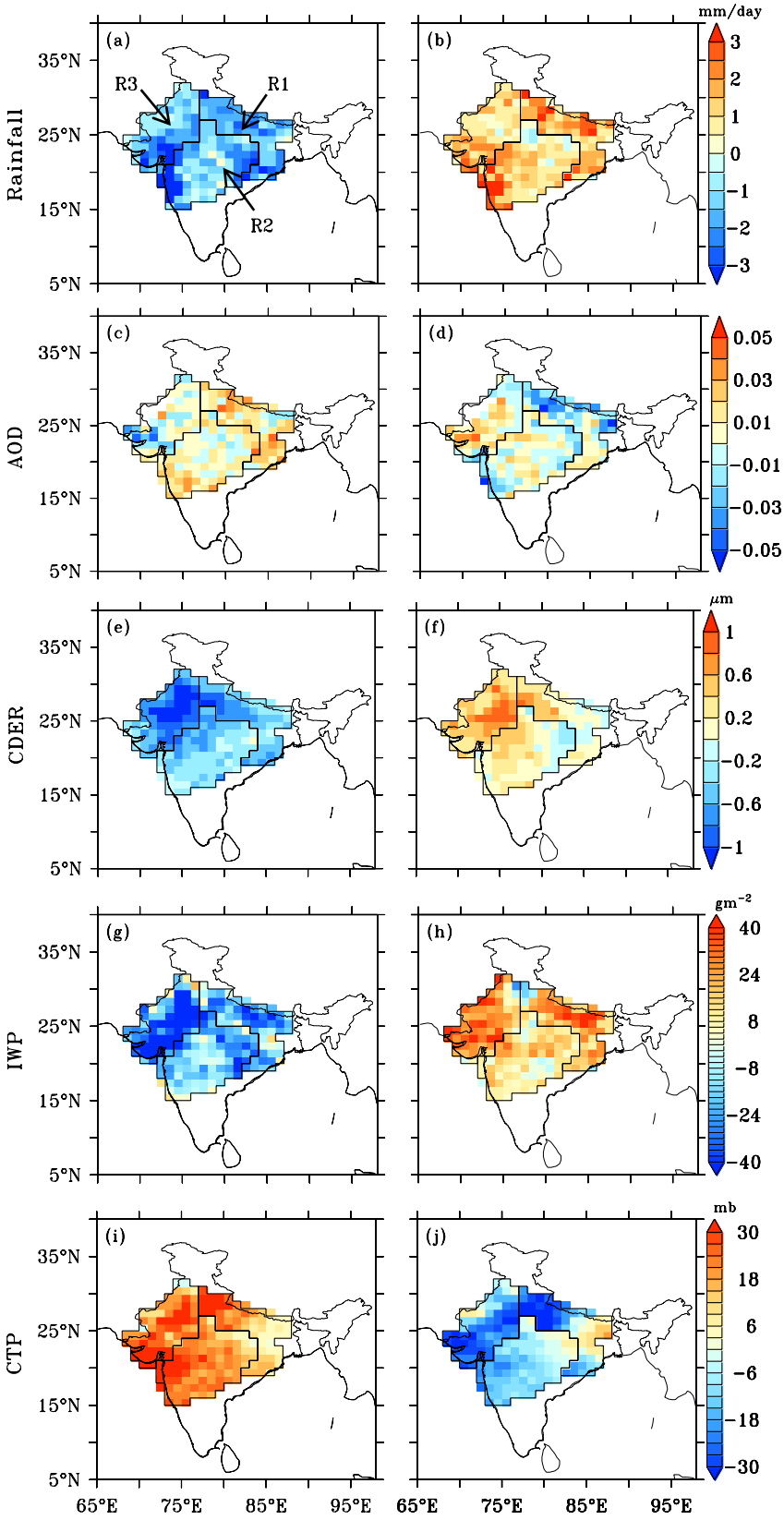

Figure 1. Spatial distribution of region-specific June–September (JJAS) anomalies during deficient (first column) and abundant (second column) rainfall years. (**a**,**b**) rainfall, (**c**,**d**) aerosol optical depth (AOD), (**e**,**f**) cloud drop effective radius (CDER, μm), (**g**,**h**) ice water path (IWP, gm^{-2}) and (**i**,**j**) cloud top pressure (CTP, mb). Figure was created using FERRET v7.0 (http://www.ferret.noaa.gov/Ferret/).

Region	Property	During deficient rainfall years				Region	Property	During abundant rainfall years			
		AOD	CDER	IWP	CTP			AOD	CDER	IWP	CTP
Region 1	AOD	1.00				Region 1	AOD	1.00			
	CDER	−0.06	1.00				CDER	−0.03	1.00		
	IWP	**0.33**	0.01	1.00			IWP	0.06	0.01	1.00	
	CTP	**0.23**	**−0.85**	**0.23**	1.00		CTP	0.09	**−0.81**	0.14	1.00
Region 2	AOD	1.00				Region 2	AOD	1.00			
	CDER	**−0.60**	1.00				CDER	**−0.13**	1.00		
	IWP	**0.26**	0.11	1.00			IWP	−0.1	−0.05	1.00	
	CTP	**0.44**	**−0.37**	0.03	1.00		CTP	0.04	**−0.52**	**0.18**	1.00
Region 3	AOD	1.00				Region 3	AOD	1.00			
	CDER	**−0.20**	1.00				CDER	−0.10	1.00		
	IWP	**−0.30**	**0.56**	1.00			IWP	0.08	**0.54**	1.00	
	CTP	**0.24**	**−0.56**	**−0.23**	1.00		CTP	**0.39**	**−0.65**	**−0.33**	1.00

Table 1. Correlations between season mean aerosol abundance and different cloud properties during deficient and abundant monsoon years in each region studied. Bold indicates a statistically significant correlation ($P < 0.10$).

(312–317 K). These results are consistent with observations of larger cloud vertical extents, and greater liquid and ice water contents during active monsoon spells[31], which occur more frequently in abundant rainfall years.

The relationships between aerosol abundance and different cloud properties were first examined through correlation analyses of the season mean values at pixel level (Table 1); this was done within each homogeneous rainfall region, to limit the spatial extent and attempt to avoid spurious correlations[32] from climatological gradients of aerosol and cloud properties, which may occur over larger spatial scales. During the season in deficient monsoon years, negative correlations were found between AOD and cloud drop size, in two of the three regions (Table 1). This indicates that higher aerosol abundances were coincident with lower cloud drop sizes. In contrast, a decrease in cloud drop size was not found with increasing AOD in abundant monsoon years, in two of the three regions. Season mean column water vapor availability showed a negative anomaly in deficient, but a positive anomaly in abundant monsoon years (Supplementary Fig. S6), indicating a combined effect of aerosols and water vapour limited regime on reduced cloud drop sizes in deficient rainfall years.

Correlation analyses of the season mean AODs with CTP and IWP showed differing behaviours among the regions (Table 1). In R3, northwest India, AOD was correlated positively with CTP, during both deficient and abundant rainfall years. In addition, increases in AOD were correlated with decreases in IWP, or reduced ice processes, during deficient monsoon years, but there were no significant correlations during abundant rainfall years. This suggests that greater aerosol abundances were coincident with shallower clouds and decreased ice processes, during deficient rainfall years. These patterns differed from those observed in R1 and R2. R1 and R2 were identified in previous studies[10] as part of the core monsoon zone. In R1 and R2, the aerosol abundances were correlated with shallower clouds, but increased ice processes, during deficient monsoon years. During abundant rainfall years, there were no significant relationships between aerosol abundance and either cloud vertical extent or ice processes. The clouds were shallowest in R3 compared with the other regions (Supplementary Fig. S3d; $P < 0.10$). As the interactions between aerosols and clouds occur on short timescales, the aerosol–cloud relationships based on the season mean, as discussed above, were further evaluated with analyses at daily timescales, below.

Daily mean aerosol and cloud properties. Temporal correlation analyses between aerosols and cloud properties, of the daily mean values at pixel level, were carried out for each year, from 2000 to 2009 (Fig. 2). In each region (R1, pixels 59; R2, pixels 87; and R3, pixels 63) for every year, the correlations between AOD and the cloud properties (CDER, IWP, LWP and CTP) were calculated using the absolute values of each parameter. The statistical significance of correlation coefficient was tested at $\alpha = 0.10$. At a given pixel, to identify the cumulative frequency of occurrence, a correlation greater than zero was assigned as $+1$ and a correlation less than zero was assigned -1. The cumulative sums of these values were calculated for deficient and abundant years separately; larger, positive values of cumulative frequency indicated the presence of more number of positive correlations and vice-versa.

During deficient rainfall years, negative correlations occurred between AOD and CDER more often than positive correlations, while the opposite pattern was observed during abundant rainfall years (Fig. 2a, b). This contrast was observed most prominently in R2 and R3. At the daily timescale, greater aerosol abundances were thus coincident with decreased (increased) cloud drop sizes in deficient (abundant) rainfall years. The negative correlations between AOD and CDER during deficient periods, and positive correlations during abundant periods, were statistically significant in all three regions (Fig. 3a–c), based on the composited analyses. Thus, an opposing influence of aerosol abundance on cloud drop size is evident; higher levels of aerosols lead to smaller cloud drop sizes in deficient, and larger size in abundant, rainfall years.

The relationships between daily-mean AOD and IWP were examined by analysing the pixels with cloud top temperatures (CTTs) less than 0 °C (Fig. 2c,d). The behaviour was different among regions. In R1 and R2 negative correlations between AOD and IWP occurred more frequently during deficient rainfall years, while positive correlations were more frequent during abundant rainfall years (Fig. 3d–f). In R3, during deficient years there were

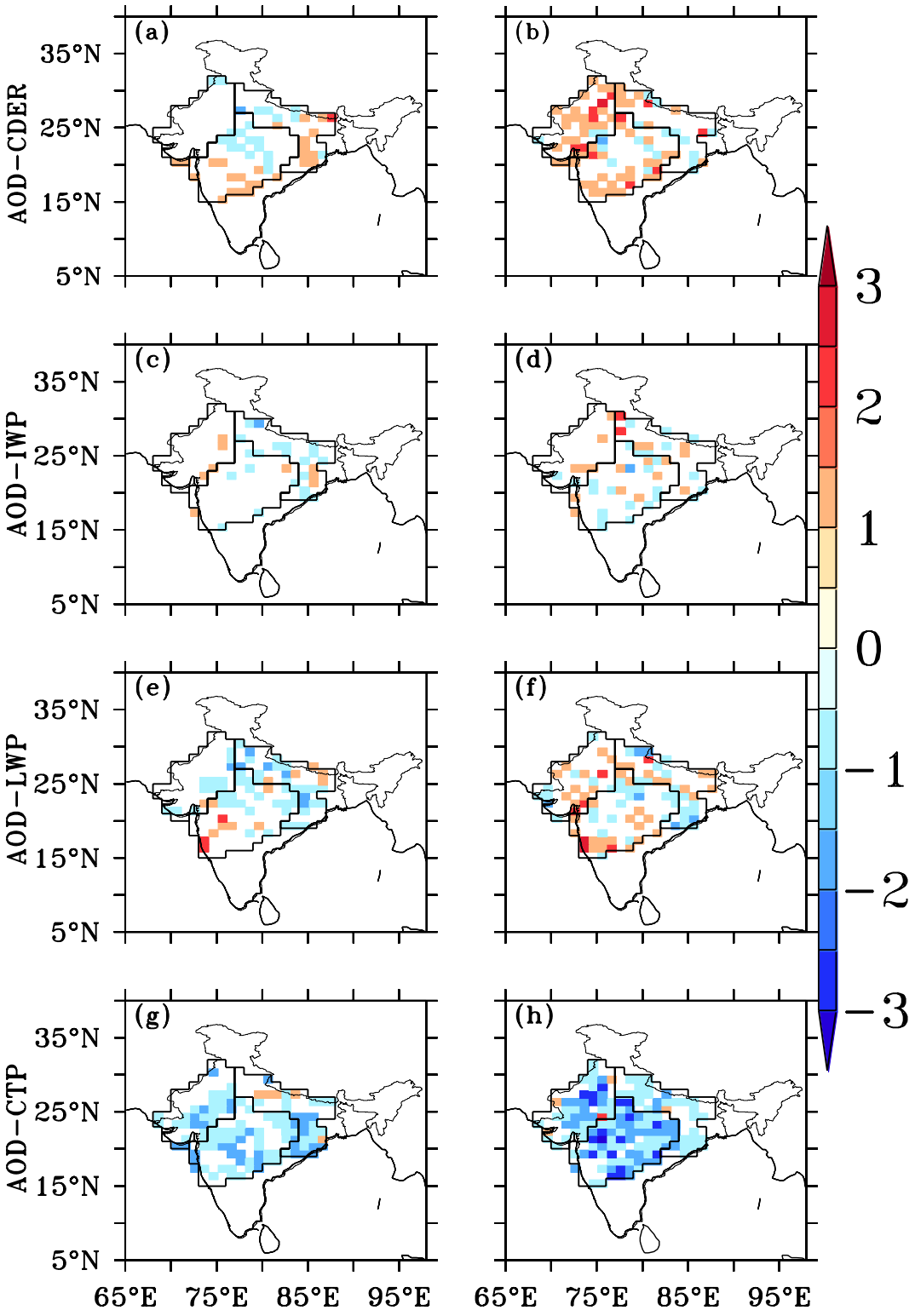

Figure 2. Temporal correlation cumulative frequency analyses during deficient (first column) and abundant (second column) rainfall years. (**a**,**b**) AOD and CDER; (**c**,**d**) AOD and IWP, where cloud top temperature (CTT) <0°; (**e**,**f**) AOD and liquid water path (LWP); and (**g**,**h**) AOD and CTP. Correlations are significant at $P < 0.1$. Figure was created using R statistical tool v3.3.1 (https://www.r-project.org/) and FERRET v7.0 (http://www.ferret.noaa.gov/Ferret/).

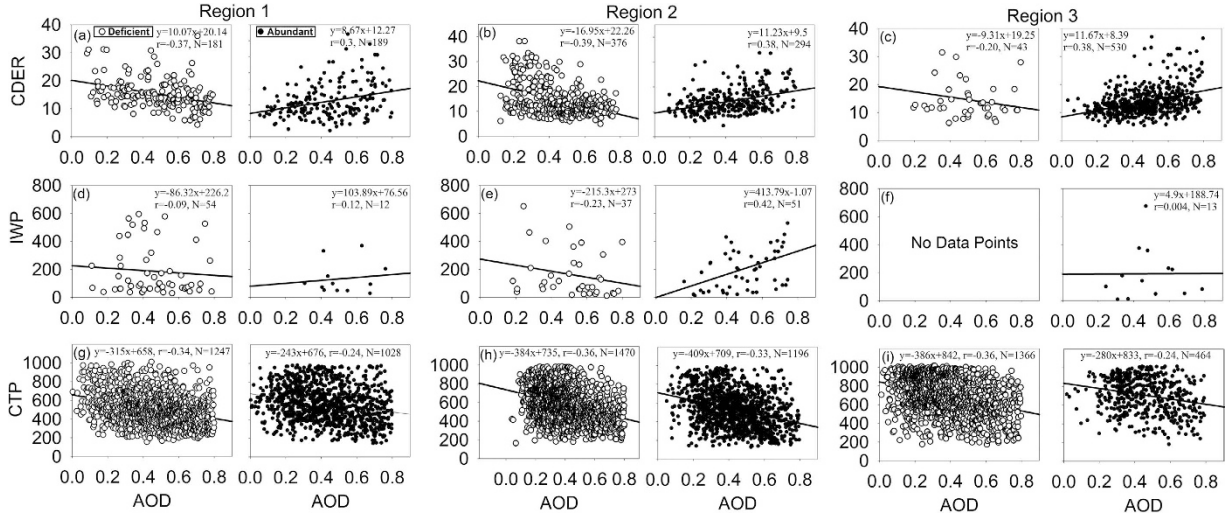

Figure 3. Scatter plot of statistically significant AOD–cloud property correlations at the pixel level, for R1, R2 and R3, during deficient and abundant rainfall years. (**a–c**) AOD and CDER (μm); (**d–f**) AOD and IWP (gm^{-2}); and (**g–i**) AOD and CTP (mb). Figure was created using SigmaPlot v11 (https://systatsoftware.com/).

not enough data points to analyse the relationship statistically, but no significant correlations were seen during the abundant rainfall years. Thus aerosols were related with a decrease in ice processes during deficient, but an increase in ice processes during abundant, rainfall years.

The relationships between AOD and LWP, were positive in both abundant and deficient rainfall years (Fig. 2e,f); positive correlations occurred more frequently during the abundant rainfall years. This implies that increases in aerosol abundance, with possibly greater availability of CCN, particularly sea salt aerosols entrained in the strong westerly monsoon flows[33], were correlated with greater amounts of liquid water in the clouds.

The AOD displayed negative anomalies in the abundant rainfall years, consistent with the rainout of aerosols. Within this depleted aerosol field, the correlations between AOD and CTP (Fig. 2g,h) were more frequently negative during abundant, than deficient, rainfall years. This indicates that with an increase in aerosol abundance, lower CTP, or higher cloud heights, occurred during the abundant monsoon years. However, the correlations between CTP and AOD (Fig. 3g–i) were not significantly different between the abundant and deficient rainfall years; this indicates that the magnitude of this effect did not change much between abundant and deficient rainfall years. We note that fewer daily data were available during the abundant monsoon years, because of missing AOD values in the satellite retrieval data.

Discussion

We used independent, but temporally and spatially coincident, data sets of rainfall data, and aerosol and cloud property data. We established contrasting correlations between aerosol abundance and cloud properties on season mean and daily mean timescales, during deficient and abundant monsoon years. The effects of aerosols act largely through microscale to mesoscale alterations of cloud microphysics and macrophysics, possibly through the alteration of lower atmospheric stability on sub-seasonal timescales. The contrasts in the correlations during deficient and abundant rainfall years, of AOD with CDER, IWP and CTP, indicate that the abundance of aerosols correlated with smaller (larger) cloud drop sizes during deficient (abundant) rainfall years. Increases in aerosol abundance were correlated with a greater persistence of lower ice processes and shallower cloud heights during deficient rainfall years, but taller clouds and, evidence of, greater ice processes, during abundant rainfall years.

Deficient monsoon years are characterized by lower levels of moisture convergence, vertical velocity and available column water vapour[24,34]. However, there is significant evidence of physical mechanisms that could explain the observed correlations between aerosol and cloud properties, while exercising caution in any interpretation. Satellite observations support the instantaneous brightening of clouds with increases in aerosol abundance, through a decrease in CDER[35] and a corresponding increase in cloud drop number concentration[36]. In addition to the microphysical effect, the presence of absorbing aerosols could potentially exert a radiative effect, through stabilization of the near-surface atmosphere because of aerosol absorption[14], which inhibits moisture transport and cloud development. Negative correlations of AOD-CDER, along with a positive anomaly in season mean lower tropospheric stability, found here in deficient monsoon years, are consistent with mechanisms suggested in previous studies.

Alternately, the aerosol–cloud invigoration mechanism[19,37], postulates that a larger abundance of aerosols at the base of warm convective clouds leads to greater vertical cloud extent, and increased invigoration, which is supported by observations[22,38]. An independent effect of aerosols on convective cloud invigoration over the Atlantic, was suggested through differences in correlations of meteorological parameters with observed aerosol optical depth from those with convective cloud properties, both in terms of the meteorological variables concerned and the correlation sign[30]. Aerosol loading was linked to invigoration of convective clouds leading to increased cloud macroscopic properties like cloud-top heights, thicknesses, and the expansion of anvil cloud fractions, in unstable, moist atmospheres in the US Great Southern Plains[39]. Positive relationships found between

cloud drop effective radius and aerosol optical depth or aerosol total concentration, in the Gulf of Mexico and South China Sea, were reproduced in model calculations upon the introduction of giant CCNs[40]. Over India, observations reveal a higher availability of sea-salt CCN in abundant monsoon years from entrainment in strong on-shore westerly flows[33].

Negative AOD–CTP correlations and positive AOD-CDER correlations, seen in this study, occurred more frequently in abundant monsoon years, along with more frequent, positive correlations between AOD and CF (Supplementary Fig. S7a,b). Negative AOD–CTP correlations observed in previous studies, were largely explained by a positive relationship between AOD and cloud fraction (CF)[22]. While AOD–CF relationships are sometimes influenced by a high-bias in aerosol retrieval, from cloud contamination or meteorological effects like aerosol humidification, these relationships have been observed using different measurement systems[22]; this suggests that they are not caused by measurement artefacts alone. The present findings imply that, when the overall greater convective activity and vertical moisture transport in abundant monsoon years is coincident with higher aerosol concentrations, deeper and taller convective clouds occur.

The main finding of the work is the opposing nature of aerosol modification of clouds in deficient versus abundant monsoon years. Overall, during deficient rainfall years, greater aerosol abundance was correlated with a smaller cloud drop size, the persistence of lower ice processes and shallower cloud heights, consistent with aerosol-mediated inhibition of cloud development. In contrast, during abundant rainfall years, aerosol abundance was correlated with a larger cloud drop size, taller clouds and greater ice processes; this implied that cloud invigoration was mediated by the coincidence of aerosols and stronger convective fields. The coincidence of aerosols and taller clouds suggests that vapour accretion during the longer duration of entrainment may explain, in part, the observed positive correlations between AOD and CDER during abundant monsoon years. Other studies have shown very important responses of the monsoon aerosol-induced changes that have acted through sea surface temperatures (linked to monsoon weakening)[1,5,41] and through temperature and pressure gradients, which facilitate moisture convergence and rainfall onset[6–11]. However, the consistent correlations seen in this work, from the daily to season timescales, show that coincident continental aerosols alter cloud properties, in diametrically opposite ways, in contrasting monsoon years. A suggestive implication of the findings is that aerosols inhibit cloud development in deficient, but invigorate it in abundant, monsoon years. Further work is needed to carefully attribute the observed relationships to the causal factors that could affect the consequent rainfall development.

Methods

Aerosol and cloud properties: MODIS Terra and Aqua Level 3 Data. Satellite measurements of cloud properties, including microphysical, optical and thermodynamic properties were used. Data included CDER, LWP, IWP, CF, CWV, CTP and CTT. Aerosol properties, including AOD, were used as measures of the columnar abundance of total and absorbed aerosols, respectively. All variables, except AAI, were downloaded from the NASA GES DISC Giovanni online data system (http://gdata1.sci.gsfc.nasa.gov/daac-bin/G3/gui.cgi?instance_id=MODIS_DAILY_L3). The data from the MODIS remote sensors on board the earth observing system (EOS) terra and aqua satellites, level 3, were used at 1° × 1°, latitude × longitude, resolution[42] for the months of JJAS, from 2000 to 2009. The MODIS instruments are flown on the Terra and Aqua satellites in sun-synchronous orbits, with equatorial crossing times of 1030 and 1330 LST, respectively. These instruments are of the same design, to reduce the error due to instrument differences. All the data products used from 2000 to 2002 were from the Terra satellite; data products from the Aqua satellite are available from July 2002 onwards. During 2003–2009, MODIS data products obtained from both the Terra and Aqua satellites were combined and utilized. Earlier studies[43] found that there are smaller differences between land and ocean AOD data from MODIS, compared with ground-based aerosol robotic network (AERONET) sun/sky radiometer measurements[44]. Since the season is characterized by the prevalence of cloudy skies, AODs larger than 0.8 were excluded from the data sets. This avoided potentially large influences of satellite retrieval errors, such as cloud contamination, or domination by aerosol swelling, from the large relative humidity around clouds. Cloud properties from MODIS L3 were derived from MODIS Atmosphere L3 Gridded Product Algorithm[28,45]. Cloud droplet effective radius retrievals from MODIS are made from the 1.6, 2.1, and 3.7 μm bands, along with analyses and L3 aggregations that enable improved spectral retrieval intercomparisons and estimate quantitative pixel level uncertainty (https://modis-atmos.gsfc.nasa.gov/_docs/C6MOD06OPUserGuide.pdf). In marine stratocumulus clouds, MODIS retrieved cloud effective radius using the 2.1 μm wavelength channel overestimated *in situ* measurements on average by 13% (ref. 46). Passive remote sensed cloud products have been widely used in previous work[12,13,22,31] investigating aerosol-cloud interactions. While data have recently become available, after 2006, from active sensors, like the Cloud-Aerosol Lidar with Orthogonal Polarization (CALIOP), a two-wavelength polarization lidar[47], and a cloud profiling radar[31], these datasets remain somewhat limited in terms of spatial and temporal coverage.

Rainfall observations. Daily mean rainfall data (1° × 1°), provided by the Indian Meteorological Department (IMD) were used for the precipitation analysis from 2000 to 2009. The rainfall data set[27] included rainfall data from 2140 stations. Deficient and abundant rainfall years in each region, were identified through the calculation of a seasonal normalized precipitation anomaly, for the monsoon months of JJAS, during the ten year period of 2000–2009.

Aerosol absorbing index (AAI): TOMS and OMI. AAI data were from the Total Ozone Mapping Spectrometer (TOMS, 1° × 1.25°) for 2000–2004[48] and the ozone monitoring instrument (OMI, 1° × 1°) for 2005–2009[49], as per their availability. To calculate anomalies, for the 10-year period (2000–2009), in the abundant and deficient monsoon years we interpolated the OMI data set on the TOMS grid (i.e. 1° × 1.25°).

Deficient and abundant rainfall years. In each region, deficient and abundant rainfall years, during the 10-year period (2000–2009), were identified through calculation of a seasonal normalized precipitation anomaly, for the monsoon months of JJAS (Supplementary Fig. S1). The normalized anomalies were calculated at the pixel level as the ratio between the difference of the annual mean from the 10-year mean, and the standard deviation of the 10-year mean values. A threshold anomaly value of ± 0.1 was used to define years as "abundant" (>0.1) and "deficient" (<-0.1) rainfall, consistent with the threshold used for the whole country (Ref: IMD Technical Circular No. 2/2007). Deficient rainfall years in R1 were 2002, 2004 and 2009; in R2 and R3 they were 2000, 2002 and 2009. Abundant rainfall years in R1 were 2003, 2007, 2008; in R2 they were 2003, 2005, 2006, and 2007; and in R3 they were 2003, 2006, 2007, and 2008 (Supplementary Fig. S1).

Pixel-level temporal correlation analysis. In each region (R1, R2 and R3) the correlations between aerosol (AOD) and cloud properties (CDER, IWP, LWP, CTP and CF) were calculated for each year (individually), using absolute values of the AOD and cloud properties. Correlation coefficients were considered statistically significant (α) at 0.10. At a given pixel, correlations greater than zero were assigned as $+1$ and correlations less than zero were assigned as -1; to identify the cumulative frequency of occurrence, these values were aggregated across deficient and abundant years. Therefore, a positive value of cumulative frequency indicates the presence of more positive correlations, and vice-versa.

Lower Tropospheric Stability (LTS). Lower tropospheric stability ($LTS = \theta_{700hPa} - \theta_{1000hPa}$; Kelvin), which is defined as the difference in potential temperature (θ) between the 700-hPa level and the surface[50], anomalies were analysed using the ERA-Interim dataset produced by the European Centre for Medium-Range Weather Forecasts[51].

References

1. Bollasina, M. A., Ming, Y. & Ramaswamy, V. Anthropogenic Aerosols and the Weakening of the South Asian Summer Monsoon. *Science*. **334,** 502–505 (2011).
2. Chung, C. E. & Ramanathan, V. Weakening of north Indian SST gradients and the monsoon rainfall in India and the Sahel. *J. Clim.* **19,** 2036–2045 (2006).
3. Meehl, G. A., Arblaster, J. M. & Collins, W. D. Effects of black carbon aerosols on the Indian monsoon. *J. Clim*. **21,** 2869–2882 (2008).
4. Wang, C., Kim, D., Ekman, A. M. L., Barth, M. C. & Rasch, P. J. Impact of anthropogenic aerosols on Indian summer monsoon. *Geophys. Res. Lett.* **36,** 1–6 (2009).
5. Ramanathan, V. *et al.* Atmospheric brown clouds: impacts on South Asian climate and hydrological cycle. *Proc. Natl. Acad. Sci. USA* **102,** 5326–33 (2005).
6. Lau, K. M., Kim, M. K. & Kim, K. M. Asian summer monsoon anomalies induced by aerosol direct forcing: The role of the Tibetan Plateau. *Clim. Dyn*. **26,** 855–864 (2006).
7. Lau, K. M. & Kim, K. M. Observational relationships between aerosol and Asian monsoon rainfall, and circulation. *Geophys. Res. Lett.* **33,** 1–5 (2006).
8. Ganguly, D., Rasch, P. J., Wang, H. & Yoon, J. H. Fast and slow responses of the South Asian monsoon system to anthropogenic aerosols. *Geophys. Res. Lett.* **39,** 1–5 (2012).
9. Manoj, M. G., Devara, P. C. S., Safai, P. D. & Goswami, B. N. Absorbing aerosols facilitate transition of Indian monsoon breaks to active spells. *Clim. Dyn*. **37,** 2181–2198 (2011).
10. Vinoj, V. *et al.* Short-term modulation of Indian summer monsoon rainfall by West Asian dust. *Nat. Geosci.* **7,** 308–313 (2014).
11. Hazra, A., Goswami, B. N. & Chen, J.-P. Role of Interactions between Aerosol Radiative Effect, Dynamics, and Cloud Microphysics on Transitions of Monsoon Intraseasonal Oscillations. *J. Atmos. Sci.* **70,** 2073–2087 (2013).
12. Ramachandran, S. & Kedia, S. Aerosol, clouds and rainfall: Inter-annual and regional variations over India. *Clim. Dyn*. **40,** 1591–1610 (2013).
13. Hazra, A. *et al.* Indian summer monsoon drought 2009: Role of aerosol and cloud microphysics. *Atmos. Sci. Lett*. **14,** 181–186 (2013).
14. Koren, I., Martins, J. V., Remer, L. A. & Afargan, H. Smoke invigoration versus inhibition of clouds over the Amazon. *Science*. **321,** 946–949 (2008).
15. Ten Hoeve, J. E., Remer, L. A. & Jacobson, M. Z. Microphysical and radiative effects of aerosols on warm clouds during the Amazon biomass burning season as observed by MODIS: Impacts of water vapor and land cover. *Atmos. Chem. Phys.* **11,** 3021–3036 (2011).
16. Huang, J. *et al.* Taklimakan dust aerosol radiative heating derived from CALIPSO observations using the Fu-Liou radiation model with CERES constraints. *Atmos. Chem. Phys. Discuss*. **9,** 5967–6001 (2009).
17. Huang, J. *et al.* Climate Effects of dust aerosols over East Asian and semiarid regions. *J. Geophys. Res. Atmos*. **119,** 11398–11416 (2014).
18. Huang, J. *et al.* Satellite-based assessment of possible dust aerosols semi-direct effect on cloud water path over East Asia. *Geophys. Res. Lett.* **33,** 2–6 (2006).
19. Rosenfeld, D. *et al.* Flood or Drought: How Do Aerosols Affect Precipitation? *Science*. **1309,** 1309–1313 (2014).
20. Khain, A., Rosenfeld, D. & Pokrovsky, A. Aerosol impact on the dynamics and microphysics of deep convective clouds. *Q. J. R. Meteorol. Soc*. **131,** 2639–2663 (2005).
21. Gryspeerdt, E. & Stier, P. Regime-based analysis of aerosol-cloud interactions. *Geophys. Res. Lett.* **39,** 1–5 (2012).
22. Gryspeerdt, E., Stier, P. & Grandey, B. S. Cloud fraction mediates the aerosol optical depth-cloud top height relationship. *Geophys. Res. Lett.* **41,** 3622–3627 (2014).
23. Parthasarathy, B., Kumar, K. R. & Munot, A. Homogeneous regional summer monsoon rainfall over India: interannual variability and teleconnections. *Research Report No*. RR-070, 0252–1075 (1996).
24. Goswami, B. N. *et al.* Increasing trend of extreme rain events over India in a warming environment. *Science*. **314,** 1442–1445 (2006).
25. Rajeevan, M., Gadgil, S. & Bhate, J. Active and break spells of the indian summer monsoon. *J. Earth Syst. Sci.* **119,** 229–247 (2010).
26. Rajeevan, M., Bhate, J., Kale, J. D. & Lal, B. Development of a High Resolution Daily Gridded Rainfall Data. *IMD - Met. Monogr. Climatol. No. 22/2005 Dev.* (2005).
27. Rajeevan, M., Bhate, J., Kale, J. D. & Lal, B. Development of a High Resolution Daily Gridded Rainfall Data Set for the Indian Region. *Curr. Sci.* **91,** 296–306 (2006).
28. Platnick, S. *et al.* The MODIS cloud products: Algorithms and examples from terra. *IEEE Trans. Geosci. Remote Sens*. **41,** 459–472 (2003).
29. Dipu, S. *et al.* Impact of elevated aerosol layer on the cloud macrophysical properties prior to monsoon onset. *Atmos. Environ.* **70,** 454–467 (2013).

30. Koren, I., Feingold, G. & Remer, L. A. The invigoration of deep convective clouds over the Atlantic: Aerosol effect, meteorology or retrieval artifact? *Atmos. Chem. Phys.* **10,** 8855–8872 (2010).
31. Rajeevan, M. *et al.* A study of vertical cloud structure of the Indian summer monsoon using CloudSat data. *Clim. Dyn.* **40,** 637–650 (2013).
32. Grandey, B. S. & Stier, P. A critical look at spatial scale choices in satellite-based aerosol indirect effect studies. *Atmos. Chem. Phys.* **10,** 11459–11470 (2010).
33. Vinoj, V. & Satheesh, S. K. Direct and indirect radiative effects of sea-salt aerosols over Arabian Sea. *Curr. Sci.* **86,** 1381–1390 (2004).
34. Roxy, M. K. *et al.* Drying of Indian subcontinent by rapid Indian Ocean warming and a weakening land-sea thermal gradient. *Nat. Commun.* **6,** 7423 (2015).
35. Kaufman, Y. J., Tanré, D. & Boucher, O. A satellite view of aerosols in the climate system. *Nature* **419,** 215–223 (2002).
36. Quaas, J., Boucher, O., Bellouin, N. & Kinne, S. Satellite-based estimate of the direct and indirect aerosol climate forcing. *J. Geophys. Res. Atmos.* **113,** 1–9 (2008).
37. Altaratz, O., Koren, I., Remer, L. A. & Hirsch, E. Review: Cloud invigoration by aerosols-Coupling between microphysics and dynamics. *Atmos. Res.* **140–141,** 38–60 (2014).
38. Gryspeerdt, E., Stier, P. & Partridge, D. G. Satellite observations of cloud regime development: The role of aerosol processes. *Atmos. Chem. Phys.* **14,** 1141–1158 (2014).
39. Yan, H. *et al.* Long-term aerosol-mediated changes in cloud radiative forcing of deep clouds at the top and bottom of the atmosphere over the Southern Great Plains. *Atmos. Chem. Phys.* **14,** 7113–7124 (2014).
40. Yuan, T., Li, Z., Zhang, R. & Fan, J. Increase of cloud droplet size with aerosol optical depth: An observation and modeling study. *J. Geophys. Res.* **113,** 1–16 (2008).
41. Ganguly, D., Rasch, P. J., Wang, H. & Yoon, J. H. Climate response of the South Asian monsoon system to anthropogenic aerosols. *J. Geophys. Res. Atmos.* **117,** 1–20 (2012).
42. Remer, L. A. *et al.* The MODIS Aerosol Algorithm, Products, and Validation. *J. Atmos. Sci.* **62,** 947–973 (2005).
43. Remer, L. A. *et al.* Global aerosol climatology from the MODIS satellite sensors. *J. Geophys. Res. Atmos.* **113,** 1–18 (2008).
44. Holben, B. N. *et al.* An emerging ground-based aerosol climatology. *J. Geophys. Res. Atmos.* **106(D11),** 12067–12 097 (2001).
45. Hubanks, P. MODIS atmosphere L3 gridded product algorithm theoretical basis document. *Modis_Atbd* (2008).
46. King, N. J., Bower, K. N., Crosier, J. & Crawford, I. Evaluating modis cloud retrievals with *in situ* observations from VOCALS-REx. *Atmos. Chem. Phys.* **13,** 191–209 (2013).
47. Winker, D. M. *et al.* The Calipso Mission: A Global 3D View of Aerosols and Clouds. *Bull. Am. Meteorol. Soc.* **91,** 1211–1229 (2010).
48. Herman, J. R. *et al.* Global distribution of UV-absorbing aerosols from Nimbus 7/TOMS data. *J. Geophys. Res.* **102,** 16911 (1997).
49. Torres, O. *et al.* Aerosols and surface UV products form Ozone Monitoring Instrument observations: An overview. *J. Geophys. Res. Atmos.* **112,** 1–14 (2007).
50. Klein, S. A. & Hartmann, D. L. The seasonal cycle of low stratiform clouds. *Journal of Climate* **6,** 1587–1606 (1993).
51. Dee, D. P. *et al.* The ERA-Interim reanalysis: Configuration and performance of the data assimilation system. *Q. J. R. Meteorol. Soc.* **137,** 553–597 (2011).

Acknowledgements

This study was supported by the Indian Institute of Technology Bombay, Centre of Excellence in Climate Studies (IITB-CECS) project of the Department of Science and Technology (DST), New Delhi, India. We thank Prof. Mani Bhushan from IIT Bombay for advice on data analysis. The author(s) wish to acknowledge use of the Ferret program for analysis and graphics in this paper. Ferret is a product of NOAA's Pacific Marine Environmental Laboratory (http://ferret.pmel.noaa.gov/Ferret/). We would also like to acknowledge R Core Team (2013): A language and environment for statistical computing. R Foundation for Statistical Computing, Vienna, Austria (http://www.R-project.org/).

Author Contributions

C.V. provided the study concept and interpretation of results; N.P. and P.D. carried out the data analysis, with guidance from C.V.; C.V., N.P. and P.D. wrote the manuscript.

Additional Information

Supplementary information accompanies this paper at http://www.nature.com/srep

Competing Interests: The authors declare no competing financial interests.

How to cite this article: Patil, N. *et al.* Contrasting influences of aerosols on cloud properties during deficient and abundant monsoon years. *Sci. Rep.* **7**, 44996; doi: 10.1038/srep44996 (2017).

Publisher's note: Springer Nature remains neutral with regard to jurisdictional claims in published maps and institutional affiliations.